UNIVERSITÉ DE LIÈGE
FACULTÉ DES SCIENCES APPLIQUÉES

Modeling of Electromagnetic Systems by Coupling of Subproblems - Application to Thin Shell Finite Element Magnetic Models

par

DANG QUOC Vuong
Ingénieur électricien

Thèse de doctorat

2013

Collection des Publcations de la Faculté des Sciences appliquées
Secretariat de la FSA, Institut de mécanique et génie civil, Sart-Tilman,
chemin des chevreuils, 1 (Bat.B52) - 4000 LIEGE 1, BELGIQUE

Thèse défendue, avec sucés, le 21 juin 2013, pour l'obtention du grade de Docteur en Sciences appliquées de l'Université de Liège.

Jury :
Professor Pierre Duysinx (Université de Liège), Président,
Professor Christophe Geuzaine (Université de Liège), Promoteur
Professor Patrick Dular (FNRS, Université de Liège), Co-promoteur,
Doctor Ruth Vazquez Sabariego (Université de Liège),
Professeur Stéphane Clénet (Ecole Nationale Supérieure d'arts et Métiers, Lille),
Professor Johan Driesen (Katholieke Universiteit Leuven),
Professor Luc Dupré (Universiteit Gent),
Professor Laurent Krähenbühl (CNRS, Laboratoire Ampère de Lyon).

Acknowledgments

First and foremost, I would like to express my deepest thanks to both my supervisor Professor Christophe Geuzaine and my co-supervisor Professor Patrick Dular for their enthusiastic guidance and excellent suggestions throughout my thesis, their kindness and encouragements. I also would like to thank them for the opportunity they gave me to do research in excellent conditions in the Department of Electrical Engineering and Computer Science of the University of Liège. In particular, I am much indebted to them for the time they have spent advising my research and teaching me many fundamental things in subproblem approach for thin shell models. I am forever grateful to them for taking me to the world of scientific research that I had hardly ever approached before. Further credit goes to Doctor Ruth Vazquez Sabariego who was always willing to give assistance at any time.

I wish to express my gratitude to the Belgium Sciency Policy (IAP 6/21 "Computational electromagnetics for electrical power applications and interactions with information technology devices" and IAP 7/02 "Multiscale Modelling of Electrical Energy Systems") for funding my research during four years.

I would like to thank Professeur Stéphane Clénet (Université de Lille 1), Professor Johan Driesen (Katholieke Universiteit Leuven), Professor Luc Dupré (Universiteit Gent), Professor Pierre Duysinx (Université de Liège), Professor Laurent Krähenbühl (CNRS, Laboratoire Ampère de Lyon) and Doctor Ruth Vazquez Sabariego (Université de Liège) for accepting to be members of my thesis committee.

In addition, I would like to thank Ir. Innocent Niyonzima, Ir. Axel Modave, Ir. Amaury Johen, Dr. David Colignon, Ir. Véronique Beauvois, Ir. Frédéric Plumier and all the other members of the research Unit of Applied and Computational Electromagnetics (ACE) I worked with for the last four years.

Finally, I am forever grateful to my wife Tuyet Thanh, my daughter Hien Minh, my parents, my brother, my sister and my family in-law who have always supported and encouraged me throughout all my studies at the University of Liège. In the same way, on behalf of my family, I wish to thank Professor Patrick Dular, Professor Christophe Geuzaine and Madame Brigitte Ernst (University of Liège), who have helped my wife and daughter in the important procedures to get the visas at Embassy of Belgium in Viet Nam. In particular, I would like warmly to thank Professor Patrick Dular, his family and parents for everything they have shared, encouraged and helped me, my wife and my daughter during the time in Liège.

Liège, April 2013 Dang Quoc Vuong

List of Symbols

Alphanumeric symbols

$\mathbb{E}^3$	: Three-dimensional oriented Euclidean space
$\mathbb{E}^2$	: Two-dimensional oriented Euclidean space
$\boldsymbol{x} = (x, y, z)$	: Point of $\mathbb{E}^3$
$\boldsymbol{x} = (x, y)$	: Point of $\mathbb{E}^2$
t	: Time instant
$\jmath$	: Imaginary unit
$L^2(\Omega)$, $\boldsymbol{L}^2(\Omega)$	: Spaces of square integrable scalar and vector fields over Ω
$\boldsymbol{H}(\mathbf{curl}; \Omega)$	: Stream function space $\{\boldsymbol{v} \in \boldsymbol{L}^2(\Omega) : \mathbf{curl}\, \boldsymbol{v} \in \boldsymbol{L}^2(\Omega)\}$
$\boldsymbol{H}(\mathrm{div}; \Omega)$	: Flux space $\{\boldsymbol{v} \in \boldsymbol{L}^2(\Omega) : \mathrm{div}\, \boldsymbol{v} \in L^2(\Omega)\}$
$\boldsymbol{h}$	: Magnetic field (A/m)
$\boldsymbol{b}$	: Magnetic flux density (T)
$\boldsymbol{e}$	: Electric field (V/m)
$\boldsymbol{d}$	: Electric flux density ($\mathrm{C/m^2}$)
$\boldsymbol{j}$	: Current density ($\mathrm{A/m^2}$)
ρ	: Electric charge density ($\mathrm{C/m^3}$)
$\boldsymbol{m}$	: Magnetization (A/m)
$\boldsymbol{p}$	: Electric polarization ($\mathrm{C/m^2}$)
$\boldsymbol{a}$	: Magnetic vector potential (Wb/m)
v	: Electric scalar potential (V)
c	: Speed of light in vacuum ($\simeq 1/\sqrt{\epsilon_0 \mu_0} = 2.99792458\, 10^8$ m/s)
T, H, P	: Reference tetrahedron, hexahedron and prism
N, E, F, V	: Sets of nodes, edges, faces and elements

Greek symbols

Ω	: Bounded open set of $\mathbb{E}^3$
Γ	: Boundary of Ω ($= \partial\Omega$)
ϕ	: Magnetic scalar potential (A)
σ	: Electric conductivity (S/m)
μ	: Magnetic permeability (H/m)
μ_0	: Magnetic permeability of vacuum ($= 4\pi\, 10^{-7}$ H/m)
μ_r	: Relative magnetic permeability ($= \mu/\mu_0$)
ν	: Magnetic reluctivity $\nu = 1/\mu$
ϵ	: Electric permittivity (F/m)

ϵ_0 : Electric permittivity of vacuum ($\simeq 8.854187817\,10^{-17}\,\mathrm{F/m}$)
ϵ_r : Relative electric permittivity ($= \epsilon/\epsilon_0$)
χ_m : Magnetic susceptibility
χ_e : Electric susceptibility (F/m)
ω : Angular frequency $2\pi f$ (rad/s)
f : Frequency (Hz)

Abbreviations

FEM : Finite element method
SPM : Subproblem method
FDM : Finite difference method
TS : Thin shell
VS : Volume source
SS : Surface source
BC : Boundary condition
IC : Interface condition
IBC : Impedance boundary condition

Operators

∂ : Boundary operator
$^{\mathrm{C}}$: Complement
∂_x, ∂_y, ∂_z : Space derivatives
∂_t : Time derivative
grad : Gradient
curl : Curl
div : Divergence
supp : Support
$\mathcal{K}$: Nullspace (kernel)
$\mathcal{D}$: Domain
$\mathcal{R}$: Range (codomain)
$\| \, \|_K$: Norm on the domain K
re, im : Real and imaginary parts

Introduction

Contents

Motivation

Electromagnetic problems are present everywhere in our daily life and it is generally recognized that electromagnetic modelling, and in particular computational electromagnetism, is an important part of electrical engineering and applied science. The purpose of computational electromagnetism is not to construct physical theories, but to use these theories to translate electromagnetic phenomena into a mathematical problem that will be solved by means of a computer. Computer simulations permit to solve problems that cannot be solved analytically, and are a crucial design tool used by engineers worldwide.

Classical electromagnetic phenomena are described by Maxwell's equations together with constitutive material laws. These equations are partial differential equations (PDEs) [78] that link the magnetic and electric fields and their sources. Nowadays, the direct application of numerical methods (e.g. the finite element method (FEM) or the finite difference method (FDM)) for the resolution of these PDEs has been extensively studied (see e.g. [37,84,96,126,132,134,136] for a review). Amongst these methods, the FEM has become the most popular technique for quasi-static (low frequency) electromagnetic problems like magnetostatics and magnetodynamics.

However, the direct application of the FEM to realistic devices is still challenging (see e.g. [17,18,60,61,89]). In particular, modelling difficulties arise when the dimensions of some parts of the structures are very small in comparison with the overall size of the devices (i.e. thin plates in electromagnetic shielding problems, steel laminations, air gaps in machines, etc.). In magnetodynamics, if these thin structures

are conducting, very fine meshes need to be generated in order to capture the skin effect, which becomes more and more difficult (and computationally expensive) as the frequency increases. The classical solution is to replace the volume meshes of the thin regions by impedance-type interface conditions, but this approximation can lead to significant modelling errors, especially near edges and corners.

Moreover, even when a direct application of the FEM is possible, using it as-is in the design or optimization phases of a complex device is often not the best. Indeed, the design and optimization phases usually require the solution of a great number of variations of the geometrical and/or material parameters of the device: solving the full problem for each variation is extremely costly—and sometimes downright impossible.

In order to overcome these two challenges, in this thesis we propose to follow a subproblem approach for thin shell finite element magnetic models.

Thin shell (TS) models

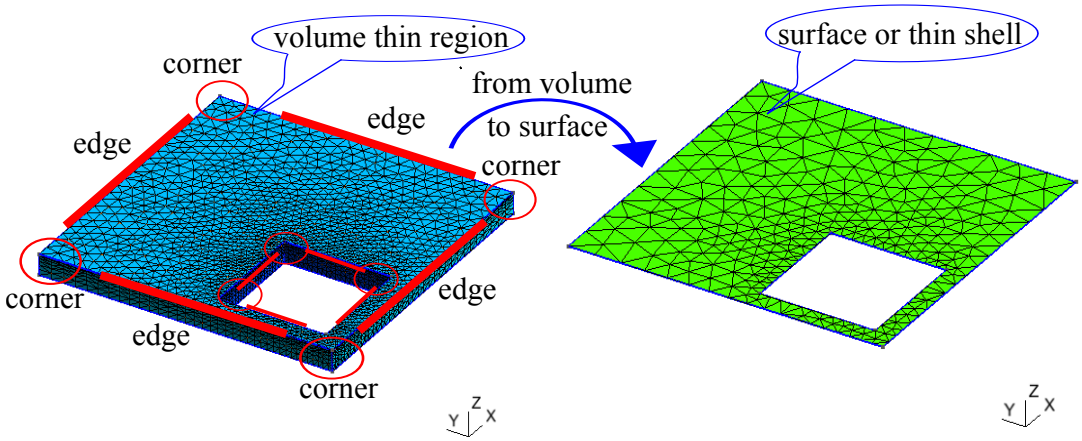

Figure 1: From volume thin region to (surface or) thin shell model.

Many papers have been published about thin electromagnetic shell modelling [17,18,60,61,65,66,89,92,105,138]: besides theoretical studies on the shielding effect and related interface conditions (ICs) [18, 60, 61, 89], several FEM formulations [17, 61, 66] or boundary element formulations [127] for the discretization of these problems have been proposed. Thin shell (TS) models [18,60,61,89] are used to avoid volumetrically meshing thin regions (Fig. 1, *left*), which are replaced by surfaces (Fig.1, *right*) with ICs. Nevertheless, as mentioned above, these ICs lead to inaccuracies on the computation of local electromagnetic quantities (current density, magnetic flux density and magnetic field) in the vicinity of geometrical discontinuities (edges and corners). Such inaccuracies increase with the thickness, and are exhacerbated for quadratic quantities like forces and Joule losses, which are often the primary quantities of interest.

In order to cope with this problem, we propose to enhance TS models by coupling them with the solution of local volumetric problems around the surfaces with ICs, on simple volume meshes that are constructed independently of the complexity of the device. The first aim of this new method is thus to correct edge and corner errors and to simplify meshing. The method is based on a subproblem approach, which separates the solution of the TS problem with ICs from the solution of the volumetric correction. This separation has two additional advantages: it can speed up the computation of variations of the design (some meshes and operator factorizations can be stored between computations) and it allows to better understand the physical contribution of different aspects of the design.

The subproblem method (SPM)

The subproblem method (SPM) consists in splitting a complete problem (e.g., in our case, a system composed of stranded inductors and conducting and magnetic, possibly thin, regions) into a series of subproblems (SPs) that define a sequence of changes, with the complete solution expressed as the sum of the SP solutions (Fig. 2). Each SP is solved on its own domain and mesh, which facilitates meshing and may increase computational efficiency. SPs can be influenced by other SPs thanks to surface sources (SSs) or volume sources (VSs): SSs express changes of ICs through surfaces from SPs, whereas VSs express changes of material properties of volume regions.

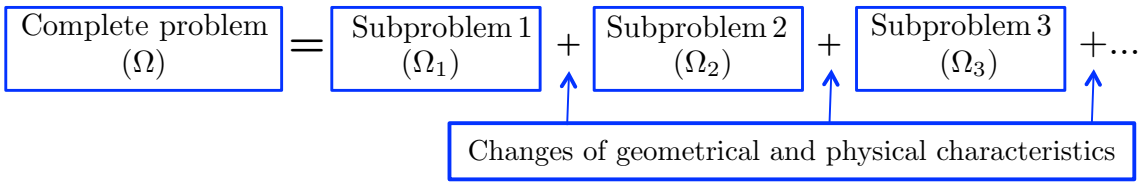

Figure 2: Decomposition of a complete problem into SPs by the SPM.

The SPM was proposed for a great variety of problems computing field distributions around multiple scattering obstacles [59, 63, 129], field distortions due to conductive regions [42], electrostatic forces on moving systems [16], eddy currents in nondestructive testing problems [41], skin and proximity effects in conductors [47], coupling between models of different dimensions [42, 44, 46] (i.e. three-dimensional with two-dimensional or one-dimensional problems), air gap and leakage flux effects [43, 45], etc.

In this thesis, the SPM is explicitly developed for adding TS models as SPs and for correcting the inherent inaccuracies of the field distributions and Joule losses near edges and corners, for both simply and multiply connected TS regions, i.e. regions with holes [21, 24]. It is also used to account for thin regions located between conducting and non-conducting regions. The method allows to couple SPs in two procedures: **one-way coupling** and **two-way coupling**. The one-way coupling is a SP sequence, where no iteration between the SPs is necessary. On the other hand,

with two-way coupling, each SP solution is influenced by all the others, which thus must be included in an iterative process.

The developments are performed for both the magnetic flux density and magnetic field formulations, with attention to the proper discretization of the constraints with SSs and VSs involved in each SP.

Goal of this thesis

This work contributes to the modelling of electromagnetic systems in two-dimensional and three-dimensional structures by coupling magnetodynamic and magnetostatic SPs via the SPM, with application to TS models. In particular, it is focused on correcting inaccuracies near edges and corners inherent to electromagnetic TS models. The SPM for TS corrections is developed for a dual approach for both magnetic flux density and magnetic field formulations, for both simply and multiply connected TS regions. The particularities linked to the computation of global quantities (e.g., voltages and currents) are considered as well. The following strategy has been followed:

1. Implement the application of the SPM inside a general software environment: GetDP [57]. GetDP (a General environment for the treatment of Discrete Problems) was developed by P. Dular and C. Geuzaine in the Department of Electrical Engineering and Computer Sciences of the University the Liège.

2. Introduce the discretization of thin regions in the weak formulations to avoid meshing the volume thin regions and to lighten the mesh of the surrounding regions.

3. Establish the sources or constraints (i.e. SSs and VSs) for two particular TS SPs: adding a TS and correcting a TS via changes of ICs through surfaces and changes of material properties of volume regions.

4. Construct all the weak formulations for SPs via SSs and VSs. A projection method for coupled SPs is introduced as well.

5. Consider the coupling between the local electromagnetic fields and global fields (i.e., currents and voltages) in the weak formulations.

6. Develop sequences to couple SPs in two procedures (one-way coupling and two-way coupling) for the two TS SPs. An iterative process for two-way coupling is then proposed.

Outline

This thesis is the result of a four year Ph.D. project carried out at the Department of Electrical Engineering and Computer Science of the University of Liège. The

main results of this work, considered in the thesis, have been published in the papers [20–24, 30, 84]. This work is organised in five chapters.

In Chapter 1, we shortly recall Maxwell's equations in differential form, ICs and BCs. The continuous mathematical structure is briefly defined, i.e. the continuous function spaces to which the unknown fields and potentials belong. For the sake of completeness, Tonti's diagram for the duality in the systems of Maxwell's equations to electromagnetic conforming formulations is then formally introduced. Some electromagnetic problems are studied as well, such as magnetostatics and magnetodynamics. A TS model is introduced.

In Chapter 2, the SPM for accurate TS models is developed for two procedures, i.e. the one-way and two-way coupling. A canonical magnetic SP is first introduced. An iterative process to improve the overall accuracy of solutions of SPs is then presented. A projection method for coupled SPs is introduced as well. In particular, two important SPs, i.e. for "adding a TS" in a configuration with an already calculated solution with other sources and for "correcting a thin shell" via a volume correction, are developed. Two procedures for the one-way and two-way coupling are next detailed. Finally, a convergence test of two-way coupling is presented to validate the developed method.

Chapters 3 and 4 deal with the development of the magnetic flux density and magnetic field formulations. The two weak formulations are first presented. The discretization of thin regions is then introduced in the weak formulations for both magnetodynamic and magnetostatic cases. SSs and VSs for SPs are next established. The coupling between local quantities and global currents and voltages is presented for the magnetodynamic weak formulations as well.

The solutions obtained for five test problems are given in Chapter 5. Two of them are based on the international TEAM (Testing Electromagnetic Analysis Methods) workshop problems 21 and 7. These test problems are chosen to validate the developed method, and allow a detailed analysis of the precision of the solution obtained by the different numerical schemes. The other test cases concern a shielded plate or shielded induction heaters or a bushing mounting plate of transformer and massive or stranded inductors. All test cases illustrate the possibilities of the developed software tools and lead to their validation.

Finally, some conclusions are drawn. The efficiency of the SPM for TS corrections is discussed and suggestions for future research are pointed out.

Original contributions

This work mainly contributes to the application of the SPM to TS models. In particular, we have developed the SPM for successive additions of TS models and then corrected their inaccuracies. Here is the list, with references to papers published in the frame of this thesis and section numbers in the manuscript, of the contributions that we believe, to the best of our knowledge, to be original:

1. The SPM is developed for correcting the inaccuracies near edges and corners

inherent to TS models, for both magnetostatic and magnetodynamic problems, for both magnetic flux density and magnetic field formulations. The SP approach developed herein couples three problems: a simplified model with only inductors, an added thin region via a TS model and a correction problem to improve the accuracy of the TS approximation, in particular near their edges and corners (see Sections 2.3.2, 2.3.3, 3.3.4, 3.3.5, 3.3.7 and 3.3.8, 4.3.4, 4.3.5, 4.3.9 and 4.3.10). This is connected with publications [20, 22, 23, 30].

2. SP approach with an $\boldsymbol{h}$-conformal magnetodynamic FE formulation is developed for accurate model of multiply connected thin regions, i.e. regions with holes, for both the associated surface model and its volume correction levels. The global currents flowing around the holes and their associated voltages are naturally coupled to the local quantities, via some cuts for magnetic scalar potential discontinuities at both TS and correction levels (see Sections 2.3.2, 2.3.3, 4.3.7, 4.3.4 and 4.3.5). This is connected with publications [21, 24].

3. The SPM is extended to account for thin regions located between conducting regions or between conducting and nonconducting regions, in the general case of multiply connected regions (see also Sections 2.3.2, 2.3.3, 4.3.7, 4.3.4 and 4.3.5). This is connected with publication [25].

My first experience with an industrial shielding problem was via a collaboration with the Ghent University, for considering influence of contact resistance on shielding efficiency of shielding gutters for high-voltage cables. Results from this work developed via the group Applied and Computational Electromagnetics (ACE) are reported in publication [84].

Chapter 1

Electromagnetic problem

Contents

1.1 Introduction

In this chapter, we briefly review some basic concepts of electromagnetic problems and Maxwell's equations [4,69,123]. They consist of a set of coupled partial differential equations (PDEs) inherent to the various components of electric and magnetic fields. Together with the material dependent constitutive laws and boundary conditions (BCs), Maxwell's equations uniquely define the electromagnetic fields. The aim of this work is to solve numerically these equations for macroscopic media.

1.2 Maxwell's equations

Maxwell's equations are a set of fundamental equations that govern all macroscopic electromagnetic phenomena. These equations constitute a system of PDEs which link the magnetic phenomena to the electric phenomena, and which unify all the principles of electromagnetism [58, 69]. The set of four equations can be written in the three-dimensional Euclidean space $\mathbb{E}^3$ as[1]:

$$\mathbf{curl}\, \boldsymbol{h} - \partial_t \boldsymbol{d} = \boldsymbol{j}, \tag{1.1}$$

$$\mathbf{curl}\, \boldsymbol{e} + \partial_t \boldsymbol{b} = 0, \tag{1.2}$$

$$\operatorname{div} \boldsymbol{b} = 0, \tag{1.3}$$

$$\operatorname{div} \boldsymbol{d} = \rho. \tag{1.4}$$

Equation (1.1) is the generalized *Ampère's law*, equation (1.2) is *Faraday's law*. Equation (1.3) is the *magnetic Gauss's law* showing the absence of *magnetic charges* and equation (1.4) is referred to *Gauss's law*. The four vector fields $\boldsymbol{h}$, $\boldsymbol{e}$, $\boldsymbol{b}$, $\boldsymbol{d}$ are called the magnetic field (A/m), the electric field (V/m), the magnetic flux density (T) and the electric flux density (C/m^2), respectively. The electric charge density ρ (C/m^3) and the current density $\boldsymbol{j}$ (A/m^2) are the source terms in these equations. When the studied phenomena are invariants in time, the time derivatives in Maxwell's equations become zero and a decoupling between magnetic and electric phenomena are decoupled.

Note that (1.1) implies, by (1.4), the equation of conservation of charge

$$\operatorname{div} \boldsymbol{j} + \partial_t \rho = 0, \tag{1.5}$$

so that, if $\boldsymbol{j}$ is given for any time, the charge can be obtained by integrating (1.5) over a volume V and by applying Gauss's theorem. This has the integral form

$$\int_{\partial V} \boldsymbol{j} \cdot \boldsymbol{n} d\boldsymbol{s} = -\frac{\partial}{\partial_t} \int_V \rho d\boldsymbol{x}, \tag{1.6}$$

which states that the total charge in a volume V changes according to the net flow of electric charges across its surface ∂V. Analogously, Gauss's law (1.3) can be deduced from (1.2) if a zero divergence of $\boldsymbol{b}$ is initially assumed.

1.2.1 Material properties

The system of Maxwell's equations (1.1)-(1.4) is still undetermined, because the number of equations is less than the number of unknowns. Hence, Maxwell's equations are only determined by taking constitutive relations into account. In free space, $\boldsymbol{b}$ and $\boldsymbol{d}$ are given by

$$\boldsymbol{b} = \mu_0 \boldsymbol{h}, \tag{1.7}$$

$$\boldsymbol{d} = \epsilon_0 \boldsymbol{e}, \tag{1.8}$$

[1] See page i for the definition of symbols.

where μ_0 is the *permeability* of free space and is the proportionality constant between $\boldsymbol{b}$ and $\boldsymbol{h}$. ϵ_0 is the *permittivity* of free space and is the proportionality constant between $\boldsymbol{d}$ and $\boldsymbol{e}$. The values of μ_0 and ϵ_0 are determined by the choice of the unit systems, and are thus not independent. In the SI system, μ_0 is given by $\mu_0 = 4\pi\, 10^{-7}\,\mathrm{H/m}$, and ϵ_0 is given by $\epsilon_0 = 1/(\mu_0 c^2)\,\mathrm{F/m}$, where c is the speed of light in vacuum. Permeable and dielectric media can be presented by the magnetisation $\boldsymbol{m}$ and the electric polarisation $\boldsymbol{p}$. Then, $\boldsymbol{b}$ and $\boldsymbol{d}$ in (1.7) and (1.8) are rewritten as [56, 75, 76, 103]

$$\boldsymbol{b} = \mu_0 \boldsymbol{h} + \mu_0 \boldsymbol{m}, \tag{1.9}$$

$$\boldsymbol{d} = \epsilon_0 \boldsymbol{e} + \boldsymbol{p}. \tag{1.10}$$

In linear magnetised media, $\boldsymbol{m}$ is given by $\boldsymbol{m} = \chi_m \boldsymbol{h}$ [91], where χ_m is the *magnetic susceptibility*, whereas in linear polarised materials, $\boldsymbol{p}$ is expressed by $\boldsymbol{p} = \epsilon_0 \chi_e \boldsymbol{e}$ [55, 75, 113], where χ_e is the *dielectric susceptibility*. Taking these relations into account, the following relations are derived:

$$\boldsymbol{b} = \mu_0(1+\chi_m)\boldsymbol{h} = \mu_0\mu_r\boldsymbol{h} = \mu\boldsymbol{h}, \tag{1.11}$$

$$\boldsymbol{d} = \epsilon_0(1+\chi_e)\boldsymbol{e} = \epsilon_0\epsilon_r\boldsymbol{e} = \epsilon\boldsymbol{e}, \tag{1.12}$$

where μ is the magnetic permeability (H/m) and ϵ is the electric permittivity (F/m). The relative permeability μ_r and electric permittivity ϵ_r of some materials are given in Tables 1.1 and 1.2 [28, 121].

The following constitutive law is expressed via the total current density, i.e.

$$\boldsymbol{j} = \boldsymbol{j}_c + \boldsymbol{j}_s\,, \tag{1.13}$$

where the term $\boldsymbol{j}_c$ is the conduction current density and is expressed by Ohm's law

$$\boldsymbol{j}_c = \sigma \boldsymbol{e}, \tag{1.14}$$

where σ is the conductivity (S/m) and is always positive (or equal to zero for insulators).

Table 1.1: Relative permeabilities μ_r of some materials.

Ferromagnetic	μ_r (H/m)	*Diamagnetic*	μ_r (H/m)	*Paramagnetic*	μ_r(H/m)
Nickel	250	Bismuth	0.99983	Aluminum	1.000021
Cobalt	600	Gold	0.99996	Magnesium	1.000012
Iron	4.000	Silver	0.99998	Palladium	1.00082
Mu metal	100.000	Copper	0.99999	Titanium	1.00018

Material characteristics μ, ϵ and σ can be non constant in nonlinear materials and can be tensors in order to take anisotropic behaviors into account. The term

Table 1.2: Relative permitivities ϵ_r of some materials.

Materials	ϵ_r (F/m)	**Materials**	ϵ_r (F/m)
Air	1.0	Polyethylene	2.3
Bakelite	5.0	Plystryrene	2.6
Glass	$4-10$	Porcelain	5.7
Mica	6.0	Rubber	$2.3-4.0$
Oil	2.3	Soil	$3-4$
Paper	$2-4$	Teflon	2.1
Paraffin max	2.2	Water	8.0
Methanol	32.6	Seawater	7.2

$\boldsymbol{j}_s$ in (1.13) is the source current density which can be taken as imposed and independent of the local electromagnetic field (e.g. in stranded conductors). Some conductivities σ are given in Table 1.3 [28, 121].

Relations (1.11), (1.12) and (1.14) are the constitutive relations or laws. In this work, we only consider linear, isotropic materials, and assume the material parameters to be time independent.

Table 1.3: Conductivities of different materials.

Materials	σ (S/m)	**Materials**	σ (S/m)
Silver	$6.17\,10^7$	Fresh water	10^{-3}
Copper	$5.80\,10^7$	Distilled water	$2\,10^{-4}$
Gold	$4.10\,10^7$	Dry soil	10^{-5}
Aluminum	$3.54\,10^7$	Transformer	10^{-11}
Brass	$1.57\,10^7$	Glass	10^{-12}
Bronze	10^7	Porcelain	$2\,10^{-13}$
Iron	10^6	Rubber	10^{-15}
Seawater	4	Fused quartz	10^{-17}

1.2.2 Boundary and interface conditions

Although the number of equations is now appropriate to the number of unknowns, the system of Maxwell's equations (1.1)–(1.4) is not yet complete. When solving PDEs in a given region, we must impose boundary conditions (BCs) as well as interface conditions (ICs) where the material parameters present discontinuities.

1.2.2.1 Interface conditions

In order to investigate the ICs of electromagnetic fields across two different materials (Fig. 1.1) [28,77], we now take the surface integral form of Maxwell's equations (1.1)–(1.4) over an open surface S with a closed contour ∂S. Applying the Stokes theorem to generalized Ampère's law (1.1) and Faraday's law (1.2), one has the corresponding integral relations [19, 28, 72, 73, 131]:

$$\oint_{\partial S} \boldsymbol{h} \cdot d\boldsymbol{r} = \int_S (\boldsymbol{j} + \partial_t \boldsymbol{d}) \cdot d\boldsymbol{s}, \tag{1.15}$$

$$\oint_{\partial S} \boldsymbol{e} \cdot d\boldsymbol{r} = -\int_S \partial_t \boldsymbol{b} \cdot d\boldsymbol{s}. \tag{1.16}$$

In a similar way, the application of Gauss' theorem to equations (1.3) and (1.4) over a volume V with a boundary ∂V, gives the following integral forms:

$$\int_{\partial V} \boldsymbol{b} \cdot d\boldsymbol{s} = 0, \tag{1.17}$$

$$\int_{\partial V} \boldsymbol{d} \cdot d\boldsymbol{s} = \int_V \rho dV. \tag{1.18}$$

Equation (1.17) shows that there is no net flux of $\boldsymbol{b}$ through a closed surface ∂V. Equation (1.18) implies that the flux of $\boldsymbol{d}$ through the surface ∂V equals the charge contained inside.

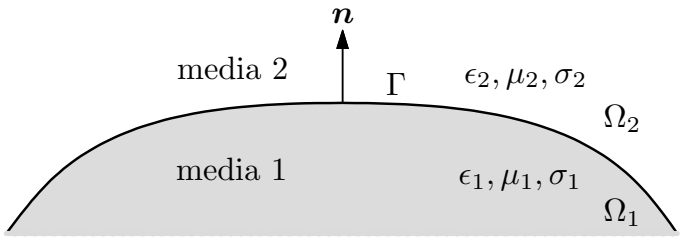

Figure 1.1: IC between two different media Ω_1 and Ω_2.

Let us now consider the boundary surface Γ between two continuous media Ω_1 and Ω_2 shown in Figure 1.1. The unit normal $\boldsymbol{n}$ on points of Γ from Ω_1 to Ω_2. Surface charge ρ^s and surface current $\boldsymbol{j}^s$ densities can exist on Γ. The ICs for the electromagnetic fields on the interface between two different media (Figure 1.1) [28, 77] can be written as

$$\boldsymbol{n} \times (\boldsymbol{h}_2 - \boldsymbol{h}_1)|_\Gamma = \boldsymbol{j}^s\,, \tag{1.19}$$

$$\boldsymbol{n} \times (\boldsymbol{e}_2 - \boldsymbol{e}_1)|_\Gamma = 0\,, \tag{1.20}$$

$$\boldsymbol{n} \cdot (\boldsymbol{b}_2 - \boldsymbol{b}_1)|_\Gamma = 0\,, \tag{1.21}$$

$$\boldsymbol{n} \cdot (\boldsymbol{d}_2 - \boldsymbol{d}_1)|_\Gamma = \rho^s\,, \tag{1.22}$$

where the subscripts 1 and 2 refer to fields on the side of the boundary surface in Ω_1 and Ω_2, respectively. These expressions are simply obtained by application of the

integral forms of Maxwell's equations to particular surfaces and volumes crossing the interface Γ.

Equations (1.19), (1.20), (1.21) and (1.22) are relative either to the tangential or normal component of the fields. This means that the normal component of $\boldsymbol{b}$ and the tangential component of $\boldsymbol{e}$ are continuous through Γ. If ρ^s and $\boldsymbol{j}^s$ are different from zero, the normal component of $\boldsymbol{d}$ and the tangential component of $\boldsymbol{h}$ are discontinuous through Γ. They are continuous when ρ^s and $\boldsymbol{j}^s$ are equal to zero.

The ICs (1.19)–(1.22) are useful for solving Maxwell's equations in different regions and then connecting the solutions to obtain the fields throughout all space.

1.2.2.2 Boundary conditions

Maxwell's equations presented in Section 1.2 uniquely define the electromagnetic fields in a finite domain if proper BCs are imposed at the boundary of the studied domain. We now consider several frequently used BCs for the normal or the tangential components of the electromagnetic fields:

- A perfectly magnetic material (PM) is denoted by Ω_{pm} (i.e. $\mu \sim \infty$). Then (1.11) implies $\boldsymbol{h} \sim 0$ on Ω_{pm}. This means that IC (1.19) thus becomes the BC, i.e.

$$\boldsymbol{n} \times \boldsymbol{h}|_{\Gamma_{pm}} = 0, \tag{1.23}$$

  where $\Gamma_{pm} = \partial\Omega_{pm}$ is the boundary of Ω_{pm}.

- A perfectly electric material (PE) is denoted by Ω_{pe} (i.e. $\sigma \sim \infty$). This means that IC (1.20) thus becomes the BC, i.e.

$$\boldsymbol{n} \times \boldsymbol{e}|_{\Gamma_{pe}} = 0, \tag{1.24}$$

  where $\Gamma_{pe} = \partial\Omega_{pe}$ is the boundary of Ω_{pe}.

- An impedance boundary condition (IBC) is finally mentioned. This is well known that in highly conducting materials, the current density distribution is concentrated near the surface. If one is interested in the field intensities in regions adjacent to highly conducting materials, the reflection at the interface can be modeled by the IBCs. These are BCs described by the relation between tangential components of the magnetic and electric fields in the following form [122]:

$$\boldsymbol{n} \times \boldsymbol{h} - Z(\boldsymbol{n} \times \boldsymbol{e}) \times \boldsymbol{n} = 0 \quad \text{on} \quad \Gamma, \tag{1.25}$$

  where Z is the impedance.

BCs (1.23) and (1.24) on the fields can take place for reasons that are either conditions at infinity or relating to symmetry conditions. More information about different types of the BCs can be found in e.g [28].

1.2.3 Time harmonic Maxwell's equations

Maxwell's equations can be solved in the frequency domain if the system is fed by a sinusoidal excitation and if all the constitutive laws are linear [67,68,100,120]. In this case, the solution fields can be presented in phasor notation as

$$\boldsymbol{h}(x,y,z,t) = \mathrm{re}(\boldsymbol{h}_m(x,y,z)e^{\jmath\omega t}), \tag{1.26}$$
$$\boldsymbol{e}(x,y,z,t) = \mathrm{re}(\boldsymbol{e}_m(x,y,z)e^{\jmath\omega t}), \tag{1.27}$$
$$\boldsymbol{b}(x,y,z,t) = \mathrm{re}(\boldsymbol{b}_m(x,y,z)e^{\jmath\omega t}), \tag{1.28}$$
$$\boldsymbol{d}(x,y,z,t) = \mathrm{re}(\boldsymbol{d}_m(x,y,z)e^{\jmath\omega t}), \tag{1.29}$$

where $\jmath = \sqrt{-1}$ is the imaginary unit, and re(.) is the real part. The vector phasors $\boldsymbol{h}_m(x,y,z), \boldsymbol{e}_m(x,y,z), \boldsymbol{b}_m(x,y,z)$ and $\boldsymbol{d}_m(x,y,z)$ depend on the position, but not on time. They contain information on the direction, magnitude, and phase of the corresponding electromagnetic field. Phasors are in general complex-valued vector fields. Analogously, the current density and charge density are expressed as

$$\boldsymbol{j}(x,y,z,t) = \mathrm{re}(\boldsymbol{j}_m(x,y,z)e^{\jmath\omega t}), \tag{1.30}$$
$$\rho(x,y,z,t) = \mathrm{re}(\rho_m(x,y,z)e^{\jmath\omega t}). \tag{1.31}$$

Via equations (1.26)–(1.31), the time derivative operator becomes a product by the factor $\jmath\omega$. If all physical fields are assumed to be phasors as in above equations, Maxwell's equations (1.1)–(1.4) in frequency domain read

$$\mathbf{curl}\,\boldsymbol{h}_m - \jmath\omega\boldsymbol{d}_m = \boldsymbol{j}_m, \tag{1.32}$$
$$\mathbf{curl}\,\boldsymbol{e}_m + \jmath\omega\boldsymbol{b}_m = 0, \tag{1.33}$$
$$\mathrm{div}\,\boldsymbol{b}_m = 0, \tag{1.34}$$
$$\mathrm{div}\,\boldsymbol{d}_m = \rho. \tag{1.35}$$

1.3 Continuous mathematical structure

1.3.1 Function spaces

Let Γ_h and Γ_e represent two complementary parts of the boundary Γ of Ω, so that

$$\Gamma = \Gamma_h \cup \Gamma_e \quad \text{and} \quad \Gamma_h \cap \Gamma_e = \emptyset, \tag{1.36}$$

where scalar fields w_h or w_e, or the trace of vector fields $\boldsymbol{w}_h$ or $\boldsymbol{w}_e$, are imposed respectively. The domains of the three operators $\mathbf{grad}_h$, $\mathbf{curl}_h$ and div_h are then defined by [28,58]

$$H_h^1(\Omega) = H_h^1(\mathbf{grad},\Omega) \stackrel{def}{=} \{w \in L^2(\Omega) : \mathbf{grad}\,w \in \boldsymbol{L}^2(\Omega)\}, \tag{1.37}$$
$$\boldsymbol{H}_h(\mathbf{curl};\Omega) \stackrel{def}{=} \{\boldsymbol{w} \in \boldsymbol{L}^2(\Omega) : \mathbf{curl}\,\boldsymbol{w} \in \boldsymbol{L}^2(\Omega)\}, \tag{1.38}$$
$$\boldsymbol{H}_h(\mathrm{div};\Omega) \stackrel{def}{=} \{\boldsymbol{w} \in \boldsymbol{L}^2(\Omega) : \mathrm{div}\,\boldsymbol{w} \in L^2(\Omega)\}, \tag{1.39}$$

and the domains of the three operators $\mathbf{grad}_e$, $\mathbf{curl}_e$ and div_e by [28, 58]

$$H^1_e(\Omega) = H^1_e(\mathbf{grad}, \Omega) \stackrel{def}{=} \{w \in L^2(\Omega) : \mathbf{grad}\, w \in \boldsymbol{L}^2(\Omega)\}, \tag{1.40}$$

$$\boldsymbol{H}_e(\mathbf{curl}; \Omega) \stackrel{def}{=} \{\boldsymbol{w} \in \boldsymbol{L}^2(\Omega) : \mathbf{curl}\, \boldsymbol{w} \in \boldsymbol{L}^2(\Omega)\}, \tag{1.41}$$

$$\boldsymbol{H}_e(\mathrm{div}; \Omega) \stackrel{def}{=} \{\boldsymbol{w} \in \boldsymbol{L}^2(\Omega) : \mathrm{div}\, \boldsymbol{w} \in L^2(\Omega)\}. \tag{1.42}$$

These spaces are the domains of the considered operators. We can denote $H^1_h(\mathbf{grad}, \Omega)$ by $H^1_h(\Omega)$ and $H^1_e(\mathbf{grad}, \Omega)$ by $H^1_e(\Omega)$. For homogeneous BCs, we obtain spaces parallel to the domains of the differential operators defined above, that will serve as function spaces for the test functions used in weak formulations. These spaces are now denoted by $H^{10}_h(\Omega)$, $\boldsymbol{H}^0_h(\mathbf{curl}; \Omega)$, $\boldsymbol{H}^0_h(\mathrm{div}; \Omega)$, $H^{10}_e(\Omega)$, $\boldsymbol{H}^0_e(\mathbf{curl}; \Omega)$ and $\boldsymbol{H}^0_e(\mathrm{div}; \Omega)$, i.e.

$$H^{10}_h(\mathbf{grad}, \Omega) \stackrel{def}{=} \{w \in H^1_h(\mathbf{grad}, \Omega), w|_{\Gamma_h} = w_h = 0\}, \tag{1.43}$$

$$\boldsymbol{H}^0_h(\mathbf{curl}; \Omega) \stackrel{def}{=} \{\boldsymbol{w} \in \boldsymbol{H}_h(\mathbf{curl}; \Omega), \boldsymbol{n} \times \boldsymbol{w}|_{\Gamma_h} = \boldsymbol{n} \times \boldsymbol{w}_h = 0\}, \tag{1.44}$$

$$\boldsymbol{H}^0_h(\mathrm{div}; \Omega) \stackrel{def}{=} \{\boldsymbol{w} \in \boldsymbol{H}_h(\mathrm{div}; \Omega), \boldsymbol{n} \cdot \boldsymbol{w}|_{\Gamma_h} = \boldsymbol{n} \cdot \boldsymbol{w}_h = 0\}, \tag{1.45}$$

and

$$H^{10}_e(\mathbf{grad}, \Omega) \stackrel{def}{=} \{w \in H^1_e(\mathbf{grad}, \Omega), w|_{\Gamma_e} = w_e = 0\}, \tag{1.46}$$

$$\boldsymbol{H}^0_e(\mathbf{curl}; \Omega) \stackrel{def}{=} \{\boldsymbol{w} \in \boldsymbol{H}_e(\mathbf{curl}; \Omega), \boldsymbol{n} \times \boldsymbol{w}|_{\Gamma_e} = \boldsymbol{n} \times \boldsymbol{w}_e = 0\}, \tag{1.47}$$

$$\boldsymbol{H}^0_e(\mathrm{div}; \Omega) \stackrel{def}{=} \{\boldsymbol{w} \in \boldsymbol{H}_e(\mathrm{div}; \Omega), \boldsymbol{n} \cdot \boldsymbol{w}|_{\Gamma_e} = \boldsymbol{n} \cdot \boldsymbol{w}_e = 0\}. \tag{1.48}$$

The operators intervening in each Green's formulas (see Section A.2), relating to each sequence, are said to be adjoint to one another [28, 58].

1.3.2 Tonti's diagram

The basic continuous structure is defined by two de Rham complexes (see Section A.1.5), put into correspondence in the following Tonti diagram [3, 10, 58, 125]:

$$\begin{array}{ccccccc}
H^1_h(\Omega) & \xrightarrow{\mathbf{grad}_h} & \boldsymbol{H}_h(\mathbf{curl}; \Omega) & \xrightarrow{\mathbf{curl}_h} & \boldsymbol{H}_h(\mathrm{div}; \Omega) & \xrightarrow{\mathrm{div}_h} & L^2(\Omega) \\
\updownarrow & & \updownarrow & & \updownarrow & & \updownarrow \\
L^2(\Omega) & \xleftarrow{\mathrm{div}_e} & \boldsymbol{H}_e(\mathrm{div}; \Omega) & \xleftarrow{\mathbf{curl}_e} & \boldsymbol{H}_e(\mathbf{curl}; \Omega) & \xleftarrow{\mathbf{grad}_e} & H^1_e(\Omega)
\end{array} \tag{1.49}$$

Both complexes in (1.49) will be referred to as either primal or dual depending on the formulation we are dealing with (e.g. the upper complex is the primal complex for magnetic field formulations, but the lower complex for magnetic flux density formulations).

Maxwell's equations (1.1)–(1.4) and the constitutive relations (1.11), (1.12) and (1.14) fit naturally in (1.49). Indeed, the vector fields such as $\boldsymbol{h}$ or $\boldsymbol{e}$, for which the useful value is its circulation along a curve, belong to $\boldsymbol{H}(\mathbf{curl}; \Omega)$. Vectors like

$\boldsymbol{b}$ or $\boldsymbol{j}$, for which the useful value is its flux across a surface, belong to $\boldsymbol{H}(\mathrm{div};\Omega)$. Analogously, scalar fields $\phi \in H^1_e(\mathbf{grad},\Omega)$ and $\rho \in L^2(\Omega)$, are evaluated locally and integrated over a volume respectively. The function spaces appropriate to the fields $\boldsymbol{h}$, $\boldsymbol{d}$, $\boldsymbol{j}$, $\boldsymbol{e}$ and $\boldsymbol{b}$ are:

$$\begin{gathered}\boldsymbol{h} \in \boldsymbol{H}_h(\mathbf{curl};\Omega), \quad \boldsymbol{d},\boldsymbol{j} \in \boldsymbol{H}_h(\mathrm{div};\Omega),\\ \boldsymbol{e} \in \boldsymbol{H}_e(\mathbf{curl};\Omega), \quad \text{and} \quad \boldsymbol{b} \in \boldsymbol{H}_e(\mathrm{div};\Omega).\end{gathered}$$

The equations and the constitutive relations are thus given in the following diagram, i.e.

$$\begin{array}{ccccccc} & \xrightarrow{\mathbf{grad}_h} & \boldsymbol{h} & \xrightarrow{\mathbf{curl}_h} & \boldsymbol{j},\boldsymbol{d} & \xrightarrow{\mathrm{div}_h} & q \\ & & \updownarrow{\scriptstyle \mu} & & \updownarrow{\scriptstyle \sigma,\epsilon} & & \\ 0 & \xleftarrow[e]{\mathrm{div}} & \boldsymbol{b} & \xleftarrow{\mathbf{curl}_e} & \boldsymbol{e} & \xleftarrow{\mathbf{grad}_e} & \end{array} \tag{1.50}$$

This diagram is very helpful for the derivation of dual finite element formulations. For electromagnetic problems, the equations always appear horizontally on both up and down sides of the diagram, whereas the constitutive laws occur vertically.

As will be seen in Chapters 3 and 4, at the discrete level, it is unfeasible to satisfy exactly both levels of Tonti's diagram and the constitutive laws in the same formulation. For the magnetodynamic case, for example, if we want to seek fields $\boldsymbol{h} \in \boldsymbol{H}_h(\mathbf{curl};\Omega)$ (1-form) on the upper level $'h'$ of (1.50), and $\boldsymbol{b} \in \boldsymbol{H}_e(\mathrm{div};\Omega)$ (2-form) on the lower level $'e'$ of (1.50), this confirms that the behavior law cannot be exactly verified in both levels. Indeed, the discretizations $\boldsymbol{H}_h(\mathbf{curl};\Omega)$ and $\boldsymbol{H}_e(\mathrm{div};\Omega)$ are generally different, i.e. no relation of the type of the behavior law between elements of these sets can exist. Based on the Tonti diagram in (1.50), we consider the magnetodynamic problem in two different ways.

First, if one exactly satisfies Ampère's law and behavior law $\boldsymbol{b} = \mu\boldsymbol{h}$, then $\boldsymbol{h} \in \boldsymbol{H}_h(\mathbf{curl};\Omega)$ and $\boldsymbol{j} \in \boldsymbol{H}_h(\mathrm{div};\Omega)$. This means that $\boldsymbol{b}$ must be in $\boldsymbol{H}_h(\mathbf{curl};\Omega)$ and thus does only let Faraday's law be weakly formulated. This approach defines the magnetic flux density formulation ($\boldsymbol{b}$-formulation).

Second, if one exactly satisfies Faraday's law and behavior law $\boldsymbol{b} = \mu\boldsymbol{h}$, then $\boldsymbol{e} \in \boldsymbol{H}_e(\mathbf{curl};\Omega)$ and $\boldsymbol{b} \in \boldsymbol{H}_e(\mathrm{div};\Omega)$. This means that $\boldsymbol{h}$ must be in $\boldsymbol{H}_e(\mathbf{curl};\Omega)$, and thus does only allow Ampere's equation be weakly formulated. This method defines the magnetic field formulation ($\boldsymbol{h}$-formulation).

The choice of one of them is made according to the type of desired conformity. The $\boldsymbol{b}$-formulation allows Ampère's law to be exactly satisfied, whereas the $\boldsymbol{h}$-formulation permits Faraday's law to be exactly satisfied. Thanks to this we can solve problem by using one of two formulations. These pairs of formulations are called dual formulations and will be presented in Chapters 3 and 4. A great variety of partial differential equation models [11, 58, 70, 71, 99] can be represented by structures like (1.49).

1.4 Definition of a general problem

Our purpose is solving Maxwell's equations (1.1)–(1.4) together with the constitutive laws (1.11), (1.12) and (1.14) in a bounded open set Ω of the oriented Euclidean space $\mathbb{E}^3$. The boundary $\partial\Omega$ of domain Ω is denoted by Γ and characterized by $\mu > 0$, $\sigma \geq 0$ and $\epsilon \geq \epsilon_0$. The studied domain Ω can be decomposed in two parts, with a conducting region Ω_c ($\sigma > 0$), and a non-conducting one $\Omega_c^{\mathrm{C}} = \Omega \backslash \Omega_c$ ($\sigma = 0$). The field of outward directed normal unit vector on Γ is denoted by $\boldsymbol{n}$. Such a configuration is depicted in Figure 1.2.

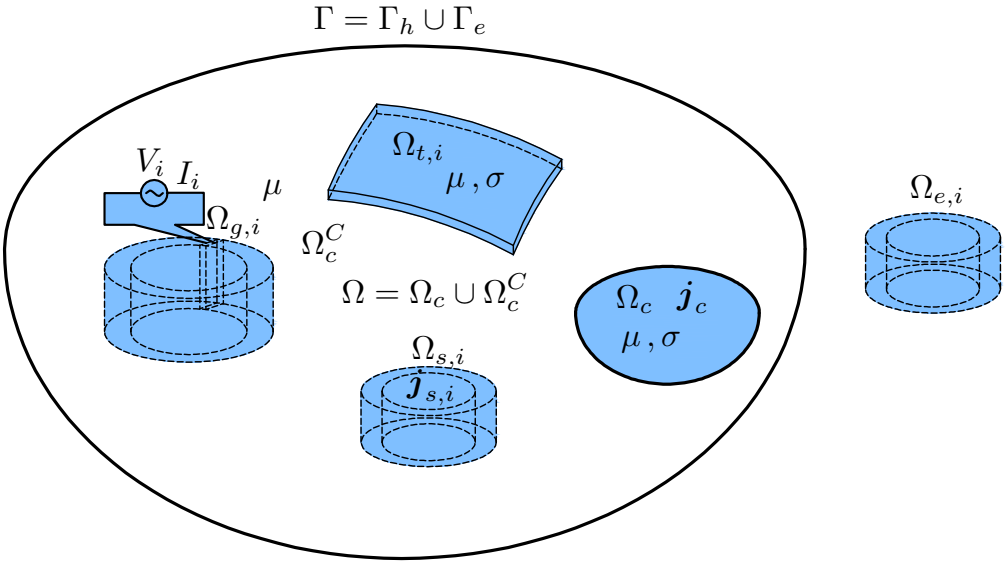

Figure 1.2: Bounded domain Ω and sub-domains Ω_s, Ω_g, and Ω_t.

In the frame of this work, the sources of electromagnetic problems can be stranded inductors defined by local quantities or global quantities (e.g. voltages and currents), and can be located inside or outside Ω (Fig. 1.2). Ω_e is considered as the set of all inductor domains $\Omega_{e,i}$, $i = 1, \ldots, e$ located outside Ω. The field created by these sources is determined *a priori*.

The sources inside studied domain Ω are confined in Ω_s and Ω_g, which are subsets of Ω presented in Sections 1.4.1 and 1.4.2. Thin regions Ω_t are presented in Section 1.4.3.

1.4.1 Inductor models Ω_s

Ω_s consists of the set of stranded inductors $\Omega_{s,i}$, $i = 1, \ldots, s$, where the source current density $\boldsymbol{j}_s$ is imposed, neglecting the skin and proximity effects in their wires. Thus Ω_s is assumed as a subset of Ω_c^{C}, with $\Omega_{s,i} \subset \Omega_c^{\mathrm{C}}$. Such inductors can be modeled by the definition of a source magnetic field $\boldsymbol{h}_s$, verifying

$$\begin{cases} \mathbf{curl}\, \boldsymbol{h}_s = \boldsymbol{j}_s & \text{in } \Omega_s \\ \mathbf{curl}\, \boldsymbol{h}_s = 0 & \text{in } \Omega \backslash \Omega_s \end{cases}. \tag{1.51}$$

Since this source field is not unique, we have some flexibility for its computation (see Section 1.5.1).

The wave form $I_i = I_i(t)$ of current density $\boldsymbol{j}_s$ can be unknown in some inductors. If the global currents I_i in inductors $\Omega_{s,i}$ are not known in advance, we have to define independent source fields $\boldsymbol{h}_{s,i}$ linked to each inductor $\Omega_{s,i}$ [28, 58], i.e. verifying

$$\begin{cases} \mathbf{curl}\, \hat{\boldsymbol{h}}_{s,i} = \hat{\boldsymbol{j}}_{s,i} & \text{in } \Omega_{s,i} \\ \mathbf{curl}\, \hat{\boldsymbol{h}}_{s,i} = 0 & \text{in } \Omega \backslash \Omega_{s,i} \end{cases}, \tag{1.52}$$

where $\hat{\boldsymbol{j}}_{s,i}$ is the equivalent current density of a unit current flowing in the N_i turns of the inductor in $\Omega_{s,i}$ [28, 58]. Thus we have

$$\boldsymbol{h_s} = \sum_i \boldsymbol{h}_{s,i} = \sum_i I_i \hat{\boldsymbol{h}}_{s,i}. \tag{1.53}$$

1.4.2 Generator models Ω_g

Ω_g is an idealization of a source of electromotive force located between two electrodes very close to each other of an inductor domain. Ω_g consists of the set of generators $\Omega_{g,i}$, $i = 1, \ldots, g$, where either a global current I_i or a global voltage V_i is imposed (Fig. 1.3) (or, in a more general way, where both V_i and I_i are *a priori* unknown when a coupling with circuit equations is considered).

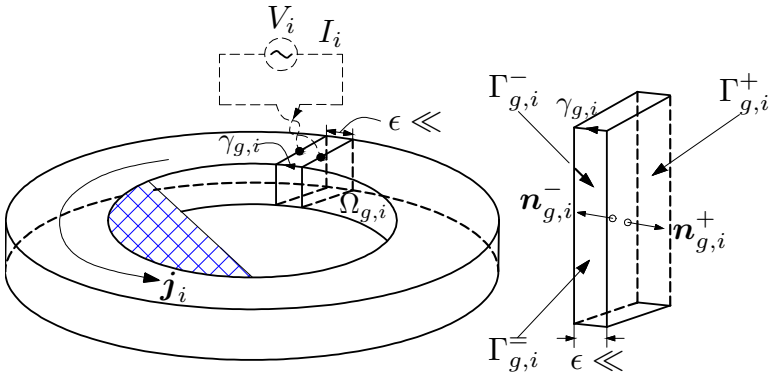

Figure 1.3: Generator $\Omega_{g,i}$ with associated global voltage V_i and current I_i.

Two different sets of inductors can be connected to these generators. We consider $\Omega_s \subset \Omega_c^{\mathrm{C}}$ and $\Omega_m \subset \Omega_c$ composed of stranded and massive inductors, respectively (Fig. 1.4).

Each $\Omega_{g,i}$ has an associated voltage V_i and current I_i flowing through one of the electrodes $\Gamma_{g,i}$ (Fig. 1.3). For massive inductors $\Omega_{m,i}$, the electric field $\boldsymbol{e}$ in $\Omega_{g,i}$ can be considered as being known and its circulation along any path $\gamma_{g,i}$ from one electrode to the other in $\Omega_{g,i}$ is actually the applied voltage V_i (see Section 3.3.6) [32, 37], i.e.

$$\oint_{\gamma_{g,i}} \boldsymbol{e} \cdot d\boldsymbol{l} = V_i \quad \text{and} \quad \int_{\Gamma_{g,i}} \boldsymbol{n} \cdot \boldsymbol{j}\, ds = I_i, \tag{1.54 a-b}$$

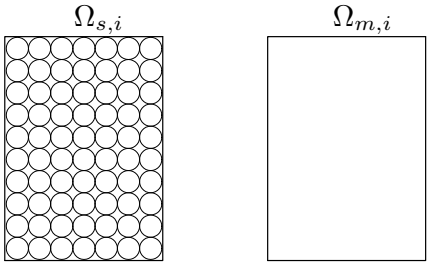

Figure 1.4: Cuts of a stranded, and massive inductor, $\Omega_{s,i}$ and $\Omega_{m,i}$.

where $\gamma_{g,i}$ is a path in $\Omega_{g,i}$ connecting two real or imaginary electrodes. Equations (1.54 a) and (1.54 b) are important in coupling of local and global quantities and will be presented in Section 3.3.6. For stranded inductors, equation (1.54 a) is expressed as the sum of the circulations of $\boldsymbol{e}$ for all the wires, and (1.54 b) is expressed as the number of turns of the winding N_i [58].

Note that the behavior of $\Omega_{g,i}$ can be described by the values of electromagnetic fields on its boundary. The abstraction of $\Omega_{g,i}$ from the studied domain Ω is replaced by a domain in which the subregion $\Omega_{g,i}$ is removed. This means that the equations are written for $\Omega \backslash \Omega_{g,i}$, whose boundary contains the boundary of $\Omega_{g,i}$ [32, 33, 58]. It is important to note that the fields of unit normals on this boundary is pointing inside each subregion $\Omega_{g,i}$, i.e.

$$\boldsymbol{n} = -\boldsymbol{n}_{g,i}. \tag{1.55}$$

As a consequence of (1.55), the following relations hold for the normals on the positive and negative sides of $\Omega_{g,i}$, i.e. $\boldsymbol{n}^{+}_{g,i} = \boldsymbol{n}_{g,i}$ and $\boldsymbol{n}^{-}_{g,i} = -\boldsymbol{n}_{g,i}$.

1.4.3 Thin regions Ω_t

Ω_t consists of the set of thin regions $\Omega_{t,i}$, $i = 1, \ldots, t$, i.e. regions for which one dimension is much smaller than the others. As proposed in [5, 38, 61, 74, 89, 97], thin shell (TS) models $\Gamma_{t,i}$ are used to avoid meshing the volume of thin regions $\Omega_{t,i}$ and to lighten the mesh of their surroundings. Thin region $\Omega_{t,i}$ is usually approximated by *a priori* known 1-D analytical distributions along the shell thickness, neglecting corner and edge effects of $\Omega_{t,i}$. The electromagnetic fields inside this region then locally obey a one-dimensional equation, whose analytical solution provides the relation between the values of the field on both sides of the region. The interior of $\Omega_{t,i}$ is thus not meshed and is rather extracted from Ω (Fig. 1.5, *left*), being reduced to a zero-thickness double layer with ICs (Fig. 1.5, *right*) linked to the inner analytical distributions [61]. This leads to inaccuracies in the vicinity of geometrical discontinuities, i.e. edges and corners, that increase with the thickness, which limits their range of validity.

Let us consider a typical thin region $\Omega_{t,i} \subset \Omega_t$ shown in Fig. 1.5. Its boundary $\partial\Omega_{t,i}$ can be split into three subsets, corresponding to the upper side $\Gamma^{+}_{t,i}$, the lower side $\Gamma^{-}_{t,i}$ and the borders $\Gamma^{=}_{t,i}$ of the region by

$$\partial\Omega_{t,i} = \Gamma^{+}_{t,i} \cup \Gamma^{-}_{t,i} \cup \Gamma^{=}_{t,i},$$

where $\Gamma^{=}_{t,i}$ is equal to zero for a closed shell. The field of outward directed normal unit vectors on the boundary $\partial\Omega_{t,i}$ of $\Omega_{t,i}$ is denoted by $\boldsymbol{n}_{t,i}$. If we denote the tangential component $\boldsymbol{n}\times(\boldsymbol{f}\times\boldsymbol{n})$ of a field $\boldsymbol{f}$ on a surface of normal $\boldsymbol{n}$ by $\boldsymbol{f}_t$, and if we keep the symbolic time derivative notation even in the Fourier space (where ∂_t should be read $i\omega$), the trace discontinuities of the magnetic field $\boldsymbol{h}$ and electric field $\boldsymbol{e}$ on both sides of TS $\Gamma_{t,i}$ are given (see Section C) by [58, 60, 61]

$$[\boldsymbol{n}_t\times\boldsymbol{h}]_{\Gamma_{t,i}} = \boldsymbol{n}_t\times\boldsymbol{h}|_{\Gamma^+_{t,i}} - \boldsymbol{n}_t\times\boldsymbol{h}|_{\Gamma^-_{t,i}} = \sigma\beta\,(\boldsymbol{e}_t|_{\Gamma^+_{t,i}} + \boldsymbol{e}_t|_{\Gamma^-_{t,i}}), \tag{1.56}$$

$$[\boldsymbol{n}_t\times\boldsymbol{e}]_{\Gamma_{t,i}} = \boldsymbol{n}_t\times\boldsymbol{e}|_{\Gamma^+_{t,i}} - \boldsymbol{n}_t\times\boldsymbol{e}|_{\Gamma^-_{t,i}} = -\partial_t\big[\mu\beta\,(\boldsymbol{h}_t|_{\Gamma^+_{t,i}} + \boldsymbol{h}_t|_{\Gamma^-_{t,i}})\big], \tag{1.57}$$

with

$$\beta = \theta^{-1}\tanh(\frac{d\theta}{2}), \qquad \theta = \frac{1+\jmath}{\delta}, \qquad \delta = \sqrt{\frac{2}{\omega\sigma\mu}}, \tag{1.58}$$

where d is the local TS thickness of $\Omega_{t,i}$, δ is the skin depth in the TS, $\omega = 2\pi f$ with f is the frequency, $\jmath$ is the imaginary unit and $\partial_t \equiv \jmath\omega$. The notation $[\cdot]_{\Gamma_{t,i}} = |_{\Gamma^+_{t,i}} - |_{\Gamma^-_{t,i}}$ expresses the discontinuities of $\boldsymbol{h}$ and $\boldsymbol{e}$ through $\Gamma_{t,i}$. When δ is large in comparison with the thickness d of the TS Ω_t ($\delta \gg d$), one has $\beta \approx d/2$.

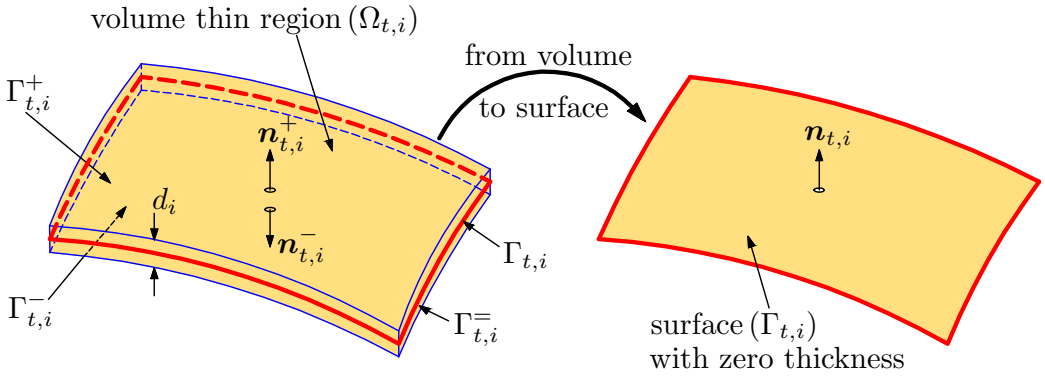

Figure 1.5: Thin region $\Omega_{t,i}$ and abstracted thin region $\Gamma_{t,i}$.

The effect of $\Omega_{t,i}$ can be described by the values of the electromagnetic fields on its boundary. The extraction of the volume $\Omega_{t,i}$ from the studied domain Ω is replaced by a domain in which the thin regions $\Omega_{t,i}$ are removed, i.e. $\Omega\backslash\Omega_{t,i}$. This means that its boundary contains the boundary of $\Omega_{t,i}$, which will be reduced to the surface $\Gamma_{t,i}$ (Fig. 1.5, *right*). The unit normal on the boundary points inside each subregion $\Omega_{t,i}$, i.e.

$$\boldsymbol{n} = -\boldsymbol{n}_{t,i}. \tag{1.59}$$

Since (1.59), the following relations hold for the normal on the positive and negative sides of $\Omega_{t,i}$, i.e., $\boldsymbol{n}^+_{t,i} = \boldsymbol{n}_{t,i}$ and $\boldsymbol{n}^-_{t,i} = -\boldsymbol{n}_{t,i}$.

1.5 Two problems

1.5.1 Magnetostatics

Two problem are considered: magnetostatics and magnetodynamics. For the magnetostatic problem, all time dependencies are dropped, i.e. $\partial_t \boldsymbol{d} = 0$ and $\partial_t \boldsymbol{b} = 0$. Maxwell's equations (1.1)–(1.4) and the constitutive law (1.11) are reduced to

$$\mathbf{curl}\, \boldsymbol{h} = \boldsymbol{j}, \quad \operatorname{div} \boldsymbol{b} = 0 \quad \text{and} \quad \boldsymbol{b} = \mu \boldsymbol{h}, \tag{1.60 a-b-c}$$

where $\boldsymbol{j} = \boldsymbol{j}_s$ is the imposed current density given in Ω_s. The magnetic flux density $\boldsymbol{b}$ in (1.60 b) can be derived from a magnetic vector potential $\boldsymbol{a}$ in the whole domain Ω, such that

$$\boldsymbol{b} = \mathbf{curl}\, \boldsymbol{a}. \tag{1.61}$$

However, $\boldsymbol{a}$ is not unique because its divergence is not specified. Indeed, if $\boldsymbol{a}$ is a solution, any function that can be written as $\boldsymbol{a}' = \boldsymbol{a} + \mathbf{grad}\, f$ is also a solution regardless of the form of f. Its uniqueness is in general imposed via a gauge condition [2, 6, 27, 28, 40, 101]. Essential BCs can be defined as

$$\boldsymbol{n} \times \boldsymbol{a} = 0 \quad \text{on} \quad \Gamma_e, \tag{1.62}$$

which implies $\boldsymbol{n} \cdot \boldsymbol{b} = 0$ on Γ_e. Note that $\boldsymbol{b}$ is always unique even if $\boldsymbol{a}$ is not.

The magnetic field $\boldsymbol{h}$ in (1.60 a) is decomposed into two parts $\boldsymbol{h}_s$ and $\boldsymbol{h}_r$, i.e.

$$\boldsymbol{h} = \boldsymbol{h}_s + \boldsymbol{h}_r, \tag{1.63}$$

where $\boldsymbol{h}_s$ is a source magnetic field due to the fixed current density $\boldsymbol{j}_s$ such that

$$\mathbf{curl}\, \boldsymbol{h}_s = \boldsymbol{j}_s. \tag{1.64}$$

The field $\boldsymbol{h}_s$ in (1.64) is only unique by imposing a gauge condition. It can be also calculated by using the Biot-Savart law [75, 107].

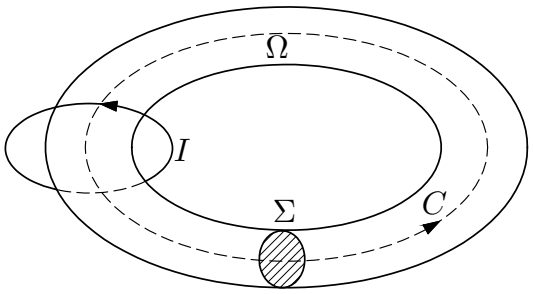

Figure 1.6: Cut surface in a multiply connected domain

The field $\boldsymbol{h}_r$ in (1.63) due to the magnetization of the magnetic materials and is called the reaction field. In regions with no current (air for intance), this field can be defined via a magnetic scalar potential ϕ, i.e.

$$\boldsymbol{h}_r = -\mathbf{grad}\, \phi. \tag{1.65}$$

Equation (1.65) seems to be simple but we must take care about the following fact. If the studied domain is not simply connected (e.g. in the case of a current loop), we must introduce a cut surface Σ through which a potential discontinuity $\Delta\phi$ is imposed [9,26,86,86,87,115,137] (see Sections 1.5.2 and 4.3.7). If the loop is carrying a current (Fig. 1.6), the magnetic field circulation on a closed curve around the wire must indeed be equal to the total current I (Ampere's theorem), i.e.

$$\oint_C \boldsymbol{h}_r \cdot d\boldsymbol{l} = \oint_C -\mathbf{grad}\,\phi \cdot d\boldsymbol{l} = -\Delta\phi = I. \tag{1.66}$$

The magnetostatic problem can be naturally presented in the Tonti diagram (1.49), where the unknown fields $\boldsymbol{h} \in \boldsymbol{H}_h(\mathbf{curl};\Omega)$, $\boldsymbol{j} \in \boldsymbol{H}_h(\mathrm{div};\Omega)$, $\boldsymbol{b} \in \boldsymbol{H}_e(\mathrm{div};\Omega)$ (solutions of (1.60) with the constitutive law (1.11)), the potentials $\phi \in H^1_e(\Omega)$ and $\boldsymbol{a} \in \boldsymbol{H}_e(\mathbf{curl};\Omega)$ can be found in (1.49), which verify (1.65) and (1.61) respectively. The spaces $H^1_h(\Omega)$, $\boldsymbol{H}_h(\mathbf{curl};\Omega)$, $\boldsymbol{H}_e(\mathbf{curl};\Omega)$ and $\boldsymbol{H}_e(\mathrm{div};\Omega)$ have been defined in Section 1.3.2 and contain the BCs applicable to the fields on the complementary parts Γ_h and Γ_e of the domain Ω. The magnetostatic Tonti's diagram is presented in (1.67)

$$\begin{array}{ccccccc} \phi & \xrightarrow{\mathbf{grad}_h} & \boldsymbol{h} & \xrightarrow{\mathbf{curl}_h} & \boldsymbol{j} & \xrightarrow{\mathrm{div}_h} & 0 \\ & & \updownarrow \mu & & & & \\ 0 & \xleftarrow{\mathrm{div}_e} & \boldsymbol{b} & \xleftarrow{\mathbf{curl}_e} & \boldsymbol{a} & & \end{array} \tag{1.67}$$

Global constraints related to the flux of $\boldsymbol{b}$ can be also introduced [28,39].

1.5.2 Magnetodynamics

In this model, the main hypothesis is that the characteristic size of the domain of Ω is much less than the wave-length $\lambda = c/f$ in each medium. Thus, the displacement current density $\partial_t \boldsymbol{d}$ in (1.1) are negligible. Maxwell's equations (1.1)–(1.4) can thus be reduced to

$$\mathbf{curl}\,\boldsymbol{e} = -\partial_t \boldsymbol{b}, \quad \mathbf{curl}\,\boldsymbol{h} = \boldsymbol{j}, \quad \mathrm{div}\,\boldsymbol{b} = 0, \tag{1.68 a-b-c}$$

with two constitutive relations (1.11) and (1.14) of materials, i.e.

$$\boldsymbol{b} = \mu \boldsymbol{h}\,, \quad \boldsymbol{j} = \sigma \boldsymbol{e}\,. \tag{1.69 a-b}$$

Equations (1.68 a-b) are to be solved with the BCs such that the fields $\boldsymbol{n} \times \boldsymbol{e}$ and $\boldsymbol{n} \times \boldsymbol{h}$ are imposed respectively on Γ_e and Γ_h.

Taking into account (1.68 c), analogously to magnetostatics, $\boldsymbol{b}$ can be derived from a vector potential $\boldsymbol{a}$ such that

$$\boldsymbol{b} = \mathbf{curl}\,\boldsymbol{a}. \tag{1.70}$$

Combining (1.70) with (1.68 a), one has $\mathbf{curl}\,(\boldsymbol{e} + \partial_t \boldsymbol{a}) = 0$, which leads to the definition of an electric scalar potential v such that

$$\boldsymbol{e} = -\partial_t \boldsymbol{a} - \mathbf{grad}\,v. \tag{1.71}$$

In a similar way to the magnetostatic case, a gauge condition must be imposed to ensure the uniqueness of $\boldsymbol{a}$. An implicit gauge in Ω_c is provided by setting v to zero (almost everywhere) in the conducting regions. This leads to a generalization of the so-called modified magnetic vector potential formulation [49, 79].

Considering (1.68 b), the magnetic field $\boldsymbol{h}$ is also decomposed as

$$\boldsymbol{h} = \boldsymbol{h}_s + \boldsymbol{h}_r - \mathbf{grad}\,\phi, \quad \text{with} \quad \mathbf{curl}\,\boldsymbol{h}_s = \boldsymbol{j}_s, \tag{1.72}$$

where the field $\boldsymbol{h}_r$ is defined in conducting regions Ω_c and the magnetic scalar potential ϕ is defined in non-conducting regions Ω_c^C. Potential ϕ in Ω_c^C is multi-valued when Ω_c^C is multiply connected, and is made single-valued via the definition of cuts Σ_i through each hole of Ω_c [9, 14, 28, 88] (see Section 4.3.7) (see [128] for information on an automatic generation of cuts).

The magnetodynamic problem is also fitted in the Tonti diagram (1.49). The unknowns fields $\boldsymbol{h} \in \boldsymbol{H}_h(\mathbf{curl};\Omega)$, $\boldsymbol{j} \in \boldsymbol{H}_h(\mathrm{div};\Omega)$, $\boldsymbol{b} \in \boldsymbol{H}_e(\mathrm{div};\Omega)$, $\boldsymbol{e} \in \boldsymbol{H}_e(\mathbf{curl};\Omega)$ (solutions of (1.68) with the constitutive laws (1.11) and (1.14)), $\phi \in H_h^1(\Omega)$, $\boldsymbol{a} \in \boldsymbol{H}_e(\mathbf{curl};\Omega)$ and $v \in H_e^1(\Omega)$ can be found in (1.49), which verify (1.72), (1.70) and (1.71) respectively. The spaces $H_h^1(\Omega)$, $\boldsymbol{H}_h(\mathbf{curl};\Omega)$, $H_e^1(\Omega)$, $\boldsymbol{H}_e(\mathbf{curl};\Omega)$ and $\boldsymbol{H}_e(\mathrm{div};\Omega)$ contain the BCs applicable to the fields on the complementary parts Γ_h and Γ_e of the domain Ω. The magnetodynamic Tonti's diagram is given by

$$\begin{array}{ccccccc}
\phi & \xrightarrow{\mathbf{grad}_h} & \boldsymbol{h} & \xrightarrow{\mathbf{curl}_h} & \boldsymbol{j} & \xrightarrow{\mathrm{div}_h} & 0 \\
 & & \updownarrow \mu & & \updownarrow \sigma & & \\
0 & \xleftarrow{\mathrm{div}_e} & \boldsymbol{b} & \xleftarrow{\mathbf{curl}_e} & \boldsymbol{e},\boldsymbol{a} & \xleftarrow{\mathbf{grad}_e} & v
\end{array} \tag{1.73}$$

Chapter 2

Subproblem method for thin regions

Contents

2.1 Introduction

In this chapter we introduce the subproblem method (SPM) for thin shell (TS) problems. We will show that the SPM allows to benefit from previous computations instead of starting a new complete finite element (FE) solution for any variation of geometrical or physical characteristics. Furthermore, each subproblem (SP) has its own geometry and is solved on its associated FE mesh, which increases computational efficiency. Two coupling strategies are analyzed: a one-way coupling where each SP only depends on the previously-solved one; and a two-way coupling where the SPs need to be solved inside an iterative procedure.

2.2 Subproblem approach

2.2.1 Canonical magnetodynamic (or static) problem

A canonical magnetodynamic (or static) problem i, to be solved at step i of the SPM, is defined in a domain Ω_i with boundary $\partial\Omega_i = \Gamma_i = \Gamma_{h,i} \cup \Gamma_{e,i}$. The eddy current conducting part of Ω_i is denoted $\Omega_{c,i}$ and the non-conducting region $\Omega_{c,i}^C$, with $\Omega_i = \Omega_{c,i} \cup \Omega_{c,i}^C$. Stranded inductors belong to $\Omega_{c,i}^C$, whereas massive inductors belong to $\Omega_{c,i}$. The equations, material relations and boundary conditions (BCs) of the SPs i are

- Equations

$$\mathbf{curl}\, \boldsymbol{h}_i = \boldsymbol{j}_i, \tag{2.1}$$
$$\mathbf{curl}\, \boldsymbol{e}_i = -\partial_t \boldsymbol{b}_i, \tag{2.2}$$
$$\operatorname{div} \boldsymbol{b}_i = 0. \tag{2.3}$$
$$\tag{2.4}$$

- Material relations

$$\boldsymbol{h}_i = \mu_i^{-1}\boldsymbol{b}_i + \boldsymbol{h}_{s,i} \quad \text{or} \quad \boldsymbol{b}_i = \mu_i \boldsymbol{h}_i + \boldsymbol{b}_{s,i}, \tag{2.5 a-b}$$
$$\boldsymbol{j}_i = \sigma_i \boldsymbol{e}_i + \boldsymbol{j}_{s,i} \quad \text{or} \quad \boldsymbol{e}_i = \sigma_i^{-1}\boldsymbol{j}_i + \boldsymbol{e}_{s,i}. \tag{2.6 a-b}$$

- Boundary conditions

$$\boldsymbol{n} \times \boldsymbol{h}_i|_{\Gamma_{h,i}} = \boldsymbol{j}_{f,i}\,,\ \boldsymbol{n} \cdot \boldsymbol{b}_i|_{\Gamma_{e,i}} = \boldsymbol{b}_{f,i}\,,\ \boldsymbol{n} \times \boldsymbol{e}_i|_{\Gamma_{e,i}} = \boldsymbol{k}_{f,i}\,, \tag{2.7 a-b-c}$$

where $\boldsymbol{n}$ is the unit normal exterior to Ω_i. The fields $\boldsymbol{h}_{s,i}$, $\boldsymbol{b}_{s,i}$, $\boldsymbol{j}_{s,i}$ and $\boldsymbol{e}_{s,i}$ in (2.5 a), (2.5 b) and (2.6 a), (2.6 b) are volume sources (VSs). With the SPM, $\boldsymbol{h}_{s,i}$, $\boldsymbol{b}_{s,i}$ are used for expressing changes of permeability, and $\boldsymbol{j}_{s,i}$ and $\boldsymbol{e}_{s,i}$ for changes of conductivity [22, 43, 45–47]. For changes in a region, from μ_t and σ_t for problem t to μ_i and σ_i for problem i, the VSs $\boldsymbol{h}_{s,i}$, $\boldsymbol{b}_{s,i}$, $\boldsymbol{j}_{s,i}$ and $\boldsymbol{e}_{s,i}$ are

$$\boldsymbol{h}_{s,i} = (\mu_i^{-1} - \mu_t^{-1})\boldsymbol{b}_t, \quad \boldsymbol{j}_{s,i} = (\sigma_i - \sigma_t)\boldsymbol{e}_t, \tag{2.8 a-b}$$
$$\boldsymbol{b}_{s,i} = (\mu_i - \mu_t)\boldsymbol{h}_t, \quad \boldsymbol{e}_{s,i} = (\sigma_i^{-1} - \sigma_t^{-1})\boldsymbol{j}_t, \tag{2.9 a-b}$$

for the total fields to be related by the updated relations $\boldsymbol{h}_t + \boldsymbol{h}_i = \mu_i^{-1}(\boldsymbol{b}_t + \boldsymbol{b}_i)$ and $\boldsymbol{j}_t + \boldsymbol{j}_i = \sigma_i(\boldsymbol{e}_t + \boldsymbol{e}_i)$.

The surface fields $\boldsymbol{j}_{f,i}, \boldsymbol{b}_{f,i}$ and $\boldsymbol{k}_{f,i}$ in (2.7 a-b-c) are generally zero for classical homogeneous BCs. Interface conditions (ICs) can define their discontinuities through any interface γ_i (with sides γ_i^+ and γ_i^-) in Ω_i, with the notation $[\cdot]_{\gamma_i} = |_{\gamma_i^+} - |_{\gamma_i^-}$. If nonzero, they define possible surface sources (SSs) that account for particular phenomena occurring at the idealized thin regions between γ_i^+ and γ_i^- [42–47], i.e.

$$[\boldsymbol{n} \times \boldsymbol{h}_i]_{\gamma_i} = \boldsymbol{n} \times \boldsymbol{h}_i|_{\gamma_i^+} - \boldsymbol{n} \times \boldsymbol{h}_i|_{\gamma_i^-} = \boldsymbol{j}_{f,i}|_{\gamma_i^+} - \boldsymbol{j}_{f,i}|_{\gamma_i^-} = [\boldsymbol{j}_{f,i}]_{\gamma_i}, \tag{2.10}$$
$$[\boldsymbol{n} \cdot \boldsymbol{b}_i]_{\gamma_i} = \boldsymbol{n} \cdot \boldsymbol{b}_i|_{\gamma_i^+} - \boldsymbol{n} \cdot \boldsymbol{b}_i|_{\gamma_i^-} = \boldsymbol{b}_{f,i}|_{\gamma_i^+} - \boldsymbol{b}_{f,i}|_{\gamma_i^-} = [\boldsymbol{b}_{f,i}]_{\gamma_i}, \tag{2.11}$$
$$[\boldsymbol{n} \times \boldsymbol{e}_i]_{\gamma_i} = \boldsymbol{n} \times \boldsymbol{e}_i|_{\gamma_i^+} - \boldsymbol{n} \times \boldsymbol{e}_i|_{\gamma_i^-} = \boldsymbol{k}_{f,i}|_{\gamma_i^+} - \boldsymbol{k}_{f,i}|_{\gamma_i^-} = [\boldsymbol{k}_{f,i}]_{\gamma_i}. \tag{2.12}$$

A typical case appears when some field traces in a previous problem are forced to be discontinuous, whereas their continuity must be recovered via a correction problem: the SSs of SP i are then fixed as the opposite of the trace discontinuity of the previous problem.

The SSs express changes of ICs through surfaces from SPs, whereas the VSs express changes of permeability and conductivity of volume regions, of which some components originate from previous problems. Mesh-to-mesh projections are thus required to express these sources in each new SP [20, 22, 30] and performed via a projection method [62, 110, 111, 114] presented in Section 2.2.3.

2.2.2 Series of coupled subproblems

The solution $\boldsymbol{x}$ ($\boldsymbol{x} \equiv \boldsymbol{h}, \boldsymbol{b}, \boldsymbol{e}, \boldsymbol{j}$,...) of a complete problem is to be expressed as the sum of SP solutions $\boldsymbol{x}_i$ supported by different meshes [43, 44]. An appropriate series of SPs is worth being defined via successive model refinements of an initially simplified model. Physical considerations usually help constructing such a series. For an ordered set P of SPs, the summation of their solutions gives the total solution, i.e.

$$\boldsymbol{x} = \sum_{i \in P} \boldsymbol{x}_i \quad \text{with} \quad \boldsymbol{x} \equiv \boldsymbol{h}, \boldsymbol{b}, \boldsymbol{e}, \boldsymbol{j}, ... \tag{2.13}$$

Each SP is governed by static or dynamic equations and constrained with SSs (2.7 a-b-c), (2.10), (2.11) and (2.12), and VSs (2.8 a-b) and (2.9 a-b).

As a consequence, each SP i is influenced by all the other SPs q in P, i.e. all the SPs are coupled. This is usually obvious for $i > q$ with the defined series. For $i < q$, it is the case when a correction becomes a significant source for any of its source SPs, which is inherent to large problems. These dependencies require iterations on the set P to calculate each solution $\boldsymbol{x}_i$ as a series of corrections $\boldsymbol{x}_{i,j}$, i.e.

$$\lim_{n \to \infty} \boldsymbol{x}_i^n = \boldsymbol{x}_i = \sum_{j=1}^{n} \boldsymbol{x}_{i,j}. \tag{2.14}$$

The total solution at iteration n is thus

$$\boldsymbol{x}^n = \sum_{i \in P} \boldsymbol{x}_i^n = \sum_{i \in P} \sum_{j=1}^{n} \boldsymbol{x}_{i,j}. \tag{2.15}$$

The error ϵ^n of a solution $\boldsymbol{x}^n$ is defined by

$$\epsilon^n = \frac{\|\boldsymbol{x}^n - \boldsymbol{x}_{\text{reference}}\|}{\|\boldsymbol{x}_{\text{reference}}\|}, \tag{2.16}$$

where $\boldsymbol{x}_{\text{reference}}$ is a reference solution (calculated for a classical numerical method). However, the reference solution is usually not known. Thus, an estimated error $\epsilon^n_{\text{estimated}}$ of a solution $\boldsymbol{x}^n$ at iteration n has to be defined, e.g. as

$$\epsilon^n_{\text{estimated}} = \frac{\|\boldsymbol{x}^n - \boldsymbol{x}^{n-1}\|}{\|\boldsymbol{x}^n\|}. \tag{2.17}$$

The computation of the corrections $\boldsymbol{x}_{i,j}$ in a SP i,j (SP i with particular constraints at iteration n) is kept on till convergence up to a desired accuracy. Each correction must account for the influence of all the previous corrections $\boldsymbol{x}_{i,j}$ of other SPs, with j the last iteration index for which a correction is known, i.e. $j = n$ or $n-1$. Initial solutions $\boldsymbol{x}_i^0$ are set to zero.

2.2.3 Projection method for coupled subproblems

Each SP is independently solved on its own mesh and its proper discretization. Thus, fields (solutions) obtained in meshes of previous SPs are then considered as SSs or VSs in the meshes of target SPs via some projections. Such projections can be implemented via an explicit interpolation or a weighted residual method based on the Galerkin method [62, 110, 111, 114]. The proposed projection method can be presented as follows.

Given a studied domain Ω and two function spaces $U \in L^2(\Omega)$ and $V \in L^2(\Omega)$ with a known field $v \in V$, find $w \in U$ by using a weighted residual method, with test function w' so that

$$\int_\Omega w(x) \cdot w'(x) dx - \int_\Omega v(x) \cdot w'(x) dx = 0, \quad \forall w' \in U. \tag{2.18}$$

In the discrete domain, fields $w \in L^2(\Omega)$ and $v \in L^2(\Omega)$ can be interpolated via the basis functions defined on the discrete domains Ω as

$$w = \sum_{j \in E_j} w_j s_{w,j}, \quad v = \sum_{i \in E_i} v_i s_{v,i}, \tag{2.19a-b}$$

where E_j and E_i are sets of geometrical entities (nodes, edges, facets or volumes) belonging to the mesh of studied domain Ω, $s_{w,j}$ and $s_{v,i}$ are the basis functions associated to the coefficients w_j and w_i. Indeed, if the field v is discretized on a mesh of SP i ($i = u$), and w on a mesh of target SP i ($i = p$), writing (2.18) in the discrete domain leads to

$$\int_\Omega w' \sum_{j \in E_p} w_{p_j} s_{p_j} dx - \int_\Omega w' \sum_{i \in E_u} v_{u_i} s_{u_i} dx = 0, \quad \forall w' \in U, \tag{2.20}$$

where E_u and E_p are sets of geometrical entities belonging to the meshes of SP u and SP p, respectively. Furthermore, s_{u_i} and s_{p_j} are the basis functions associated with the entity u on the mesh of SP u and the entity p on the mesh of SP p, respectively. Hence, the Galerkin method is applied with each basis function s_{p_j} as a test function w'. Therefore, (2.20) leads to a linear matrix system where discrete coefficients w_{p_j} are the unknown entities and discrete coefficients v_{u_i} are known. The numerical integration has to be implemented by using an appropriate number of Gauss point to accurately sample source-field variations [111]. Note that even in this case the resulting quadrature is not exact, as the variation of the field on a target element is not polynomial. To obtain an exact quadrature, the target mesh needs to be intersected with the source mesh; see e.g. [1, 52].

2.3 Subproblem coupling with TS models

2.3.1 Generalities

In the frame of the SPM, two main important SPs can be defined: for "adding a thin shell" in a configuration with an already calculated solution with other sources and for "correcting a thin shell" via its actual volume extension.

2.3.2 Subproblem: "Adding a thin shell"

The solution of an SP u is first known for a particular configuration, e.g. for an inductor alone (Fig. 2.1, a), or more generally resulting from the superposition of several SP solutions. The next SP p consists in adding a TS to this configuration (Fig. 2.1, b). From SP u to SP p, the solution u gives SSs for the added TS γ_p, through TS ICs [61].

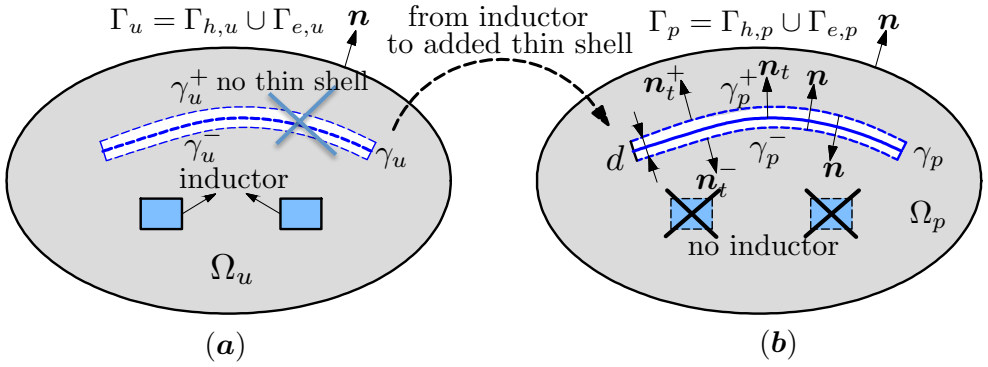

Figure 2.1: IC between SP u and SP p.

From (2.13), the total solution will thus be

$$\boldsymbol{h} = \boldsymbol{h}_u + \boldsymbol{h}_p, \quad \boldsymbol{b} = \boldsymbol{b}_u + \boldsymbol{b}_p, \quad \boldsymbol{e} = \boldsymbol{e}_u + \boldsymbol{e}_p. \tag{2.21}$$

The discontinuities of the traces $[\boldsymbol{n} \times \boldsymbol{h}_p]_{\gamma_p}$, $[\boldsymbol{n} \cdot \boldsymbol{b}_p]_{\gamma_p}$ and $[\boldsymbol{n} \times \boldsymbol{e}_p]_{\gamma_p}$ can be expressed as

$$[\boldsymbol{n} \times \boldsymbol{h}_p]_{\gamma_p} = [\boldsymbol{n} \times (\boldsymbol{h}_u + \boldsymbol{h}_p)]_{\gamma_p} - [\boldsymbol{n} \times \boldsymbol{h}_u]_{\gamma_p} = [\boldsymbol{n} \times \boldsymbol{h}]_{\gamma_p}, \tag{2.22}$$
$$[\boldsymbol{n} \cdot \boldsymbol{b}_p]_{\gamma_p} = [\boldsymbol{n} \cdot (\boldsymbol{b}_u + \boldsymbol{b}_p)]_{\gamma_p} - [\boldsymbol{n} \cdot \boldsymbol{b}_u]_{\gamma_p} = [\boldsymbol{n} \cdot \boldsymbol{b}]_{\gamma_p}, \tag{2.23}$$
$$[\boldsymbol{n} \times \boldsymbol{e}_p]_{\gamma_p} = [\boldsymbol{n} \times (\boldsymbol{e}_u + \boldsymbol{e}_p)]_{\gamma_p} - [\boldsymbol{n} \times \boldsymbol{e}_u]_{\gamma_p} = [\boldsymbol{n} \times \boldsymbol{e}]_{\gamma_p}, \tag{2.24}$$

because there are no discontinuities in SP u (before adding γ_p). Also, the traces of $\boldsymbol{h}_p$, $\boldsymbol{b}_p$ and $\boldsymbol{e}_p$ on the positive side of γ_p^+ can be expressed as

$$\boldsymbol{n} \times \boldsymbol{h}_p|_{\gamma_p^+} = \boldsymbol{n} \times (\boldsymbol{h}_u + \boldsymbol{h}_p)|_{\gamma_{p^+}} - \boldsymbol{n} \times \boldsymbol{h}_u|_{\gamma_p^+} = \boldsymbol{n} \times \boldsymbol{h}|_{\gamma_{p^+}} - \boldsymbol{n} \times \boldsymbol{h}_u|_{\gamma_p^+}, \tag{2.25}$$
$$\boldsymbol{n} \cdot \boldsymbol{b}_p|_{\gamma_p^+} = \boldsymbol{n} \cdot (\boldsymbol{b}_u + \boldsymbol{b}_p)|_{\gamma_{p^+}} - \boldsymbol{n} \cdot \boldsymbol{b}_u|_{\gamma_p^+} = \boldsymbol{n} \cdot \boldsymbol{b}|_{\gamma_{p^+}} - \boldsymbol{n} \cdot \boldsymbol{b}_u|_{\gamma_p^+}, \tag{2.26}$$
$$\boldsymbol{n} \times \boldsymbol{e}_p|_{\gamma_p^+} = \boldsymbol{n} \times (\boldsymbol{e}_u + \boldsymbol{e}_p)|_{\gamma_{p^+}} - \boldsymbol{n} \times \boldsymbol{e}_u|_{\gamma_p^+} = \boldsymbol{n} \times \boldsymbol{e}|_{\gamma_{p^+}} - \boldsymbol{n} \times \boldsymbol{e}_u|_{\gamma_p^+}. \tag{2.27}$$

The traces $\boldsymbol{n} \times \boldsymbol{h}_u|_{\gamma_p^+}$, $\boldsymbol{n} \cdot \boldsymbol{b}_u|_{\gamma_p^+}$ and $\boldsymbol{n} \times \boldsymbol{e}_u|_{\gamma_p^+}$ are thus SSs for TS SP p and denoted by $\boldsymbol{j}_{f,u}$, $\boldsymbol{b}_{f,u}$ and $\boldsymbol{k}_{f,u}$, respectively. Thus, (2.25), (2.26) and (2.27) become

$$\boldsymbol{n} \times \boldsymbol{h}_p|_{\gamma_p^+} = \boldsymbol{n} \times \boldsymbol{h}|_{\gamma_{p^+}} - \boldsymbol{j}_{f,u}, \tag{2.28}$$

$$\boldsymbol{n} \cdot \boldsymbol{b}_p|_{\gamma_p^+} = \boldsymbol{n} \cdot \boldsymbol{b}|_{\gamma_{p^+}} - \boldsymbol{b}_{f,u}, \tag{2.29}$$

$$\boldsymbol{n} \times \boldsymbol{e}_p|_{\gamma_p^+} = \boldsymbol{n} \times \boldsymbol{e}|_{\gamma_{p^+}} - \boldsymbol{k}_{f,u}. \tag{2.30}$$

The traces of the total fields in (2.28), (2.29), (2.30) and their discontinuities in (2.22), (2.23), (2.24) are given by the TS model [60, 61] (see Section 1.4.3).

The SSs $\boldsymbol{j}_{f,u}$ in (2.28), $\boldsymbol{b}_{f,u}$ in (2.29) and $\boldsymbol{f}_{f,u}$ in (2.30) completely define the sources for TS SP p. At the weak formulation level, some of them will have to be expressed strongly (essential BCs and ICs) and others weakly (natural BCs and ICs) via the weak formulation of SP u as will be presented in Chapters 3 and 4.

2.3.3 Subproblem: "Correcting a thin shell'

A TS solution obtained in an SP p can be further improved by a volume correction SP k via SSs and VSs that overcome the TS assumptions [61]. SP k has to suppress the TS representation via SSs opposed to TS discontinuities, in parallel to VSs in the added actual volume that account for changes of material properties in the added volume region (Fig. 2.2). This defines a surface-to-volume correction. Such a correction generally leads to local modifications of the solution, which thus allows to reduce the calculation domain and its mesh in the surroundings of the thin regions.

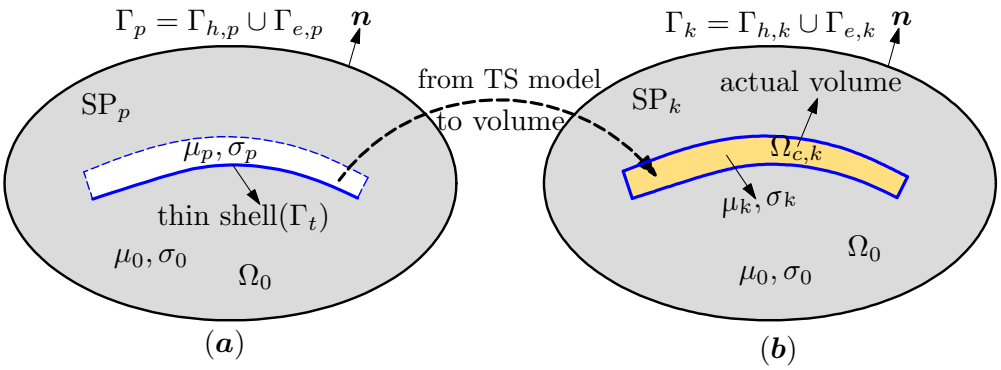

Figure 2.2: Change of material properties from SP p to SP k.

From the general VSs in (2.8 a-b) and (2.9 a-b) (with the total previous field $\boldsymbol{x}_t$ being $\boldsymbol{x}_u + \boldsymbol{x}_p$), the associated VSs herein express a change of μ_p and σ_p in SP p (Fig. 2.2, a) to μ_k and σ_k in SP k (Fig. 2.2, b), i.e [20, 22, 30]:

$$\boldsymbol{b}_{s,k} = (\mu_k - \mu_p)(\boldsymbol{h}_u + \boldsymbol{h}_p), \tag{2.31}$$

$$\boldsymbol{j}_{s,k} = (\sigma_k - \sigma_p)(\boldsymbol{e}_u + \boldsymbol{e}_p). \tag{2.32}$$

Note that in SP k, we get $\mu_p = \mu_0$, $\mu_k = \mu_{volume}$, $\sigma_p = 0$ and $\sigma_k = \sigma_{volume}$. Thus, expressions (2.31) and (2.32) become

$$\boldsymbol{b}_{s,k} = (\mu_k - \mu_0)(\boldsymbol{h}_u + \boldsymbol{h}_p), \tag{2.33}$$
$$\boldsymbol{j}_{s,k} = \sigma_k(\boldsymbol{e}_u + \boldsymbol{e}_p). \tag{2.34}$$

For the $\boldsymbol{h}_k - \boldsymbol{b}_k$ and $\boldsymbol{e}_k - \boldsymbol{j}_k$ relations, the associated VSs can be written

$$\boldsymbol{h}_{s,k} = (\mu_k^{-1} - \mu_p^{-1})(\boldsymbol{b}_u + \boldsymbol{b}_p), \tag{2.35}$$
$$\boldsymbol{e}_{s,k} = -(\boldsymbol{e}_u + \boldsymbol{e}_p). \tag{2.36}$$

Combining (2.33), (2.34), (2.5 b) and (2.6 b), the respectively fields $\boldsymbol{b}_k$ and $\boldsymbol{j}_k$ are

$$\boldsymbol{b}_k = \mu_k \boldsymbol{h}_k + (\mu_k - \mu_0)(\boldsymbol{h}_u + \boldsymbol{h}_p), \tag{2.37}$$
$$\boldsymbol{j}_k = \sigma_k \boldsymbol{e}_k + \sigma_k(\boldsymbol{e}_u + \boldsymbol{e}_p). \tag{2.38}$$

Analogously, combining (2.35), (2.36), (2.5 a) and (2.6 a), fields $\boldsymbol{h}_k$ and $\boldsymbol{e}_k$ are

$$\boldsymbol{h}_k = \mu_k^{-1} \boldsymbol{b}_k + (\mu_k^{-1} - \mu_0^{-1})(\boldsymbol{b}_p + \boldsymbol{b}_u), \tag{2.39}$$
$$\boldsymbol{e}_k = \sigma_k^{-1} \boldsymbol{j}_k + [-(\boldsymbol{e}_p + \boldsymbol{e}_u)]. \tag{2.40}$$

Simultaneously to VSs in (2.37), (2.38), (2.39) and (2.40), SSs have to remove the TS discontinuities, with ICs (2.10), (2.11) and (2.12) to be defined as

$$[\boldsymbol{n} \times \boldsymbol{h}_k]_{\gamma_k} = -[\boldsymbol{n} \times \boldsymbol{h}_p]_{\gamma_k}, \tag{2.41}$$
$$[\boldsymbol{n} \cdot \boldsymbol{b}_k]_{\gamma_k} = -[\boldsymbol{n} \cdot \boldsymbol{b}_p]_{\gamma_k}, \tag{2.42}$$
$$[\boldsymbol{n} \times \boldsymbol{e}_k]_{\gamma_k} = -[\boldsymbol{n} \times \boldsymbol{e}_p]_{\gamma_k}. \tag{2.43}$$

At the weak formulation level, some of the involved trace discontinuities $[\boldsymbol{n} \times \boldsymbol{h}_p]_{\gamma_k}$, $[\boldsymbol{n} \cdot \boldsymbol{b}_p]_{\gamma_k}$ and $[\boldsymbol{n} \times \boldsymbol{e}_p]_{\gamma_k}$ can be naturally expressed via the weak formulations of SP p, as it will be presented in Chapters 3 and 4.

In general, each SP is influenced by all the other SPs, except for SP u because this problem needs no artificial sources imposed via BCs or ICs (SSs or VSs). In case each SP solution is not a source for all the previously solved SPs, no iterations are needed, which defines a one-way coupling. Otherwise, a two-way coupling, i.e. with iterations, is needed.

2.3.4 One-way coupling

Two SP sequences, involving the previously defined SPs, are considered:

- **Three SPs**: A problem (SP u) involving current driven stranded inductors is first solved on a simplified mesh without any thin regions (Figs. 2.3 and 2.4, *top right*). Its solution gives SSs for the added TS problem (SP p) (Figs. 2.3 and 2.4, *bottom left*) through TS ICs based on 1-D approximations. The TS solution of SP p is then corrected by a correction problem (SP k) (Figs. 2.3 and 2.4, *bottom right*) via SSs and VSs, that suppress the TS representation and simultaneously add the actual volume. This corrects the field distributions near edges and corners, where the TS model inaccuracies occur.

- **Two SPs**: A problem (SP f) involving massive or stranded inductors and the TS models (Figs. 2.7 and 2.8, *top right*) can be also first solved, followed by a correction problem SP k (Figs. 2.7 and 2.8, *bottom*) with the actual volume thin regions. This is a simplification of the "tree SPs" sequence. When only a simple configuration of the TS is to be studied, thus two SP sequences can be more efficient than the three SP sequences.

The coupled sequences of three SPs (SP $u \rightarrow$ SP $p \rightarrow$ SP k) and two SPs (SP $f \rightarrow$ SP k) are shown in Fig. 2.5 and Fig. 2.6, respectively, with no iteration [22, 30].

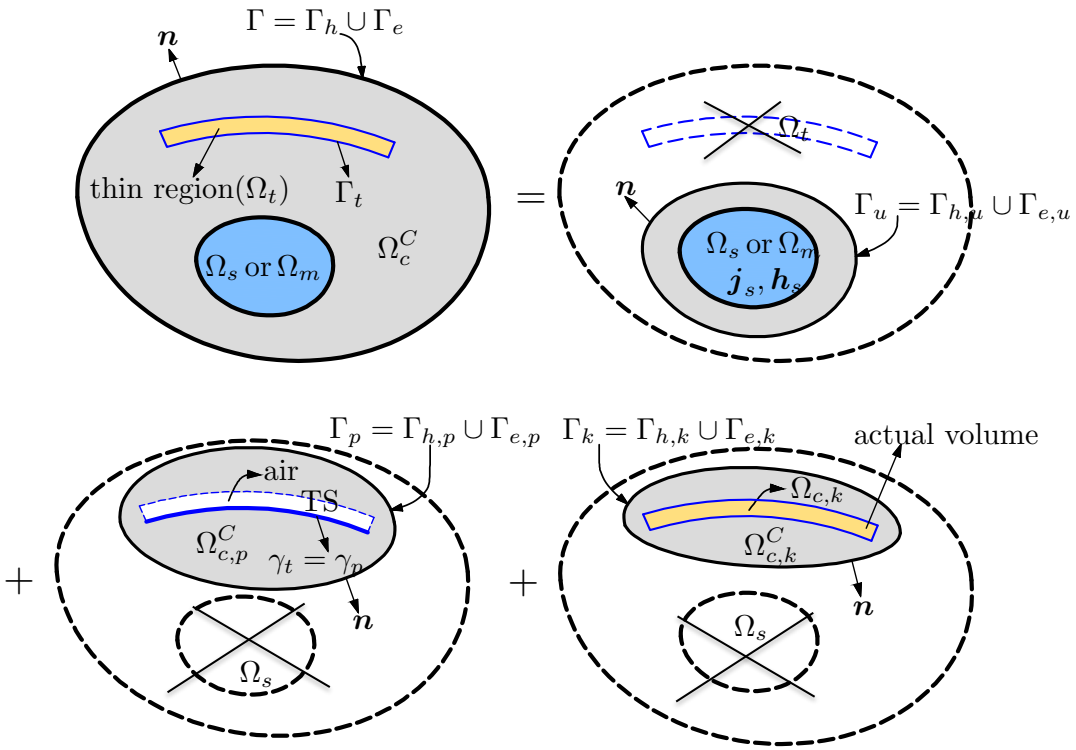

Figure 2.3: Decomposition of a complete problem into three SPs: SP u + SP p + SP k.

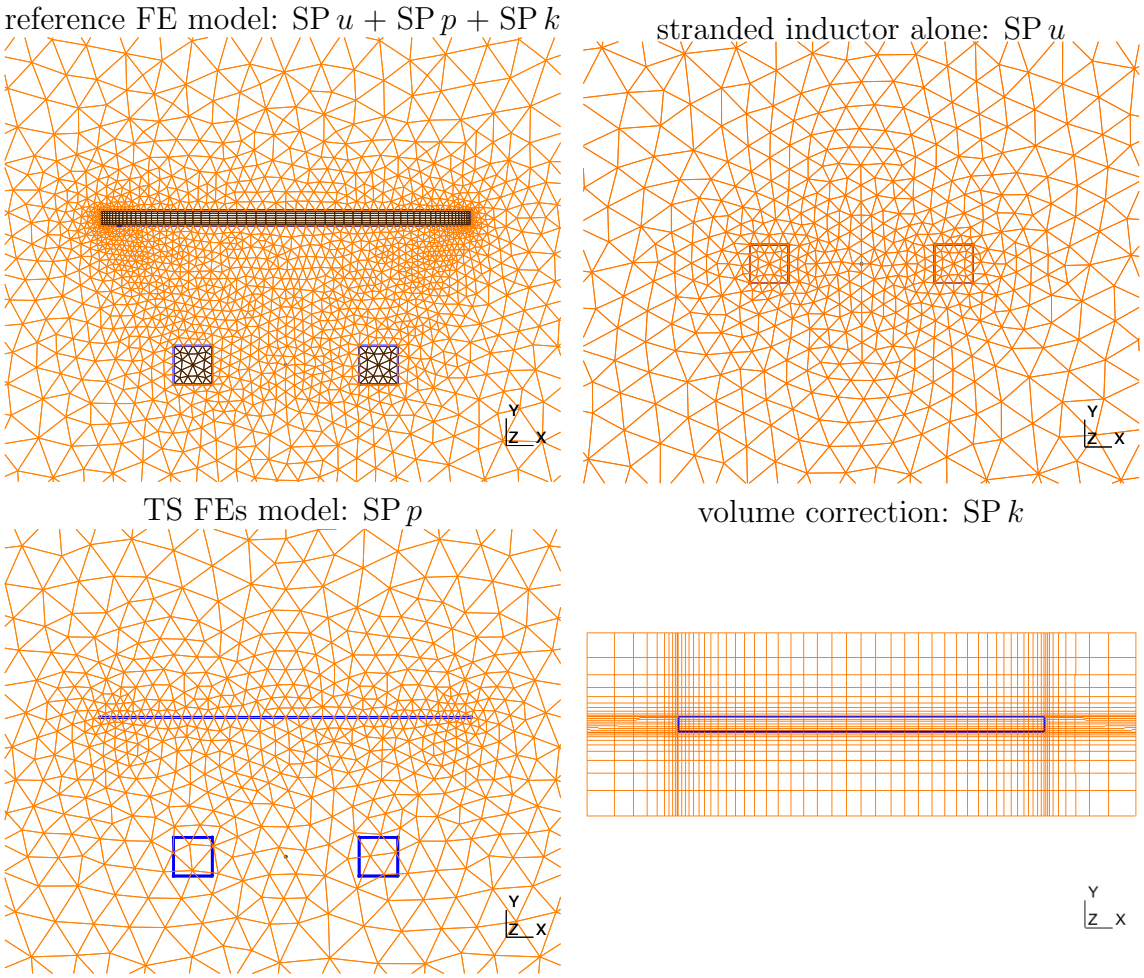

Figure 2.4: Decomposition of a complete mesh into three sub-meshes: SP u + SP p + SP k

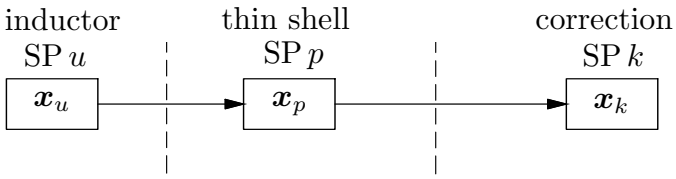

Figure 2.5: Sequence of three SPs with no iteration: SP $u \rightarrow$ SP $p \rightarrow$ SP k.

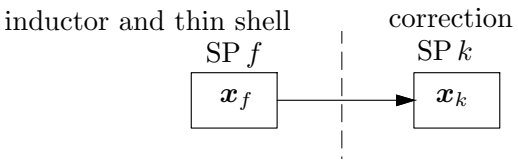

Figure 2.6: Sequence of two SPs with no iteration: SP $f \rightarrow$ SP k.

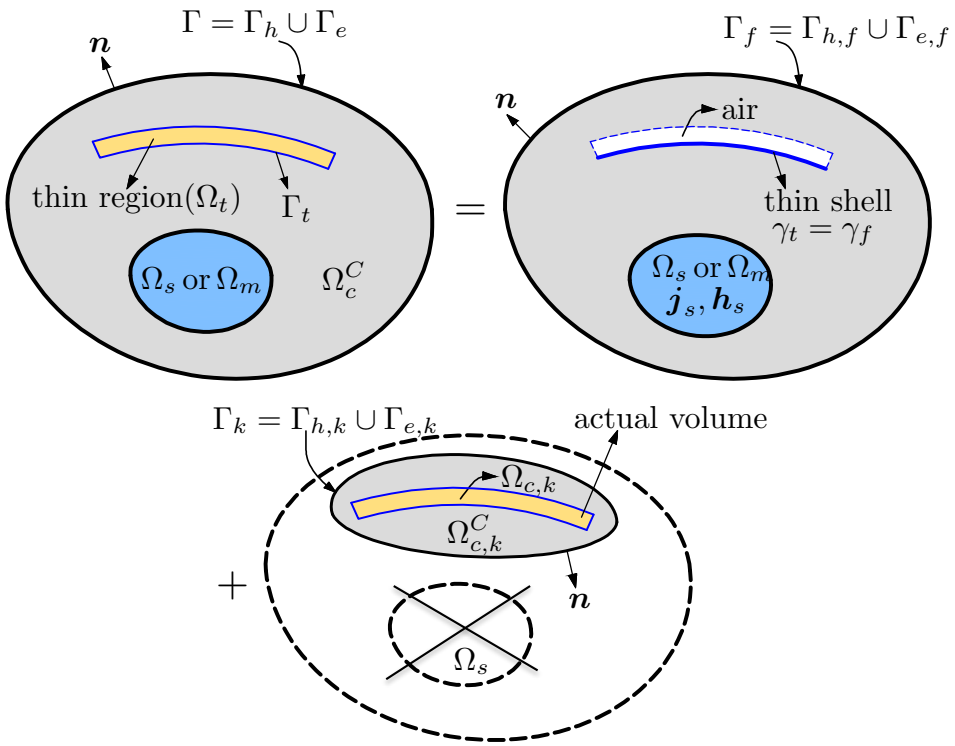

Figure 2.7: Decomposition of a complete problem into two SPs: SP f + SP k.

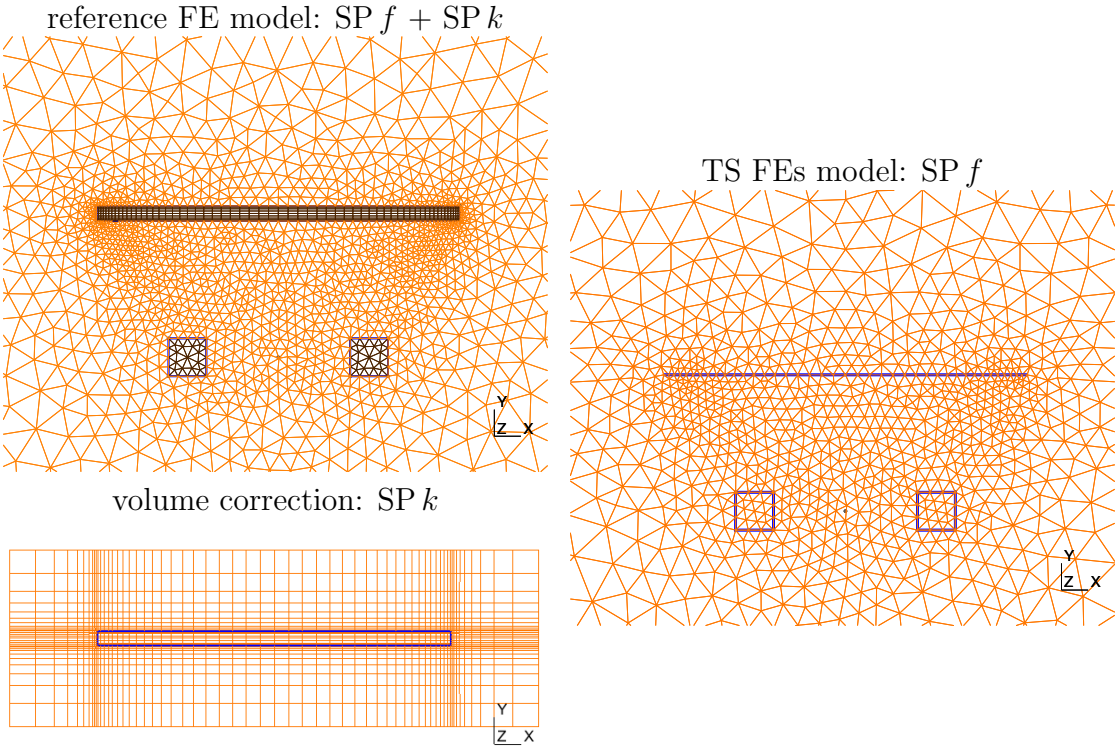

Figure 2.8: Decomposition of a complete mesh into two sub-meshes: SP f + SP k.

2.3.5 Two-way coupling

As an example of a how two-way coupling procedure, let us consider the following **five SPs** (Fig. 2.9), where three SPs (i.e. SP u, SP p and SP k) are already known from the one-way coupling example (Fig. 2.3). SP p and SP k are then renamed SP p_1 (Fig. 2.9, *middle left*) and SP k_1 (Fig. 2.9, *middle right*), and called TS 1 and volume correction 1, respectively.

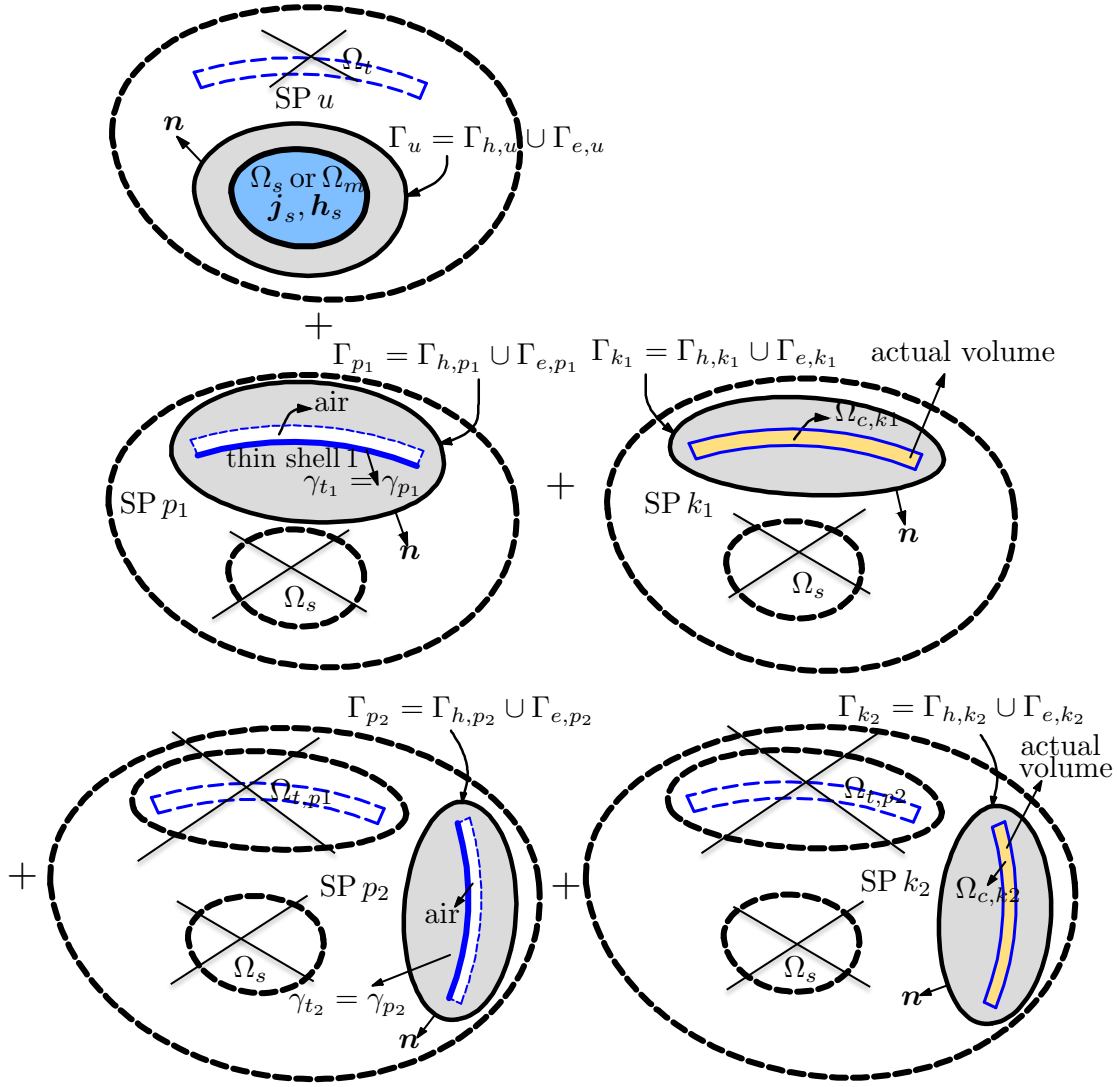

Figure 2.9: Decomposition of a complete problem into five SPs: SP u + SP p_1 + SP k_1 + SP p_2 + SP k_2.

Two new added SPs are respectively called TS 2 (SP p_2) (Fig. 2.9, *bottom left*) and volume correction 2 (SP k_2) (Fig. 2.9, *bottom right*). Here, SP p_2 and SP k_2 are independently solved in their own domains that do not include all previous SP regions anymore. Once obtained, the solutions of all the previous SPs then give SSs for the new added TS SP p_2 through ICs [61]. The TS solution of SP p_2 is then corrected by an SP k_2, that also suppresses the TS representation and simultaneously add the

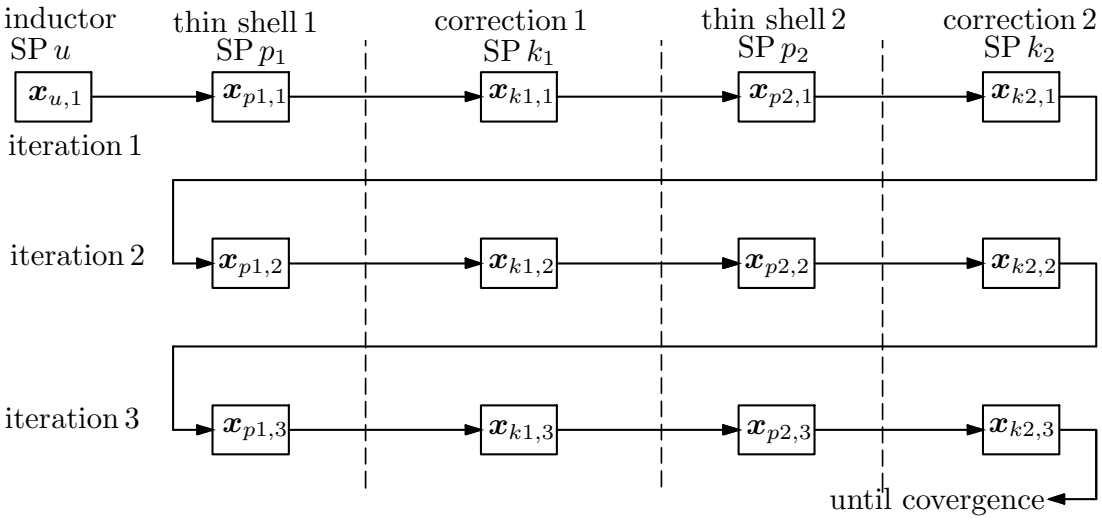

Figure 2.10: Iterative sequence of four SPs: SP p_1 → SP k_1 → SP p_2 → SP k_2.

actual volume FEs. The fields generated in SP p_2 and SP k_2 globally influence the

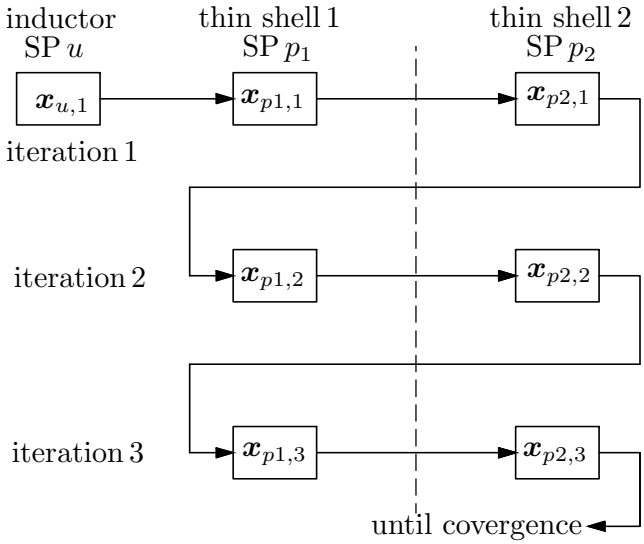

Figure 2.11: Iterative sequence of two SPs: SP p_1 → SP p_2.

sources of SP p_1 and SP k_1. SP u needs no artificial sources and is therefore not influenced. This leads to changes of all the previous corrections [42–44, 47]. Therefore, each solution has to be calculated as a series of corrections by iterating between SPs (see Section 2.2.2). Fig. 2.10 illustrates an iterative process dealing with five SPs (SP u, SP p_1, SP k_1, SP p_2, SP k_2), where SP u does not need to be corrected. The steps of the iterations between these SPs are repeated until obtaining the convergence of $\boldsymbol{x}_i$. Fig. 2.11 shows the iterative process between SP p_1 and SP p_2 only. The convergences of SP p_1 and SP p_2 are then corrected by two volume corrections SP k_1 and SP k_2, with iterations between SP k_1 and SP k_2 only (Fig. 2.12). This process is also done until obtaining the convergence of SP k_1 and SP k_2.

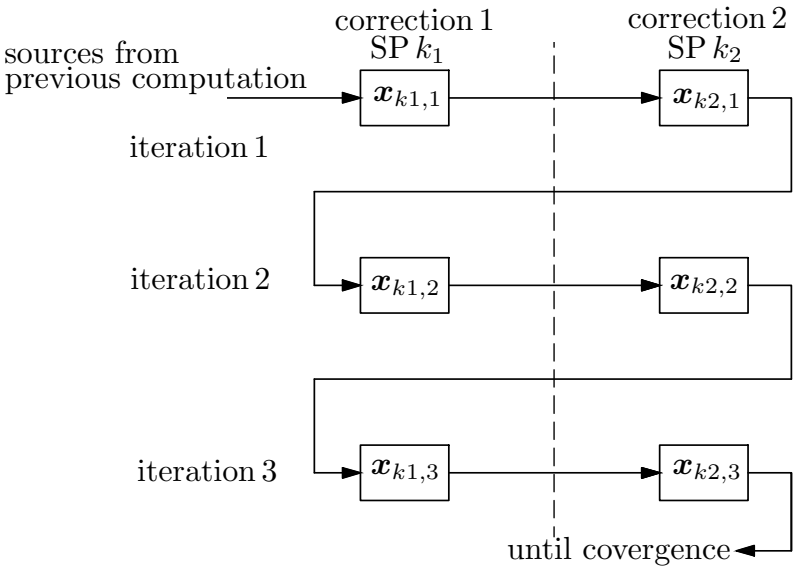

Figure 2.12: Iterative sequence of two SPs: SP $k_1 \rightarrow$ SP k_2.

2.3.6 A convergence test of the two-way coupling

Let us consider a simple didactic example ($f = 50\,\text{Hz}$, $\mu_r = 1$, $\sigma = 59\,\text{MS/m}$) (Fig. 2.13).

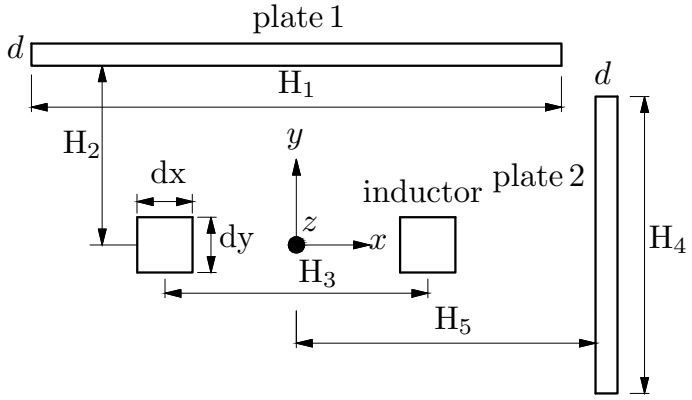

Figure 2.13: 2-D geometry of an inductor and two plates ($d = 5\,\text{mm}$, $H_1 = 120\,\text{mm}$, $H_2 = 45\,\text{mm}$, $H_3 = 45\,\text{mm}$, $H_4 = 80\,\text{mm}$, $H_5 = 67.5\,\text{mm}$, dx = dy = 12 mm).

The test at hand is considered in five SPs (see Section 2.3.5 and Figs. 2.9 and 2.10). It is first solved via an SP u with the stranded inductor alone, then adding a TS FE SP p_1 that does not include the stranded inductor anymore. An SP k_1 then replaces the TS SP p_1 with an actual volume covering the plate 1. Next, another TS SP p_2 is added. An SP k_2 eventually replaces the TS SP p_2 with another actual volume covering the plate 2. In the correction process of SP p_1, the fields generated by SP p_2 and SP k_2 are reaction fields that influence the source solutions calculated from previous SP p_1. This means that some iterations between the SPs are required to determine an accurate solution considered as a series of corrections.

The iterative process is repeated until convergence for a given tolerance (Fig. 2.10). The problem herein is first tested on the same mesh supporting to avoid an additional error due to mesh-to-mesh projections. It is then solved with the different meshes taking the projection errors into account.

Table 2.1: Values of exact and estimated local errors at left end of plate 1, for both no projection and projection.

Iteration n	No projection (same mesh)		Projection (different mesh)	
	Exact local error (%)	Estimated local error (%)	Exact local error (%)	Estimated local error (%)
1	83.82	–	87.82	–
2	46.47	40.59	47.79	44.4
3	25.76	23.04	27.76	25.94
4	14.26	13.81	16.26	15.2
5	7.89	7.76	9.19	8.46
6	4.37	4.23	5.34	4.73
7	2.42	2.33	2.92	2.71
8	1.33	1.23	1.66	1.55
9	0.78	0.70	1.17	1.09
10	0.41	0.39	1.06	0.99
11	0.22	0.21	1.04	0.989
12	0.12	0.118	1.03	0.986

Table 2.2: Values of exact and estimated local errors at right end of plate 1, for both no projection and projection.

Iteration n	No projection (same mesh)		Projection (different mesh)	
	Exact local error (%)	Estimated local error (%)	Exact local error (%)	Estimated local error (%)
1	91.13	–	95.31	–
2	49.94	40.05	51.83	43.15
3	27.35	20.81	28.81	21.60
4	15.06	11.76	16.02	11.91
5	8.36	6.76	9.15	7.13
6	4.65	3.86	5.17	4.19
7	2.59	2.17	2.71	2.36
8	1.45	1.23	1.78	1.32
9	0.81	0.67	1.35	1.14
10	0.44	0.37	1.23	1.03
11	0.242	0.21	1.14	1.02
12	0.133	0.12	1.12	1.01

Fig. 2.14 illustrates an iterative process (with three iterations) of four SPs (i.e. SP p_1, SP k_1, SP p_2 and SP k_2) for the magnetic vector potential $\boldsymbol{a}$, where SP p_1

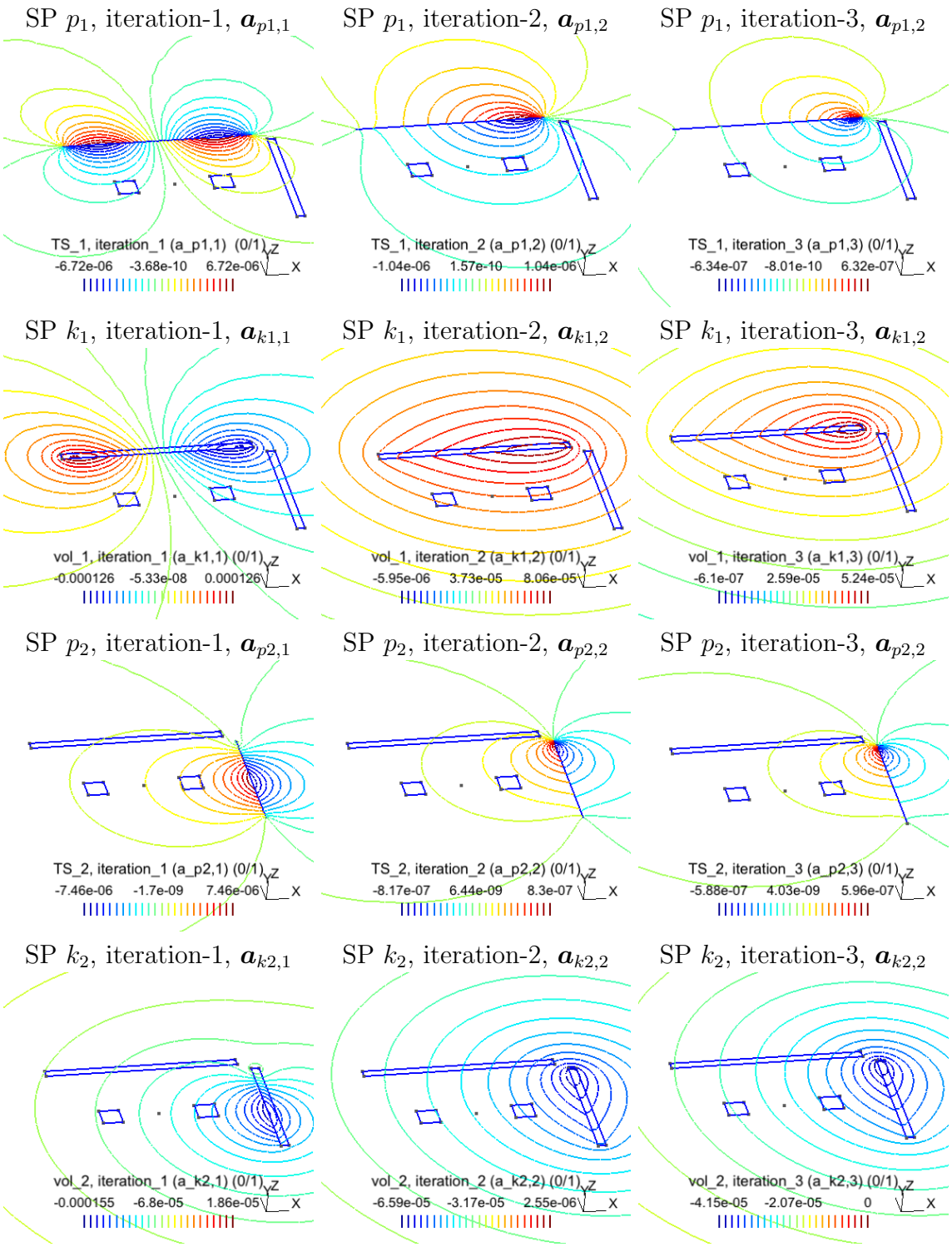

Figure 2.14: Flux lines of the z-component of the magnetic vector potential corrections (real part) calculated in each SP, i.e. SP p_1, SP k_1, SP p_2 and SP k_2, with three iterations. SP p_1 is chosen as the reference of source SP. The imaginary part presents an analogous behavior.

$$\xrightarrow{\text{Convergence}} \boldsymbol{a} = \sum_{i\in P} \boldsymbol{a}_i = \boldsymbol{a}_{u,0} + \sum_{j=1}^{n} \boldsymbol{a}_{p1,j} + \sum_{j=1}^{n} \boldsymbol{a}_{k1,j} + \sum_{j=1}^{n} \boldsymbol{a}_{p2,j} + \sum_{j=1}^{n} \boldsymbol{a}_{k2,j}$$
$$= \boldsymbol{a}_{u,0}$$
$$+ \boldsymbol{a}_{p1,1} + \boldsymbol{a}_{p1,2} + \boldsymbol{a}_{p1,3} + \ldots + \boldsymbol{a}_{p1,8}$$
$$+ \boldsymbol{a}_{k1,1} + \boldsymbol{a}_{k1,2} + \boldsymbol{a}_{k1,3} + \ldots + \boldsymbol{a}_{k1,8}$$
$$+ \boldsymbol{a}_{p2,1} + \boldsymbol{a}_{p2,2} + \boldsymbol{a}_{p2,3} + \ldots + \boldsymbol{a}_{p2,8}$$
$$+ \boldsymbol{a}_{k2,1} + \boldsymbol{a}_{k2,2} + \boldsymbol{a}_{k2,3} + \ldots + \boldsymbol{a}_{k2,8}$$

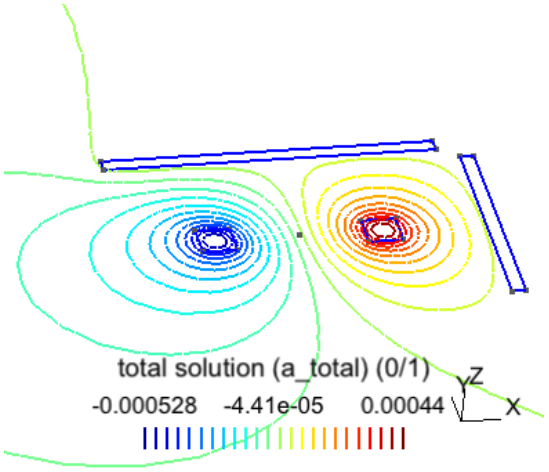

Figure 2.15: The total solutions $\boldsymbol{a}$ of SPs after convergence.

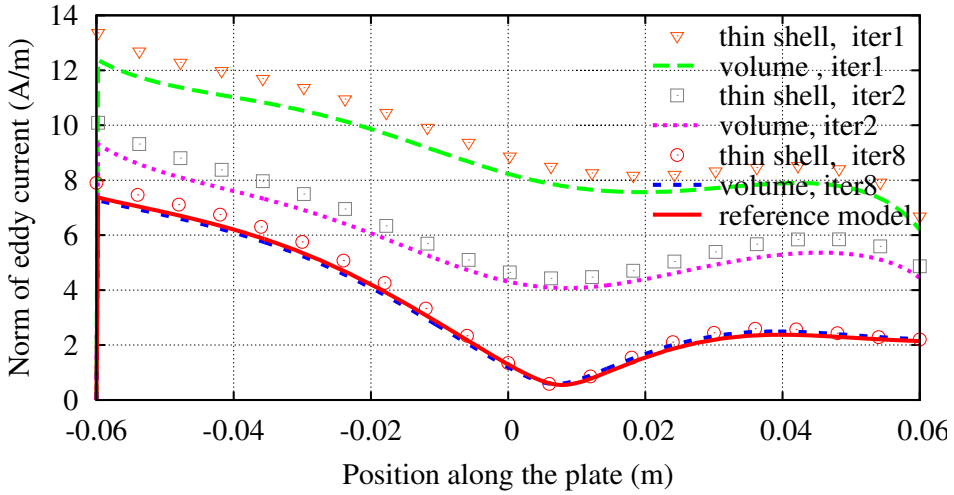

Figure 2.16: Norm of the eddy current density $\|\boldsymbol{j}\|$ (A/m) along the plate 1 at different iterations.

is chosen as a source SP. Note that the source problem SP u does not need to be corrected, because it only contains the current driven inductor and needs no SS nor VS. Fig. 2.15 gives the tolerance of the total solution $\boldsymbol{a}$ of the convergnece

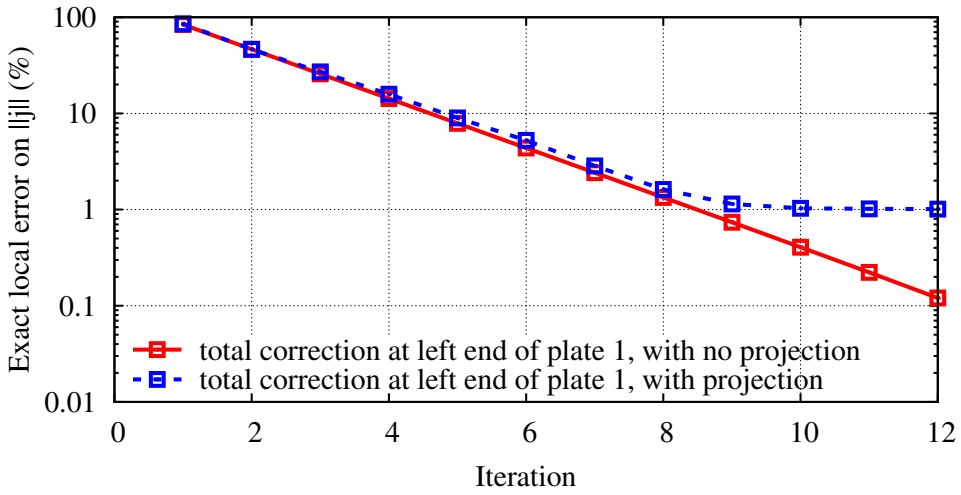

Figure 2.17: Exact local errors on the norm of eddy current density $\|\boldsymbol{j}\|$ between the total solution and the complete solution at left end of plate 1 for both no projection and projection, with the number of iterations.

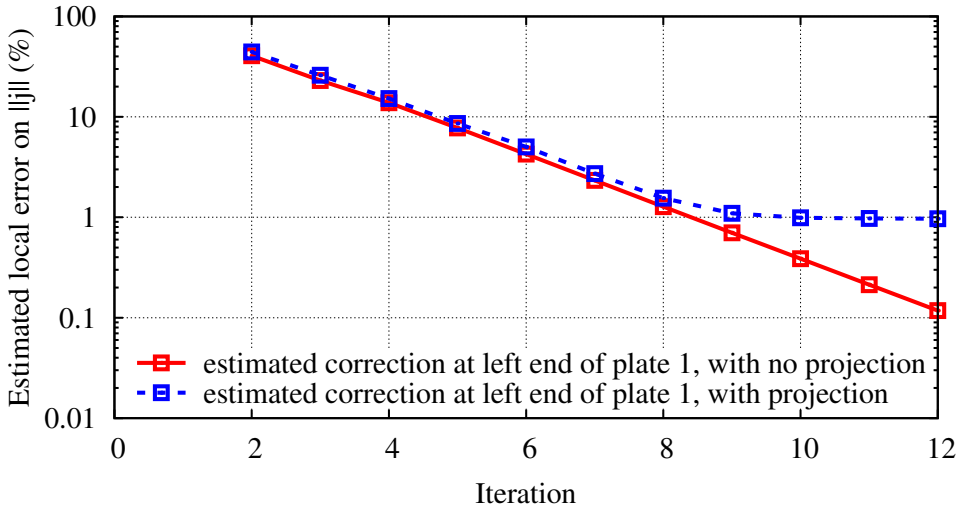

Figure 2.18: Estimated local errors on the norm of the eddy current density $\|\boldsymbol{j}\|$ between the solution at iteration n and n-1, at left end of plate 1, for both no projection and projection.

(8 iterations). Fig. 2.16 represents the convergence of the volume correction SP k_1 along the plate 1, for different iterations. The TS solution is also pointed out as a function of the number of iterations. Relative local errors on the norm of eddy current density $\|\boldsymbol{j}\|$ between the total solution and the reference solution at the left end of plate 1 are shown in Fig. 2.17. The error is less than 1% (0.78%) with no projection, and increases slightly up to 1.17% with projection error, after 9 iterations for both cases. Estimated local errors on the norm of eddy current density $\|\boldsymbol{j}\|$ between the SP solution at iteration n and the solution at previous iteration n-1 at left end of plate 1 is pointed out in Fig. 2.18, for both cases (no projection and

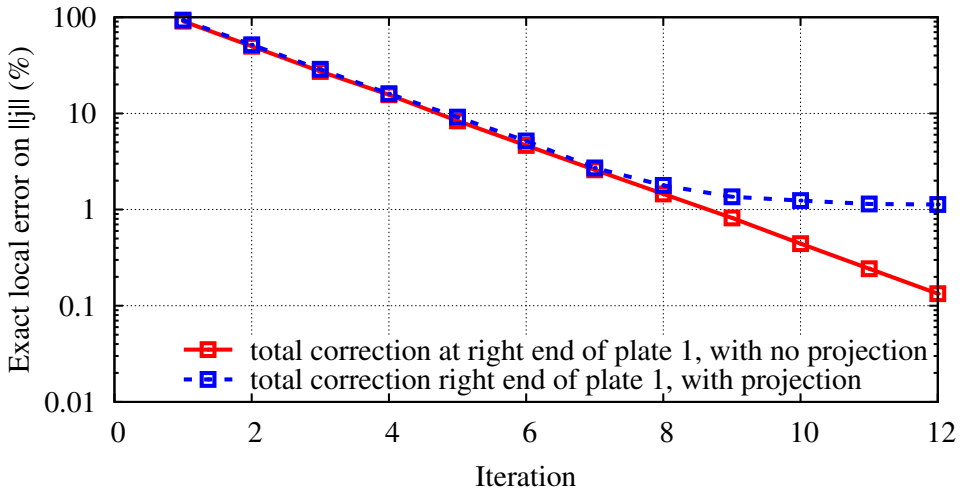

Figure 2.19: Exact local errors on the norm of eddy current density $\|\boldsymbol{j}\|$ between the total solution and the complete solution at right end of plate 1 for both no projection and projection, with the number of iterations.

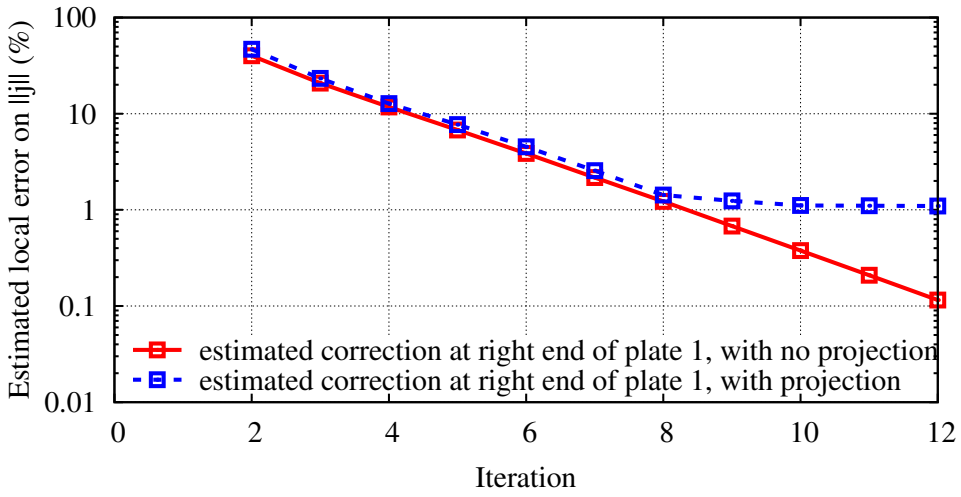

Figure 2.20: Estimated local errors on the norm of the eddy current density $\|\boldsymbol{j}\|$ between the solution at iteration n and n-1, at right end of plate 1, for both no projection and projection.

projection). Also, the errors are below 1% with no projection and stagnates at 1.09% with projection, which is an indication of the error due to mesh-to-mesh projections, after 9 iterations for both cases. The values of exact and estimated local errors at left end of plate 1 are pointed out in Table 2.1, for both no projection and projection. Analogously, Figs. 2.19 and 2.20 show exact and estimated local errors at right end of plate 1. Their values are also given in Table 2.2.

The global errors with projection and no projection on the norm of the magnetic vector potential $\|\boldsymbol{a}\|$ are eventually illustrated in Fig. 2.21. The errors are below 1% after 8 iterations. The projection error is also approximately 1%.

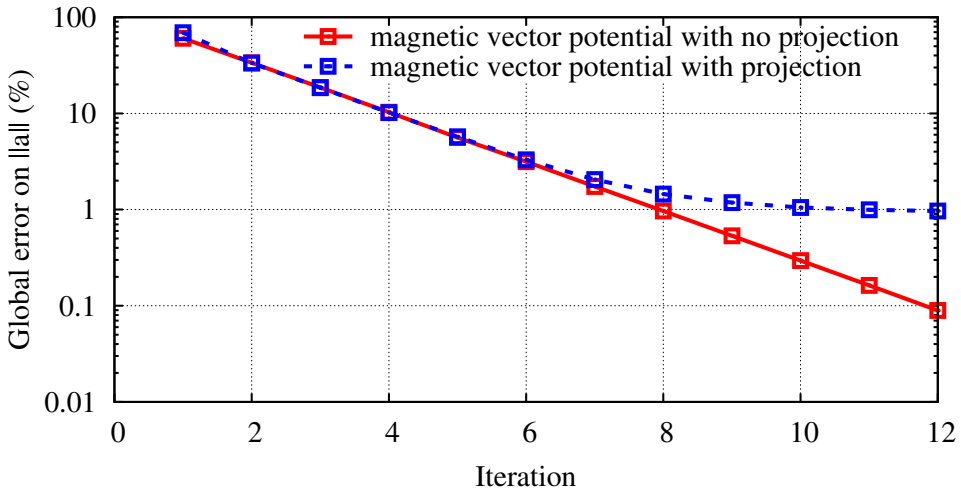

Figure 2.21: Global errors on the norm of the magnetic vector potential $\|\boldsymbol{a}\|$ between the total solution and the reference solution, with the number of iterations.

The convergence of local and global solutions in SPs are successfully obtained in a two-way coupling. The iterative procedure as presented amounts to a Gauss-Seidel iteration. This iteration could be accelerated (to reduce the number of iterations), e.g. by extrapolation or by using Krylov subspace techniques [59, 63, 129]. Indeed, the iteration operator that maps the solution of a SP to the source of another SP is a linear operator, which can be seen as a general domain decomposition operator with (large) overlaps [59, 63, 129]; the stronger the coupling between the SPs, the larger the number of iterations. For application in the high-frequency regime, when the coupling between the SPs is linked to multiple reflections, see e.g. [15, 59, 63, 129].

Chapter 3

Thin shell subproblems with magnetic flux density formulations

Contents

3.1 Introduction

In this chapter we first present the classical magnetic flux density formulations (***b***-formulations) for magnetodynamic and magnetostatics. A formulation adapted to the discretization of the thin conducting and magnetic structures [60, 61] is then presented. The way to construct SSs and VSs for each SP is introduced, as well as two sequences of coupling SPs with TS models. The coupling between the local electromagnetic quantities and the global currents and voltages is eventually presented for the weak formulations.

The contributions developed in this chapter are extensions of the work by C. Geuzaine and P. Dular for the ***b***-formulations [58,60,61]. Most original contributions of this chapter have been published separately in [20, 22, 30].

3.2 Weak formulations

3.2.1 Magnetodynamic weak formulations

In this part, we construct the magnetodynamic formulation that has been defined in Section 1.5.2. The particularized Maxwell's equations (1.68) together with the constitutive relations (1.11) and (1.14) establish the system to be solved. To satisfy Faraday's law (1.68 a) in a strong sense, we take $\boldsymbol{b}_i \in \boldsymbol{H}_{e,i}(\mathrm{div};\Omega_i)$ and $\boldsymbol{e}_i \in \boldsymbol{H}_{e,i}(\mathbf{curl};\Omega_i)$. This is equivalent to verifying the lower part of the Tonti diagram (1.73) in a strong sense. Furthermore, verifying exactly the constitutive laws (1.11) and (1.14) implies choosing $\boldsymbol{h}_i \in \boldsymbol{H}_{e,i}(\mathrm{div};\Omega_i)$ and $\boldsymbol{j}_i \in \boldsymbol{H}_{e,i}(\mathbf{curl};\Omega_i)$. Ampère's law (1.68 b) can be weakly verified. We start by writing the weak form of Ampère's law (1.68 b) (see Section A.2), i.e.

$$(\mathbf{curl}\,\boldsymbol{h}_i, \boldsymbol{a}'_i)_{\Omega_i} = (\boldsymbol{j}_i, \boldsymbol{a}'_i)_{\Omega_i}, \quad \forall \boldsymbol{a}'_i \in \boldsymbol{H}^0_{e,i}(\mathbf{curl};\Omega_i), \tag{3.1}$$

where the field $\boldsymbol{a}'_i \in \boldsymbol{H}^0_{e,i}(\mathbf{curl};\Omega_i)$ is a field of test functions independent of time. Applying the Green formula of type **curl-curl** (A.39) in Ω_i to the fields $\boldsymbol{h}_i$ and $\boldsymbol{a}'_i$ in (3.1), we get

$$(\boldsymbol{h}_i, \mathbf{curl}\,\boldsymbol{a}'_i)_{\Omega_i} + \langle \boldsymbol{n}\times\boldsymbol{h}_i, \boldsymbol{a}'_i\rangle_{\Gamma_i} = (\boldsymbol{j}_i, \boldsymbol{a}'_i)_{\Omega_i}, \quad \forall \boldsymbol{a}'_i \in \boldsymbol{H}^0_{e,i}(\mathbf{curl};\Omega_i). \tag{3.2}$$

Satisfying in a strong sense the lower part of the Tonti diagram (1.73) (i.e. Faraday's and Gauss's law), we first introduce the constitutive laws (1.11) and (1.13) in the weak form (3.2) to get

$$\begin{aligned}(\mu_i^{-1}\boldsymbol{b}_i, \mathbf{curl}\,\boldsymbol{a}'_i)_{\Omega_i} - (\sigma_i\boldsymbol{e}_i, \boldsymbol{a}'_i)_{\Omega_{c,i}} + \langle \boldsymbol{n}\times\boldsymbol{h}_i, \boldsymbol{a}'_i\rangle_{\Gamma_i} = (\boldsymbol{j}_{s,i}, \boldsymbol{a}'_i)_{\Omega_{s,i}},\\ \forall \boldsymbol{a}'_i \in \boldsymbol{H}^0_{e,i}(\mathbf{curl};\Omega_i).\end{aligned} \tag{3.3}$$

Let us now introduce the magnetic vector potential $\boldsymbol{a}_i$ and the electric field $\boldsymbol{e}_i$ (i.e. $\boldsymbol{b}_i = \mathbf{curl}\,\boldsymbol{a}_i$ and $\boldsymbol{e}_i = -\partial_t \boldsymbol{a}_i - \mathbf{grad}\, v_i$), defined by (1.70) and (1.71), in (3.3), and splitting Γ_i into $\Gamma_{h,i}$ and $\Gamma_{e,i}$, we have

$$(\mu_i^{-1}\mathbf{curl}\,\boldsymbol{a}_i, \mathbf{curl}\,\boldsymbol{a}'_i)_{\Omega_i} + (\sigma_i\,\partial_t \boldsymbol{a}_i, \boldsymbol{a}'_i)_{\Omega_{c,i}} + (\sigma_i\,\mathbf{grad}\, v_i, \boldsymbol{a}'_i)_{\Omega_{c,i}} + \langle \boldsymbol{n}\times\boldsymbol{h}_i, \boldsymbol{a}'_i\rangle_{\Gamma_{h,i}} + \langle \boldsymbol{n}\times\boldsymbol{h}_i, \boldsymbol{a}'_i\rangle_{\Gamma_{e,i}} = (\boldsymbol{j}_{s,i}, \boldsymbol{a}'_i)_{\Omega_{s,i}}, \quad \forall \boldsymbol{a}'_i \in \boldsymbol{H}^0_{e,i}(\mathbf{curl};\Omega_i), \tag{3.4}$$

where $\boldsymbol{H}^0_{e,i}(\mathbf{curl};\Omega_i)$ is a function space defined on Ω_i containing the basis functions for $\boldsymbol{a}_i$ as well as for the test function $\boldsymbol{a}'_i$ (see Section 1.3.1 for the definition of the function spaces); $(\cdot\,,\cdot)_{\Omega_i}$ and $<\cdot\,,\cdot>_{\Gamma_i}$ respectively denote a volume integral in Ω_i and a surface integral on Γ_i of the product of their vector field arguments. The electric scalar potential v_i is only defined in the conducting regions $\Omega_{c,i}$. The magnetic vector potential $\boldsymbol{a}_i$ is uniquely defined in the conducting regions $\Omega_{c,i}$. A gauge condition has to be imposed everywhere else (see Section 1.5.2).

The weak formulation (3.4) implies, by taking $\boldsymbol{a}'_i = \mathbf{grad}\, v'_i$ as a test function, that

$$(\sigma_i\,\partial_t \boldsymbol{a}_i, \mathbf{grad}\, v'_i)_{\Omega_{c,i}} + (\sigma_i\,\mathbf{grad}\, v_i, \mathbf{grad}\, v'_i)_{\Omega_{c,i}} = \langle \boldsymbol{n}\cdot\boldsymbol{j}_i, v'_i\rangle_{\Gamma_{g,i}}, \quad \forall v'_i \in {H^1}^0_{e,i}(\Omega_{c,i}), \tag{3.5}$$

where $\Gamma_{g,i}$ is the part of the boundary $\Omega_{c,i}$ carrying a current (see Section 1.4.2) [28, 33, 38]. Formulation (3.5) is actually also the weak form of $\operatorname{div}\boldsymbol{j}_i = 0$ in $\Omega_{c,i}$.

The term on the surface $\Gamma_{e,i}$ with essential BCs on $\boldsymbol{n}.\boldsymbol{b}_i$ is usually omitted because it does not locally contribute to (3.4). The trace of the magnetic field $\boldsymbol{n}\times\boldsymbol{h}_i$ in (3.4) is subject to a natural BC on the boundaries $\Gamma_{h,i}$ of the domain Ω_i. This BC can adopt several forms:

- The trace of $\boldsymbol{h}_i$ can be locally specified. This is the case for a homogeneous Neumann BC, e.g. imposing a symmetry condition of "zero crossing current" $(\boldsymbol{n}\times\boldsymbol{h}_i\big|_{\Gamma_{h,i}} = 0 \Rightarrow \boldsymbol{n}\cdot\mathbf{curl}\,\boldsymbol{h}_i\big|_{\Gamma_{h,i}} = 0 \Leftrightarrow \boldsymbol{n}\cdot\boldsymbol{j}_i\big|_{\Gamma_{h,i}} = 0)$.
- The trace of $\boldsymbol{h}_i$ can be a field for which only associated global quantities are known. This can be presented for the modelling of the treatment of massive and stranded inductors (see Sections 3.3.6).
- The trace of $\boldsymbol{h}_i$ can appear in local implicit BCs, such as those established for the the treatment of thin regions [58,60,61]. This is presented in Section 3.2.3.

3.2.2 Magnetostatic weak formulations

The magnetostatic formulation is considered as a simplification of the magnetodynamic formulation for which all time dependent phenomena are neglected. The weak form of Ampère's law (1.60 a) is now given by

$$(\mathbf{curl}\,\boldsymbol{h}_i, \boldsymbol{a}'_i)_{\Omega_i} = (\boldsymbol{j}_i, \boldsymbol{a}'_i)_{\Omega_i}, \quad \forall \boldsymbol{a}'_i \in \boldsymbol{H}^0_{e,i}(\mathbf{curl};\Omega_i). \tag{3.6}$$

Let us consider the Green formula of type **curl-curl** (A.39) in Ω_i applied to the fields $\boldsymbol{h_i}$ and $\boldsymbol{a_i}'$ in (3.6), and taking into account that $\boldsymbol{j}_i = \boldsymbol{j}_{s,i}$, we get

$$(\boldsymbol{h}_i, \mathbf{curl}\, \boldsymbol{a}'_i)_{\Omega_i} + \langle \boldsymbol{n} \times \boldsymbol{h}_i, \boldsymbol{a}'_i \rangle_{\Gamma_i} = (\boldsymbol{j}_{s,i}, \boldsymbol{a}'_i)_{\Omega_{s,i}}, \quad \forall \boldsymbol{a}'_i \in \boldsymbol{H}^0_{e,i}(\mathbf{curl}; \Omega_i). \tag{3.7}$$

Satisfying in a strong sense the lower part of the Tonti diagram (1.67), we first introduce the constitutive law (1.11) into (3.7) to obtain

$$(\mu_i^{-1}\boldsymbol{b}_i, \mathbf{curl}\, \boldsymbol{a}'_i)_{\Omega_i} + \langle \boldsymbol{n} \times \boldsymbol{h}_i, \boldsymbol{a}'_i \rangle_{\Gamma_i} = (\boldsymbol{j}_{s,i}, \boldsymbol{a}'_i)_{\Omega_{s,i}}, \quad \forall \boldsymbol{a}'_i \in \boldsymbol{H}^0_{e,i}(\mathbf{curl}; \Omega_i). \tag{3.8}$$

The field $\boldsymbol{b}_i \in \boldsymbol{H}_{e,i}(\mathrm{div}; \Omega_i)$ can be derived from a vector potential $\boldsymbol{a}_i$ such that $\boldsymbol{b}_i = \mathbf{curl}\, \boldsymbol{a}_i$ everywhere in Ω_i. The weak form (3.8) can be then written as

$$\begin{aligned}(\mu_i^{-1}\mathbf{curl}\, \boldsymbol{a}_i, \mathbf{curl}\, \boldsymbol{a}'_i)_{\Omega_i} + \langle \boldsymbol{n} \times \boldsymbol{h}_i, \boldsymbol{a}'_i \rangle_{\Gamma_{h,i}} + \langle \boldsymbol{n} \times \boldsymbol{h}_i, \boldsymbol{a}'_i \rangle_{\Gamma_{e,i}} = (\boldsymbol{j}_{s,i}, \boldsymbol{a}'_i)_{\Omega_{s,i}}, \\ \forall \boldsymbol{a}'_i \in \boldsymbol{H}^0_{e,i}(\mathbf{curl}; \Omega_i).\end{aligned} \tag{3.9}$$

3.2.3 Thin shell model in the weak formulations

As explained in Section 1.4.3, the thin regions $\Omega_{t,i}$ can be extracted from the studied domain Ω_i and then considered with the double layer TS surface $\Gamma_{t,i}$ [58,60,61]. This means that the boundary $\Gamma_{h,i}$ in (3.4) and (3.9) contains the boundary $\Gamma_{t,i}$ of $\Omega_{t,i}$. The surface integral term $\langle \boldsymbol{n} \times \boldsymbol{h}_i, \boldsymbol{a}'_i \rangle_{\Gamma_{h,i}}$ in (3.4) and (3.9) can be then expressed as

$$\langle \boldsymbol{n} \times \boldsymbol{h}_i, \boldsymbol{a}'_i \rangle_{\Gamma_{h,i}} = \langle \boldsymbol{n} \times \boldsymbol{h}_i, \boldsymbol{a}'_i \rangle_{\Gamma_{h,i} - \Gamma_{t,i}} + \langle [\boldsymbol{n} \times \boldsymbol{h}_i], \boldsymbol{a}'_i \rangle_{\Gamma_{t,i}}. \tag{3.10}$$

The term in (3.10) with magnetic field trace on TS $\Gamma_{t,i}$, i.e. $\langle [\boldsymbol{n} \times \boldsymbol{h}_i], \boldsymbol{a}'_i \rangle_{\Gamma_{t,i}}$, can be written as

$$\langle [\boldsymbol{n} \times \boldsymbol{h}_i], \boldsymbol{a}'_i \rangle_{\Gamma_{t,i}} = -\langle \boldsymbol{n}_t \times \boldsymbol{h}_i|_{\Gamma^+_{t,i}}, \boldsymbol{a}'_i \rangle_{\Gamma^+_{t,i}} + \langle \boldsymbol{n}_t \times \boldsymbol{h}_i|_{\Gamma^-_{t,i}}, \boldsymbol{a}'_i \rangle_{\Gamma^-_{t,i}}. \tag{3.11}$$

The tangential electric field is discontinuous across the thin regions (see Section 1.4.3) [58,61]. Thus, the magnetic vector potential $\boldsymbol{a}_i$ is split into

$$\boldsymbol{a}_i = \boldsymbol{a}_{c,i} + \boldsymbol{a}_{d,i}, \tag{3.12}$$

where $\boldsymbol{a}_{c,i,t}$ and $\boldsymbol{a}_{d,i,t}$ are the tangential components of $\boldsymbol{a}_{c,i}$ and $\boldsymbol{a}_{d,i}$ and are continuous and discontinuous across $\Omega_{t,i}$, respectively. Here, we assume that $\boldsymbol{a}_{d,t,i}$ is equal to zero on the negative side $\Gamma^-_{t,i}$ of $\Gamma_{t,i}$ [58,61]. Analysing the cross product of $\boldsymbol{n}_t$ by (1.57)

$$\begin{aligned}\boldsymbol{n}_t \times \boldsymbol{e}_i|_{\Gamma^+_{t,i}} - \boldsymbol{n}_t \times \boldsymbol{e}_i|_{\Gamma^-_{t,i}} &= -\partial_t \left[\mu_i \beta_i (\boldsymbol{n}_t \times (\boldsymbol{h}_i \times \boldsymbol{n}_t)|_{\Gamma^+_{t,i}} + \boldsymbol{n}_t \times (\boldsymbol{h}_i \times \boldsymbol{n}_t)|_{\Gamma^-_{t,i}})\right] \\ &= \partial_t \left[\mu_i \beta_i (\boldsymbol{n}_t \times (\boldsymbol{n}_t \times \boldsymbol{h}_i)|_{\Gamma^+_{t,i}} + \boldsymbol{n}_t \times (\boldsymbol{n}_t \times \boldsymbol{h}_i)|_{\Gamma^-_{t,i}})\right]\end{aligned} \tag{3.13}$$

and developing (1.56), we obtain

$$\boldsymbol{n}_t \times \boldsymbol{h}_i|_{\Gamma^+_{t,i}} + \boldsymbol{n}_t \times \boldsymbol{h}_i|_{\Gamma^-_{t,i}} = -(\mu_i \beta_i)^{-1} \boldsymbol{a}_{d,t,i}\,, \tag{3.14}$$

$$\boldsymbol{n}_t \times \boldsymbol{h}_i|_{\Gamma^+_{t,i}} - \boldsymbol{n}_t \times \boldsymbol{h}_i|_{\Gamma^-_{t,i}} = -\sigma_i \beta_i \, \partial_t (2\boldsymbol{a}_{c,t,i} + \boldsymbol{a}_{d,t,i}). \tag{3.15}$$

Solving equations (3.14) and (3.15), we get

$$\boldsymbol{n}_t \times \boldsymbol{h}_i|_{\Gamma^+_{t,i}} = \frac{1}{2}\big[- \sigma_i \beta_i \, \partial_t (2\boldsymbol{a}_{c,t,i} + \boldsymbol{a}_{d,t,i}) - \frac{1}{\mu_i \beta_i} \, \boldsymbol{a}_{d,t,i}\big], \tag{3.16}$$

$$\boldsymbol{n}_t \times \boldsymbol{h}_i|_{\Gamma^-_{t,i}} = \frac{1}{2}\big[\sigma_i \beta_i \, \partial_t (2\boldsymbol{a}_{c,t,i} + \boldsymbol{a}_{d,t,i}) - \frac{1}{\mu_i \beta_i} \, \boldsymbol{a}_{d,t,i}\big]. \tag{3.17}$$

Substituting (3.16) and (3.17) into (3.11), and then (3.11) into (3.4), we get the magnetic field trace term $\langle [\boldsymbol{n} \times \boldsymbol{h}_i], \boldsymbol{a}'_i \rangle_{\Gamma_{t,i}}$ on TS, i.e.

$$\begin{aligned} \langle [\boldsymbol{n} \times \boldsymbol{h}_i], \boldsymbol{a}'_i \rangle_{\Gamma_{t,i}} = \langle \frac{1}{2}\big[\sigma_i \beta_i \, \partial_t (2\boldsymbol{a}_{c,t,i} + \boldsymbol{a}_{d,t,i}) + \frac{1}{\mu_i \beta_i} \, \boldsymbol{a}_{d,t,i}\big], \boldsymbol{a}'_{c,t,i} + \boldsymbol{a}'_{d,t,i} \rangle_{\Gamma^+_{t,i}} \\ + \langle \frac{1}{2}\big[\sigma_i \beta_i \, \partial_t (2\boldsymbol{a}_{c,t,i} + \boldsymbol{a}_{d,t,i}) - \frac{1}{\mu_i \beta_i} \, \boldsymbol{a}_{d,t,i}\big], \boldsymbol{a}'_{c,t,i} \rangle_{\Gamma^-_{t,i}}. \end{aligned} \tag{3.18}$$

For the magnetostatic case, we have $\beta_i = d_i/2$ and $\partial_t \cdot = 0$ [58, 61]. Thus, the traces of magnetic field $\boldsymbol{n}_t \times \boldsymbol{h}_i|_{\Gamma^+_{t,i}}$ and $\boldsymbol{n}_t \times \boldsymbol{h}_i|_{\Gamma^-_{t,i}}$ in (3.16) and (3.17) on both sides of $\Gamma_{t,i}$ become

$$\boldsymbol{n}_t \times \boldsymbol{h}_i|_{\Gamma^+_{t,i}} = \boldsymbol{n}_t \times \boldsymbol{h}_i|_{\Gamma^-_{t,i}} = -\frac{1}{\mu_i d_i} \, \boldsymbol{a}_{d,t,i}. \tag{3.19}$$

The traces of magnetic field $\langle [\boldsymbol{n} \times \boldsymbol{h}_i], \boldsymbol{a}'_i \rangle_{\Gamma_{t,i}}$ in (3.9) for the magnetostatic case is expressed as

$$\langle [\boldsymbol{n} \times \boldsymbol{h}_i], \boldsymbol{a}'_i \rangle_{\Gamma_{t,i}} = \langle (\mu_i d_i)^{-1} \, \boldsymbol{a}_{d,t,i}, \boldsymbol{a}'_{c,t,i} + \boldsymbol{a}'_{d,t,i} \rangle_{\Gamma^+_{t,i}} - \langle (\mu_i d_i)^{-1} \, \boldsymbol{a}_{d,t,i}, \boldsymbol{a}'_{c,t,i} + \boldsymbol{a}'_{d,t,i} \rangle_{\Gamma^-_{t,i}}. \tag{3.20}$$

Note that $\boldsymbol{a}'_{d,i}$ is also null on the negative side $\Gamma^-_{t,i}$ of $\Gamma_{t,i}$ [58,61]; (3.20) thus becomes

$$\langle [\boldsymbol{n} \times \boldsymbol{h}_i], \boldsymbol{a}'_i \rangle_{\Gamma_{t,i}} = \langle (\mu_i d_i)^{-1} \boldsymbol{a}_{d,t,i}, \boldsymbol{a}'_{d,t,i} \rangle_{\Gamma^+_{t,i}}. \tag{3.21}$$

3.3 Coupled magnetodynamic and magnetostatic SPs

3.3.1 Generalities

As presented in Sections 3.2.1 and 3.2.2, the magnetodynamic and magnetostatic weak formulations have been established. In Section 3.2.3, the adapted formulations for the discretization of TS FE model [18, 60, 61] were formulated. Based on the developments in Chapter 2, we present two sequences of SP coupling, i.e. **three SPs** and **two SPs**.

3.3.2 From SP u to SP p−inductor alone to TS model

Keeping in mind the developments presented in Sections 2.3.2 and 3.2.3, the TS model [60, 61] is defined in SP p following the already calculated inductor source field from SP u. The constraint between SP u and SP p is thus expressed via an SS, i.e. $\boldsymbol{j}_{f,u}$ (see Section 2.3.2). The SS is defined via the BC and IC of the IBCs given by the TS model [60, 61] combined with contributions from the SP u. The TS model for the magnetic flux density formulation presented in Section 3.2.3 requires the unknown discontinuity of $\boldsymbol{a}_{d,t,p}$ of the tangential component $\boldsymbol{a}_{t,p} = (\boldsymbol{n} \times \boldsymbol{a}_p) \times \boldsymbol{n}$ of $\boldsymbol{a}_p$ through the TS as

$$[\boldsymbol{a}_{t,p}]_{\Gamma_{t,p}} = \boldsymbol{a}_{d,t,p} \;\text{ or }\; [\boldsymbol{n} \times \boldsymbol{a}_{t,p}]_{\Gamma_{t,p}} = \boldsymbol{n} \times \boldsymbol{a}_{d,t,p}\,, \tag{3.22}$$

with a fixed zero value along the border of the TS, i.e. $\partial\Gamma_{t,p}$, which neglects the magnetic flux entering there. In order to explicitly express this discontinuity, based on the equation (3.12), the field $\boldsymbol{a}_p$ is expressed on both sides of $\Gamma_{t,p}$ as

$$\boldsymbol{a}_p|_{\Gamma^+_{t,p}} = \boldsymbol{a}_{c,t,p} + \boldsymbol{a}_{d,t,p}\,,\;\; \boldsymbol{a}_p|_{\Gamma^-_{t,p}} = \boldsymbol{a}_{c,t,p}\,, \tag{3.23 a-b}$$

where $\boldsymbol{a}_{c,t,p}$ is the continuous component of $\boldsymbol{a}_p$. (3.23 a) and (3.23 b) also apply on $\Gamma_{t,p}$ for the tangential components $\boldsymbol{a}_{t,p}$, $\boldsymbol{a}_{c,t,p}$ and $\boldsymbol{a}_{d,t,p}$.

The relative constraint between SP u and SP p via the corresponding IC with $\gamma^{\pm}_{t,u} = \gamma^{\pm}_{p,u} = \Gamma^{\pm}_{t,u} = \Gamma^{\pm}_{t,p}$ and $\boldsymbol{n}_t = -\boldsymbol{n}$ for the TS is defined via (3.16). Associating (2.22) with (3.15), the trace discontinuity $[\boldsymbol{n} \times \boldsymbol{h}_p]_{\Gamma_{t,p}}$ of SP p is

$$[\boldsymbol{n} \times \boldsymbol{h}_p]_{\Gamma_{t,p}} = [\boldsymbol{n} \times (\boldsymbol{h}_u + \boldsymbol{h}_p)]_{\Gamma_{t,p}} = [\boldsymbol{n} \times \boldsymbol{h}]_{\Gamma_{t,p}} = \sigma_p \beta_p\, \partial_t (2\boldsymbol{a}_{c,t,p} + \boldsymbol{a}_{d,t,p}), \tag{3.24}$$

where β_p is given in (1.58).

Combining (2.25) and (3.16), the trace of the magnetic field $\boldsymbol{n} \times \boldsymbol{h}_p|_{\Gamma^+_{t,p}}$ on the positive side $\Gamma^+_{t,p}$ of the TS is expressed as

$$\begin{aligned}
\boldsymbol{n} \times \boldsymbol{h}_p|_{\Gamma^+_{t,p}} &= \boldsymbol{n} \times (\boldsymbol{h}_u + \boldsymbol{h}_p)|_{\Gamma^+_{t,p}} - \boldsymbol{n} \times \boldsymbol{h}_u|_{\Gamma^+_{t,p}} \\
&= \frac{1}{2}\Big[\sigma_p \beta_p\, \partial_t (2\boldsymbol{a}_{c,t,p} + \boldsymbol{a}_{d,t,p}) + \frac{1}{\mu_p \beta_p}\, \boldsymbol{a}_{d,t,p}\Big] - \boldsymbol{n} \times \boldsymbol{h}_u|_{\Gamma^+_{t,p}} \\
&= \frac{1}{2}\Big[\sigma_p \beta_p\, \partial_t (2\boldsymbol{a}_{c,t,p} + \boldsymbol{a}_{d,t,p}) + \frac{1}{\mu_p \beta_p}\, \boldsymbol{a}_{d,t,p}\Big] - \boldsymbol{j}_{f,u}.
\end{aligned} \tag{3.25}$$

In statics, $\partial_t \cdot = 0$ and $\beta_p = d/2$ (see Section 1.4.3), the trace of the magnetic field $\boldsymbol{n} \times \boldsymbol{h}_p|_{\Gamma^+_{t,p}}$ in (3.25) thus becomes

$$\boldsymbol{n} \times \boldsymbol{h}_p|_{\Gamma^+_{t,p}} = \frac{1}{2}\frac{1}{\mu_p \beta_p}\, \boldsymbol{a}_{d,t,p} - \boldsymbol{j}_{f,u} = \frac{1}{\mu_p d_p}\, \boldsymbol{a}_{d,t,p} - \boldsymbol{j}_{f,u}. \tag{3.26}$$

3.3.3 From SP p to SP k−TS model to volume correction

Once obtained, the TS solution in SP p is corrected by the volume correction SP k that overcomes the TS assumptions. In order to correct the TS model, one has to

suppress the TS representation via SSs opposed to TS discontinuities, in parallel to VSs in the added volume shell that account for volume changes of μ_k and σ_k from the properties of ambient region in SP p to these of actual volume shell in SP k (with $\mu_p = \mu_0$, $\mu_k = \mu_{volume}$, $\sigma_p = 0$ and $\sigma_k = \sigma_{volume}$). This correction can be limited to the neighborhood of the shell, which allows to benefit from a reduction of the extension of the associated mesh [20, 22, 30].

Based on the developments in Section 2.3.3, the changes of properties from μ_p and σ_p in SP p to μ_k and σ_k in SP k, leads to the associated VSs in the $\boldsymbol{h}_k - \boldsymbol{b}_k$ and $\boldsymbol{j}_k - \boldsymbol{e}_k$ relations presented in (2.32) and (2.35). VSs for SP k are recalled, i.e.

$$\boldsymbol{h}_{s,k} = (\mu_k^{-1} - \mu_p^{-1})(\boldsymbol{b}_u + \boldsymbol{b}_p)\,, \tag{3.27}$$

$$\boldsymbol{j}_{s,k} = (\sigma_k - \sigma_p)(\boldsymbol{e}_u + \boldsymbol{e}_p), \tag{3.28}$$

where $\boldsymbol{h}_{s,k}$ and $\boldsymbol{j}_{s,k}$ are the VSs for SP k.

3.3.4 Sequence of magnetodynamic SP formulations−three SPs

Collecting the results of Sections 3.3.2 and 3.3.3, we develop the weak formulations for each SP in the sequence: SP $u \rightarrow$ SP $p \rightarrow$ SP k.

3.3.4.1 Inductor model−SP u

Based on the equation (3.4) in Section 3.2.1, a weak form for the simplified model SP u with only the inductors is written as

$$(\mu_u^{-1}\mathbf{curl}\,\boldsymbol{a}_u, \mathbf{curl}\,\boldsymbol{a}'_u)_{\Omega_u} + \langle \boldsymbol{n}\times\boldsymbol{h}_u, \boldsymbol{a}'_u\rangle_{\Gamma_{h,u}} = (\boldsymbol{j}_{s,u}, \boldsymbol{a}'_u)_{\Omega_u}, \quad \forall \boldsymbol{a}'_u \in \boldsymbol{H}^0_{e,u}(\mathbf{curl};\Omega_u), \tag{3.29}$$

where $\boldsymbol{j}_{s,u}$ is the fixed current density in the inductor. The surface integral term on $\Gamma_{h,u}$ in (3.29) accounts for a natural BC of type (2.7 a), usually zero.

3.3.4.2 Thin shell FEs model−SP p

The TS model is defined via the term $\langle [\boldsymbol{n}\times\boldsymbol{h}_p], \boldsymbol{a}'_p\rangle_{\Gamma_{t,p}}$ in (3.18). It is used to weakly express the magnetic field TS IC proper to the weak form of SP p, i.e.

$$(\mu_p^{-1}\mathbf{curl}\,\boldsymbol{a}_p, \mathbf{curl}\,\boldsymbol{a}'_p)_{\Omega_p} + (\sigma_p\,\partial_t\boldsymbol{a}_p, \boldsymbol{a}'_p)_{\Omega_{c,p}} + (\sigma_p\,\mathbf{grad}\,v_p, \boldsymbol{a}'_p)_{\Omega_{c,p}} + \langle \boldsymbol{n}\times\boldsymbol{h}_p, \boldsymbol{a}'_p\rangle_{\Gamma_{h,p}-\Gamma_{t,p}} + \langle [\boldsymbol{n}\times\boldsymbol{h}_p]_{\Gamma_{t,p}}, \boldsymbol{a}'_p\rangle_{\Gamma_{t,p}} = 0, \quad \forall \boldsymbol{a}'_p \in \boldsymbol{H}^0_{e,p}(\mathbf{curl};\Omega_p). \tag{3.30}$$

Note that the second and third volume integrals in (3.30) do not contribute to (3.30) if $\Omega_{c,p}$ is empty or contains no conducting regions in SP p. The test function $\boldsymbol{a}'_p$ in the term $\langle [\boldsymbol{n}\times\boldsymbol{h}_p]_{\Gamma_{t,p}}, \boldsymbol{a}'_p\rangle_{\Gamma_{t,p}}$ in (3.30) is split into the continuous and discontinuous parts $\boldsymbol{a}'_{c,t,p}$ and $\boldsymbol{a}'_{d,t,p}$, respectively (see Section 3.2.1). Thus, one has

$$\langle[\boldsymbol{n}\times\boldsymbol{h}_p]_{\Gamma_{t,p}},\boldsymbol{a}'_p\rangle_{\Gamma_{t,p}} =$$
$$\langle[\boldsymbol{n}\times\boldsymbol{h}_p]_{\Gamma_{t,p}},\boldsymbol{a}'_{c,t,p}+\boldsymbol{a}'_{d,t,p}\rangle_{\Gamma_{t,p}} = \langle[\boldsymbol{n}\times\boldsymbol{h}_p]_{\Gamma_{t,p}},\boldsymbol{a}'_{c,t,p}\rangle_{\Gamma_{t,p}} + \langle[\boldsymbol{n}\times\boldsymbol{h}_p]_{\Gamma_{t,p}},\boldsymbol{a}'_{d,t,p}\rangle_{\Gamma_{t,p}}$$
$$= \langle[\boldsymbol{n}\times\boldsymbol{h}_p]_{\Gamma_{t,p}},\boldsymbol{a}'_{c,t,p}\rangle_{\Gamma_{t,p}} + \langle\boldsymbol{n}\times\boldsymbol{h}_p|_{\Gamma^+_{t,p}},\boldsymbol{a}'_{d,t,p}\rangle_{\Gamma^+_{t,p}} - \langle\boldsymbol{n}\times\boldsymbol{h}_p|_{\Gamma^-_{t,p}},\boldsymbol{a}'_{d,t,p}\rangle_{\Gamma^-_{t,p}}. \quad (3.31)$$

As said in the previous section, $\boldsymbol{a}'_{d,t,p}$ is defined as equal to zero on the negative side $\Gamma^-_{t,p}$ of the TS [60,61]. Therefore, (3.31) becomes

$$\langle[\boldsymbol{n}\times\boldsymbol{h}_p]_{\Gamma_{t,p}},\boldsymbol{a}'_p\rangle_{\Gamma_{t,p}} = \langle[\boldsymbol{n}\times\boldsymbol{h}_p]_{\Gamma_{t,p}},\boldsymbol{a}'_{c,t,p}\rangle_{\Gamma_{t,p}} + \langle\boldsymbol{n}\times\boldsymbol{h}_p|_{\Gamma^+_{t,p}},\boldsymbol{a}'_{d,t,p}\rangle_{\Gamma^+_{t,p}}. \quad (3.32)$$

The trace discontinuity $\langle[\boldsymbol{n}\times\boldsymbol{h}_p]_{\Gamma_{t,p}},\boldsymbol{a}'_{c,t,p}\rangle_{\Gamma_{t,p}}$ in (3.32) is given by (3.24), i.e.

$$\begin{aligned}\langle[\boldsymbol{n}\times\boldsymbol{h}_p]_{\Gamma_{t,p}},\boldsymbol{a}'_{c,t,p}\rangle_{\Gamma_{t,p}} &= \langle[\boldsymbol{n}\times\boldsymbol{h}]_{\Gamma_{t,p}},\boldsymbol{a}'_{c,t,p}\rangle_{\Gamma_{t,p}}\\ &= \langle\sigma_p\beta_p\,\partial_t(2\boldsymbol{a}_{c,t,p}+\boldsymbol{a}_{d,t,p}),\boldsymbol{a}'_{c,t,p}\rangle_{\Gamma_{t,p}}. \quad (3.33)\end{aligned}$$

The term $\langle\boldsymbol{n}\times\boldsymbol{h}_p|_{\Gamma^+_{t,p}},\boldsymbol{a}'_{d,t,p}\rangle_{\Gamma^+_{t,p}}$ in (3.32) related to the positive side $\Gamma^+_{t,p}$ of TS is given by (3.25), one has

$$\begin{aligned}\langle\boldsymbol{n}\times\boldsymbol{h}_p|_{\Gamma^+_{t,p}},\boldsymbol{a}'_{d,t,p}\rangle_{\Gamma^+_{t,p}} = \langle\frac{1}{2}\big[\sigma_p\beta_p\,\partial_t(2\boldsymbol{a}_{c,t,p}+\boldsymbol{a}_{d,t,p})+\frac{1}{\mu_p\beta_p}\,\boldsymbol{a}_{d,t,p}\big],\boldsymbol{a}'_{d,t,p}\rangle_{\Gamma^+_{t,p}}\\ -\langle\boldsymbol{n}\times\boldsymbol{h}_u|_{\Gamma^+_{t,p}},\boldsymbol{a}'_{d,t,p}\rangle_{\Gamma^+_{t,p}}, \quad (3.34)\end{aligned}$$

suppressing $\boldsymbol{n}\times\boldsymbol{h}_u|_{\Gamma^+_{t,p}}$ of SP u and simultaneously adding the actual TS BC. For that, the resulting surface integral term $\langle\boldsymbol{n}\times\boldsymbol{h}_u|_{\Gamma^+_{t,p}},\boldsymbol{a}'_{d,t,p}\rangle_{\Gamma^+_{t,p}}$ (weighted by $\boldsymbol{a}'_{d,t,p}$) is a SS for SP p that can be correctly expressed via the weak formulation of SP u in (3.29), i.e.

$$-\langle\boldsymbol{n}\times\boldsymbol{h}_u|_{\Gamma^+_{t,p}},\boldsymbol{a}'_{d,t,p}\rangle_{\Gamma^+_{t,p}} = (\mu_u^{-1}\mathbf{curl}\,\boldsymbol{a}_u,\mathbf{curl}\,\boldsymbol{a}'_{d,t,p})_{\Omega^+_p} = -\boldsymbol{j}_{f,u}. \quad (3.35)$$

The contribution of the volume integral in (3.35) is limited to a single layer of FEs on the positive side of Ω^+_p touching $\Gamma^+_{t,p}$ (Fig. 3.1), because it involves only the associated trace $\boldsymbol{n}\times\boldsymbol{a}'_{d,t,p}|_{\Gamma^+_{t,p}}$.

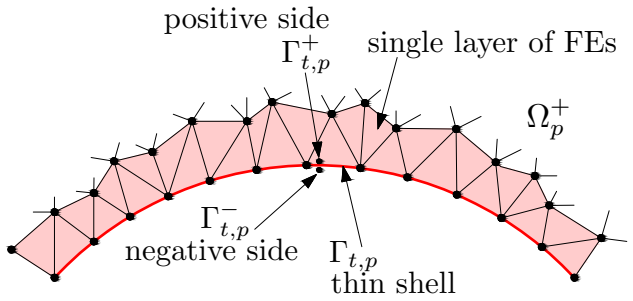

Figure 3.1: Transition layer for the TS SP p.

Substituting (3.35) into (3.34); (3.34) and (3.33) into (3.32); (3.32) into (3.31) and then (3.31) into (3.30) we obtain the final weak form of SP p, i.e.

$$(\mu_p^{-1}\mathbf{curl}\,\boldsymbol{a}_p,\mathbf{curl}\,\boldsymbol{a}'_p)_{\Omega_p} + \langle\frac{1}{2}\big[\sigma_p\beta_p\,\partial_t(2\boldsymbol{a}_{c,t,p}+\boldsymbol{a}_{d,t,p})+\frac{1}{\mu_p\beta_p}\,\boldsymbol{a}_{d,t,p}\big],\boldsymbol{a}'_{d,t,p}\rangle_{\Gamma^+_{t,p}}$$

$$+\langle \sigma_p \beta_p \, \partial_t (2\boldsymbol{a}_{c,t,p} + \boldsymbol{a}_{d,t,p}), \boldsymbol{a}'_{c,t,p} \rangle_{\Gamma_{t,p}} + (\mu_u^{-1} \mathbf{curl}\, \boldsymbol{a}_u, \mathbf{curl}\, \boldsymbol{a}'_{d,t,p})_{\Omega_p^+}$$
$$+\langle \boldsymbol{n} \times \boldsymbol{h}_p, \boldsymbol{a}'_p \rangle_{\Gamma_{h,p} - \Gamma_{t,p}} = 0, \quad \forall \boldsymbol{a}'_p \in \boldsymbol{H}^0_{e,p}(\mathbf{curl}; \Omega_p). \tag{3.36}$$

The surface integral term on $\Gamma_{h,p} - \Gamma_{t,p}$ in (3.36) also accounts for a natural BC of type (2.7 a), usually zero. At the discrete level, the source $\boldsymbol{a}_u$ in (3.36), initially in mesh of SP u, has to be projected to the mesh of SP p via a projection method (see Section 2.2.3).

3.3.4.3 Volume correction replacing the thin shell representation−SP k

The TS solution of SP p in (3.36) is further improved by SP k via the VSs given by (3.27) and (3.28). The fields have to be also transferred from the mesh of SP p to the mesh of SP k via a projection method. From that, the weak form for SP k is

$$(\mu_k^{-1} \mathbf{curl}\, \boldsymbol{a}_k, \mathbf{curl}\, \boldsymbol{a}'_k)_{\Omega_k} + (\sigma_k \, \partial_t \boldsymbol{a}_k, \boldsymbol{a}'_k)_{\Omega_{c,k}} + (\sigma_k \, \mathbf{grad}\, v_k, \boldsymbol{a}'_k)_{\Omega_{c,k}} + (\boldsymbol{h}_{s,k}, \mathbf{curl}\, \boldsymbol{a}'_k)_{\Omega_{c,k}}$$
$$+(\boldsymbol{j}_{s,k}, \boldsymbol{a}'_k)_{\Omega_{c,k}} + \langle \boldsymbol{n} \times \boldsymbol{h}_k, \boldsymbol{a}'_k \rangle_{\Gamma_{h,k} - \Gamma_{t,k}} + \langle [\boldsymbol{n} \times \boldsymbol{h}_k]_{\Gamma_{t,k}}, \boldsymbol{a}'_k \rangle_{\Gamma_{t,k}} = 0,$$
$$\forall \boldsymbol{a}'_k \in \boldsymbol{H}^0_{e,k}(\mathbf{curl}; \Omega_k). \tag{3.37}$$

The surface integral term on $\Gamma_{h,k} - \Gamma_{t,k}$ in (3.37) also accounts for natural BCs, usually zero. In (3.37), the changes of material properties from SP p to SP k are expressed via two volume integrals, i.e. $(\boldsymbol{h}_{s,k}, \mathbf{curl}\, \boldsymbol{a}'_k)_{\Omega_{c,k}}$ and $(\boldsymbol{j}_{s,k}, \boldsymbol{a}'_k)_{\Omega_{c,k}}$. The VS $\boldsymbol{h}_{s,k}$ is given by (3.27), with $\boldsymbol{b}_u = \mathbf{curl}\, \boldsymbol{a}_u$ and $\boldsymbol{b}_p = \mathbf{curl}\, \boldsymbol{a}_p$. The VS $\boldsymbol{j}_{s,k}$ given by (3.28), can be generally reduced to

$$\boldsymbol{j}_{s,k} = (\sigma_k - 0)(\boldsymbol{e}_p + \boldsymbol{e}_u) = \sigma_k(-\partial_t \boldsymbol{a}_p - \mathbf{grad}\, v_p - \partial_t \boldsymbol{a}_u - \mathbf{grad}\, v_u). \tag{3.38}$$

The potentials v_u and v_p are unknown in non-conducting region $\Omega^C_{c,k}$ of SP k, but their determination via an electric problem [41, 42] prior to SP p is not needed: relation (2.38) in Section 2.3.3 is then

$$\begin{aligned} \boldsymbol{j}_k &= \sigma_k(\boldsymbol{e}_k + \boldsymbol{e}_p + \boldsymbol{e}_u) \\ &= \sigma_k(-\partial_t \boldsymbol{a}_k - \mathbf{grad}\, v_k - \partial_t \boldsymbol{a}_p - \mathbf{grad}\, v_p - \partial_t \boldsymbol{a}_u - \mathbf{grad}\, v_u), \end{aligned} \tag{3.39}$$

with the freedom to fix v_k, v_p and v_u to zero and allow $\boldsymbol{a}_k$ to react alone to $\boldsymbol{a}_p$ and $\boldsymbol{a}_u$.

Simultaneously to the VSs, the SSs have to suppress the TS discontinuities of SP p in SP k, with the IC in (2.41) to be defined as

$$[\boldsymbol{n} \times \boldsymbol{h}_k]_{\Gamma_{t,k}} = -[\boldsymbol{n} \times \boldsymbol{h}_p]_{\Gamma_{t,k}}, \tag{3.40}$$
$$[\boldsymbol{n} \times \boldsymbol{a}_k]_{\Gamma_{t,k}} = -\boldsymbol{n} \times \boldsymbol{a}_{d,t,p}|_{\Gamma_{t,k}}, \tag{3.41}$$

respectively in weak and strong senses, i.e. via a surface integral and in the function space $\boldsymbol{H}^0_{e,k}(\mathbf{curl}; \Omega_k)$. IC (3.41) strongly fixes $\boldsymbol{a}_{d,t,k} = -\boldsymbol{a}_{d,t,p}$. IC (3.40) is weakly expressed through the surface integral term $\langle [\boldsymbol{n} \times \boldsymbol{h}_k]_{\Gamma_{t,k}}, \boldsymbol{a}'_k \rangle_{\Gamma_{t,k}}$ in (3.37), with $\Gamma_{t,k} = \Gamma_{t,p}$. The discontinuity $[\boldsymbol{n} \times \boldsymbol{h}_k]_{\Gamma_{t,k}}$ in (3.40) is expressed as

$$\langle [\boldsymbol{n} \times \boldsymbol{h}_k]_{\Gamma_{t,k}}, \boldsymbol{a}'_k \rangle_{\Gamma_{t,k}} = -\langle [\boldsymbol{n} \times \boldsymbol{h}_p]_{\Gamma_{t,k}}, \boldsymbol{a}'_k \rangle_{\Gamma_{t,k}}. \tag{3.42}$$

The term $\langle[\boldsymbol{n}\times\boldsymbol{h}_p]_{\Gamma_{t,k}},\boldsymbol{a}'_k\rangle_{\Gamma_{t,k}}$ in (3.42) is weakly evaluated from the volume integrals similarly to (3.35). At the discrete level, these integrals are limited to the layers of FEs on both sides $\Gamma_{t,k}$ of TS, because they involve only the associated trace $\boldsymbol{n}\times\boldsymbol{a}'_k|_{\Gamma_{t,k}}$.

From above analyses, the weak form of SP k now becomes

$$(\mu_k^{-1}\mathbf{curl}\,\boldsymbol{a}_k,\mathbf{curl}\,\boldsymbol{a}'_k)_{\Omega_k}+(\sigma_k\,\partial_t\boldsymbol{a}_k,\boldsymbol{a}'_k)_{\Omega_{c,k}}+\langle-[\boldsymbol{n}\times\boldsymbol{h}_p]_{\Gamma_{t,k}},\boldsymbol{a}'_k\rangle_{\Gamma_{t,k}}+(\sigma_k\partial_t(\boldsymbol{a}_p+\boldsymbol{a}_u),\boldsymbol{a}'_k)_{\Omega_{c,k}}$$
$$+((\mu_k^{-1}-\mu_p^{-1})(\mathbf{curl}\,\boldsymbol{a}_u+\mathbf{curl}\,\boldsymbol{a}_p),\mathbf{curl}\,\boldsymbol{a}'_k)_{\Omega_k}=0,\forall\boldsymbol{a}'_k\in\boldsymbol{H}^0_{e,k}(\mathbf{curl};\Omega_k). \quad (3.43)$$

At the discrete level, the source quantities $\boldsymbol{a}_u$ and $\boldsymbol{a}_p$ defined in the mesh of SP u and SP p are projected to the mesh of SP k in (3.43), with $\Omega_{s,k}$ limited to the volume shell, which thus decreases the computational effort of the projection process.

The volume correction is quite sensitive to cancellation errors, with dramatic effects on the computation of $\boldsymbol{a}_k$ (see Fig. 3.2). A method to avoid the cancellation error is presented in [46]. We combine an SP k_a with $\boldsymbol{h}_{k_a}=\mu_{k_a}^{-1}\boldsymbol{b}_{k_a}+(\mu_{k_a}^{-1}-\mu_p^{-1})(\boldsymbol{b}_p+$

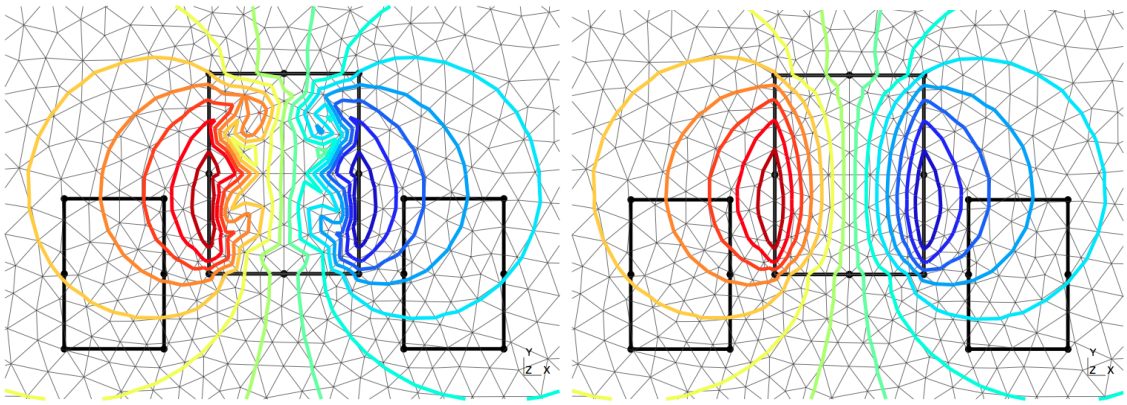

Figure 3.2: Flux lines on the conducting region (plate or core) with cancellation error (*left*) and using the robust procedure described in [46] (*right*).

$\boldsymbol{b}_u$), considering a perfect magnetic region in $\Omega_{c,k}$ ($\mu_{k_a}=\infty$, $\mu_{k_a}^{-1}=0$), and an SP k_b with $\boldsymbol{h}_{k_b}=\mu_{k_b}^{-1}\boldsymbol{b}_{k_b}+(\mu_{k_b}^{-1}-\mu_{k_a}^{-1})(\boldsymbol{b}_{k_a}+\boldsymbol{b}_p+\boldsymbol{b}_u)$, considering a change to the actual finite permeability ($\mu_{k_b}=\mu_{volume}=\mu_k$); SP k_a uses an SS only contributing on positive side $\Gamma^+_{c,k}$ of $\Gamma_{c,k}$, i.e.

$$[\boldsymbol{n}\times\boldsymbol{h}_{k_a}]_{\Gamma_{c,k}}=\boldsymbol{n}\times\boldsymbol{h}_{k_a}|_{\Gamma^+_{c,k}}=-\boldsymbol{n}\times\boldsymbol{h}_p|_{\Gamma^+_{c,k}}=\boldsymbol{j}_{f,k_a}, \quad (3.44)$$

with $\boldsymbol{h}_{s,k_a}=0$ and $\boldsymbol{b}_{k_a}\neq 0$. The trace $\boldsymbol{n}\times\boldsymbol{h}_p|_{\Gamma^+_{c,k}}$ originally appears in (3.30) for SP p restricted to $\Gamma_{c,k}=\Gamma_{t,p}$. It can be also naturally expressed via the volume integral in (3.30), i.e.

$$\begin{aligned}\langle[\boldsymbol{n}\times\boldsymbol{h}_{k_a}]_{\Gamma_{c,k}},\boldsymbol{a}'_{k_a}\rangle_{\Gamma_{c,k}}&=-\langle\boldsymbol{n}\times\boldsymbol{h}_p|_{\Gamma^+_{c,k}},\boldsymbol{a}'_{k_a}\rangle_{\Gamma_{c,k}}\\&=(\mu_p^{-1}\mathbf{curl}\,\boldsymbol{a}_p,\mathbf{curl}\,\boldsymbol{a}'_{k_a}|_{\Gamma^+_{c,k}})_{\Omega_{\mathrm{TL}}}, \quad (3.45)\end{aligned}$$

where Ω_{TL} in (3.45) is limited to one single layer of FEs touching $\Gamma^+_{c,k}$, because it involves only the associated trace $\boldsymbol{n} \times \boldsymbol{a}'_{k_a}|_{\Gamma^+_{c,k}}$ [45] ($\boldsymbol{a}'_{k_a} = \boldsymbol{a}'_{k_b} = \boldsymbol{a}'_k$ because of the same property on the mesh). For SP k_b, we have the VS

$$\boldsymbol{h}_{s,k_b} = (\mu_{k_b}^{-1} - \mu_{k_a}^{-1})(\boldsymbol{b}_{k_a} + \boldsymbol{b}_p + \boldsymbol{b}_u), \tag{3.46}$$

with $\mu_{k_b} = \mu_{volume} = \mu_k$ and $\mu_{k_a}^{-1} = 0$. Both SP k_a and SP k_b gain at being solved simultaneously, with the SS $\boldsymbol{j}_{f,k} = \boldsymbol{n} \times \boldsymbol{h}_k|_{\Gamma^+_{c,k}} = \boldsymbol{j}_{f,k_a}$ and the resulting relation

$$\begin{aligned} \boldsymbol{h}_k = \boldsymbol{h}_{k_a} + \boldsymbol{h}_{k_b} &= -\mu_p^{-1}(\boldsymbol{b}_p + \boldsymbol{b}_u) + \mu_{k_b}^{-1}\boldsymbol{b}_{k_b} + \mu_{k_b}^{-1}(\boldsymbol{b}_{k_a} + \boldsymbol{b}_p + \boldsymbol{b}_u) \\ &= \mu_k^{-1}(\boldsymbol{b}_{k_a} + \boldsymbol{b}_{k_a}) + (\mu_k^{-1} - \mu_p^{-1})(\boldsymbol{b}_p + \boldsymbol{b}_u) \\ &= \mu_k^{-1}\boldsymbol{b}_k + (\mu_k^{-1} - \mu_p^{-1})(\boldsymbol{b}_p + \boldsymbol{b}_u). \end{aligned} \tag{3.47}$$

This procedure asks for the projection of the source field in the added magnetic region (for VSs) as well as in the layer of FEs surrounding this region (for SSs).

Thus, (3.43) becomes

$$\begin{aligned} &(\mu_k^{-1}\mathbf{curl}\,\boldsymbol{a}_k, \mathbf{curl}\,\boldsymbol{a}'_k)_{\Omega_k} + (\sigma_k\,\partial_t\boldsymbol{a}_k, \boldsymbol{a}'_k)_{\Omega_{c,k}} + (\sigma_k\partial_t(\boldsymbol{a}_p + \boldsymbol{a}_u), \boldsymbol{a}'_k)_{\Omega_{c,k}} \\ &+((\mu_k^{-1} - \mu_p^{-1})(\mathbf{curl}\,\boldsymbol{a}_u + \mathbf{curl}\,\boldsymbol{a}_p), \mathbf{curl}\,\boldsymbol{a}'_k)_{\Omega_{c,k}} + \langle -[\boldsymbol{n} \times \boldsymbol{h}_p]_{\Gamma_{t,k}}, \boldsymbol{a}'_k\rangle_{\Gamma_{t,k}} \\ &+(\mu_p^{-1}\mathbf{curl}\,\boldsymbol{a}_p, \mathbf{curl}\,\boldsymbol{a}'_k|_{\Gamma^+_{c,k}})_{\Omega_{\mathrm{TL}}} = 0, \forall \boldsymbol{a}'_k \in \boldsymbol{H}^0_{e,k}(\mathbf{curl}; \Omega_k). \end{aligned} \tag{3.48}$$

3.3.5 Sequence of magnetodynamic SP formulations—two SPs

Collecting the results of Sections 3.3.2 and 3.3.3, we develop the weak formulations for each SP in the sequence: SP $f \rightarrow$ SP k. The weak form for SP f is established by substituting (3.16) and (3.17) into (3.11), and (3.11) into (3.4), i.e.

$$\begin{aligned} &(\mu_f^{-1}\mathbf{curl}\,\boldsymbol{a}_f, \mathbf{curl}\,\boldsymbol{a}'_f)_{\Omega_f} + (\sigma_f(\partial_t\boldsymbol{a}_f + \mathbf{grad}\,v_f), \boldsymbol{a}'_f)_{\Omega_{c,f}} + \langle \frac{1}{2\mu_f\beta_f}\,\boldsymbol{a}_{d,t,f}, \boldsymbol{a}'_{d,t,f}\rangle_{\Gamma^+_{t,p}} \\ &+\langle \sigma_f\beta_f\,\partial_t(2\boldsymbol{a}_{c,t,f} + \boldsymbol{a}_{d,t,f}), \boldsymbol{a}'_{c,t,f}\rangle_{\Gamma_{t,f}} + \langle \frac{1}{2}\left[\sigma_f\beta_f\,\partial_t(2\boldsymbol{a}_{c,t,f} + \boldsymbol{a}_{d,t,f})\right], \boldsymbol{a}'_{d,t,f}\rangle_{\Gamma^+_{t,p}} \\ &+\langle \boldsymbol{n} \times \boldsymbol{h}_f, \boldsymbol{a}'_f\rangle_{\Gamma_{h,f}-\Gamma_t} = (\boldsymbol{j}_{s,f}, \boldsymbol{a}'_f)_{\Omega_{s,f}}, \forall \boldsymbol{a}'_f \in \boldsymbol{H}^0_{e,f}(\mathbf{curl}; \Omega_f), \end{aligned} \tag{3.49}$$

where the surface integral term on $\Gamma_{h,f} - \Gamma_t$ is subject to a natural BC of type (2.7 a), usually zero. At this point, the second volume integral in (3.49) is omitted because $\Omega_{c,f}$ contains only the inductor and the TS without any conducting regions.

Analogously to Section 3.3.4.3, the solution of (3.49) that governs the TS problem SP f is then corrected by SP k via the VSs ($\boldsymbol{j}_{s,k}$ and $\boldsymbol{h}_{s,k}$) given by (3.43), with $\boldsymbol{b}_f = \boldsymbol{b}_u + \boldsymbol{b}_p = \mathbf{curl}\,\boldsymbol{a}_f$. The weak form for SP k is thus given by thanks to (3.43), with $\boldsymbol{h}_f = \boldsymbol{h}_p$, $\mu_f = \mu_p$ and $\boldsymbol{a}_f = \boldsymbol{a}_u + \boldsymbol{a}_p$.

The treatment of the TS discontinuities of SP f in SP k is similar to the treatment of the TS discontinuities of SP p in SP k in Section 3.3.4.3. Cancellation errors can be avoided using the same strategy as in the three SP case.

3.3.6 SPs coupled to global quantities

In Sections 3.3.4 and 3.3.5, the source field to calculate SP u or SP f is the imposed current density $\boldsymbol{j}_{s,u}$ or $\boldsymbol{j}_{s,f}$. Other kinds of sources can be defined and used in the weak form of SP u or SP f to lead to circuit relations [33, 39]. Voltage driven massive inductors can be considered through a unit source electric scalar potential $v_{s,i}$ associated with a unit voltage for each massive inductor $\Omega_{m,i}$, and leading to

$$v_i = \sum_i V_i v_{s,i}, \tag{3.50}$$

where V_i is the voltage drop between the electrodes $\Gamma^+_{g,i}$ and $\Gamma^-_{g,i}$ of the massive inductor $\Omega_{g,i}$ (see Fig. 1.3). The weak form for SP u thus becomes

$$\begin{aligned}(\mu_u^{-1}\mathbf{curl}\,\boldsymbol{a}_u, \mathbf{curl}\,\boldsymbol{a}'_u)_{\Omega_u} + (\sigma_u \partial_t \boldsymbol{a}_u, \boldsymbol{a}'_u)_{\Omega_m} + \sum_i V_i (\sigma_u\,\mathbf{grad}\, v_{s,i}, \boldsymbol{a}'_u)_{\Omega_m} \\ + \langle \boldsymbol{n} \times \boldsymbol{h}_u, \boldsymbol{a}'_u \rangle_{\Gamma_{h,u}} = 0, \forall \boldsymbol{a}'_u \in \boldsymbol{H}^0_{e,u}(\mathbf{curl}; \Omega)_u.\end{aligned} \tag{3.51}$$

Analogously, the weak form for SP f is

$$\begin{aligned}(\mu_f^{-1}\mathbf{curl}\,\boldsymbol{a}_f, \mathbf{curl}\,\boldsymbol{a}'_f)_{\Omega_f} + (\sigma_f \partial_t \boldsymbol{a}_f, \boldsymbol{a}'_f)_{\Omega_m} + \sum_i V_i (\sigma_f\,\mathbf{grad}\, v_{s,i}, \boldsymbol{a}'_f)_{\Omega_m} \\ + \langle \frac{1}{2\mu_f\beta_f}\,\boldsymbol{a}_{d,t,f}, \boldsymbol{a}'_{d,t,f} \rangle_{\Gamma^+_{t,f}} + \langle \sigma_f\beta_f\,\partial_t(2\boldsymbol{a}_{c,t,f} + \boldsymbol{a}_{d,t,f}), \boldsymbol{a}'_{c,t,f} \rangle_{\Gamma_{t,f}} \\ + \langle \frac{1}{2}\big[\sigma_f\beta_f\,\partial_t(2\boldsymbol{a}_{c,t,f} + \boldsymbol{a}_{d,t,f})\big], \boldsymbol{a}'_{d,t,f} \rangle_{\Gamma^+_{t,f}} + \langle \boldsymbol{n} \times \boldsymbol{h}_f, \boldsymbol{a}'_f \rangle_{\Gamma_{h,f} - \Gamma_{t,f}} = 0, \\ \forall \boldsymbol{a}'_f \in \boldsymbol{H}^0_{e,f}(\mathbf{curl}; \Omega_f).\end{aligned} \tag{3.52}$$

The voltage associated with a massive inductor then explicitly appears in equations through (3.50), as a global quantity defined in a strong sense. Formulations (3.51) and (3.52) are actually generalization of the modified vector potential formulation given in [8, 49, 94]. The pre-computation of the source scalar potential $v_{s,i}$ can be done by solving an electrokinetic problem ($v_{s,i}$ is equal to 1 on one electrode, to 0 on the other and varies continuously in $\Omega_{c,i}$, which gives the electric field needed in the electromotive force region $\Omega_{emf,i}$) [33, 39].

3.3.7 Sequence of magnetostatic SP formulations—three SPs

Based on the developments that were made for the magnetodynamic formulations in Section 3.3.4, the SP approach is now considered for the magnetostatic problem. Note that the weak form for SP u is herein similar to the weak form of SP u written in the magnetodynamic formulations (see Section 3.3.4.1). In this part, we only consider the case of SP p and SP k.

3.3.7.1 Thin shell FEs model−SP p

Analogously to Section 3.3.4.2, the TS model is expressed via the term $\langle[\boldsymbol{n}\times\boldsymbol{h}_p],\boldsymbol{a}'_p\rangle_{\Gamma_{t,i}}$ in (3.20). It is used to weakly express the magnetic field TS IC proper to the weak form of SP p, i.e.

$$(\mu_p^{-1}\mathbf{curl}\,\boldsymbol{a}_p,\mathbf{curl}\,\boldsymbol{a}'_p)_{\Omega_p}+\langle\boldsymbol{n}\times\boldsymbol{h}_p,\boldsymbol{a}'_p\rangle_{\Gamma_{h,p}-\Gamma_{t,p}}+\langle[\boldsymbol{n}\times\boldsymbol{h}_p]_{\Gamma_{t,p}},\boldsymbol{a}'_p\rangle_{\Gamma_{t,p}}=0,\quad\forall\boldsymbol{a}'_p\in\boldsymbol{H}^0_{e,p}(\mathbf{curl};\Omega_p).\tag{3.53}$$

As in the magnetodynamic case, the term $\langle[\boldsymbol{n}\times\boldsymbol{h}_p]_{\Gamma_{t,p}},\boldsymbol{a}'_p\rangle_{\Gamma_{t,p}}$ in (3.53) gives

$$\langle[\boldsymbol{n}\times\boldsymbol{h}_p]_{\Gamma_{t,p}},\boldsymbol{a}'_p\rangle_{\Gamma_{t,p}}=\langle[\boldsymbol{n}\times\boldsymbol{h}_p]_{\Gamma_{t,p}},\boldsymbol{a}'_{c,t,p}+\boldsymbol{a}'_{d,t,p}\rangle_{\Gamma_{t,p}}=\langle[\boldsymbol{n}\times\boldsymbol{h}_p]_{\Gamma_{t,p}},\boldsymbol{a}'_{c,t,p}\rangle_{\Gamma_{t,p}}+\langle[\boldsymbol{n}\times\boldsymbol{h}_p]_{\Gamma_{t,p}},\boldsymbol{a}'_{d,t,p}\rangle_{\Gamma_{t,p}}.\tag{3.54}$$

As said in Section 3.3.4, the discontinuity $\boldsymbol{a}'_{d,t,p}$ is defined as equal to zero on the negative side $\Gamma^-_{t,p}$ of the TS, (3.54) thus becomes

$$\langle[\boldsymbol{n}\times\boldsymbol{h}_p]_{\Gamma_{t,p}},\boldsymbol{a}'_p\rangle_{\Gamma_{t,p}}=\langle[\boldsymbol{n}\times\boldsymbol{h}_p]_{\Gamma_{t,p}},\boldsymbol{a}'_{c,t,p}\rangle_{\Gamma_{t,p}}+\langle\boldsymbol{n}\times\boldsymbol{h}_p|_{\Gamma^+_{t,p}},\boldsymbol{a}'_{d,t,p}\rangle_{\Gamma^+_{t,p}}.\tag{3.55}$$

The $\boldsymbol{h}_p$ trace discontinuity $\langle[\boldsymbol{n}\times\boldsymbol{h}_p]_{\Gamma_{t,p}},\boldsymbol{a}'_{c,t,p}\rangle_{\Gamma_{t,p}}$ in (3.55) is given by (3.24) and is equal to zero because $\partial_t\cdot=0$. The term $\langle\boldsymbol{n}\times\boldsymbol{h}_p|_{\Gamma^+_{t,p}},\boldsymbol{a}'_{d,t,p}\rangle_{\Gamma^+_{t,p}}$ in (3.55) related to the positive side $\Gamma^+_{t,p}$ of TS is given by (3.26), i.e.

$$\langle\boldsymbol{n}\times\boldsymbol{h}_p|_{\Gamma^+_{t,p}},\boldsymbol{a}'_{d,t,p}\rangle_{\Gamma^+_{t,p}}=\langle\frac{1}{\mu_p d_p}\,\boldsymbol{a}_{d,t,p},\boldsymbol{a}'_{d,t,p}\rangle_{\Gamma^+_{t,p}}-\langle\boldsymbol{n}\times\boldsymbol{h}_u|_{\Gamma^+_{t,p}},\boldsymbol{a}'_{d,t,p}\rangle_{\Gamma^+_{t,p}}\tag{3.56}$$

also suppressing $\boldsymbol{n}\times\boldsymbol{h}_u|_{\Gamma^+_{t,p}}$ of SP u and adding the actual TS BC. Therefore, the resulting surface integral term $\langle\boldsymbol{n}\times\boldsymbol{h}_u|_{\Gamma^+_{t,p}},\boldsymbol{a}'_{d,t,p}\rangle_{\Gamma^+_{t,p}}$ appearing in (3.55) is a SS for SP p. This SS is given by (3.35).

Substituting (3.35) into (3.56); (3.56) into (3.55); (3.55) into (3.54) and then (3.54) into (3.53), the weak form of SP p is rewritten as

$$(\mu_p^{-1}\mathbf{curl}\,\boldsymbol{a}_p,\mathbf{curl}\,\boldsymbol{a}'_p)_{\Omega_p}+\langle\frac{1}{\mu_p d_p}\,\boldsymbol{a}_{d,t,p},\boldsymbol{a}'_{d,t,p}\rangle_{\Gamma^+_{t,p}}+\langle\boldsymbol{n}\times\boldsymbol{h}_p,\boldsymbol{a}'_p\rangle_{\Gamma_{h,p}-\Gamma_{t,p}}+(\mu_u^{-1}\mathbf{curl}\,\boldsymbol{a}_u,\mathbf{curl}\,\boldsymbol{a}'_{d,t,p})_{\Omega^+_p}=0,\quad\forall\boldsymbol{a}'_p\in\boldsymbol{H}^0_{e,p}(\mathbf{curl};\Omega_p).\tag{3.57}$$

At the discrete level, the source $\boldsymbol{a}_u$, initially in mesh of SP u, has to be projected to the mesh of SP p (see Section 2.2.3).

3.3.7.2 Volume correction replacing the thin shell representation−SP k

In a same way, the obtained TS solution from SP p is next corrected by SP k via the VS $\boldsymbol{h}_{s,k}$ given by (3.27). A weak form for SP k is thus

$$(\mu_k^{-1}\mathbf{curl}\,\boldsymbol{a}_k,\mathbf{curl}\,\boldsymbol{a}'_k)_{\Omega_k}+((\mu_k^{-1}-\mu_p^{-1})\mathbf{curl}\,(\boldsymbol{a}_u+\boldsymbol{a}_p),\mathbf{curl}\,\boldsymbol{a}'_k)_{\Omega_k}+\langle\boldsymbol{n}\times\boldsymbol{h}_k,\boldsymbol{a}'_k\rangle_{\Gamma_{h,k}-\Gamma_{t,k}}+\langle[\boldsymbol{n}\times\boldsymbol{h}_k]_{\Gamma_{t,k}},\boldsymbol{a}'_k\rangle_{\Gamma_{t,k}}=0,\quad\forall\boldsymbol{a}'_k\in\boldsymbol{H}^0_{e,k}(\mathbf{curl};\Omega_k).\tag{3.58}$$

Analogously to Section 3.3.4.3, the trace term $\langle[\boldsymbol{n}\times\boldsymbol{h}_k]_{\Gamma_{t,k}},\boldsymbol{a}'_k\rangle_{\Gamma_{t,k}}$ in (3.58) allows to suppress the TS discontinuities of SP p in SP k. Cancellation errors can be avoided using the same strategy as in the magnetodynamic case.

3.3.8 Sequence of magnetosatic SP formulations−two SPs

Analogously to Section 3.3.5, the sequence is considered in two SPs: SP $f \rightarrow$ SP f. Based on the equations (3.9) and (3.20) that were established in Section 3.2.2, the weak form for SP f is written as

$$(\mu_f^{-1}\mathbf{curl}\,\boldsymbol{a}_f, \mathbf{curl}\,\boldsymbol{a}'_f)_{\Omega_f} + \langle(\mu_f d_f)^{-1}\boldsymbol{a}_{d,t,f}, \boldsymbol{a}'_{d,f}\rangle_{\Gamma_{t,f}} + \langle \boldsymbol{n}\times\boldsymbol{h}_f, \boldsymbol{a}'_f\rangle_{\Gamma_{h,f}-\Gamma_{t,f}} = (\boldsymbol{j}_{s,f}, \boldsymbol{a}'_f)_{\Omega_{s,f}}, \forall \boldsymbol{a}'_f \in \boldsymbol{H}^0_{e,f}(\mathbf{curl};\Omega_f). \quad (3.59)$$

In a same way, the TS obtained solution in (3.59) is corrected by SP k given by (3.58), with $\mu_f = \mu_p$ and $\boldsymbol{a}_f = \boldsymbol{a}_u + \boldsymbol{a}_p$. The treatment of the TS discontinuity and the robust procedure in SP k is similar to the treatment in the previous sections.

3.3.9 Projection of solutions between meshes

As presented in Section 2.2.3, the aim is to project the magnetic vector potential $\boldsymbol{a}_i$ obtained from the previous SP (e.g. SP u) in a source mesh onto a mesh of target SP (e.g. SP p). At the discrete level, the source quantity $\boldsymbol{a}_u$ has to be expressed in the mesh of target SP p, while initially given in the mesh of previous SP u. This is done via (2.20), applied to its curl and limited to $\Omega_{s,p}$, that is

$$(\mathbf{curl}\,\boldsymbol{a}_{u,p-\mathrm{proj}}, \mathbf{curl}\,\boldsymbol{a}')_{\Omega_{s,p}} = (\mathbf{curl}\,\boldsymbol{a}_u, \mathbf{curl}\,\boldsymbol{a}')_{\Omega_{s,p}}, \quad \forall \boldsymbol{a}' \in \boldsymbol{H}^1_p(\mathbf{curl};\Omega_{s,p}), \quad (3.60)$$

where $\Omega_{s,p}$ is a subset of Ω_p of the target SP p, and $\boldsymbol{H}^1_p(\mathbf{curl};\Omega_{s,p})$ is a gauged curl-conform function space for the u-projected source $\boldsymbol{a}_{u,p-\mathrm{proj}}$ (the projection of $\boldsymbol{a}_u$ on the mesh of SP p) and the test function $\boldsymbol{a}'$. Directly projecting $\boldsymbol{a}_u$ (not its curl) is not possible in regions where a tree-cotree gauge is applied (see next Section).

3.3.10 Discretization of the magnetic vector potential and the electric scalar potential

The magnetic vector potential $\boldsymbol{a}_i$ in the magnetic flux density formulations (3.29), (3.36) and (3.37) is discretized by Whitney edge elements [12] and their extension to prism and hexahedron (see Section B.2) [35]. We thus have

$$\boldsymbol{a}_i = \sum_{e\in E(\Omega_i)} a_{e,i}\, s_{e,i}, \quad (3.61)$$

where $E(\Omega_i)$ is the set of edges of Ω_i, $s_{e,i}$ is the edge basis function associated with edge e, and $a_{e,i}$ is the circulation of $\boldsymbol{a}_i$ along e. This vector potential has to be gauged in order to make it unique. A natural gauge in the Whitney edge element space is to impose the circulation of the field along the edges of a spanning tree built in the domain [2, 34, 82]. In magnetodynamic formulation, its discretization is expressed as

$$\boldsymbol{a}_i = \sum_{e\in E(\Omega_{c,i})} a_{c,e,i}\, s_{c,e,i} + \sum_{e\in E(\Omega^{\mathrm{C}}_{c,i})\setminus E(\partial\Omega_{c,i})} a_{c,e,i}\, s_{c,e,i} + \sum_{i\in TS}\Big(\sum_{e\in E(\Gamma_{t,i})} a_{d,e,i} s_{d,e,i}\Big), \quad (3.62)$$

where $e \in E(\cdot)$ is the set of edges of the mesh of a given region.

In the case of the magnetostatic formulation, one has

$$\boldsymbol{a}_i = \sum_{e \in E(\Omega_i)} a_{c,e,i}\, s_{c,e,i} + \sum_{i \in TS} \Big(\sum_{e \in E(\Gamma_{t,i})} a_{d,e,i}\, s_{d,e,i} \Big). \tag{3.63}$$

The source potential $v_{s,i}$ is then discretized as the sum of the nodal basis functions

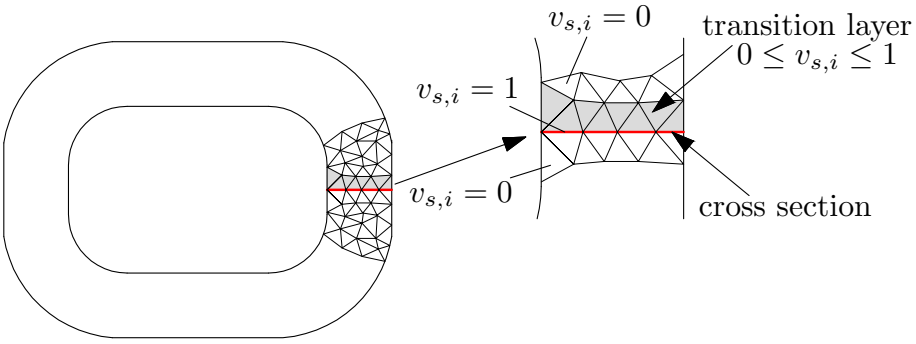

Figure 3.3: Cross-section and associated transition layer in an inductor

$s_{n,i}$ of all the nodes located on the cross-section $\Gamma_{g,i}$ (Fig. 1.3) [13, 35], i.e.,

$$v_{s,i} = s_i = \sum_{n \in N(\Gamma_{g,i})} s_{n,i}, \tag{3.64}$$

with a support limited to a transition layer containing all the elements adjacent to one side of the cross-section in Figure 3.3. Potential $v_{s,i}$ is equal to 1, the unit voltage, on $\Gamma_{g,i}$ [33, 39]. For massive inductors, the generalized source potential $v_{s,i}$ is equal to 1 on one electrode ($\Gamma^+_{g,i}$), is equal to 0 on the other one ($\Gamma^-_{g,i}$) and varies continuously in $\Omega_{m,i}$ (see Fig. 1.3) [48, 58, 64, 93, 116]. Thus, the discretization of $v_{s,i}$ is constructed by restricting its support to layer of elements connected to the "+" side of the removed generator $\Gamma_{g,i}$. This layer is also called transition layer and is denoted by supp $(v_{s,i})$. One has

$$v_{s,i} = \sum_{n \in N(\Gamma_{g,i})} g_{n,i}, \quad \text{with} \quad g_n = \begin{cases} s_1^{0,n} & \text{in supp}(v_{s,i}) \\ 0 & \text{otherwise} \end{cases}, \tag{3.65}$$

where $N(\Gamma_{g,i})$ is the set of nodes of the mesh of $\Gamma_{g,i}$. The reduction of the support of $v_{s,i}$ to a transition layer permits to reduce the number of unknowns involved in the circuit relations in Section 3.3.6.

Chapter 4

Thin shell subproblems with magnetic field formulations

Contents

4.1 Introduction

In this chapter we develop the TS SP coupling for the magnetic field formulations ($\boldsymbol{h}$-formulations), for both simply and multiply connected TS regions. Classical weak formulations are first presented, taking thin conducting and magnetic structures into account [58, 60, 61]. The coupling between the local electromagnetic quantities and the global currents and voltages is presented, as well as a method to define source electric fields involved in SPs.

The contributions developed in this chapter are also extensions of the work by C. Geuzaine and P. Dular for the $\boldsymbol{h}$-formulations [58,60,61]. Most original contributions of this chapter have been published separately in [20–25].

4.2 Weak formulations

4.2.1 Magnetodynamic weak formulations

The system formed by the particularized Maxwell's equation (1.68) and the constitutive laws (1.11) and (1.14) has to be solved.

In order to satisfy Ampere's law (1.68 b) in a strong sense, we take $\boldsymbol{h}_i \in \boldsymbol{H}_{h,i}(\mathbf{curl};\Omega_i)$ and $\boldsymbol{j}_i \in \boldsymbol{H}_{h,i}(\mathrm{div};\Omega_i)$. Both constitutive laws (1.11) and (1.14) are exactly verified as well. The upper part of the Tonti diagram (1.73) is then satisfied in a strong sense. This is equivalent to placing $\boldsymbol{b}_i \in \boldsymbol{H}_{e,i}(\mathrm{div};\Omega_i)$ and $\boldsymbol{e}_i \in \boldsymbol{H}_{e,i}(\mathbf{curl};\Omega_i)$, what implies that Faraday's law (1.68 a) holds approximately.

We start by writing a weak form of Faraday's law (1.68 a) (see Section A.2), i.e.

$$\partial_t(\boldsymbol{b}_i,\boldsymbol{h}'_i)_{\Omega_i} + (\mathbf{curl}\,\boldsymbol{e}_i,\boldsymbol{h}'_i)_{\Omega_i} = 0, \quad \forall \boldsymbol{h}'_i \in \boldsymbol{H}^0_{h,i}(\mathbf{curl};\Omega_i), \tag{4.1}$$

where the field $\boldsymbol{h}'_i \in \boldsymbol{H}^0_{h,i}(\mathbf{curl};\Omega_i)$ is a field of test functions independent of time. Applying the Green formula of type **curl-curl** (A.2) in Ω_i to second term in (4.1), we get

$$\partial_t(\boldsymbol{b}_i,\boldsymbol{h}'_i)_{\Omega_i} + (\boldsymbol{e}_i,\mathbf{curl}\,\boldsymbol{h}'_i)_{\Omega_i} + \langle \boldsymbol{n}\times\boldsymbol{e}_i,\boldsymbol{h}'_i\rangle_{\Gamma_i} = 0, \quad \forall \boldsymbol{h}'_i \in \boldsymbol{H}^0_{h,i}(\mathbf{curl};\Omega_i). \tag{4.2}$$

We first introduce the constitutive law (1.11) in (4.2) to obtain

$$\partial_t(\mu_i\boldsymbol{h}_i,\boldsymbol{h}'_i)_{\Omega_i} + (\boldsymbol{e}_i,\mathbf{curl}\,\boldsymbol{h}'_i)_{\Omega_i} + \langle \boldsymbol{n}\times\boldsymbol{e}_i,\boldsymbol{h}'_i\rangle_{\Gamma_i} = 0, \quad \forall \boldsymbol{h}'_i \in \boldsymbol{H}^0_{h,i}(\mathbf{curl};\Omega)_i. \tag{4.3}$$

Combining Ohm's law (1.14) with Ampère's law (1.68 b), $\mathbf{curl}\, \boldsymbol{h}_i = \boldsymbol{j}_i = \sigma_i \boldsymbol{e}_i$ in $\Omega_{c,i}$, we get

$$\partial_t(\mu_i \boldsymbol{h}_i, \boldsymbol{h}'_i)_{\Omega_i} + (\sigma_i^{-1}\mathbf{curl}\, \boldsymbol{h}_i, \mathbf{curl}\, \boldsymbol{h}'_i)_{\Omega_{c,i}} + (\boldsymbol{e}_i, \mathbf{curl}\, \boldsymbol{h}'_i)_{\Omega^{\mathrm{C}}_{c,i}} + \langle \boldsymbol{n} \times \boldsymbol{e}_i, \boldsymbol{h}'_i \rangle_{\Gamma_i} = 0, \forall \boldsymbol{h}'_i \in \boldsymbol{H}^0_{h,i}(\mathbf{curl}; \Omega_i). \quad (4.4)$$

As presented in Section 1.5.2, the magnetic field $\boldsymbol{h}_i$ in Ω_i is expressed as

$$\boldsymbol{h}_i = \boldsymbol{h}_{s,i} + \boldsymbol{h}_{r,i}, \quad (4.5)$$

where $\boldsymbol{h}_{s,i}$ is a source magnetic field defined via an imposed current density $\boldsymbol{j}_{s,i} = \boldsymbol{j}_i$ in stranded inductors $\Omega_{s,i}$ (see Section 1.4.1) and will be studied in Section 4.2.4, and field $\boldsymbol{h}_{r,i}$ is the associated reaction magnetic field, which is indeed the unknown of our problem. Since

$$\begin{cases} \mathbf{curl}\, \boldsymbol{h}_i = \boldsymbol{j}_{s,i} & \text{in } \Omega_{s,i} \\ \mathbf{curl}\, \boldsymbol{h}_i = 0 & \text{in } \Omega^{\mathrm{C}}_{c,i} - \Omega_{s,i} \end{cases}, \quad (4.6)$$

one has

$$\mathbf{curl}\, \boldsymbol{h}_{r,i} = 0 \quad \text{in } \Omega^{\mathrm{C}}_{c,i}. \quad (4.7)$$

In the non-conducting regions $\Omega^{\mathrm{C}}_{c,i}$, the reaction field $\boldsymbol{h}_{r,i}$ can be thus defined via a scalar potential ϕ_i such that $\boldsymbol{h}_{r,i} = -\mathbf{grad}\, \phi_i$. Potential ϕ_i in $\Omega^{\mathrm{C}}_{c,i}$ is multi-valued and made single-valued via the definition of cuts Σ_i through each hole of $\Omega_{c,i}$ in [9, 14], which will be presented in detail in Section 4.3.7. The test field $\boldsymbol{h}'_i$ in the weak form (4.4) is thus chosen in a subspace of $\boldsymbol{H}^0_{h,i}(\mathbf{curl}; \Omega_i)$ for which $\mathbf{curl}\, \boldsymbol{h}'_{r,i} = 0$ in $\Omega^{\mathrm{C}}_{c,i}$, with $\boldsymbol{h}'_i = \boldsymbol{h}'_{s,i} + \boldsymbol{h}'_{r,i}$. Thus, the term $(\boldsymbol{e}_i, \mathbf{curl}\, \boldsymbol{h}'_i)_{\Omega^{\mathrm{C}}_{c,i}}$ (4.4) is omitted and (4.4) can be rewritten as

$$\partial_t(\mu_i \boldsymbol{h}_{r,i}, \boldsymbol{h}'_i)_{\Omega_i} + \partial_t(\mu_i \boldsymbol{h}_{s,i}, \boldsymbol{h}'_i)_{\Omega_i} + (\sigma_i^{-1}\mathbf{curl}\, \boldsymbol{h}_{r,i}, \mathbf{curl}\, \boldsymbol{h}'_i)_{\Omega_{c,i}} + \langle \boldsymbol{n} \times \boldsymbol{e}_i, \boldsymbol{h}'_i \rangle_{\Gamma_{e,i}} = 0, \quad \forall \boldsymbol{h}'_i \in \boldsymbol{H}^0_{h,i}(\mathbf{curl}; \Omega_i) \quad \text{with} \quad \mathbf{curl}\, \boldsymbol{h}'_{r,i} = 0 \text{ in } \Omega^{\mathrm{C}}_{c,i} \quad \text{and} \quad \boldsymbol{h}'_i = \boldsymbol{h}'_{s,i} + \boldsymbol{h}'_{r,i}, \quad (4.8)$$

where $\boldsymbol{H}^0_{h,i}(\mathbf{curl}; \Omega_i)$ is defined on Ω_i and contains the basis functions for $\boldsymbol{h}_i$ (coupled to scalar potential ϕ_i) as well as for the test function $\boldsymbol{h}'_i$ (see Section 1.3.1 for the definition of the function spaces).

The trace of electric field $\boldsymbol{n} \times \boldsymbol{e}_i$ in (4.8) is subject to an inherent BC on the boundaries $\Gamma_{e,i}$ of the domain Ω_i. This can take several forms:

- The trace of $\boldsymbol{e}_i$ can be locally specified. This is the case for a homogeneous Neumann BC, e.g. imposing a symmetry condition of "perpendicular current" or "zero magnetic flux", i.e. $\boldsymbol{n} \times \boldsymbol{e}_i\big|_{\Gamma_{e,i}} = 0$ implies $\boldsymbol{n} \cdot \boldsymbol{b}_i\big|_{\Gamma_{e,i}} = 0$.
- The trace of $\boldsymbol{e}_i$ can be a field for which only associated global quantities are known (i.e. a functional of $\boldsymbol{n} \times \boldsymbol{e}_i$). This is presented in the modelling of the treatment of massive and stranded inductors (see Section 4.3.8).
- The trace of $\boldsymbol{e}_i$ can appear in local implicit BCs, such as those established for the the treatment of thin regions [58, 60, 61]. This is presented in Section 4.2.3.

4.2.2 Magnetostatic weak formulations

As in Section 4.2.1, the magnetostatic formulation can be seen as a particularization of the magnetodynamic formulation for which all time dependent phenomena are removed. Based on the development defined in Section 1.5.1, we start by writing a weak form of (1.60 b), i.e.

$$(\operatorname{div} \boldsymbol{b}_i, \phi'_i)_{\Omega_i} = 0, \quad \forall \phi'_i \in {H^1}_{0,h,i}(\Omega_i). \tag{4.9}$$

Considering the Green formula of type grad-div (A.2) of Ω_i applied to first term of (4.9), it gets

$$(\boldsymbol{b}_i, -\mathbf{grad}\, \phi'_i)_{\Omega_i} + \langle \boldsymbol{n} \cdot \boldsymbol{b}_i, \phi'_i \rangle_{\Gamma_i} = 0, \quad \forall \phi'_i \in {H^1}_{0,h,i}(\Omega_i). \tag{4.10}$$

In order to satisfy the upper part of the Tonti diagram (1.67) in a strong sense, we first introduce (1.11) into (4.10) to get

$$(\mu_i \boldsymbol{h}_i, -\mathbf{grad}\, \phi'_i)_{\Omega_i} + \langle \boldsymbol{n} \cdot \boldsymbol{b}_i, \phi'_i \rangle_{\Gamma_i} = 0, \quad \forall \phi'_i \in {H^1}_{0,h,i}(\Omega_i). \tag{4.11}$$

As said in Section 4.2.1, Field $\boldsymbol{h}_i \in \boldsymbol{H}(\mathbf{curl}; \Omega_i)$ is given by (4.5) (i.e., $\boldsymbol{h}_{s,i} + \boldsymbol{h}_{r,i}$). The field $\boldsymbol{h}_{s,i}$ is defined through the fixed current density $\boldsymbol{j}_{s,i}$ (see Section 4.2.4), and the reaction field $\boldsymbol{h}_{r,i}$ is defined as a scalar potential ϕ_i such that $\boldsymbol{h}_{r,i} = -\mathbf{grad}\, \phi_i$ everywhere in Ω_i. If the domain Ω_i is not simply connected, the scalar potential ϕ_i is multi-valued. This means that cuts have to be introduced to avoid the multiplicity of ϕ_i (see Section 4.3.7) [9, 14]. The weak form (4.11) can then be written as

$$-(\mu_i \boldsymbol{h}_{s,i}, \mathbf{grad}\, \phi'_i)_{\Omega_i} + (\mu_i \mathbf{grad}\, \phi_i, \mathbf{grad}\, \phi'_i)_{\Omega_i} + \langle \boldsymbol{n} \cdot \boldsymbol{b}_i, \phi'_i \rangle_{\Gamma_{e,i}} = 0, \quad \forall \phi'_i \in {H^1}_{0,h,i}(\Omega_i). \tag{4.12}$$

4.2.3 Thin shell model in weak formulations

Keeping in mind the developments in Section 3.2.3, the thin regions $\Omega_{t,i}$ are now extracted from the studied domain Ω_i and then replaced by the double layer TS surface $\Gamma_{t,i}$ (see Section 1.4.3) [58, 60, 61]. This means that the boundary $\Gamma_{t,i}$ of $\Omega_{t,i}$ is a part of the boundary $\Gamma_{e,i}$ defined in (4.8). The surface integral term $\langle \boldsymbol{n} \times \boldsymbol{e}_i, \boldsymbol{h}'_i \rangle_{\Gamma_{e,i}}$ (4.8) can be then split as

$$\langle \boldsymbol{n} \times \boldsymbol{e}_i, \boldsymbol{h}'_i \rangle_{\Gamma_{e,i}} = \langle \boldsymbol{n} \times \boldsymbol{e}_i, \boldsymbol{h}'_i \rangle_{\Gamma_{e,i} - \Gamma_{t,i}} + \langle [\boldsymbol{n} \times \boldsymbol{e}_i], \boldsymbol{h}'_i \rangle_{\Gamma_{t,i}}. \tag{4.13}$$

The term with the trace discontinuity of electric field through the TS, i.e. $\langle [\boldsymbol{n} \times \boldsymbol{e}_i], \boldsymbol{h}'_i \rangle_{\Gamma_{t,i}}$ in (4.13) can be written as

$$\langle [\boldsymbol{n} \times \boldsymbol{e}_i], \boldsymbol{h}'_i \rangle_{\Gamma_{t,i}} = -\langle \boldsymbol{n}_t \times \boldsymbol{e}_i|_{\Gamma^+_{t,i}}, \boldsymbol{h}'_i \rangle_{\Gamma^+_{t,i}} + \langle \boldsymbol{n}_t \times \boldsymbol{e}_i|_{\Gamma^-_{t,i}}, \boldsymbol{h}'_i \rangle_{\Gamma^-_{t,i}}. \tag{4.14}$$

The tangential magnetic field is discontinuous across the thin regions $\Omega_{t,i}$ (see Section 1.4.3). Thus, the magnetic field $\boldsymbol{h}_i$ is split into

$$\boldsymbol{h}_i = \boldsymbol{h}_{c,t,i} + \boldsymbol{h}_{d,t,i}, \tag{4.15}$$

where $\boldsymbol{h}_{c,i,t}$ and $\boldsymbol{h}_{d,i,t}$ are the tangential components of $\boldsymbol{h}_{c,i}$ and $\boldsymbol{h}_{d,i}$ and are continuous and discontinuous across $\Omega_{t,i}$, respectively. Here, we assume that $\boldsymbol{h}_{d,t,i}$ is equal to zero on the negative side $\Gamma^-_{t,i}$ of $\Gamma_{t,i}$ [58, 61]. Analysing the cross product of $\boldsymbol{n}_t$ by (1.56)

$$\begin{aligned}\boldsymbol{n}_t \times \boldsymbol{h}_i|_{\Gamma^+_{t,i}} - \boldsymbol{n}_t \times \boldsymbol{h}_i|_{\Gamma^-_{t,i}} &= \big[\sigma_i\beta_i(\boldsymbol{n}_t \times (\boldsymbol{e}_i \times \boldsymbol{n}_t)|_{\Gamma^+_{t,i}} + \boldsymbol{n}_t \times (\boldsymbol{e}_i \times \boldsymbol{n}_t)|_{\Gamma^-_{t,i}})\big] \\ &= \big[\sigma_i\beta_i(\boldsymbol{n}_t \times (\boldsymbol{n}_t \times \boldsymbol{e}_i)|_{\Gamma^+_{t,i}} + \boldsymbol{n}_t \times (\boldsymbol{n}_t \times \boldsymbol{e}_i)|_{\Gamma^-_{t,i}})\big] \quad (4.16)\end{aligned}$$

and developing (1.57), we get

$$\boldsymbol{n}_t \times \boldsymbol{e}_i|_{\Gamma^+_{t,i}} + \boldsymbol{n}_t \times \boldsymbol{e}_i|_{\Gamma^-_{t,i}} = -(\sigma_i\beta_i)^{-1}\,\boldsymbol{h}_{d,t,i}\,, \quad (4.17)$$

$$\boldsymbol{n}_t \times \boldsymbol{e}_i|_{\Gamma^+_{t,i}} - \boldsymbol{n}_t \times \boldsymbol{e}_i|_{\Gamma^-_{t,i}} = -\mu_i\beta_i\,\partial_t(2\boldsymbol{h}_{c,t,i} + \boldsymbol{h}_{d,t,i}). \quad (4.18)$$

Combining equations (4.17) and (4.18), we get

$$\boldsymbol{n}_t \times \boldsymbol{e}_i|_{\Gamma^+_{t,i}} = \frac{1}{2}\big[-\mu_i\beta_i\,\partial_t(2\boldsymbol{h}_{c,t,i} + \boldsymbol{h}_{d,t,i}) - \frac{1}{\sigma_i\beta_i}\,\boldsymbol{h}_{d,t,i}\big], \quad (4.19)$$

$$\boldsymbol{n}_t \times \boldsymbol{e}_i|_{\Gamma^-_{t,i}} = \frac{1}{2}\big[\mu_i\beta_i\,\partial_t(2\boldsymbol{h}_{c,t,i} + \boldsymbol{h}_{d,t,i}) - \frac{1}{\sigma_i\beta_i}\,\boldsymbol{h}_{d,t,i}\big]. \quad (4.20)$$

Substituting (4.19) and (4.20) into (4.14), and then (4.14) in (4.8), we get the integral contribution of electric field discontinuity $\langle[\boldsymbol{n} \times \boldsymbol{e}_i], \boldsymbol{h}'_i\rangle_{\Gamma_{t,i}}$ on the TS, i.e.

$$\begin{aligned}\langle[\boldsymbol{n} \times \boldsymbol{e}_i], \boldsymbol{h}'_i\rangle_{\Gamma_{t,i}} = \langle\frac{1}{2}\big[\mu_i\beta_i\,\partial_t(2\boldsymbol{h}_{c,t,i} + \boldsymbol{h}_{d,t,i}) + \frac{1}{\sigma_i\beta_i}\,\boldsymbol{h}_{d,t,i}\big], \boldsymbol{h}'_{c,t,i} + \boldsymbol{h}'_{d,t,i}\rangle_{\Gamma^+_{t,i}} \\ + \langle\frac{1}{2}\big[\mu_i\beta_i\,\partial_t(2\boldsymbol{h}_{c,t,i} + \boldsymbol{h}_{d,t,i}) - \frac{1}{\sigma_i\beta_i}\,\boldsymbol{h}_{d,t,i}\big], \boldsymbol{h}'_{c,t,i}\rangle_{\Gamma^-_{t,i}}. \quad (4.21)\end{aligned}$$

For the magnetostatic case, we have $\beta_i = d_i/2$ and $\partial_t = 0$ [58, 61]. The traces of electric field $\boldsymbol{n}_t \times \boldsymbol{e}_i|_{\Gamma^+_{t,i}}$ and $\boldsymbol{n}_t \times \boldsymbol{e}_i|_{\Gamma^-_{t,i}}$ in (4.19) and (4.20) on both sides of $\Gamma_{t,i}$ thus become

$$\boldsymbol{n}_t \times \boldsymbol{e}_i|_{\Gamma^+_{t,i}} = \boldsymbol{n}_t \times \boldsymbol{e}_i|_{\Gamma^-_{t,i}} = -\frac{1}{\sigma_i d_i}\,\boldsymbol{h}_{d,t,i}. \quad (4.22)$$

The integral contribution of magnetic flux density $\langle\boldsymbol{n} \cdot \boldsymbol{b}_i, \phi'_i\rangle_{\Gamma_{t,i}}$ in (4.12) is then found via the term $\langle\boldsymbol{n} \times \boldsymbol{e}_i, \boldsymbol{h}'_i\rangle_{\Gamma_{t,i}}$ in (4.8), i.e.

$$\begin{aligned}\langle\boldsymbol{n} \times \boldsymbol{e}_i, \boldsymbol{h}'_i\rangle_{\Gamma_{t,i}} = -\langle\boldsymbol{n} \times \boldsymbol{e}_i, \mathbf{grad}\,\phi'_i\rangle_{\Gamma_{t,i}} = -\langle\boldsymbol{n}, \phi'_i\,\mathbf{curl}\,\boldsymbol{e}_i\rangle_{\Gamma_{t,i}} + \langle\boldsymbol{n}, \mathbf{curl}\,(\phi'_i\boldsymbol{e}_i)\rangle_{\Gamma_{t,i}} \\ = \langle\partial_t(\boldsymbol{n} \cdot \boldsymbol{b}_i), \phi'_i\rangle_{\Gamma_{t,i}}, \quad (4.23)\end{aligned}$$

and that $\boldsymbol{h}_{d,i} = 0$ since there is no current flowing in the shell [61].

Taking into account (4.23) and (4.18), it reads

$$\begin{aligned}\langle\partial_t(\boldsymbol{n} \cdot \boldsymbol{b}_i), \phi'_i\rangle_{\Gamma_{t,i}} = \langle\frac{1}{2}\mu_i\beta_i\,\partial_t(2\boldsymbol{h}_{c,t,i}), \boldsymbol{h}'_{c,t,i}\rangle_{\Gamma^+_{t,i}} + \langle\frac{1}{2}\mu_i\beta_i\,\partial_t(2\boldsymbol{h}_{c,t,i}), \boldsymbol{h}'_{c,t,i}\rangle_{\Gamma^-_{t,i}} \\ = \langle\mu_i d_i\,\partial_t\boldsymbol{h}_{c,t,i}, \boldsymbol{h}'_{c,t,i}\rangle_{\Gamma_{t,i}}. \quad (4.24)\end{aligned}$$

Since (4.24), we get the term $\langle \boldsymbol{n}\cdot\boldsymbol{b}_i, \phi_i'\rangle_{\Gamma_{t,i}}$ in (4.12), i.e.

$$\begin{aligned}\langle [\boldsymbol{n}\cdot\boldsymbol{b}_i], \phi_i'\rangle_{\Gamma_{t,i}} &= -\langle \boldsymbol{n}\cdot\boldsymbol{b}_i|_{\Gamma_{t,i}^+}, \phi_i'\rangle_{\Gamma_{t,i}^+} + \langle \boldsymbol{n}\cdot\boldsymbol{b}_i|_{\Gamma_{t,i}^-}, \phi_i'\rangle_{\Gamma_{t,i}^-} = \langle \mu_i d_i\, \boldsymbol{h}_{c,t,i}, \boldsymbol{h}_{c,i}'\rangle_{\Gamma_{t,i}} \\ &= -\langle \mu_i d_i\, \boldsymbol{h}_{s,i}, \mathbf{grad}\,\phi_i'\rangle_{\Gamma_{t,i}} + \langle \mu_i d_i\, \mathbf{grad}\,\phi_i, \mathbf{grad}\,\phi_i'\rangle_{\Gamma_{t,i}}. \quad (4.25)\end{aligned}$$

The scalar potential ϕ_i is now continuous across the TS models $\Gamma_{t,i}$ (except across the cuts).

4.2.4 Pre-calculation of source magnetic fields

The methods to define the source magnetic field $\boldsymbol{h}_{s,i}$ have been already proposed in [29, 83, 102, 112, 133]. These methods differ by the way the source fields are approximated as well as by the extent of their domains of definition.

The field $\boldsymbol{h}_{s,i}$ can be computed by the Biot-Savart law [75, 107]. It thus has a zero divergence, which is a condition, or gauge, one could do without. Actually, there exists a whole family of fields $\boldsymbol{h}_{s,i}$ verifying $\mathbf{curl}\,\boldsymbol{h}_{s,i} = \boldsymbol{j}_{s,i}$ and $\boldsymbol{h}_{s,i}$ calculated by the Biot-Savart law is only one of those, whose divergence vanishes and which has therefore a physical meaning. But at the discrete level, it can be interesting to choose other fields (without physical meaning) thanks to other gauges, e.g. similar to the gauges presented in [40, 80, 109]. The technique proposed in [29, 34], using the reaction field characterization of type (4.80), is used to characterize efficiently source fields, being generalized source fields (non-physical fields). The support of the source $\boldsymbol{h}_{s,i}$ is thus limited to the inductor $\Omega_{s,i}$ and to a transition layer associated with a cut (layer of elements located on one side of a cut), i.e., the associated source scalar potential out of the inductor is freely fixed to zero. The co-tree gauge condition is used, i.e., the circulation of the source field is fixed to zero along the edges of a tree built in the inductor. The basis functions of the field are thus associated with the co-tree edges (classical edge basis functions) in the inductor and associated transition layer.

Two methods to determine $\boldsymbol{h}_{s,i}$, i.e., coefficients for the defined characterization (see Section 4.3.12), are proposed:

- The first method consists in computing $\boldsymbol{h}_{s,i}$ through a projection method of a known distribution $\boldsymbol{j}_s$ [32, 34, 62, 98], i.e.

$$(\mathbf{curl}\,\boldsymbol{h}_{s,i}, \mathbf{curl}\,\boldsymbol{h}_{s,i}')_{\Omega_{s,i}} = (\boldsymbol{j}_{s,i}, \mathbf{curl}\,\boldsymbol{h}_{s,i}')_{\Omega_{s,i}}, \quad \forall \boldsymbol{h}_{s,i}' \in H(\Omega_{s,i}). \quad (4.26)$$

  The sources for this problem are direct constraints on the function space coming from the *a priori* known form of $\boldsymbol{h}_{s,i}$ in the transition layer (not included in $\Omega_{s,i}$); the coefficient of the cut basis function is directly given by the magnetomotive force of the fixed unit current.

- The second method consists in solving an electrokinetic problem with a tensorial conductivity having a principal value along the wires of the inductor, i.e.

$$(\sigma_i^{-1}\mathbf{curl}\,\boldsymbol{h}_{s,i}, \mathbf{curl}\,\boldsymbol{h}_{s,i}')_{\Omega_{s,i}} = 0, \quad \forall \boldsymbol{h}_{s,i}' \in H(\Omega_{s,i}). \quad (4.27)$$

In both methods, the coefficient of the cut basis function is directly given by the magnetomotive force of the fixed current. The degrees of freedom can be fixed to zero on the lateral boundary of the inductor, which implies that the tree of edges must be complete on this boundary before entering the volume [40, 80, 109].

4.3 Coupled magnetodynamic and magnetostatic SPs

4.3.1 Generalities

As developed in Sections 4.2.1 and 4.2.2, the magnetodynamic and magnetostatic weak formulations were developed. In Section 4.2.3, the adapted formulations for the discretization of TS FE model [18, 60, 61] were formulated in the weak formulations. Thanks to the developments in Chapter 2, we elaborately present two sequences of SP coupling, i.e. **three SPs** and **two SPs**

4.3.2 From SP u to SP p−inductors alone to TS model

The constraint between SP u and SP p is expressed via a SS, i.e. $\boldsymbol{k}_{u,f}$ (see Section 2.3.2). The SS related to the BC and IC is given by the TS model [60, 61] combined with contributions from SP u. The TS model for the magnetic field presented in Section 4.2.1 needs the unknown discontinuity of $\boldsymbol{h}_{d,t,p}$ of the tangential component $\boldsymbol{h}_{t,p} = (\boldsymbol{n} \times \boldsymbol{h}_p) \times \boldsymbol{n}$ of $\boldsymbol{h}_p$ on the TS $\Gamma_{t,p}$ [20–22, 24], i.e.

$$[\boldsymbol{h}_{t,p}]_{\Gamma_{t,p}} = \boldsymbol{h}_{d,t,p} \;\text{ or }\; [\boldsymbol{n} \times \boldsymbol{h}_{t,p}]_{\Gamma_{t,p}} = \boldsymbol{n} \times \boldsymbol{h}_{d,t,p}\,, \tag{4.28}$$

fixed to zero along the TS border, i.e. $\partial\Gamma_{t,p}$, to prevent any current flow through it. In order to explicitly express this discontinuity, from (4.15), field $\boldsymbol{h}_p$ is written on both sides of $\Gamma_{t,p}$ as

$$\boldsymbol{h}_p|_{\Gamma^+_{t,p}} = \boldsymbol{h}_{c,t,p} + \boldsymbol{h}_{d,t,p}\,,\;\; \boldsymbol{h}_p|_{\Gamma^-_{t,p}} = \boldsymbol{h}_{c,t,p}\,, \tag{4.29 a-b}$$

where $\boldsymbol{h}_{c,t,p}$ is the continuous component of $\boldsymbol{h}_p$. Definitions (4.29 a) and (4.29 b) also apply on $\Gamma_{t,p}$ for the tangential components $\boldsymbol{h}_{t,p}$, $\boldsymbol{h}_{c,t,p}$ and $\boldsymbol{h}_{d,t,p}$.

From the development of TS model in Sections 2.3.2 and 4.2.3, combining (2.24) with (4.18), the trace discontinuity $[\boldsymbol{n} \times \boldsymbol{e}_p]_{\Gamma_{t,p}}$ of SP p is

$$[\boldsymbol{n} \times \boldsymbol{e}_p]_{\Gamma_{t,p}} = [\boldsymbol{n} \times (\boldsymbol{e}_u + \boldsymbol{e}_p)]_{\Gamma_{t,p}} = [\boldsymbol{n} \times \boldsymbol{e}]_{\Gamma_{t,p}} = \mu_p \beta_p\, \partial_t (2\boldsymbol{h}_{c,t,p} + \boldsymbol{h}_{d,t,p}), \tag{4.30}$$

where β_p is given in (1.58) (see Section 1.4.3).

Combining (2.27) and (4.19), the trace of electric field $\boldsymbol{n} \times \boldsymbol{e}_p|_{\Gamma^+_{t,p}}$ on the positive side $\Gamma^+_{t,p}$ of the TS is expressed as

$$\boldsymbol{n} \times \boldsymbol{e}_p|_{\Gamma^+_{t,p}} = \boldsymbol{n} \times (\boldsymbol{e}_u + \boldsymbol{e}_p)|_{\Gamma^+_{t,p}} - \boldsymbol{n} \times \boldsymbol{e}_u|_{\Gamma^+_{t,p}}$$

$$= \frac{1}{2}\left[\mu_p\beta_p\,\partial_t(2\boldsymbol{h}_{c,t,p}+\boldsymbol{h}_{d,t,p})+\frac{1}{\sigma_p\beta_p}\,\boldsymbol{h}_{d,t,p}\right]-\boldsymbol{n}\times\boldsymbol{e}_u|_{\Gamma^+_{t,p}}$$
$$= \frac{1}{2}\left[\mu_p\beta_p\,\partial_t(2\boldsymbol{h}_{c,t,p}+\boldsymbol{h}_{d,t,p})+\frac{1}{\sigma_p\beta_p}\,\boldsymbol{h}_{d,t,p}\right]-\boldsymbol{k}_{f,u}. \tag{4.31}$$

4.3.3 From SP p to SP k−TS model to volume correction

The TS solution obtained in SP p is then corrected by the volume correction SP k that takes inaccuracies occurring near corners and edges into account. Similarly to the $\boldsymbol{b}$-formulation presented in Chapter 3, in order to correct the TS model, SP k has to suppress the TS representation via SSs opposed to TS discontinuities, simultaneously to VSs in the added volume shell that account for volume changes of μ_p and σ_p in SP p to μ_k and σ_k in SP k (with $\mu_p = \mu_0$, $\mu_k = \mu_{volume}$, $\sigma_p = 0$ and $\sigma_k = \sigma_{volume}$). This correction is usually limited to the neighborhood of the shell, which permits to benefit from a reduction of the extension of the associated mesh [20, 22]. The VSs $\boldsymbol{b}_{s,k}$ and $\boldsymbol{e}_{s,k}$ in the $\boldsymbol{b}_k - \boldsymbol{h}_k$ and $\boldsymbol{e}_k - \boldsymbol{j}_k$ relations presented in (2.31) and (2.36) are

$$\boldsymbol{b}_{s,k} = (\mu_k - \mu_p)(\boldsymbol{h}_u + \boldsymbol{h}_p)\,, \tag{4.32}$$
$$\boldsymbol{e}_{s,k} = -(\boldsymbol{e}_u + \boldsymbol{e}_p)\,. \tag{4.33}$$

Note that the electric fields $\boldsymbol{e}_u$ and $\boldsymbol{e}_p$ are unknown in any non-conducting regions $\Omega^C_{c,i}$. Hence, their determination require to solve an electric problem defined by Faraday's law and the electric conservation, which will be presented in Section 4.3.6.

4.3.4 Sequence of magnetodynamic SP formulations−three SPs

Collecting results of Sections 4.3.2 and 4.3.3, we develop the weak formulations for each SP in the sequence: SP u → SP p → SP k.

4.3.4.1 Inductors model−SP u

Based on equation (4.3) with (4.13), a weak form is now developed for SP u, i.e.

$$\partial_t(\mu_u\boldsymbol{h}_{r,u},\boldsymbol{h}'_u)_{\Omega_u}+\partial_t(\mu_u\boldsymbol{h}_{s,u},\boldsymbol{h}'_u)_{\Omega_u}+\langle\boldsymbol{n}\times\boldsymbol{e}_u,\boldsymbol{h}'_u\rangle_{\Gamma_{e,u}}=0,\quad\forall\boldsymbol{h}'_u\in\boldsymbol{H}^0_{h,u}(\mathbf{curl};\Omega_u). \tag{4.34}$$

Note that the source field $\boldsymbol{h}_{s,u}$ in (4.34) is defined via a projection method of a known distribution $\boldsymbol{j}_{s,u}$ (see Section 4.2.4). The surface integral on $\Gamma_{e,u}$ accounts for a natural BC of type (2.7 c), usually zero.

4.3.4.2 Thin shell FEs model−SP p

The TS model is defined via the term $\langle[\boldsymbol{n}\times\boldsymbol{e}_p],\boldsymbol{h}'_p\rangle_{\Gamma_{t,p}}$ in (4.2.3). It is used to weakly express the electric field TS IC proper to the weak form of SP p, i.e.

$$\partial_t(\mu_p \boldsymbol{h}_p, \boldsymbol{h}'_p)_{\Omega_p} + (\sigma_p^{-1}\mathbf{curl}\,\boldsymbol{h}_p, \mathbf{curl}\,\boldsymbol{h}'_p)_{\Omega_{c,p}} + \langle \boldsymbol{n}\times\boldsymbol{e}_p, \boldsymbol{h}'_p\rangle_{\Gamma_{e,p}-\Gamma_{t,p}} + \langle [\boldsymbol{n}\times\boldsymbol{e}_p]_{\Gamma_{t,p}}, \boldsymbol{h}'_p\rangle_{\Gamma_{t,p}} = 0\,, \forall \boldsymbol{h}'_p \in \boldsymbol{H}^0_{h,p}(\mathbf{curl};\Omega_p). \quad (4.35)$$

Note that the volume integral term in $\Omega_{c,p}$ does not contribute to (4.35) if $\Omega_{c,p}$ is empty in SP p. Test function $\boldsymbol{h}'_p$ in the term $\langle [\boldsymbol{n}\times\boldsymbol{e}_p]_{\Gamma_{t,p}}, \boldsymbol{h}'_p\rangle_{\Gamma_{t,p}}$ in (4.35) is split into the continuous and discontinuous parts $\boldsymbol{h}'_{c,t,p}$ and $\boldsymbol{h}'_{d,t,p}$, respectively (see Section 4.2.1). One thus has

$$\begin{aligned}\langle [\boldsymbol{n}\times\boldsymbol{e}_p]_{\Gamma_{t,p}}, \boldsymbol{h}'_p\rangle_{\Gamma_{t,p}} &= \langle [\boldsymbol{n}\times\boldsymbol{e}_p]_{\Gamma_{t,p}}, \boldsymbol{h}'_{c,t,p} + \boldsymbol{h}'_{d,t,p}\rangle_{\Gamma_{t,p}} \\ &= \langle [\boldsymbol{n}\times\boldsymbol{e}_p]_{\Gamma_{t,p}}, \boldsymbol{h}'_{c,t,p}\rangle_{\Gamma_{t,p}} + \langle [\boldsymbol{n}\times\boldsymbol{e}_p]_{\Gamma_{t,p}}, \boldsymbol{h}'_{d,t,p}\rangle_{\Gamma_{t,p}} \\ = \langle [\boldsymbol{n}\times\boldsymbol{e}_p]_{\Gamma_{t,p}}, \boldsymbol{h}'_{c,t,p}\rangle_{\Gamma_{t,p}} &+ \langle \boldsymbol{n}\times\boldsymbol{e}_p|_{\Gamma^+_{t,p}}, \boldsymbol{h}'_{d,t,p}\rangle_{\Gamma^+_{t,p}} - \langle \boldsymbol{n}\times\boldsymbol{e}_p|_{\Gamma^-_{t,p}}, \boldsymbol{h}'_{d,t,p}\rangle_{\Gamma^-_{t,p}}. \quad (4.36)\end{aligned}$$

As discussed, $\boldsymbol{h}'_{d,t,p}$ equals zero on the negative side $\Gamma^-_{t,p}$ of TS. Hence, (4.36) becomes

$$\langle [\boldsymbol{n}\times\boldsymbol{e}_p]_{\Gamma_{t,p}}, \boldsymbol{h}'_p\rangle_{\Gamma_{t,p}} = \langle [\boldsymbol{n}\times\boldsymbol{e}_p]_{\Gamma_{t,p}}, \boldsymbol{h}'_{c,t,p}\rangle_{\Gamma_{t,p}} + \langle \boldsymbol{n}\times\boldsymbol{e}_p|_{\Gamma^+_{t,p}}, \boldsymbol{h}'_{d,t,p}\rangle_{\Gamma^+_{t,p}}. \quad (4.37)$$

The trace discontinuity $\langle [\boldsymbol{n}\times\boldsymbol{e}_p]_{\Gamma_{t,p}}, \boldsymbol{h}'_{c,t,p}\rangle_{\Gamma_{t,p}}$ in (4.37) is given by (4.30), i.e.

$$\begin{aligned}\langle [\boldsymbol{n}\times\boldsymbol{e}_p]_{\Gamma_{t,p}}, \boldsymbol{h}'_{c,t,p}\rangle_{\Gamma_{t,p}} &= \langle [\boldsymbol{n}\times\boldsymbol{e}]_{\Gamma_{t,p}}, \boldsymbol{h}'_{c,t,p}\rangle_{\Gamma_{t,p}} \\ &= \langle \mu_p\beta_p\,\partial_t(2\boldsymbol{h}_{c,t,p} + \boldsymbol{h}_{d,t,p}), \boldsymbol{h}'_{c,t,p}\rangle_{\Gamma_{t,p}}. \quad (4.38)\end{aligned}$$

The term $\langle \boldsymbol{n}\times\boldsymbol{e}_p|_{\Gamma^+_{t,p}}, \boldsymbol{h}'_{d,t,p}\rangle_{\Gamma^+_{t,p}}$ in (4.37) related to the positive side $\Gamma^+_{t,p}$ of TS is given by (4.31), one has

$$\begin{aligned}\langle \boldsymbol{n}\times\boldsymbol{e}_p|_{\Gamma^+_{t,p}}, \boldsymbol{h}'_{d,t,p}\rangle_{\Gamma^+_{t,p}} = \langle \frac{1}{2}\big[\mu_p\beta_p\,\partial_t(2\boldsymbol{h}_{c,t,p} + \boldsymbol{h}_{d,t,p}) + \frac{1}{\sigma_p\beta_p}\,\boldsymbol{h}_{d,t,p}\big], \boldsymbol{h}'_{d,t,p}\rangle_{\Gamma^+_{t,p}} \\ - \langle \boldsymbol{n}\times\boldsymbol{e}_u|_{\Gamma^+_{t,p}}, \boldsymbol{h}'_{d,t,p}\rangle_{\Gamma^+_{t,p}}, \quad (4.39)\end{aligned}$$

suppressing $\boldsymbol{n}\times\boldsymbol{e}_u|_{\Gamma^+_{t,p}}$ of SP u and simultaneously adding the actual TS BC. The resulting surface integral term $\langle \boldsymbol{n}\times\boldsymbol{e}_u|_{\Gamma^+_{t,p}}, \boldsymbol{h}'_{d,t,p}\rangle_{\Gamma^+_{t,p}}$ (weighted by $\boldsymbol{h}'_{d,t,p}$ is thus a SS that is naturally expressed via the weak formulation of SP u in (4.34), i.e.

$$-\langle \boldsymbol{n}\times\boldsymbol{e}_u|_{\Gamma^+_{t,p}}, \boldsymbol{h}'_{d,t,p}\rangle_{\Gamma^+_u} = \partial_t(\mu_u\boldsymbol{h}_{r,u}, \boldsymbol{h}'_{d,t,p})_{\Omega^+_p} + \partial_t(\mu_u\boldsymbol{h}_{s,u}, \boldsymbol{h}'_{d,t,p})_{\Omega^+_p} = -\boldsymbol{k}_{f,u}. \quad (4.40)$$

The contributions of the volume integrals in (4.40) are limited to a single layer of FEs on the positive side of Ω^+_p touching $\Gamma^+_{t,p}$ (see Fig. 3.1), because they involve only the associated trace $\boldsymbol{n}\times\boldsymbol{h}'_{d,t,p}|_{\Gamma^+_{t,p}}$.

Substituting (4.40) into (4.39); (4.39) and (4.38) into (4.37); (4.37) into (4.36) and finally (4.36) into (4.35), we obtain the final weak form of problem SP p, i.e.

$$\begin{aligned}\partial_t(\mu_p\boldsymbol{h}_p, \boldsymbol{h}'_p)_{\Omega_p} + \langle \mu_p\beta_p\,\partial_t(2\boldsymbol{h}_{c,t,p} + \boldsymbol{h}_{d,t,p}), \boldsymbol{h}'_{c,t,p}\rangle_{\Gamma_{t,p}} + \langle \boldsymbol{n}\times\boldsymbol{e}_p, \boldsymbol{h}'_p\rangle_{\Gamma_{e,p}-\Gamma_{t,p}} \\ + \langle \frac{1}{2}\big[\mu_p\beta_p\,\partial_t(2\boldsymbol{h}_{c,t,p} + \boldsymbol{h}_{d,t,p}) + \frac{1}{\sigma_p\beta_p}\,\boldsymbol{h}_{d,t,p}\big], \boldsymbol{h}'_{d,t,p}\rangle_{\Gamma_{t,p}} + \\ \partial_t(\mu_u\boldsymbol{h}_{r,u}, \boldsymbol{h}'_{d,t,p})_{\Omega^+_p} + \partial_t(\mu_u\boldsymbol{h}_{s,u}, \boldsymbol{h}'_{d,t,p})_{\Omega^+_p} = 0\,, \forall \boldsymbol{h}'_p \in \boldsymbol{H}^0_{h,p}(\mathbf{curl};\Omega_p), \quad (4.41)\end{aligned}$$

The surface integral term on $\Gamma_{e,p} - \Gamma_{t,p}$ in (4.41) also accounts for a natural BC of type (2.7 c), usually zero.

At the discrete level, the source $\boldsymbol{h}_u$ in (4.41), initially in mesh of SP u, has to be projected to the mesh of SP p via a projection method (see Section 2.2.3).

4.3.4.3 Volume correction replacing the thin shell representation−SP k

The obtained solution of TS SP p in (4.41) is then corrected by SP k via the VSs given by (4.32) and (4.33). The weak form for SP k is then expressed as

$$\partial_t(\mu_k \boldsymbol{h}_k, \boldsymbol{h}'_k)_{\Omega_k} + (\sigma_k^{-1}\mathbf{curl}\,\boldsymbol{h}_k, \mathbf{curl}\,\boldsymbol{h}'_k)_{\Omega_{c,k}} + \partial_t(\boldsymbol{b}_{s,k}, \boldsymbol{h}'_k)_{\Omega_{c,k}} + (\boldsymbol{e}_{s,k}, \mathbf{curl}\,\boldsymbol{h}'_k)_{\Omega_{c,k}} + \langle \boldsymbol{n}\times\boldsymbol{e}_k, \boldsymbol{h}'_k\rangle_{\Gamma_{e,k}-\Gamma_{t,k}} + \langle [\boldsymbol{n}\times\boldsymbol{e}_k]_{\Gamma_{t,k}}, \boldsymbol{h}'_k\rangle_{\Gamma_{t,k}} = 0, \forall \boldsymbol{h}'_k \in \boldsymbol{H}^0_{h,k}(\mathbf{curl};\Omega_k). \quad (4.42)$$

The surface integral term on $\Gamma_{e,k} - \Gamma_{t,k}$ also accounts for natural BCs, usually zero. In (4.42), changes of material properties from SP p to SP k, that appear in the volume shell, are expressed via the volume integrals $\partial_t(\boldsymbol{b}_{s,k}, \boldsymbol{h}'_k)_{\Omega_{c,k}}$ and $(\boldsymbol{e}_{s,k}, \mathbf{curl}\,\boldsymbol{h}'_k)_{\Omega_k}$. The VSs $\boldsymbol{b}_{s,k}$ and $\boldsymbol{e}_{s,k}$ are given by (4.32) and (4.33), respectively. The weak form of SP k in (4.42) thus becomes

$$\partial_t(\mu_k \boldsymbol{h}_k, \boldsymbol{h}'_k)_{\Omega_k} + (\sigma_k^{-1}\mathbf{curl}\,\boldsymbol{h}_k, \mathbf{curl}\,\boldsymbol{h}'_k)_{\Omega_{c,k}} + \partial_t((\mu_k - \mu_p)(\boldsymbol{h}_u + \boldsymbol{h}_p), \boldsymbol{h}'_k)_{\Omega_{c,k}} + (-(\boldsymbol{e}_u + \boldsymbol{e}_p), \mathbf{curl}\,\boldsymbol{h}'_k)_{\Omega_{c,k}} + \langle \boldsymbol{n}\times\boldsymbol{e}_k, \boldsymbol{h}'_k\rangle_{\Gamma_{e,k}-\Gamma_{t,k}} + \langle [\boldsymbol{n}\times\boldsymbol{e}_k]_{\Gamma_{t,k}}, \boldsymbol{h}'_k\rangle_{\Gamma_{t,k}} = 0, \quad \forall \boldsymbol{h}'_k \in \boldsymbol{H}^0_{h,k}(\mathbf{curl};\Omega_k). \quad (4.43)$$

The fields $\boldsymbol{e}_u$ and $\boldsymbol{e}_p$ in (4.43) are unknown in any non-conducting regions. Their determination requires to solve an electric problem (see Section 4.3.6). At the discrete level, the source quantities $\boldsymbol{h}_u$ and $\boldsymbol{h}_p$ in (4.43) have also to be transferred from the meshes of SP u and SP p to the mesh of SP k via a projection method.

Simultaneously to the VSs in (4.43), SSs related to ICs compensate the TS and cut discontinuities (if some cuts exist). It can be defined via ICs apposed to $\phi_{d,p}|_{\Gamma_{t,p}}$ (discontinuity on TS) and $\phi_{d,p}|_{\Gamma_{cut,p}}$ (discontinuity on cut), and $[\boldsymbol{n}\times\boldsymbol{e}_p]_{\Gamma_{t,p}}$ to suppress the TS representation via SSs in (2.43), i.e.

$$[\boldsymbol{n}\times\boldsymbol{e}_k]_{\Gamma_{t,k}} = -[\boldsymbol{n}\times\boldsymbol{e}_p]_{\Gamma_{t,k}}, \quad (4.44)$$

$$[\boldsymbol{n}\times\boldsymbol{h}_k]_{\Gamma_{t,k}} = -\boldsymbol{n}\times\boldsymbol{h}_{d,t,p}|_{\Gamma_{t,k}}. \quad (4.45)$$

The IC (4.45) strongly fixes $\boldsymbol{h}_{d,t,k} = -\boldsymbol{h}_{d,t,p}$ and $\phi_{d,k} = -\phi_{d,p}$. The IC (4.44) is weakly expressed through the last surface integral in (4.43), with $\Gamma_{t,k} = \Gamma_{t,p}$. The so involved trace discontinuity $[\boldsymbol{n}\times\boldsymbol{e}_k]_{\Gamma_{t,k}}$ in (4.44) is naturally expressed as

$$\langle [\boldsymbol{n}\times\boldsymbol{e}_k]_{\Gamma_{t,k}}, \boldsymbol{h}'_k\rangle_{\Gamma_{t,k}} = -\langle [\boldsymbol{n}\times\boldsymbol{e}_p]_{\Gamma_{t,k}}, \boldsymbol{h}'_k\rangle_{\Gamma_{t,k}}. \quad (4.46)$$

The surface integral $\langle [\boldsymbol{n}\times\boldsymbol{e}_p]_{\Gamma_{t,k}}, \boldsymbol{h}'_k\rangle_{\Gamma_{t,k}}$ in (4.46) is used at step of SP p and is weakly evaluated from the volume integrals similarly to (4.40). At the discrete level, these surface integrals are restricted to the layers of FEs on both sides $\Gamma_{t,k}$ of TS, because they involve only the associated trace $\boldsymbol{n}\times\boldsymbol{h}'_k|_{\Gamma_{t,k}}$. At the discrete level, the source quantities $\boldsymbol{h}_u$ and $\boldsymbol{h}_p$ with its discontinuity $\boldsymbol{h}_{d,t,p}$ in (4.43) have also to be transferred from the meshes of SP u and SP p to the mesh of SP k via a projection method.

4.3.5 Sequence of magnetodynamic SP formulations−two SPs

Collecting results of Sections 4.3.2 and 4.3.3, we develop the weak formulations for each SP in the sequence: SP f → SP k. The weak form for SP f is constructed by

introducing (4.14) into (4.8) to obtain

$$\partial_t(\mu_f(\boldsymbol{h}_{r,f}+\boldsymbol{h}_{s,f}),\boldsymbol{h}'_f)_{\Omega_f}+(\sigma_f^{-1}\mathbf{curl}\,\boldsymbol{h}_f,\mathbf{curl}\,\boldsymbol{h}'_f)_{\Omega_{c,f}}+\langle\mu_f\beta_f\,\partial_t(2\boldsymbol{h}_{c,t,p}+\boldsymbol{h}_{d,t,f}),\boldsymbol{h}'_{c,t,f}\rangle_{\Gamma_{t,f}}$$
$$+\langle\frac{1}{2}\big[\mu_f\beta_f\,\partial_t(2\boldsymbol{h}_{c,t,f}+\boldsymbol{h}_{d,t,f})+\frac{1}{\sigma_f\beta_f}\,\boldsymbol{h}_{d,t,f}\big],\boldsymbol{h}'_{d,t,f}\rangle_{\Gamma_{t,f}}+\langle\boldsymbol{n}\times\boldsymbol{e}_f,\boldsymbol{h}'_f\rangle_{\Gamma_{e,f}-\Gamma_{t,f}}=0,$$
$$\forall\boldsymbol{h}'_f\in\boldsymbol{H}^0_{h,f}(\mathbf{curl};\Omega_f),\quad(4.47)$$

where the surface integral term on $\Gamma_{e,f}-\Gamma_{t,f}$ is subject to a natural BC of type (2.7 c), usually zero. The source field $\boldsymbol{h}_{s,f}$ in (4.47) is defined via the fixed current density $\boldsymbol{j}_{s,u}$ presented in Section 4.2.4. In this case, the second volume integral does not contribute to (4.47) if $\Omega_{c,f}$ contains no conducting regions.

The achieved TS solution in SP f is now corrected by SP k. Keeping in mind the equation (4.43) and replacing subscript p by f, $\boldsymbol{h}_u+\boldsymbol{h}_p$ by $\boldsymbol{h}_f$ and $\boldsymbol{e}_u+\boldsymbol{e}_p$ by $\boldsymbol{e}_f$ (see Section 4.3.4), one has for SP k

$$\partial_t(\mu_k\boldsymbol{h}_k,\boldsymbol{h}'_k)_{\Omega_k}+(\sigma_k^{-1}\mathbf{curl}\,\boldsymbol{h}_k,\mathbf{curl}\,\boldsymbol{h}'_k)_{\Omega_{c,k}}+\partial_t((\mu_k-\mu_f)\boldsymbol{h}_f,\boldsymbol{h}'_k)_{\Omega_{c,k}}+(-\boldsymbol{e}_f,\mathbf{curl}\,\boldsymbol{h}'_k)_{\Omega_{c,k}}$$
$$+\langle\boldsymbol{n}\times\boldsymbol{e}_k,\boldsymbol{h}'_k\rangle_{\Gamma_{e,k}-\Gamma_{t,k}}+\langle[\boldsymbol{n}\times\boldsymbol{e}_k]_{\Gamma_{t,k}},\boldsymbol{h}'_k\rangle_{\Gamma_{t,k}}=0,\quad\forall\boldsymbol{h}'_k\in\boldsymbol{H}^0_{h,k}(\mathbf{curl};\Omega_k).\quad(4.48)$$

The field $\boldsymbol{e}_f$ is also defined via an electric problem (see Section 4.3.6).

The treatment of the TS representation via term $\langle[\boldsymbol{n}\times\boldsymbol{e}_k]_{\Gamma_{t,k}},\boldsymbol{h}'_k\rangle_{\Gamma_{t,k}}$ of the TS and cut discontinuities of SP f in SP k is similar to the case of three SPs in Section 4.3.4.3.

4.3.6 Electric problem in added conducting regions

The electric field $\boldsymbol{e}_i$ in each SP i ($i=u$, p or f) is to be determined in the new added conducting region $\Omega_{c,i}$ to define the source quantity $\boldsymbol{e}_{k,s}$ in (4.43) or $\boldsymbol{e}_{f,s}$ (4.48). It can be computed via an electric problem defined in $\Omega_{c,i}$ [36, 42, 51], i.e.

$$\mathbf{curl}\,\boldsymbol{e}_i=-\partial_t\boldsymbol{b}_i,,\quad \mathrm{div}\,\boldsymbol{d}_i=\rho_i\,,\quad \boldsymbol{d}_i=\epsilon_i\,\boldsymbol{e}_i.\qquad(4.49\text{ a-b-c})$$

It is assumed in (4.49 b) that no charge density exists in $\Omega_{c,i}$ such that $\mathrm{div}\,\boldsymbol{d}_i=0$. The required conformity of $\boldsymbol{e}_i$ is the one of $\mathbf{curl}\,\boldsymbol{h}_i$, i.e. of a curl field. This can be satisfied through the definition of an electric vector potential $\boldsymbol{u}_i$ as primal unknown field, with

$$\boldsymbol{d}_i=\mathbf{curl}\,\boldsymbol{u}_i.\qquad(4.50)$$

thus satisfying (4.49 b). The electric problem is then obtained by the weak form of (4.49 a) in the conducting region $\Omega_{c,k}$ of SP k, i.e., an electric flux density conform formulation [36, 42]

$$(\mathbf{curl}\,\boldsymbol{e}_i,\boldsymbol{u}'_i)_{\Omega_{c,k}}+(\partial_t(\mu_i\boldsymbol{h}_i),\boldsymbol{u}'_i)_{\Omega_{c,k}}=0,\quad\forall\boldsymbol{u}'_i\in\boldsymbol{H}^0_{h,k}(\mathbf{curl};\Omega_{c,k}).\qquad(4.51)$$

Applying the Green formula of type **curl-curl** (A.39) in $\Omega_{c,k}$ to the fields $\boldsymbol{e}_i$ and $\boldsymbol{u}'_i$ in (4.51), we get

$$(\boldsymbol{e}_i, \mathbf{curl}\, \boldsymbol{u}_i')_{\Omega_{c,k}} + (\partial_t(\mu_i \boldsymbol{h}_i), \boldsymbol{u}_i')_{\Omega_{c,k}} + \langle \boldsymbol{n} \times \boldsymbol{e}_i, \boldsymbol{u}_i' \rangle_{\Gamma_{c,k}} = 0, \quad \forall \boldsymbol{u}_i' \in \boldsymbol{H}^0_{h,k}(\mathbf{curl}; \Omega_{c,k}). \quad (4.52)$$

Let us introduce the constitutive law (1.12) and equation (4.50) in the weak form (4.52) to obtain

$$(\epsilon_i \mathbf{curl}\, \boldsymbol{u}_i, \mathbf{curl}\, \boldsymbol{u}_i')_{\Omega_{c,k}} + (\partial_t(\mu_i \boldsymbol{h}_i), \boldsymbol{u}_i')_{\Omega_{c,k}} + \langle \boldsymbol{n} \times \boldsymbol{e}_i, \boldsymbol{u}_i' \rangle_{\Gamma_{c,k}} = 0, \quad \forall \boldsymbol{u}_i' \in \boldsymbol{H}^0_{h,k}(\mathbf{curl}; \Omega_{c,k}), \quad (4.53)$$

where $\boldsymbol{H}^0_{h,k}(\mathbf{curl}; \Omega_{c,k})$ is a curl-conform function space defined on $\Omega_{c,k}$ and containing the basis functions for $\boldsymbol{u}_i$ as well as its associated test function $\boldsymbol{u}_i'$, and has to be constrained with a gauge condition. At the discrete level, $\boldsymbol{u}_i$ is discretized with edge FEs and is associated with a gauge condition by the tree-co-tree technique.

The electric problem to be posed in $\Omega_{c,k}$ gets information regarding the tangential electric field on the boundary of $\Omega_{c,k}$, i.e. $\partial\Omega_{c,k}$ via a natural BC that occurs in the surface integral term of (4.53). Its expression for each test function $\boldsymbol{u}_i'$ can be directly written only for non-conducting region $\Omega^C_{c,k} = \Omega_k \backslash \Omega_{c,k}$, i.e.,

$$(\partial_t(\mu_i \boldsymbol{h}_i), \boldsymbol{u}_i')_{\Omega_k \backslash \Omega_{c,k}} + (\sigma_i^{-1} \mathbf{curl}\, \boldsymbol{h}_i, \mathbf{curl}\, \boldsymbol{u}_i')_{\Omega_c \backslash \Omega_{c,k}} + \langle \boldsymbol{n} \times \boldsymbol{e}_i, \boldsymbol{u}_i' \rangle_{\partial\Gamma^C_{c,k}} = 0, \quad \forall \boldsymbol{u}_i' \in \boldsymbol{H}^0_{h,k}(\mathbf{curl}; \Omega_{c,k}), \quad (4.54)$$

Combining (4.53) and (4.54), with normal vectors $\boldsymbol{n}$ exterior to $\Omega_{c,k}$ and $\Omega_k - \Omega_{c,k}$, respectively (i.e. $\boldsymbol{n} \times \boldsymbol{e}_i|_{\partial\Gamma^C_{c,k}} = -\boldsymbol{n} \times \boldsymbol{e}_i|_{\partial\Gamma_{c,k}}$), of opposite signs, the following thus becomes

$$(\epsilon_i^{-1} \mathbf{curl}\, \boldsymbol{u}_i, \mathbf{curl}\, \boldsymbol{u}_i')_{\Omega_{c,k}} + (\partial_t(\mu_i \boldsymbol{h}_i), \boldsymbol{u}_i')_{\Omega_{c,k}} + (\partial_t(\mu_i \boldsymbol{h}_i), \boldsymbol{u}')_{\Omega_k \backslash \Omega_{c,k}} + (\sigma_i^{-1} \mathbf{curl}\, \boldsymbol{u}_i, \mathbf{curl}\, \boldsymbol{u}_i')_{\Omega_c \backslash \Omega_{c,k}} = 0, \quad \forall \boldsymbol{u}_i' \in \boldsymbol{H}^0_{h,k}(\mathbf{curl}; \Omega_{c,k}). \quad (4.55)$$

Here, $\boldsymbol{h}_i$ is expressed as a source for determining $\boldsymbol{u}_i$ in the conducting region $\Omega_{c,k}$ and its boundary. The volume integral term on $\Omega_k \backslash \Omega_{c,k}$ in (4.55) is limited to a single layer of of FEs touching $\partial\Omega_{c,k}$ in $\Omega_k \backslash \Omega_{c,k}$. At the discrete level, the source field $\boldsymbol{h}_i$ is projected from the mesh of SP p or SP f to the mesh of $\Omega_{c,k}$ via the projection method.

The obtained solution $\boldsymbol{u}_i$ from (4.55) is then combined with (4.50) and the constitutive law (1.12) to get the electric field $\boldsymbol{e}_i$, i.e. $\boldsymbol{e}_i = \epsilon_i^{-1} \mathbf{curl}\, \boldsymbol{u}_i$. Finally, the obtained solution $\boldsymbol{e}_i$ is added back to (4.43) and (4.48) in Sections 4.3.4 and 4.3.5.

4.3.7 Field discontinuities for multiply connected thin shell regions

As presented in Section 4.2.3, for the TS SP i ($i = p$ or f), a volume region initially in $\Omega_{c,i}$ is extracted from Ω_i and then considered with the double layer TS surface $\Gamma_{t,i}$ [61]. In addition to the electric field IC weakly defined in (4.35) or (4.47), the TS model requires a magnetic field discontinuity $[\boldsymbol{h}_i]_{\Gamma_{t,i}} = \boldsymbol{h}_{d,t,i}$ strongly defined

in $\boldsymbol{H}^0_{h,i}(\mathbf{curl};\Omega_i)$ via an IC on both sides of the TS via (4.29) [61]. This can be formulated via a TS discontinuity of ϕ_i (Fig. 4.1), i.e.

$$[\phi_i]_{\Gamma_{t,i}} = \Delta\phi_i|_{\Gamma_{t,i}} = \phi_{d,i}|_{\Gamma_{t,i}}, \tag{4.56}$$

with

$$\phi_i|_{\Gamma^+_{t,i}} = \phi_{c,i} + \phi_{d,i} \quad \text{and} \quad \phi_i|_{\Gamma^-_{t,i}} = \phi_{c,i}. \tag{4.57}$$

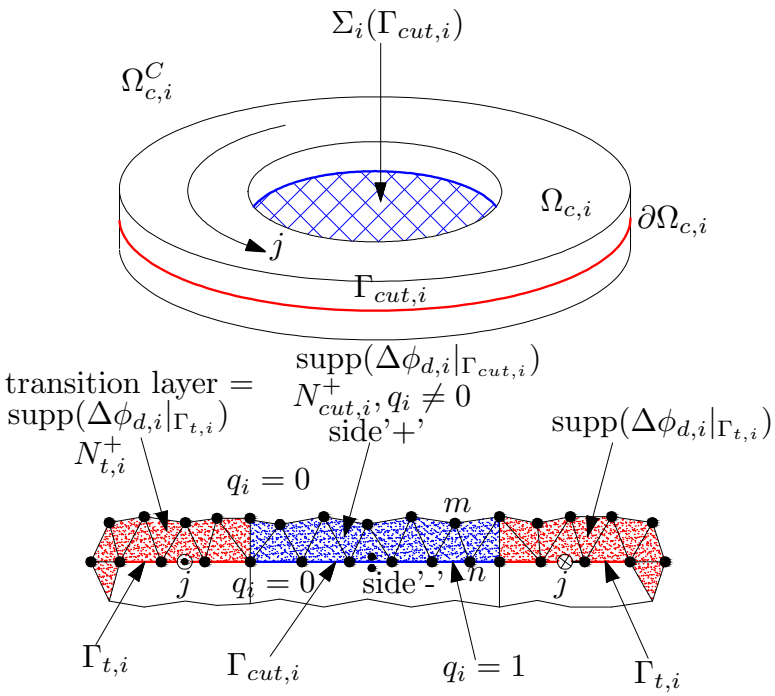

Figure 4.1: Thin region and its section with a hole, with the associated cut and transition layer for $\Delta\phi_i$.

The discontinuity $\phi_{d,i}$ of ϕ_i is constant on each cut (Fig. 4.1) and can be written as [21, 24]

$$\phi_i = \phi_{c,i} + \phi_{d,i} \quad \text{with} \quad \phi_{d,i} = \Delta\phi_d|_{\Gamma_{cut,i}} = [\phi_{d,i}]_{cut,i}, \tag{4.58}$$

$$[\phi_i]_{cut,i} = \phi_i|_{\Gamma^+_{cut,i}} - \phi_i|_{\Gamma^-_{cut,i}} = \phi_{d,i}|_{\Gamma_{cut,i}} = I_i \tag{4.59}$$

where I_i is the global current flowing around the cut [39]. Discontinuities $\phi_{d,i}|_{\Gamma_{ts,i}}$ and $\phi_{d,i}|_{\Gamma_{cut,i}}$ have to be matched at the TS - cuts intersections. i.e [9,39,81,106,135].

$$\phi_{d,i}|_{\Gamma_{cut,i}} = \sum_{i\in cut} I_i q_i, \tag{4.60}$$

where q_i is the ith basis function of $\mathcal{H}^1(\Omega^C_c)$ (see Section A.1.6), exhibiting a unit discontinuity across the cut Σ_i. It is continuous in a transition layer denoted by supp $(\Delta\phi_{d,i}|_{\Gamma_{cut,i}})$ and is continuously extended to zero out of this layer (Fig. 4.1).

Note that for a thin region located between conducting regions, the potential ϕ is not defined anymore on both sides of the TS and the problem has to be expressed in terms of the discontinuities of $\boldsymbol{h}$, i.e. $\boldsymbol{h}_i|_{\Gamma^+_{t,i}} = \boldsymbol{h}_{c,i}|_{\Gamma_{t,i}} + \boldsymbol{h}_{d,i}|_{\Gamma_{t,i}}$ and $\boldsymbol{h}_i|_{\Gamma^-_{t,i}} = \boldsymbol{h}_{c,i}|_{\Gamma_{t,i}}$ (with the discontinuity $\Delta\phi_i|_{\Gamma_t} = 0$).

4.3.8 SPs coupled to global quantities

The surface integral term $\langle \boldsymbol{n} \times \boldsymbol{e}_i, \boldsymbol{h}'_i \rangle_{\Gamma_{e,i}}$ in the weak form of SP u or SP f can be extended to a global condition defining a voltage V_i [32,39], for a test magnetic field $\boldsymbol{h}'_i$ equal to the current basis function $\boldsymbol{c}_i$. The only contributing part of $\Gamma_{e,i}$ is the lateral boundary of $\Omega_{g,i}$ (i.e. $\Gamma_{g,i}$) (see Section 1.4.2) made simply connected [32,39]. The other parts of the boundary of $\Omega_{g,i}$, i.e., its terminals, give no contribution because $\boldsymbol{n} \times \boldsymbol{e}_i$ on them. The function $\boldsymbol{c}_i$, associated with the cut Σ_i, is expressed as the gradient of the scalar potential q_i appearing in (4.60), i.e.

$$\boldsymbol{c}_i = -\mathbf{grad}\, q_i \quad \text{in} \quad \Omega^{\mathrm{C}}_{c,i} \quad \text{with} \quad \boldsymbol{n} \times \boldsymbol{c}_i = -\boldsymbol{n} \times \mathbf{grad}\, q_i \quad \text{on} \quad \partial\Omega_{c,i}, \tag{4.61}$$

the potential q_i being defined made simply connected by the cuts Σ_i (see Fig. 4.1). This potential q_i is fixed to 1 on one side of the cut Σ_i and to 0 on the other side (see Fig. 4.1). The continuous transition of q_i between these values can be performed in a transition layer in $\Omega^{\mathrm{C}}_{c,i}$ adjacent to side '+' (Fig. 4.1), which reduces the support of q_i and $\boldsymbol{c}_i$. One has [32,39]

$$\begin{aligned} \langle \boldsymbol{n} \times \boldsymbol{e}_i, \boldsymbol{c}_i \rangle_{\Gamma_{g,i}} = \langle \boldsymbol{n} \times \boldsymbol{e}_i, \boldsymbol{c}_i \rangle_{\Gamma^=_{g,i}} = \langle \boldsymbol{n} \times \boldsymbol{e}_i, -\mathbf{grad}\, q_i \rangle_{\Gamma^=_{g,i}} = \langle \mathbf{grad}\, q_i \times \boldsymbol{e}_i, \boldsymbol{n} \rangle_{\Gamma^=_{g,i}} \\ = \langle \mathbf{curl}\, (q_i\, \boldsymbol{e}_i), \boldsymbol{n} \rangle_{\Gamma^=_{g,i}} - \langle q_i\, \mathbf{curl}\, \boldsymbol{e}_i, \boldsymbol{n} \rangle_{\Gamma^=_{g,i}}. \end{aligned} \tag{4.62}$$

Using the Stokes formula for the first integral and seeing that the second integral vanishes (with the thickness of generator is small enough), one gets

$$\langle \boldsymbol{n} \times \boldsymbol{e}_i, \boldsymbol{c}_i \rangle_{\Gamma_{g,i}} = \oint_{\partial\Gamma_{g,i}} q_i \boldsymbol{e}_i \cdot d\boldsymbol{l} = \oint_{\gamma_{g,i}} \boldsymbol{e}_i \cdot d\boldsymbol{l} = V_i, \tag{4.63}$$

where $\gamma_{g,i}$ is a path connecting two real or imaginary electrodes of the thin region (see Fig. 1.3).

Consequently, for the test function $\boldsymbol{h}'_i = \boldsymbol{c}_i$, combining (4.63) into (4.34), the weak form for SP u (with massive inductors alone) can be written as

$$\partial_t(\mu_u \boldsymbol{h}_u, \boldsymbol{c}_i)_{\Omega_u} + (\sigma_u^{-1} \mathbf{curl}\, \boldsymbol{h}_u, \mathbf{curl}\, \boldsymbol{c}_i)_{\Omega_{c,u}} = -V_i, \tag{4.64}$$

which is the natural weak circuit relation for the massive inductor i and can be interpreted "∂_t(magnetic flux) + resistance × current = voltage". Analogously, by adding (4.63) into (4.47), one has for SP f (see Section 4.3.5).

4.3.9 Sequence of magnetostatic SP formulations−three SPs

In this case, the weak formulations for each SP are also considered in the sequence: SP $u \to$ SP $p \to$ SP k.

4.3.9.1 Inductor model−SP u

From the equation (4.12) established in Section 4.2.2, we start by writing a weak form for SP u, i.e.

$$(\mu_u \boldsymbol{h}_{s,u}, \mathbf{grad}\, \phi'_u)_{\Omega_u} - (\mu_u \mathbf{grad}\, \phi_u, \mathbf{grad}\, \phi'_u)_{\Omega_u} + \langle \boldsymbol{n} \cdot \boldsymbol{b}_u, \phi'_u \rangle_{\Gamma_{e,u}} = 0, \quad \forall \phi'_u \in {H^1}^0{}_{h,u}(\Omega_u). \tag{4.65}$$

The term $\langle \boldsymbol{n} \cdot \boldsymbol{b}_u, \phi'_u \rangle_{\Gamma_{e,u}}$ accounts for a natural BC of type (2.7 b), usually zero. Analogously to the magnetodynamic case, the source field $\boldsymbol{h}_{s,u}$ in (4.34) is defined via a projection method of a known distribution $\boldsymbol{j}_{s,u}$ (see Section 4.2.4).

4.3.9.2 Thin shell FEs model−SP p

The TS model is defined via the term $\langle [\boldsymbol{n} \cdot \boldsymbol{b}_p]_{\Gamma_{t,p}}, \phi'_p \rangle_{\Gamma_{t,p}}$ in (4.25). It is used to weakly express the magnetic flux density TS IC proper to the weak form of SP p, i.e.

$$(\mu_p \mathbf{grad}\, \phi_p, \mathbf{grad}\, \phi'_p)_{\Omega_p} + \langle \boldsymbol{n} \cdot \boldsymbol{b}_p, \phi'_p \rangle_{\Gamma_{e,p} - \Gamma_{t,p}} + \langle [\boldsymbol{n} \cdot \boldsymbol{b}_p]_{\Gamma_{t,p}}, \phi'_p \rangle_{\Gamma_{t,p}} = 0, \quad \forall \phi'_p \in {H^1}^0{}_{h,p}(\Omega_p). \tag{4.66}$$

The term $\langle [\boldsymbol{n} \cdot \boldsymbol{b}_p]_{\Gamma_{t,p}}, \phi'_p \rangle_{\Gamma_{t,p}}$ in (4.66) is expressed as

$$\begin{aligned} \langle [\boldsymbol{n} \cdot \boldsymbol{b}_p]_{\Gamma_{t,p}}, \phi'_p \rangle_{\Gamma_{t,p}} &= \langle [\boldsymbol{n} \cdot \boldsymbol{b}_p]_{\Gamma_{t,p}}, \phi'_{c,p} + \phi'_{d,p} \rangle_{\Gamma_{t,p}} \\ &= \langle [\boldsymbol{n} \cdot \boldsymbol{b}_p]_{\Gamma_{t,p}}, \phi'_{c,p} \rangle_{\Gamma_{t,p}} + \langle \boldsymbol{n} \cdot \boldsymbol{b}_p|_{\Gamma^+_{t,p}}, \phi'_{d,p} \rangle_{\Gamma^+_{t,p}}. \end{aligned} \tag{4.67}$$

From (2.23) and (4.25), the trace discontinuity term $\langle [\boldsymbol{n} \cdot \boldsymbol{b}_p]_{\Gamma_{t,p}}, \phi'_{c,p} \rangle_{\Gamma_{t,p}}$ is written as

$$\begin{aligned} \langle [\boldsymbol{n} \cdot \boldsymbol{b}_p]_{\Gamma_{t,p}}, \phi'_{c,p} \rangle_{\Gamma_{t,p}} &= \langle \boldsymbol{n} \cdot [\boldsymbol{b}_u + \boldsymbol{b}_p], \phi'_{c,p} \rangle_{\Gamma_{t,p}} \\ &= -\langle \mu_p d_p\, \boldsymbol{h}_{s,p}, \mathbf{grad}\, \phi'_p \rangle_{\Gamma_{t,p}} + \langle \mu_p d_p\, \mathbf{grad}\, \phi_p, \mathbf{grad}\, \phi'_p \rangle_{\Gamma_{t,p}}. \end{aligned} \tag{4.68}$$

The term $\langle \boldsymbol{n} \cdot \boldsymbol{b}_p|_{\Gamma^+_{t,p}}, \phi'_{d,p} \rangle_{\Gamma^+_{t,p}}$ in (4.67) is weakly expressed via the surface source integral term, i.e. $\langle \boldsymbol{n} \cdot \boldsymbol{b}_p|_{\Gamma^+_{t,p}}, \phi'_{d,p} \rangle_{\Gamma^+_{t,p}} = -\langle \boldsymbol{n} \cdot \boldsymbol{b}_u|_{\Gamma^+_{t,p}}, \phi'_{d,p} \rangle_{\Gamma^+_{t,p}} = -\boldsymbol{b}_{f,u}$, where $\boldsymbol{b}_{f,u}$ is a SS naturally expressed through the weak formulation of SP u in (4.65), i.e.

$$\langle \boldsymbol{n} \cdot \boldsymbol{b}_u|_{\Gamma^+_{t,p}}, \phi'_{d,p} \rangle_{\Gamma^+_{t,p}} = -(\mu_u \mathbf{grad}\, \phi_u, \mathbf{grad}\, \phi'_{d,p})_{\Omega^+_p} + (\mu_u \boldsymbol{h}_{s,u}, \mathbf{grad}\, \phi'_{d,p})_{\Omega^+_p}. \tag{4.69}$$

The volume integrals in (4.69) are also limited to a single layer of FEs on the positive side of Ω^+_p touching $\Gamma^+_{t,p}$. Introducing (4.69) and (4.68) into (4.65) to obtain the full weak form of SP p, i.e.

$$\begin{aligned} &(\mu_p \mathbf{grad}\, \phi_p, \mathbf{grad}\, \phi'_p)_{\Omega_p} - \langle \mu_p d_p\, \boldsymbol{h}_{s,p}, \mathbf{grad}\, \phi'_p \rangle_{\Gamma_{t,p}} + \langle \mu_p d_p\, \mathbf{grad}\, \phi_p, \mathbf{grad}\, \phi'_p \rangle_{\Gamma_{t,p}} \\ &\quad - (\mu_u \mathbf{grad}\, \phi_u, \mathbf{grad}\, \phi'_{d,p})_{\Omega^+_p} + (\mu_u \boldsymbol{h}_{s,u}, \mathbf{grad}\, \phi'_{d,p})_{\Omega^+_p} + \langle \boldsymbol{n} \cdot \boldsymbol{b}_p, \phi'_p \rangle_{\Gamma_{e,p} - \Gamma_{t,p}} = 0, \\ &\qquad \forall \phi' \in {H^1}^0{}_{h,p}(\Omega_p). \end{aligned} \tag{4.70}$$

At the discrete level, the source quantities ϕ_u and $\boldsymbol{h}_{s,u}$, initially in mesh of SP u, have to be projected to the mesh of SP p via a projection method.

4.3.9.3 Volume correction replacing the thin shell representation−SP k

Analogously, the TS solution obtained from SP p is then corrected by SP k via a VS given by (4.32), with $\boldsymbol{h}_p = \mathbf{grad}\,\phi_p$ and $\boldsymbol{h}_u = \boldsymbol{h}_{s,u} - \mathbf{grad}\,\phi_p$ (see Section 4.3.3). Hence, the weak form of SP k is

$$\begin{aligned}(\mu_k \mathbf{grad}\,\phi_k, \mathbf{grad}\,\phi'_k)_{\Omega_k} + (-(\mu_k - \mu_p)\mathbf{grad}\,\phi_p, \mathbf{grad}\,\phi'_k)_{\Omega_k} + \langle \boldsymbol{n}\cdot\boldsymbol{b}_k, \phi'_k\rangle_{\Gamma_{e,k}-\Gamma_{t,k}} \\ +((\mu_k - \mu_p)(\boldsymbol{h}_{s,u} - \mathbf{grad}\,\phi_u), \mathbf{grad}\,\phi'_k)_{\Omega_k} + \langle [\boldsymbol{n}\cdot\boldsymbol{b}_k]_{\Gamma_{t,k}}, \phi'_k\rangle_{\Gamma_{t,k}} = 0, \quad \forall \phi' \in {H^1}^0_{h,p}(\Omega_k).\end{aligned} \tag{4.71}$$

At the discrete level, the source quantities ϕ_u, $\boldsymbol{h}_{s,u}$ and ϕ_p in (4.71) defined in SP u and SP p are also projected to the mesh of SP k via a projection method.

Simultaneously to the VS, the SS has to suppress the TS discontinuities of SP p in SP k, with the IC in (2.42). It can be defined via the TS discontinuity, i.e.

$$[\boldsymbol{n}\cdot\boldsymbol{b}_k]_{\Gamma_{t,k}} = -[\boldsymbol{n}\cdot\boldsymbol{b}_p]_{\Gamma_{t,k}}. \tag{4.72}$$

IC (4.72) is weakly expressed through the last surface integral in (4.71), with $\Gamma_{t,k} = \Gamma_{t,p}$. The involved trace discontinuity $[\boldsymbol{n}\cdot\boldsymbol{b}_k]_{\Gamma_{t,k}}$ is naturally expressed as

$$\langle [\boldsymbol{n}\cdot\boldsymbol{b}_k]_{\Gamma_{t,k}}, \phi'_k\rangle_{\Gamma_{t,k}} = -\langle [\boldsymbol{n}\cdot\boldsymbol{b}_p]_{\Gamma_{t,k}}, \phi'_k\rangle_{\Gamma_{t,k}}. \tag{4.73}$$

4.3.10 Sequence of magnetosatic SP formulations−two SPs

The sequence is now considered in two SPs: SP f $\rightarrow$ SP k. Based on the developments that were made for the magnetostatic weak formulations in Section 4.2.2. Combining (4.25) into (4.12), a weak form for SP f is

$$\begin{aligned}-(\mu_f\,\boldsymbol{h}_{s,f}, \mathbf{grad}\,\phi'_f)_{\Omega_f} + (\mu_f\,\mathbf{grad}\,\phi_f, \mathbf{grad}\,\phi'_f)_{\Omega_f} + \langle \boldsymbol{n}\cdot\boldsymbol{b}_f, \phi'_f\rangle_{\Gamma_{e,f}-\Gamma_{t,f}} \\ -\langle \mu_f d_f\,\boldsymbol{h}_{s,f}, \mathbf{grad}\,\phi'_f\rangle_{\Gamma_{t,f}} + \langle \mu_f d_f\,\mathbf{grad}\,\phi_f, \mathbf{grad}\,\phi'_f\rangle_{\Gamma_{t,f}} = 0, \quad \forall \phi'_f \in {H^1}^0_{h,f}(\Omega_f),\end{aligned} \tag{4.74}$$

where the source field $\boldsymbol{h}_{s,f}$ is defined by the imposed electric current density $\boldsymbol{j}_{s,f}$ (see Section 4.2.4). A similar way as in Section 4.3.5, the TS solution obtained in SP f is next improved by SP k. From (4.71), by replacing p by f and cancelling the term $\boldsymbol{h}_{s,u} - \mathbf{grad}\,\phi_u$ in (4.71), one has for SP k

$$\begin{aligned}-(\mu_k\,\mathbf{grad}\,\phi_k, \mathbf{grad}\,\phi'_k)_{\Omega_k} - ((\mu_k - \mu_f)\mathbf{grad}\,\phi_f, \mathbf{grad}\,\phi'_k)_{\Omega_k} + \langle \boldsymbol{n}\cdot\boldsymbol{b}_k, \phi'_k\rangle_{\Gamma_{e,k}-\Gamma_{t,k}} \\ +\langle [\boldsymbol{n}\cdot\boldsymbol{b}_k]_{\Gamma_{t,k}}, \phi'_k\rangle_{\Gamma_{t,k}} = 0, \quad \forall \phi'_k \in {H^1}^0_{h,k}(\Omega_p).\end{aligned} \tag{4.75}$$

The treatment for suppressing the TS representation in SP k via the SS expressed via the term $\langle [\boldsymbol{n}\cdot\boldsymbol{b}_k]_{\Gamma_{t,k}}, \phi'_k\rangle_{\Gamma_{t,k}}$ is similar to the one with three SPs (see Section 4.3.9).

4.3.11 Projection of solutions between meshes

As the magnetic vector potential in Section 3.3.9, the magnetic field $\boldsymbol{h}_u$ resulting from the previous computation in a source mesh of SP i (e.g. SP u) is projected

onto a mesh of target SP i (e.g. SP p) while keeping discrete properties of the source field. At the discrete level, the source quantity $\boldsymbol{h}_u$ has to be expressed in the mesh of target SP p, while initially given in the mesh of previous SP u. By applying (2.20) to $\boldsymbol{h}_u$ limited to $\Omega_{s,p}$, with the edge basis functions on the target mesh as a test function $\boldsymbol{h}'$, one has

$$(\boldsymbol{h}_{u,p-\text{proj}}, \boldsymbol{h}')_{\Omega_{s,p}} = (\boldsymbol{h}_u, \boldsymbol{h}')_{\Omega_{s,p}}, \quad \forall \boldsymbol{h}' \in \boldsymbol{H}^1_p(\mathbf{curl}; \Omega_{s,p}), \tag{4.76}$$

where $\boldsymbol{H}^1_p(\mathbf{curl}; \Omega_{s,p})$ is curl-conform function space for the p-projected source $\boldsymbol{h}_{u,p-\text{proj}}$ (the projection of $\boldsymbol{h}_u$ on mesh of SP p) and the test function $\boldsymbol{h}'$ defined on $\Omega_{s,p}$. Note that for the magnetostatic case, $\boldsymbol{h}_p$ can be defined by a magnetic scalar potential ϕ_p such that $\boldsymbol{h}_p = -\mathbf{grad}\,\phi_p$. In this case, it is possible to project the grad of ϕ_u instead of the potential ϕ_u, i.e.

$$(\mathbf{grad}\,\phi_{u,p-\text{proj}}, \mathbf{grad}\,\phi')_{\Omega_{s,p}} = (\mathbf{grad}\,\phi_u, \mathbf{grad}\,\phi')_{\Omega_{s,p}}, \quad \forall \phi'_i \in {H^1}_0{}_p(\Omega_{s,p}), \tag{4.77}$$

where ${H^1}_0{}_p(\Omega_{s,p})$ is grad-conform function space for the p-projected source $\phi_{u,p-\text{proj}}$ (the projection of ϕ_u on mesh of SP p) and the test function ϕ' defined on $\Omega_{s,p}$.

4.3.12 Discretization of the magnetic field

At the discrete level, the use of edge FEs [29, 32, 35, 58] to interpolate curl-conform fields, such as the magnetic $\boldsymbol{h}_i$, first gives facilities in defining currents. Indeed, the circulation of such a field along a closed path, also being the flux of its curl and consequently the current, is directly obtained from coefficients of the interpolation, in this case those associated with the edges of the path [35].

The magnetic field $\boldsymbol{h}_i$ in the weak formulations is thus discretized by edge FEs, generating the function space defined on a mesh of Ω_i [29, 32, 35, 58], i.e.

$$\boldsymbol{h}_i = \sum_{e \in E(\Omega_i)} h_{e,i} s_{e,i}, \tag{4.78}$$

where $E(\Omega_i)$ is the set of edges of Ω_i, $s_{e,i}$ is the edge basis function associated with edge e and $h_{e,i}$ is the circulation of $\boldsymbol{h}_i$ along edge e. Here, geometrical element of the mesh can be triangles and quadrangles in two dimensions, or tetrahedra, hexahedra and prism in three dimensions (see Sections B.2 and B.3).

Now, characterization (4.78) can be transformed in order to give explicitly the basis functions of the considered discrete space for $\boldsymbol{H}^0_{h_i,\phi_i}(\mathbf{curl}; \Omega_i)$ with the essential constraint, i.e., $\boldsymbol{h}_{r,i} = -\mathbf{grad}\,\phi_i$ using the developments in Section 4.3.7. The scalar potential ϕ_i is expressed as

$$\phi_i|_{\Omega_i} = \phi_{c,i}|_{\Omega_c^{\mathrm{C}}} + \phi_{d,i}|_{\Gamma_{cut,i}} + \phi_{d,i}|_{\Gamma_{t,i}} = \phi_{c,i}|_{\Omega_c^{\mathrm{C}}} + \sum_{i \in cut} \phi_{d,i}|_{\Gamma_{cut,i}} + \sum_{i \in TS} \phi_{d,i}|_{\Gamma_{t,i}}. \tag{4.79}$$

The discontinuous fields $\phi_{d,i}|_{\Gamma_{cut,i}}$ and $\phi_{d,i}|_{\Gamma_{t,i}}$ are defined by restricting their support to layers of elements of $\Omega^{\mathrm{C}}_{c,i}$ adjacent to the "+" side of the surfaces $\Gamma_{cut,i}$ and $\Gamma_{t,i}$, to which are added the elements of $\Omega_{c,i}$ which touch this layer by at least

one edge e so that $e \in E(\Omega_{c,i}^{\mathrm{C}})$ and $e \notin E(\Gamma_{cut,i})$ or $e \notin E(\Gamma_{t,i})$. These layers are called transition layers and are denoted by $N_{cut,i}^{+}$ and $N_{t,i}^{+}$ the set of nodes of $\mathrm{supp}\,(\Delta\phi_{d,i}|_{\Gamma_{cut,i}} = \phi_{g,i}|_{\Gamma_{cut,i}})$ and $\mathrm{supp}\,(\Delta\phi_{d,i}|_{\Gamma_{t,i}} = \phi_{d,i}|_{\Gamma_{t,i}})$, respectively (Fig. 4.1) and by $\{n, m\}$ the edge joining the nodes n and m.

Combining (4.79) and (4.78), the discretization of $\boldsymbol{h}_i - \phi_i$ coupling is now expressed as [21, 24, 60]

$$\boldsymbol{h}_i = \boldsymbol{h}_{s,i} + \sum_{e \in E(\Omega_{c,i})} h_{k,i} s_{k,i} + \sum_{n \in N(\Omega_{c,i}^{\mathrm{C}})} \phi_{c,n,i}\, v_{c,n,i} + \sum_{i \in cut} \left(I_{c_i} \sum_{n \in N(\Gamma_{cut,i})} c_{g,n,i} \right) + \sum_{i \in TS} \left(\sum_{n \in N(\Gamma_{t,i})} \phi_{d,i}\, t_{d,n,i} \right), \quad (4.80)$$

where $\Gamma_{cut,i}$ is a set of cuts making $\Omega_{c,i}^{C}$ simply connected (Fig. 4.1). Coefficients I_{c_i} represent circulations of $\boldsymbol{h}_i$ along well-defined paths (equal to the fluxes of their **curl** and thus to the currents through associated surfaces) and functions $c_{g,n,i}$ are vector basis functions associated with cuts $\Gamma_{cut,i}$. Note that such a characterization enables function $v_{c,n,i}$, and thus the associated scalar potential, to be fully continuous in a multiply connected domain, the discontinuity being taken into account by functions $c_{g,n,i}$. The functions $v_{c,n,i}$, $t_{d,n,i}$ and $c_{g,n,i}$ can be respectively expressed as [21, 24, 34, 60]

$$v_{c,n,i} = \sum_{\{n,m\} \in E(\Omega_{c,i}^{C})} s_{e,\{n,m\}},$$

$$t_{d,n,i} = \begin{cases} \displaystyle\sum_{\substack{\{n,m\} \in E(\Omega_{c,i}^{C}) \\ n \in N(\Gamma_{t,i}) \\ m \notin N(\Gamma_{ts,i}) \\ m \in N_{t,i}^{+}}} s_{e,\{n,m\}} & \text{in } \mathrm{supp}\,(\Delta\phi_{d,i}|_{\Gamma_{t,i}}) \\ 0 & \text{otherwise} \end{cases},$$

and

$$c_{g,n,i} = \begin{cases} \displaystyle\sum_{\substack{\{n,m\} \in E(\Omega_{c,i}^{C}) \\ n \in N(\Gamma_{cut,i}) \\ m \notin N(\Gamma_{cut,i}) \\ m \in N_{cut,i}^{+}}} s_{e,\{n,m\}} & \text{in } \mathrm{supp}\,(\Delta\phi_{g,i}|_{\Gamma_{cut,i}}) \\ 0 & \text{otherwise} \end{cases}.$$

where $m \in N_{t,i}^{+}$ and $m \in N_{cut,i}^{+}$ represent the set of nodes of the transition layers $\mathrm{supp}(\Delta\phi_{d,i}|_{\Gamma_{t,i}})$ and $\mathrm{supp}(\Delta\phi_{cut,i}|_{\Gamma_{cut,i}})$, respectively (Fig. 4.1).

In the case of the studied domain is simply connected, the characterization of $\boldsymbol{h}_i - \phi_i$ coupling in (4.80) becomes

$$\boldsymbol{h}_i = \boldsymbol{h}_{s,i} + \sum_{e \in E(\Omega_{c,i})} h_{k,i} s_{k,i} + \sum_{n \in N(\Omega^{\mathrm{C}}_{c,i})} \phi_{c,n,i}\, v_{c,n,i} + \sum_{i \in TS} \Big(\sum_{n \in N(\Gamma_{t,i})} \phi_{d,i}\, t_{d,n,i} \Big). \quad (4.81)$$

In the magnetostatic case, the relation $\boldsymbol{h}_i = -\mathbf{grad}\,\phi_i$ holds in the whole domain $\Omega^{\mathrm{C}}_{c,i} = \Omega_i$. The field $\boldsymbol{h}_i$ can then be defined from a scalar potential ϕ_i everywhere in Ω_i, and (4.80) is simply written as

$$\boldsymbol{h}_i = \boldsymbol{h}_{s,i} + \sum_{n \in N(\Omega^{\mathrm{C}}_{c,i})} \phi_{c,n,i}\, v_{c,n,i} + \sum_{i \in TS} \Big(\sum_{n \in N(\Gamma_{t,i})} \phi_{d,i}\, t_{d,n,i} \Big). \quad (4.82)$$

Chapter 5

Numerical tests

Contents

5.1 Introduction

In this chapter, we present a series of numerical tests to validate the theoretical developments presented in Chapters 2, 3, 4 and their implementation, both in two and three dimensions. The computer codes (Gmsh and GetDP) used for all the simulations are freely available over the Internet at the addresses http://www.geuz.org/gmsh and http://www.geuz.org/getdp.

The first numerical test (Section 5.2) consists of the study of (one or two) shield plates located in the vicinity of an inductor. Both the one-way and the two-way coupling strategy are analyzed, and a comparison of the computational effort is provided in the case of repetitive analyses.

The second test case consists in the study of a shielded induction heater with two stranded inductors, a plate in the middle, and two screens (Section 5.3). The purpose of these tests is to validate the SPM in both the magnetic flux density formulation ($\boldsymbol{b}$-formulation) and the magnetic field formulation ($\boldsymbol{h}$-formulation) in two dimensions.

The third numerical test is based on an international TEAM (Testing Electromagnetic Analysis Methods) workshop problem 21 -model B (Section 5.4). The goal of this test is to illustrate the SPM with both $\boldsymbol{b}$- and $\boldsymbol{h}$-formulations in both two and three dimensions.

The fourth test is a bushing mounting plate (of a transformer) consisting of a plate and bus bars (Section 5.5). The aim of this test is to show the coupling between local and global quantities for the considered massive inductors.

The fifth numerical test is the TEAM workshop problem 7 (Section 5.6). The purpose of this test is to validate the $\boldsymbol{h}$-conform magetodynamic formulation for multiply connected regions.

Finally, the last numerical test presented in Section 5.7 shows how our SPM strategy can be used for modelling of thin regions located between conducting regions or between conducting and nonconducting regions.

Note that all the dynamic cases have been solved in the frequency domain, using the complex formalism.

5.2 Inductor-shielded plate

This test problem comprises a shielding plate located above an inductor (Fig. 5.1, a). The shielding plate is a thin region. The inductor (dx = dy = 12.5 mm, H_3 = 60 mm) carries an imposed current density $\boldsymbol{j}_s$ (electric current $I = 1$ A, frequency $f = 50$ Hz and 300 Hz, number of turns N = 1000). The dimensions and position of the plate are $H_1 = 120$ mm, $H_2 = 60$ mm and $d = 1.25$ mm $\div$ 10 mm, with its relative permeability $\mu_r = \mu/\mu_0$ and conductivity σ.

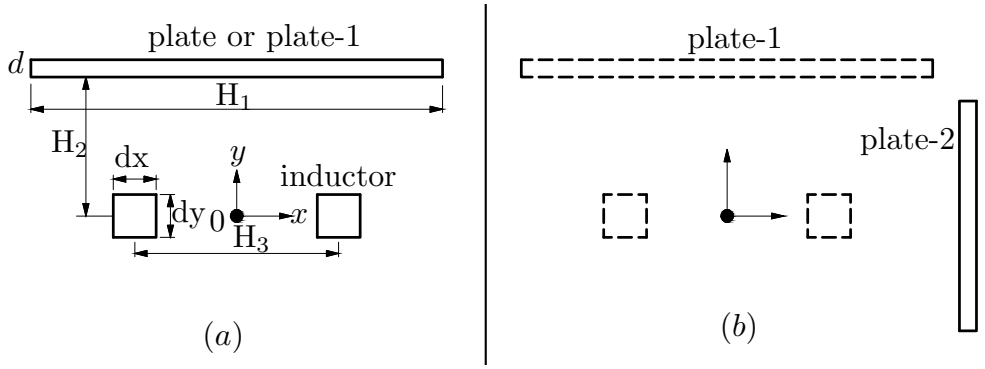

Figure 5.1: Inductor $\Omega_{s,i}$ and thin shielding plate $\Omega_{c,i}$

The problem is herein solved with both a three and a two SPs strategy (see Sections 3.3.4, 3.3.5, 3.3.7 and 3.3.8). Fig. 5.2 shows detailed meshes of each SP (SP u, SP p, SP k and complete or full problem). The solutions on the magnetic vector potential $\boldsymbol{a}$ of each SP in magnetodynamics are illustrated in Fig. 5.3. A first problem SP u involving the stranded inductor alone is solved on a simplified mesh without any thin regions (Fig. 5.3, *top left*, $\boldsymbol{a}_u$). A TS model SP p is then added with a lighter mesh than the one of the complete problem (Fig. 5.3, *top right*, $\boldsymbol{a}_p$) that does not include the inductor anymore. Finally, a volume correction SP k replaces the TS FEs with volume FEs covering the plate and their neighborhood (Fig. 5.3, *middle right*, $\boldsymbol{a}_k$). The projection of the inductor solution for SS in SP p is shown (Fig. 5.3, *middle left*, $\boldsymbol{a}_{proj}$, SS). The projections of the TS solutions for

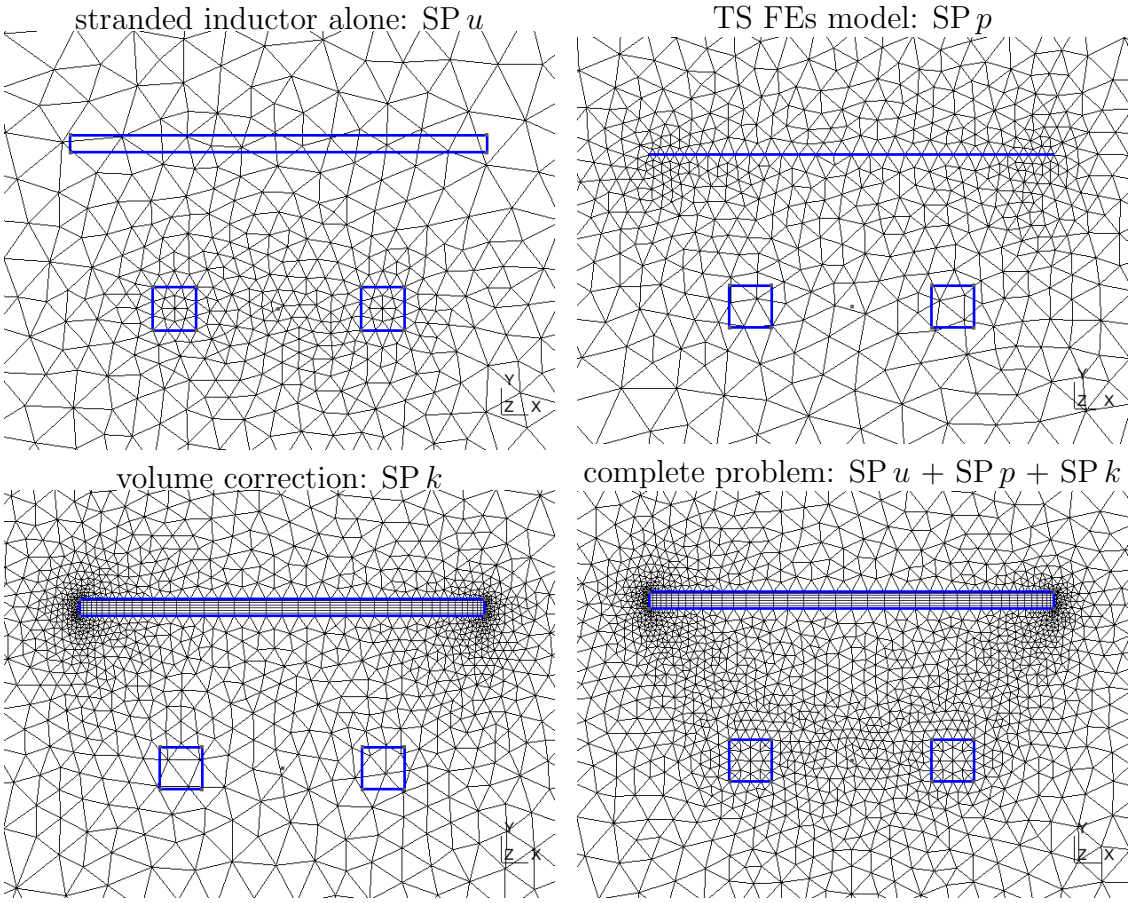

Figure 5.2: Different meshes of the three SPs and complete problem: stranded inductor alone SP u (*top left*), TS model SP p (*top right*), volume correction SP k (*bottom left*) and complete problem (*bottom right*).

the VS and SS in SP k are also illustrated (Fig. 5.3, *top left*, $\boldsymbol{a}_{proj}$, VS-SS). For each set of parameters, the superposition of the SPM solutions is compared with the reference or complete solution calculated on a single mesh (Fig. 5.3, *bottom right*) ($d = 5\,\text{mm}$, $f = 300\,\text{Hz}$, $\mu_r = 1$ and $\sigma = 59\,\text{MS/m}$). Analogously, the distribution of the magnetic flux densities for each SP governed by different meshes is also pointed out in detail (Fig. 5.4).

The problem is now solved in two SPs depicted in Fig. 5.5. A reduced model SP f with the inductor and a thin plate is first considered (Fig. 5.5, $\boldsymbol{a}_f$, *top left*), and then followed by the volume correction SP k (Fig. 5.5, *top right*, $\boldsymbol{a}_k$). The projections of portions of TS solutions for the VS and SS in SP k are then represented (Fig. 5.5, *bottom left*, $\boldsymbol{a}_{proj}$, VS-SS). The summation of both solutions is compared with the complete solution computed on a single mesh (Fig. 5.5, *bottom right*, $\boldsymbol{a} = \boldsymbol{a}_f + \boldsymbol{a}_k$).

It is worth noting that the mesh of SP k shown in Figs. 5.2, 5.4 and 5.5 is chosen to be "global" (covering the complete domain) only to analyze how large the SP k mesh should be. The actual mesh that should be used in the proposed SP

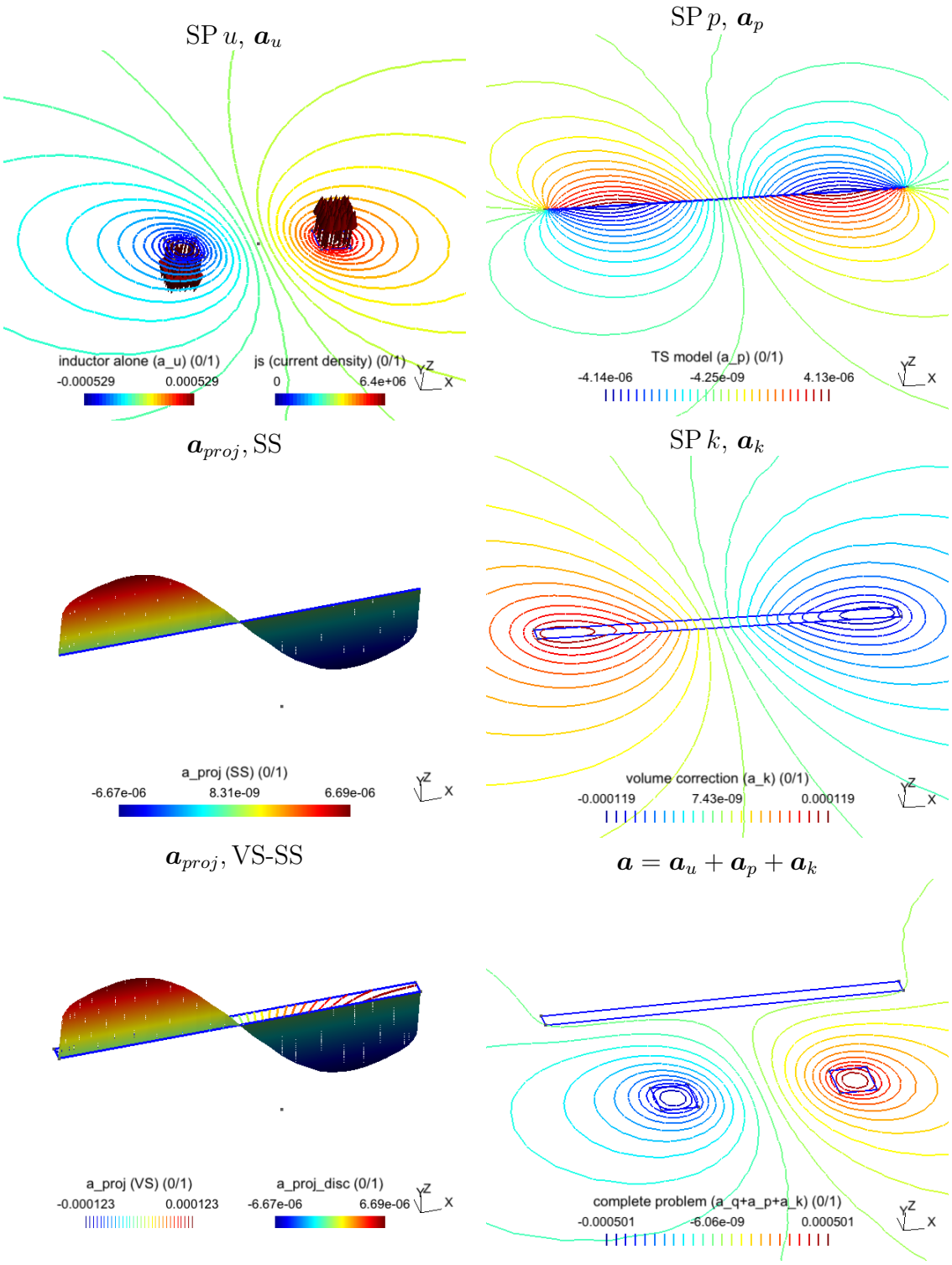

Figure 5.3: Flux lines (real part) for SP u ($\boldsymbol{a}_u$), added SP p ($\boldsymbol{a}_p$), volume correction SP k ($\boldsymbol{a}_k$) and the complete solution ($\boldsymbol{a}_u + \boldsymbol{a}_p + \boldsymbol{a}_k$) ($d = 5\,\text{mm}$, $f = 300\,\text{Hz}$, $\mu_r = 1$ and $\sigma = 59\,\text{MS/m}$). Projection of SP u solution ($\boldsymbol{a}_{proj}$, SS) in the SP p, and of SP p solution ($\boldsymbol{a}_{proj}$, VS-SS) in SP k. The imaginary presents an analogous behavior.

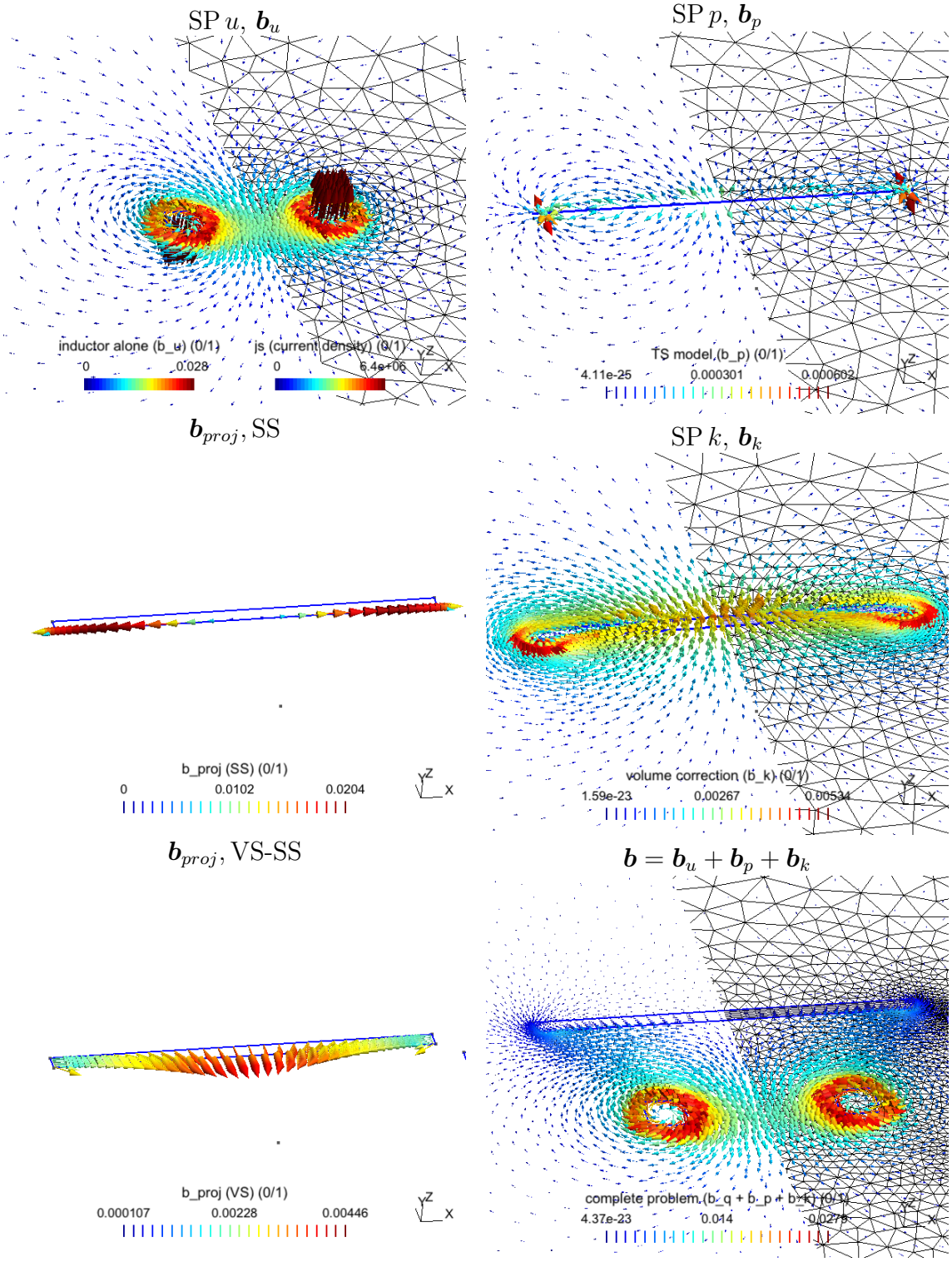

Figure 5.4: Magnetic flux densities (real part) for SP u ($\boldsymbol{b}_u$), added SP p ($\boldsymbol{b}_p$), correction SP k ($\boldsymbol{b}_k$) and the complete solution ($\boldsymbol{b} = \boldsymbol{b}_u + \boldsymbol{b}_p + \boldsymbol{b}_k$) with the different meshes used ($d = 5\,\text{mm}$, $f = 300\,\text{Hz}$, $\mu_r = 1$ and $\sigma = 59\,\text{MS/m}$). Projection of SP u solution ($\boldsymbol{b}_{proj}$, SS) in the SP p, and of SP p solution ($\boldsymbol{b}_{proj}$, VS-SS) in SP k.

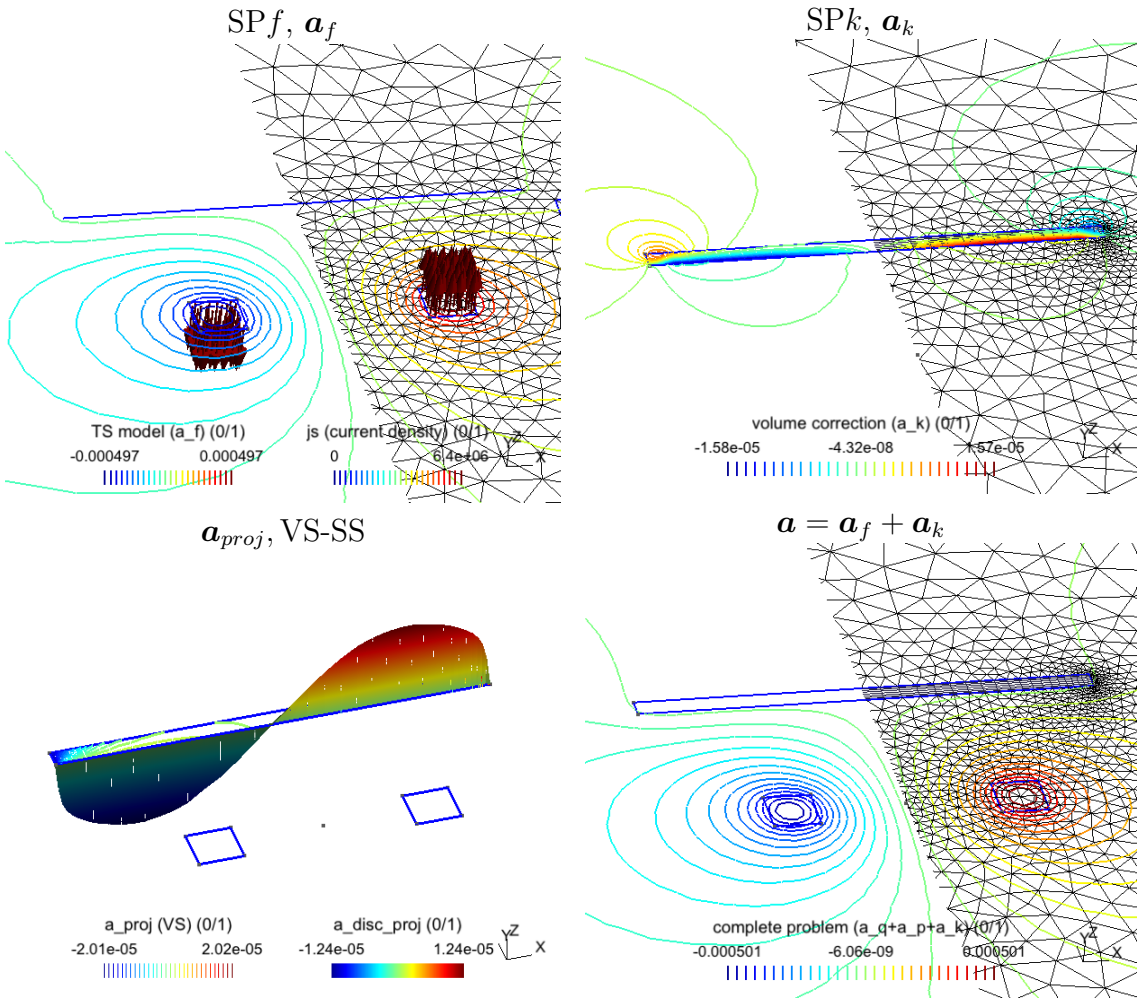

Figure 5.5: Flux lines (real part) for SP f ($\boldsymbol{a}_f$), volume correction SP k ($\boldsymbol{a}_k$) and the total solution ($\boldsymbol{a} = \boldsymbol{a}_f + \boldsymbol{a}_k$) with the different meshes used ($d = 5\,\text{mm}$, $f = 300\,\text{Hz}$, $\mu_r = 1$ and $\sigma = 59\,\text{MS/m}$). Projection of SP p solution ($\boldsymbol{a}_{proj}$, VS-SS) in SP k. The imaginary presents an analogous behavior. Note that this process is considered in two SPs.

strategy can be localized around the plate. Moreover, the mesh can be constructed completely independently of the plate surroundings (Fig. 5.6). Solutions shown in Figs. 5.7, 5.8, 5.10, 5.11 and 5.12 are solved with the local mesh of SP k indicated in Fig. 5.6 (*bottom left*). The inaccuracy on the eddy current density of TS SP p or SP f (Fig. 5.7, *left*) is pointed out by the volume correction SP k (Fig. 5.7, *right*). The TS error locally reaches 15%, with $\delta = 3.78\,\text{mm}$, $d = 5\,\text{mm}$, $f = 300\,\text{Hz}$, $\mu_r = 1$ and $\sigma = 59\,\text{MS/m}$. The errors on the power loss densities of TS SP p along the plate, with different positions of the plate, are indicated in Fig. 5.8. For a distance between the plate and the inductor $D = H_2/2$ (with H_2 is given in Fig. 5.1), the error on the TS SP p reaches 25% near the plate ends ($\delta = 3.78\,\text{mm}$) or 89% with ($\delta = 2.25\,\text{mm}$, $f = 50\,\text{Hz}$, $\mu_r = 100$ and $\sigma = 10\,\text{MS/m}$) (Fig. 5.8, *top*), with $d = 5\,\text{mm}$ for both cases. For $D = 2H_2$, it reaches 22% near the plate end ($\delta = 3.78\,\text{mm}$) or

85% with ($\delta = 2.25\,\mathrm{mm}$) (Fig. 5.8, *bottom*), with $d = 5\,\mathrm{mm}$ for both cases. Accurate local corrections with SP k calculated on the local mesh are checked to be close to the one calculated on the global mesh (Fig. 5.9).

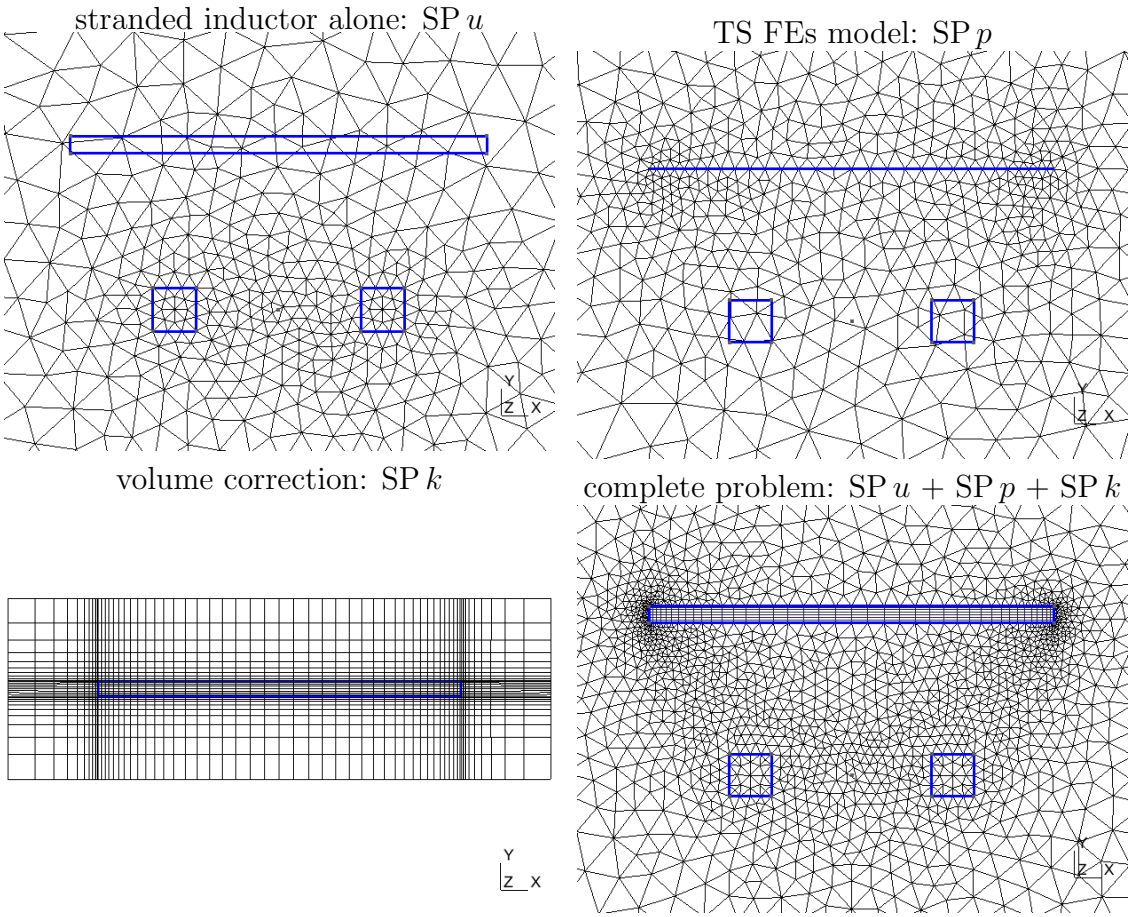

Figure 5.6: Different meshes of the three SPs: mesh $\mathcal{M}_u$ of stranded inductor alone SP u (*top left*), mesh $\mathcal{M}_p$ of TS model SP p (*top right*), mesh $\mathcal{M}_k$ of volume correction SP k (*bottom left*) and mesh $\mathcal{M}$ of complete problem (*bottom right*).

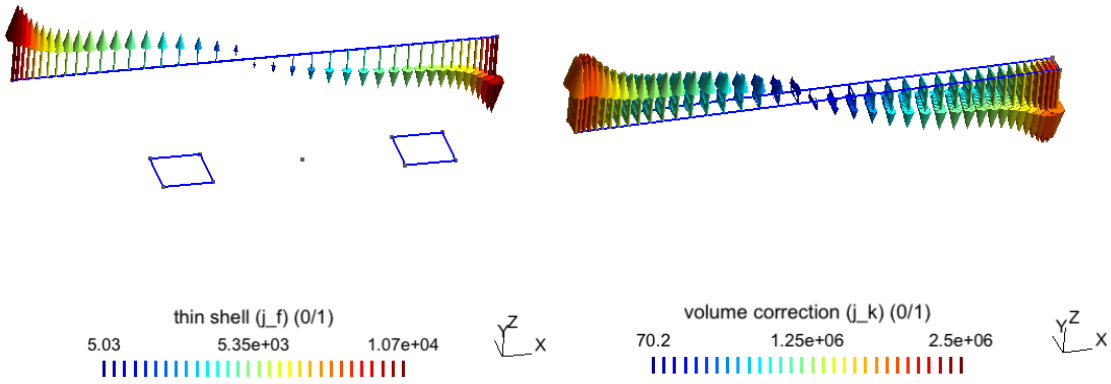

Figure 5.7: Eddy current density for TS FEs model (real part) (SP f, $\boldsymbol{j}_f$) and correction solution (SP k, $\boldsymbol{j}_k$) ($d = 5\,\mathrm{mm}$, $f = 300\,\mathrm{Hz}$, $\mu_r = 1$ and $\sigma = 59\,\mathrm{MS/m}$).

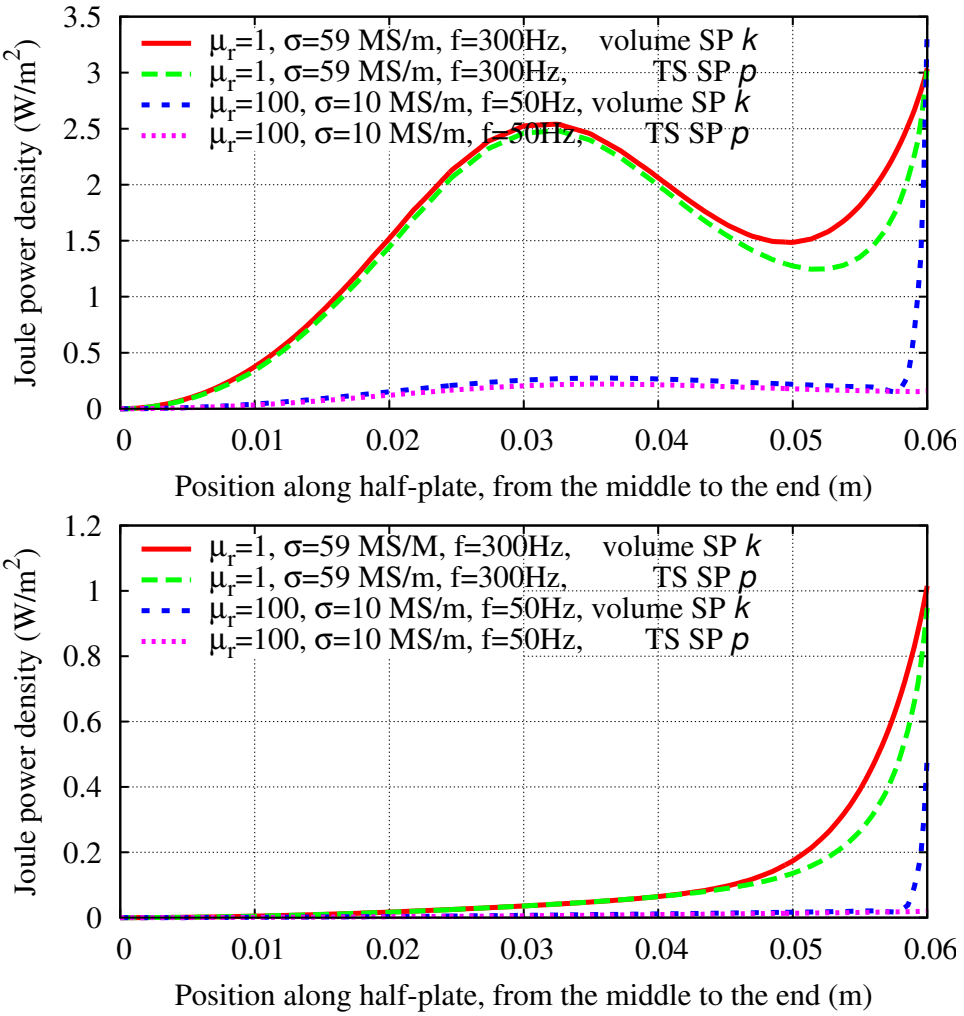

Figure 5.8: Power loss density with TS and volume correction along the plate with two positions of a 5 mm thickness plate $D = H_2/2$ (*top*), for $D = 2H_2$ (*bottom*) (with H_2 is given in Fig. 5.1).

The inaccuracies of the TS SP p, that increase with the thickness, particularly near the plate ends, are perfectly corrected whatever their order of magnitude (Figs. 5.10, 5.11 and 5.12). In magetostatics, the accuracy of the correction is directly linked to the volume mesh of the volume correction SP k and its neighboring. The corrections, usually of a few percents in the exterior region, can reach several tens of percents in the shells. For magnetic shells, the TS longitudinal magnetic flux is usually of poor quality near the shell ends (Fig. 5.11), which is then perfectly corrected by a correction SP k via the SPM. In magnetodynamics, a problem with a mainly longitudinal flux suffers from the same flux inaccuracies, whereas these will be lower with a transversed flux. The TS error on the eddy current density and the ensuing Joule power density depends on several parameters, as shown in Fig. 5.12. The inaccuracies on the Joule losses can reach 50% in the end regions for some critical parameters: e.g., 45% with the 3rd set, with $\delta = 2.3$ mm, or 30% with

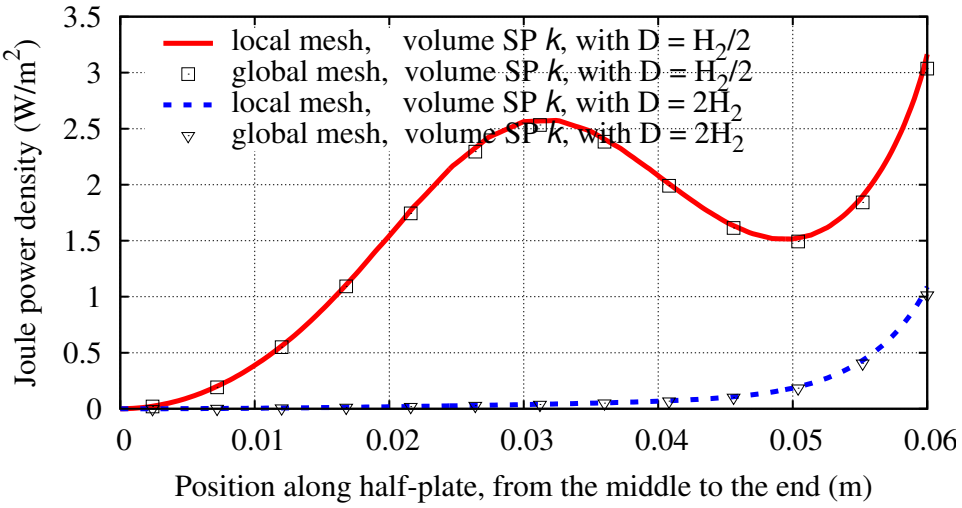

Figure 5.9: Comparison of the volume correction SP k calculated in the global mesh (Fig. 5.2, *bottom left*) and in the local mesh (Fig. 5.6, *bottom left*), for two positions of the plate. D is a distance between the plate and the inductor and H_2 is given in Fig. 5.1 ($d = 5\,\text{mm}$, $\mu_r = 1$, $\sigma = 59\,\text{MS/m}$, $f = 300\,\text{Hz}$).

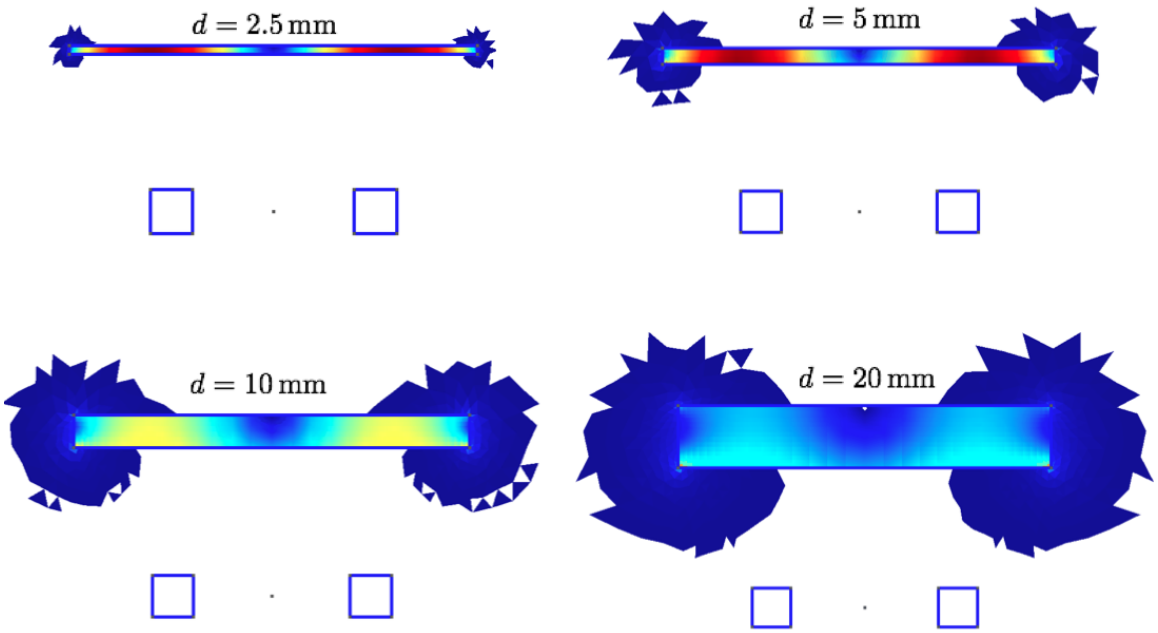

Figure 5.10: Colored map pointing out the regions with a relative correction higher than 1% (in the plates and the vicinity of their ends), with different thicknesses ($\mu_r = 100$).

the 2nd set, with $\delta = 3.8\,\text{mm}$, with $d = 5\,\text{mm}$ in both cases.

The test is now considered for the **two-way** coupling if a shielded plate 2 is added (Fig. 5.1, *b*), with TS SP p_2 and volume correction SP k_2. As presented in Section 2.3.5, the calculation for TS SP p_2 allows to benefit from previous compu-

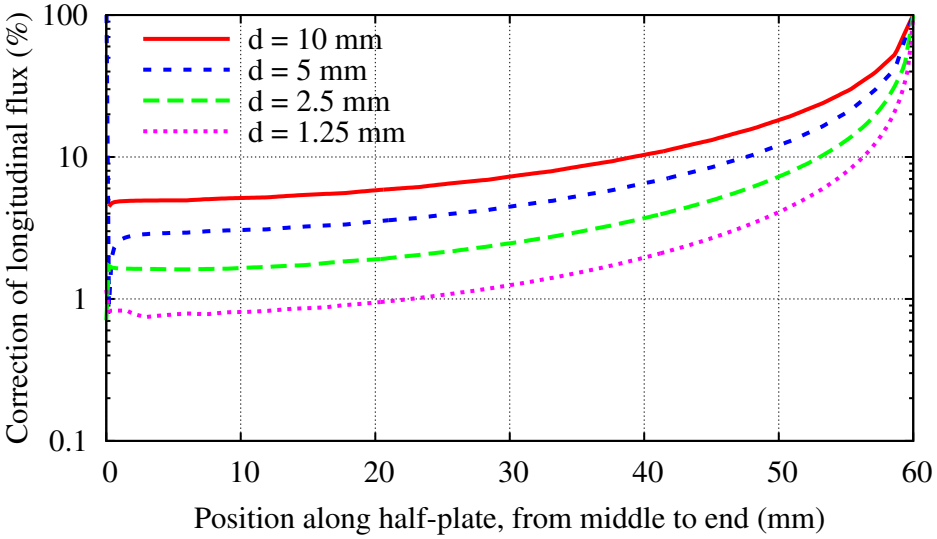

Figure 5.11: Relative correction of the longitudinal magnetic flux along the plate for different plate thicknesses ($\mu_r = 100$) for magnetostatic case.

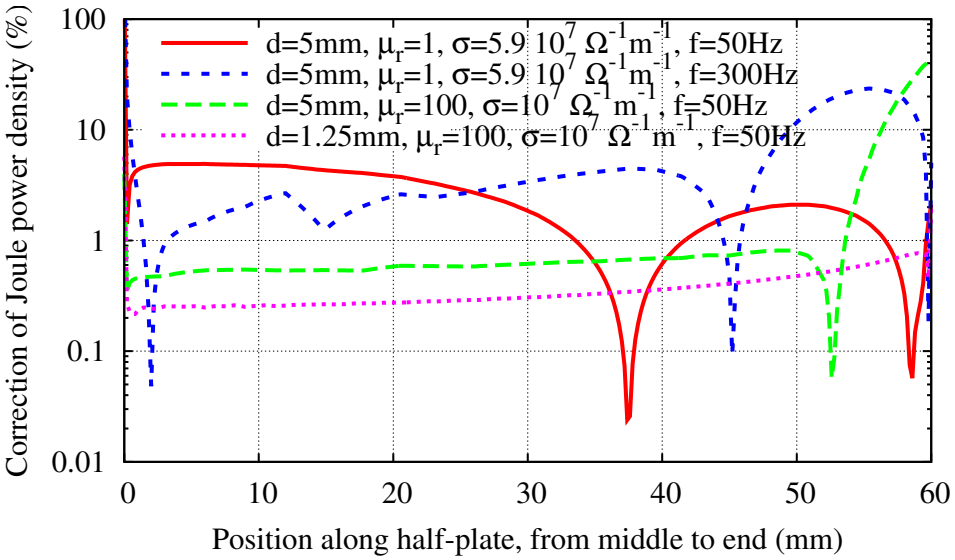

Figure 5.12: Relative correction of the Joule power density along the plate, with effects of d, μ_r, σ and f.

tations in SP p (or renamed by SP p_1) without starting a new complete FE solution for any variation physical data. The field created by the TS SP p_2 is a reaction field that influences the source solutions calculated from previous SP p_1. Twelve iterations between the SPs were required to converge to $\epsilon^n_{\text{estimated}} = 10^{-3}$. The TS error on the Joule power density in the plate 1 and 2 depends on several parameters, as depicted in Fig. 5.13. It can reach 60% in the end region of plate 1 (Fig. 5.13, *top*) and 40% in the end region of plate 2 (Fig. 5.13, *bottom*).

The proposed correction scheme of TS models via a SPM leads to accurate field and current distributions in critical regions, the edges of plates, and so of the ensuing

forces and Joules distributions. In particular, SPs in the SPM allow to use previous local meshes instead of starting a new complete mesh for any position of the plate. This can drastically reduce the overall computation time when many variations of the problem have to be solved e.g. optimisation problems. Table 5.1 summarizes the computational effort required by the direct FEM and the one-way and two-way SPM.

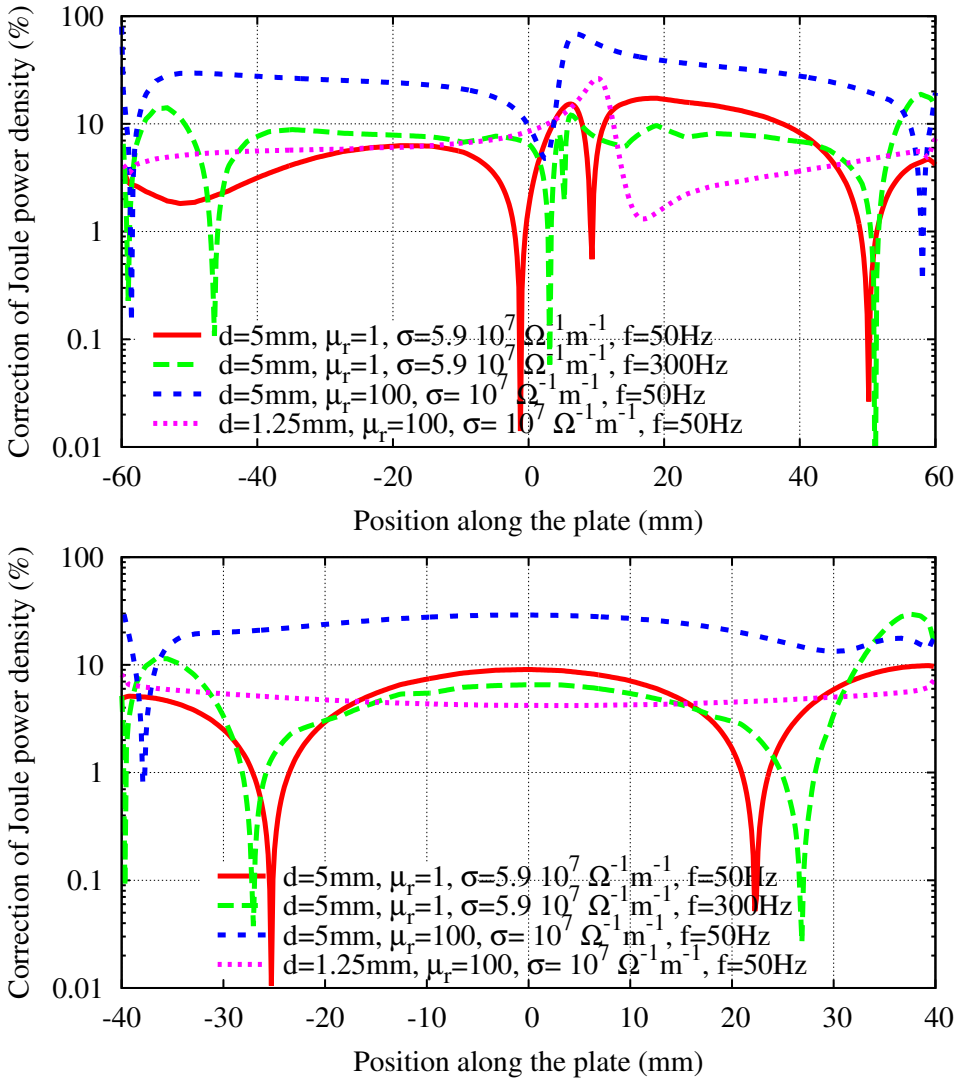

Figure 5.13: Relative correction of the Joule power density along the plate 1 (*top*) and the plate 2 (*bottom*) for the two-way coupling, with effects of d, μ_r, σ and f.

Table 5.1: Comparison of direct FEM and one-way/two-way SPM. The meshes $\mathcal{M}$, $\mathcal{M}_u$, $\mathcal{M}_p$ and $\mathcal{M}_k$ are shown on Fig. 5.6, leading to the solution of linear systems (LS) of n_f, n_u, n_p and n_k equations, respectively. Local meshes for the two-way coupling ($\mathcal{M}_{p_1}$, $\mathcal{M}_{p_2}$, $\mathcal{M}_{k_1}$ and $\mathcal{M}_{k_2}$) are similar to the one-way coupling meshes; the number of iterations of the two-way coupling is n.

Variation of position of the plate	Classical method	Subproblem method	
	Full problem	One-way coupling	Two-way coupling
N times	- N times full mesh $\mathcal{M}$ - N solutions of $n_f \times n_f$ LS	SP u: - 1 time mesh $\mathcal{M}_u$ - 1 solution of $n_u \times n_u$ LS SP p: - 1 time mesh $\mathcal{M}_p$ - 2 solutions of $n_p \times n_p$ LS SP k: - 1 time mesh $\mathcal{M}_k$ - 2 solutions of $n_k \times n_k$ LS	SP u: - 1 time mesh $\mathcal{M}_u$ - 1 solution of $n_u \times n_u$ LS SP p_1: - 1 time mesh $\mathcal{M}_{p_1}$ - $2 \times n$ solutions of $n_{p_1} \times n_{p_1}$ LS SP k_1: - 1 time mesh $\mathcal{M}_{k_1}$ - $2 \times n$ solutions of $n_{k_1} \times n_{k_1}$ LS SP p_2: - 1 time mesh $\mathcal{M}_{p_2}$ - $2 \times n$ solutions of $n_{p_2} \times n_{p_2}$ LS SP k_2: - 1 time mesh $\mathcal{M}_{k_2}$ - $2 \times n$ solutions of $n_{k_2} \times n_{k_2}$ LS

5.3 Shielded induction heater

The next test problem is a shielded induction heater. It comprises a plate surrounded by two stranded inductors in which an excitation current flows. Magnetic shields ($\mu_{r,shield} = 1$ and $\sigma = 37.7\,\mathrm{MS/m}$) surround the plate and the stranded inductors (Fig. 5.14). Several frequencies are considered.

This test is performed with both $\boldsymbol{b}$- and $\boldsymbol{h}$-formulations. The problem is solved in three SPs. It is first considered via a SP u with the stranded inductors alone (Fig. 5.15, *top left*, $\boldsymbol{a}_u$), followed by a TS FE SP p (Fig. 5.15, *middle top*, $\boldsymbol{a}_p$) that does not include the inductors anymore. A correction SP k finally replaces the TS FEs with the actual volume FEs (Fig. 5.15, *top right*, $\boldsymbol{a}_k$). The projection of a

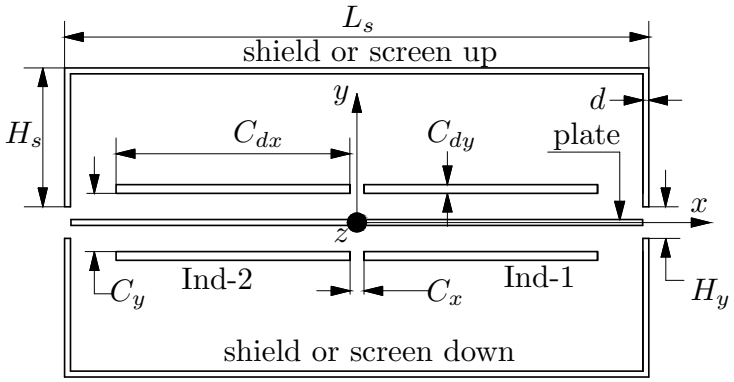

Figure 5.14: Shielded induction heater ($d = 2 \div 6\,\text{mm}$, $L_{pl} = 2\,\text{m}$, $L_s = 2\,\text{m}+2d$, $H_s = 0.4\,\text{m}$, $H_y = 0.14\,\text{m}$, $C_{dx} = 0.8\,\text{m}$, $C_{dy} = 0.01\,\text{m}$, $C_y = 0.2\,\text{m}$, $C_x = 0.05\,\text{m}$).

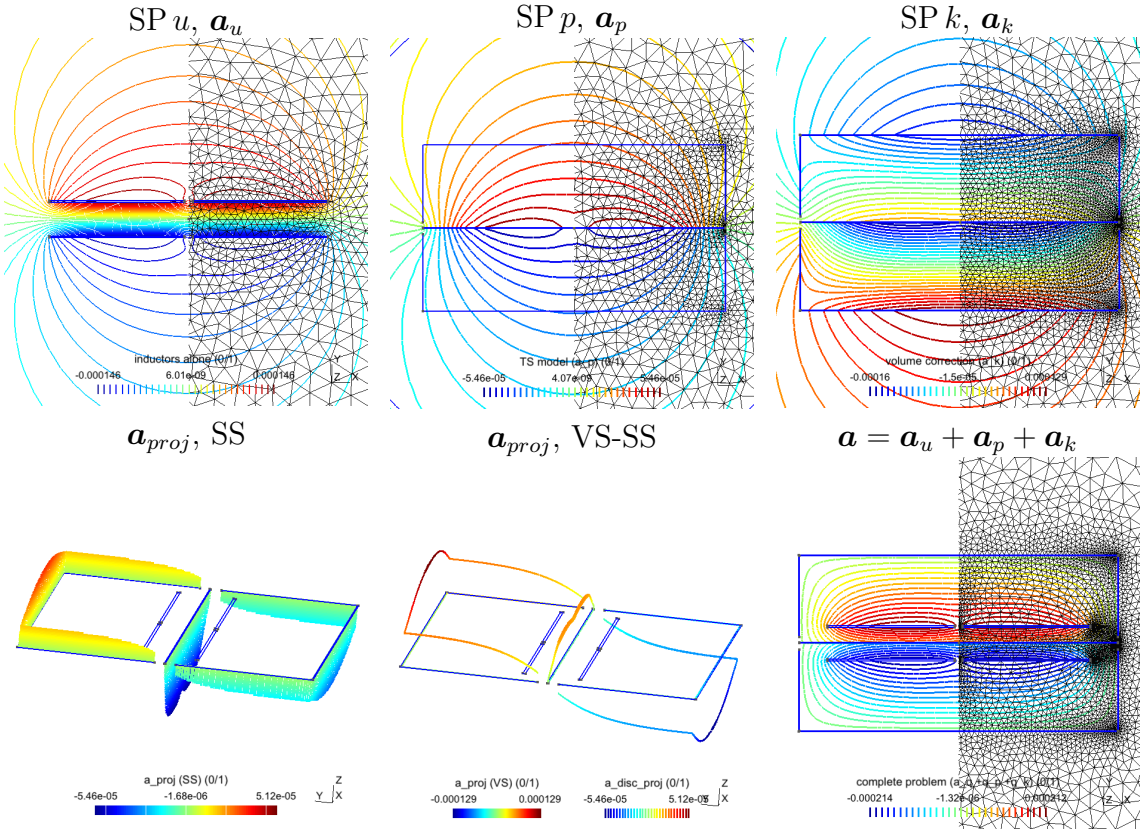

Figure 5.15: Flux lines (real part) for the SP u ($\boldsymbol{a}_u$), added TS SP p ($\boldsymbol{a}_p$), volume correction SP k ($\boldsymbol{a}_k$) and the complete solution ($\boldsymbol{a} = \boldsymbol{a}_u + \boldsymbol{a}_p + \boldsymbol{a}_k$) with the different meshes used ($d = 4\,\text{mm}$, $f = 1\,\text{kHz}$, $\mu_{r,plate} = 100$ and $\sigma_{plate} = 1\,\text{MS/m}$). Projection of SP u solution ($\boldsymbol{a}_{proj}$, SS) in the SP p, and of SP p solution ($\boldsymbol{a}_{proj}$, VS-SS) in SP k.

solution, from SP u to SP p, is expressed via the SS (Fig 5.15, *bottom left*, $\boldsymbol{a}_{proj}$, SS). The projection of the solution, from SP p to SP k, is expressed through the VS and SS (Fig 5.15, *bottom middle*, $\boldsymbol{a}_{proj}$, VS-SS). The superposition of the solutions of SP u, SP p and SP k is compared with the reference solution (Fig 5.15, *bottom*

right, $\boldsymbol{a} = \boldsymbol{a}_u + \boldsymbol{a}_p + \boldsymbol{a}_k$). The relative error on the magnetic flux density error is shown in Fig. 5.16 for different plate parameters. The error can reach 90% in the end regions of the plate, with $\delta = 1.12\,\text{mm}$ and $d = 4\,\text{mm}$, and 85% with $\delta = 1.59\,\text{mm}$ and $d = 2\,\text{mm}$.

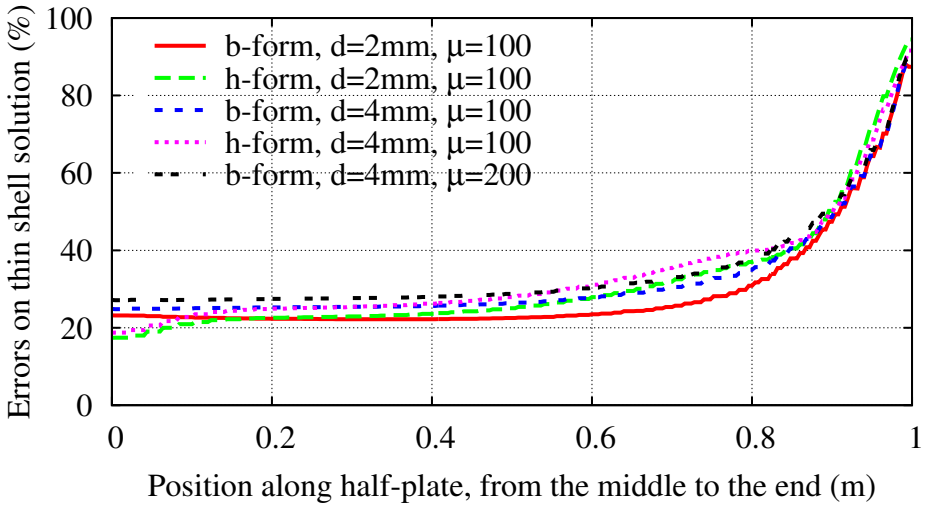

Figure 5.16: TS error on the magnetic flux density along the plate, with effects of d, μ ($\sigma_{plate} = 1\,\text{MS/m}$, $f = 1\,\text{kHz}$).

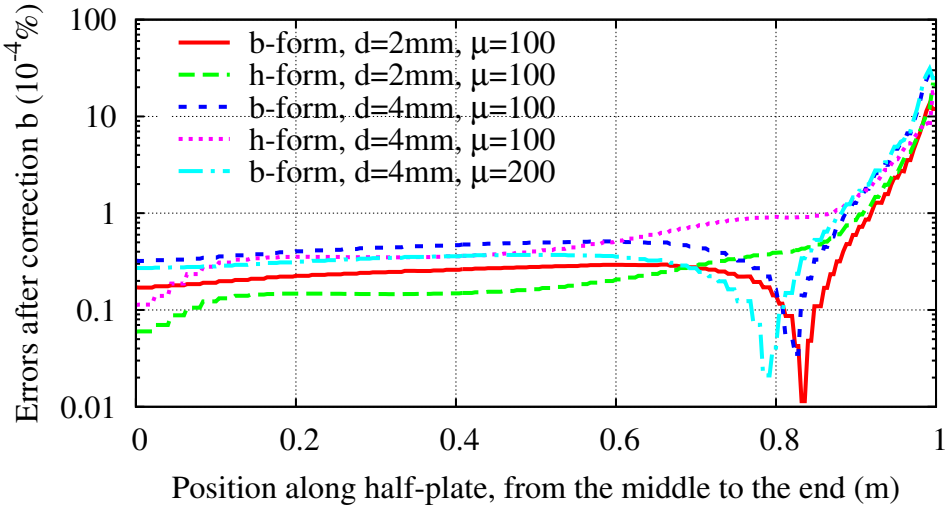

Figure 5.17: Comparison of the corrected solution with the classical FE volume models, with effects of d and μ ($\sigma_{plate} = 1\,\text{MS/m}$, $f = 1\,\text{kHz}$).

Accurate local corrections with SP k are checked to be close to the reference or complete volume FE solution (Fig. 5.17). The errors are less than 0.01% for both $\boldsymbol{b}$- and $\boldsymbol{h}$-formulations. Relative corrections of the TS longitudinal magnetic flux and eddy current density are respectively shown in Figures 5.18 and 5.19 for different plate thicknesses and frequencies. They can reach several tens of percents in the shells, up to 60% near the screen or shield ends (Figs. 5.18 and 5.19), with skin

depth $\delta = 0.92\,\text{mm}$ and $f = 3$ kHz, or 40% (Fig. 5.19), with $\delta = 1.5\,\text{mm}$ and $f = 1$ kHz. They reduce to 30% (Fig. 5.18), or 50% (Fig. 5.19), with $\delta = 2.59\,\text{mm}$, $d = 4\,\text{mm}$ and $f = 1$ kHz in both cases. Significant errors on the total Joule losses in

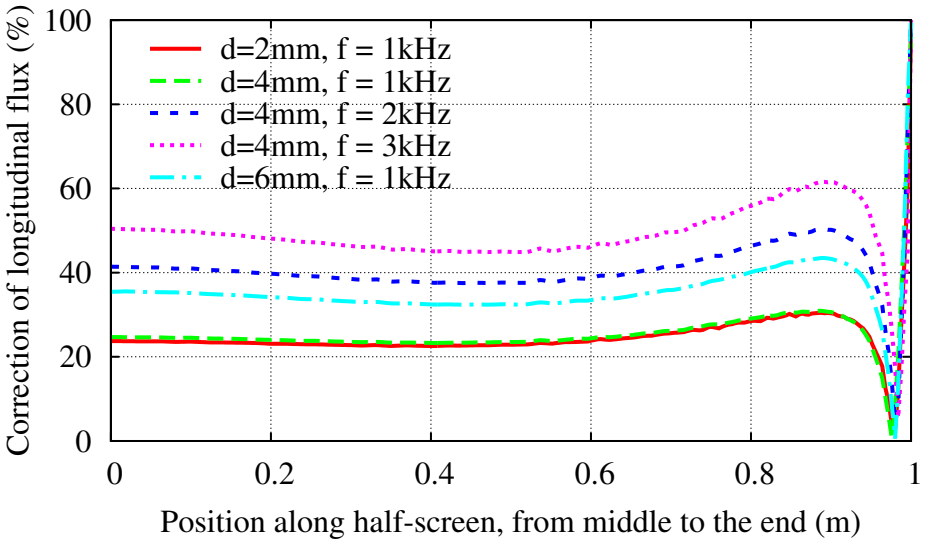

Figure 5.18: Relative correction of the longitudinal magnetic flux density along the screen for different effects of d and f ($\mu = 100$, $\sigma_{plate} = 1\,\text{MS/m}$), with $\boldsymbol{b}$-formulation.

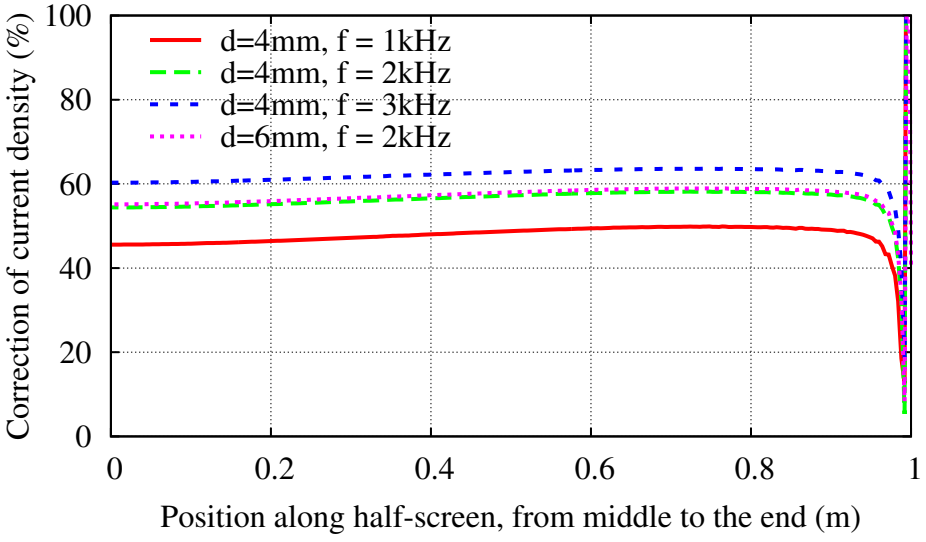

Figure 5.19: Relative correction of the eddy current density along the screen for different effects of d and f ($\mu = 100$, $\sigma_{plate} = 1\,\text{MS/m}$), with $\boldsymbol{b}$-formulation.

two shields for TS SP p are pointed by the importance of the correction SP k and are shown in Table 5.2. The inaccuracies on the TS increase with both the thickness of the plate and the frequency. Namely, with $d = 2\,\text{mm}$ and $f = 1$ kHz, the TS errors are 2.80% and 2.32% for $\boldsymbol{b}$- and $\boldsymbol{h}$-formulations, respectively. With $d = 6\,\text{mm}$ and $f = 1$ kHz, the TS errors are 47.6% and 45.0% for $\boldsymbol{b}$- and $\boldsymbol{h}$-formulations, respectively.

Table 5.2: Joule losses in two shields ($\mu_{r,shield} = 1$, $\sigma_{shield} = 37.7\,\mathrm{MS/m}$, $\mu_{r,plate} = 100$, $\sigma_{plate} = 1\,\mathrm{MS/m}$).

Thickness d (mm)	Frequency f (Hz)	***b***-formulation			***h***-formulation		
		Thin Shell P_{thin} (W)	Volume P_{vol} (W)	Error (%)	Thin Shell P_{thin} (W)	Volume P_{vol} (W)	Error (%)
2	1000	5.56	5.72	2.79	5.62	5.76	2.47
4	1000	3.40	4.60	26.00	3.47	4.60	24.5
6	1000	2.32	4.43	47.60	2.45	4.45	45.0
2	2000	5.14	5.69	9.66	5.25	5.70	8.77
4	2000	2.68	4.93	45.6	2.85	4.94	42.3
6	2000	2.31	4.85	52.32	2.40	4.92	51.25

Significant errors on TS increase with higher frequency, i.e., 52.32% (***b***-formulation) and 51.25% (***h***-formulation), with $d = 6\,\mathrm{mm}$ and $f = 2$ kHz.

5.4 TEAM workshop problem 21

The test problem herein is based on the international TEAM problem 21 (model B). It comprises two stranded inductors and a thin plate (Fig 5.20).

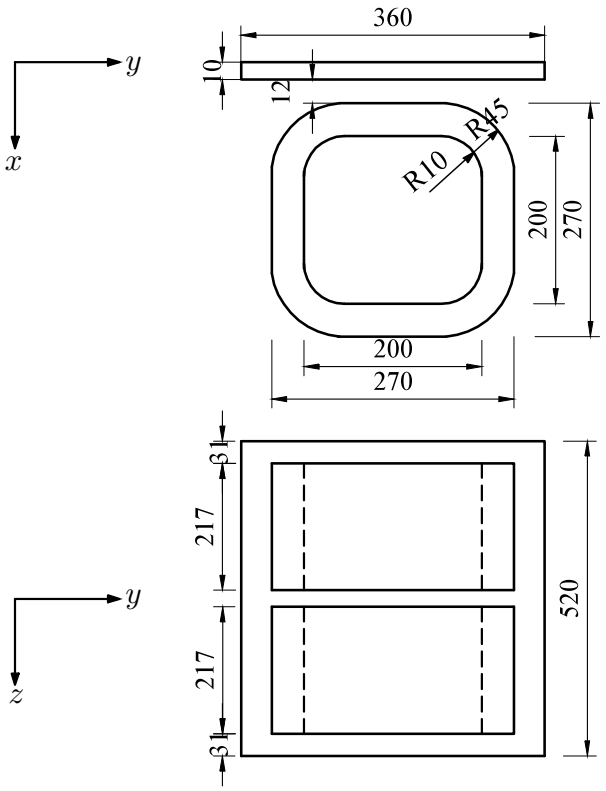

Figure 5.20: TEAM problem 21 (model B), with two stranded inductors and a thin plate. All dimensions are in mm.

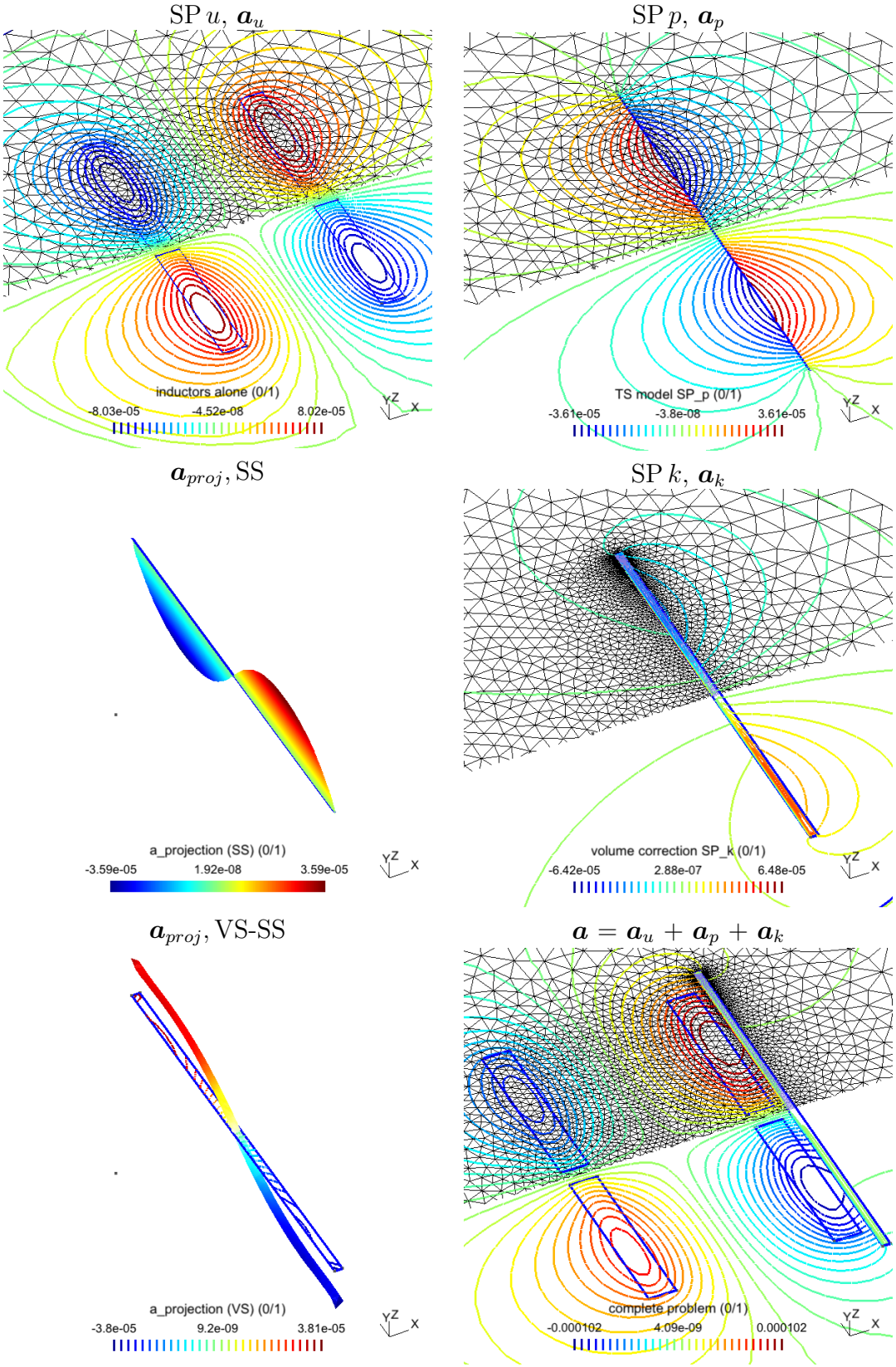

Figure 5.21: Flux lines (real part) for SP u ($\boldsymbol{a}_u$), added TS SP p ($\boldsymbol{a}_p$), volume correction SP k ($\boldsymbol{a}_k$) and the complete solution ($\boldsymbol{a} = \boldsymbol{a}_u + \boldsymbol{a}_p + \boldsymbol{a}_k$), with the different meshes used ($d = 10\,\text{mm}$, $f = 50\,\text{Hz}$, $\mu_r = 200$ and $\sigma = 6.484\,\text{MS/m}$). The imaginary presents an analogous behavior.

The magnetodynamic SP scheme is solved in both 2-D and 3-D cases. The first test of the a 2-D model considers three SPs. Flux lines for magnetodynamics in each SP are shown in Figure 5.21. As the previous tests, we have: a first SP u considered on a simplified mesh with the stranded inductors alone (Fig. 5.21, *top left*, $\boldsymbol{a}_u$); a TS SP p inserted with its own mesh (Fig. 5.21, *top right*, $\boldsymbol{a}_p$); a volume correction SP k with an adequate mesh (Fig. 5.21, *middle right*, $\boldsymbol{a}_k$); SS for SP p (Fig. 5.21, *middle left*, $\boldsymbol{a}_{proj}$, SS) and VS for SP k (Fig. 5.21, *bottom left*, $\boldsymbol{a}_{proj}$, VS); a complete problem (Fig. 5.21, *bottom right*, $\boldsymbol{a} = \boldsymbol{a}_u + \boldsymbol{a}_p + \boldsymbol{a}_k$). The errors on

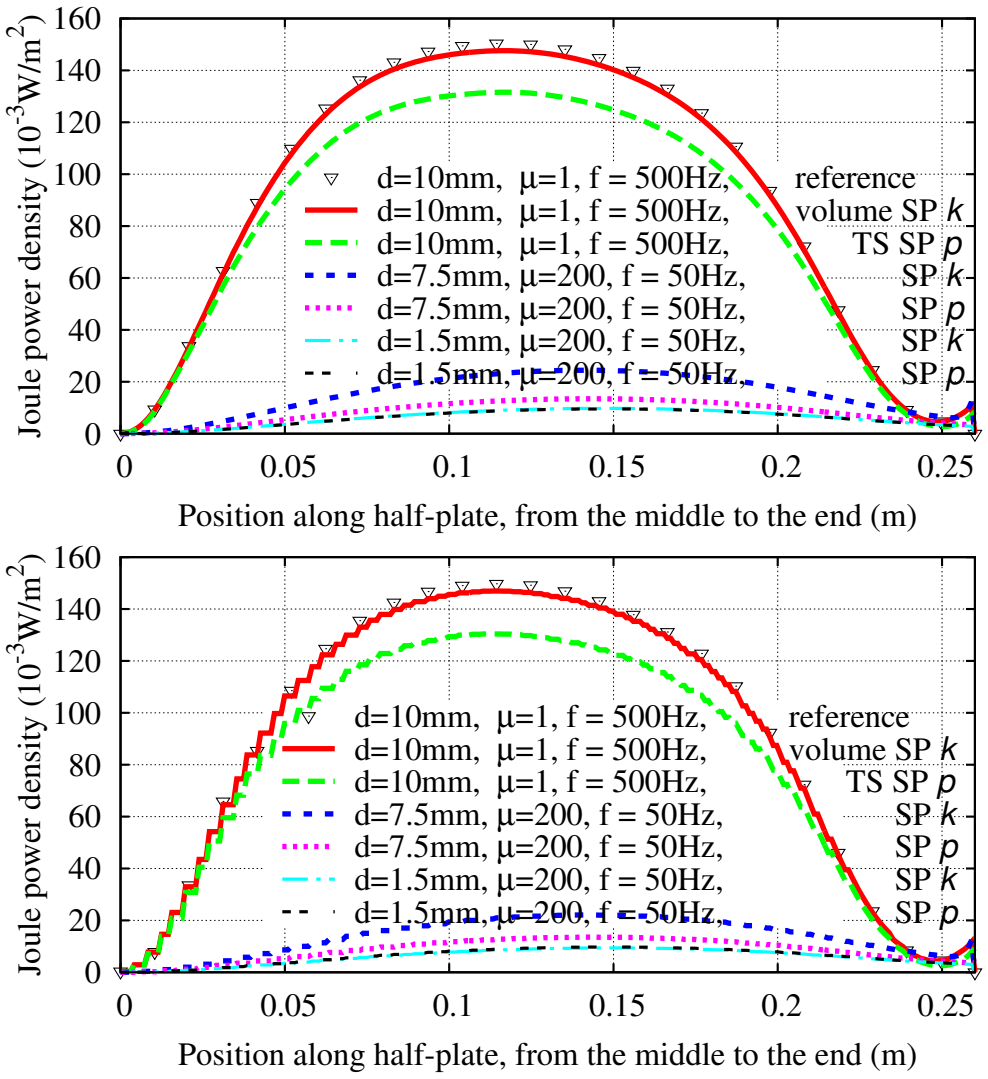

Figure 5.22: Power loss density with TS and VS correction along the plate for $\boldsymbol{b}$-formulation (*top*) and $\boldsymbol{h}$-formulation (*bottom*), with effects of d, μ and f for 2-D model ($\sigma = 6.484\,\mathrm{MS/m}$).

the power loss density of TS SP p along the plate are pointed out by the correction SP k, checked to be close to the reference or complete volume FE solution (Fig. 5.22) for different parameters. They reach 40% for both $\boldsymbol{b}$- formulation (Fig. 5.22, *top*) and $\boldsymbol{h}$- formulation (Fig. 5.22, *bottom*) ($\delta = 1.977\,\mathrm{mm}$, $d = 7.5\,\mathrm{mm}$, $f = 50\,\mathrm{Hz}$,

$\mu = 200$, $\sigma = 6.484\,\mathrm{MS/m}$). Significant error decreases with a thinner thickness, being lower than 5% ($d = 1.5\mathrm{mm}$) in both formulations. The second test of the 2-D model is now considered with two SPs. The relative corrections of the longitudinal

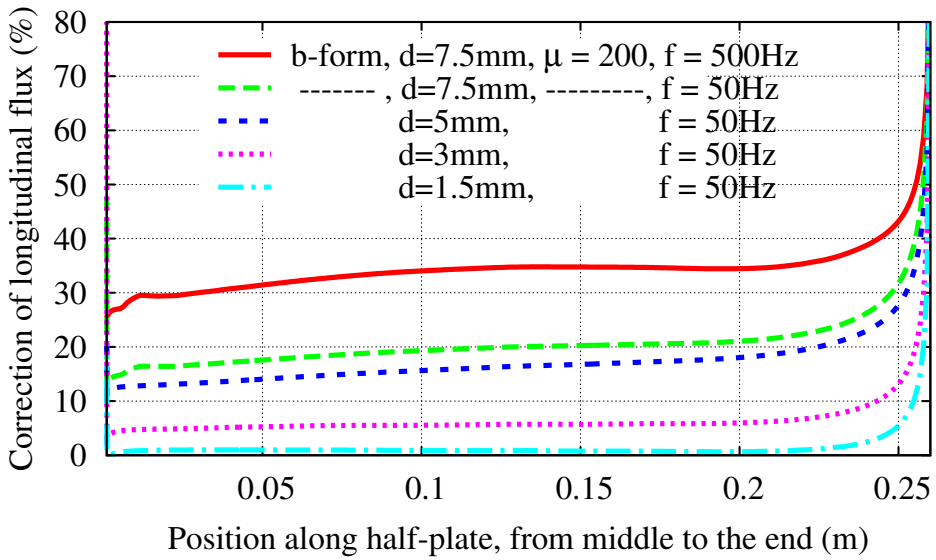

Figure 5.23: Relative correction of the longitudinal magnetic flux along the plate, with effects of d, μ and f for 2-D model ($\sigma = 6.484\,\mathrm{MS/m}$).

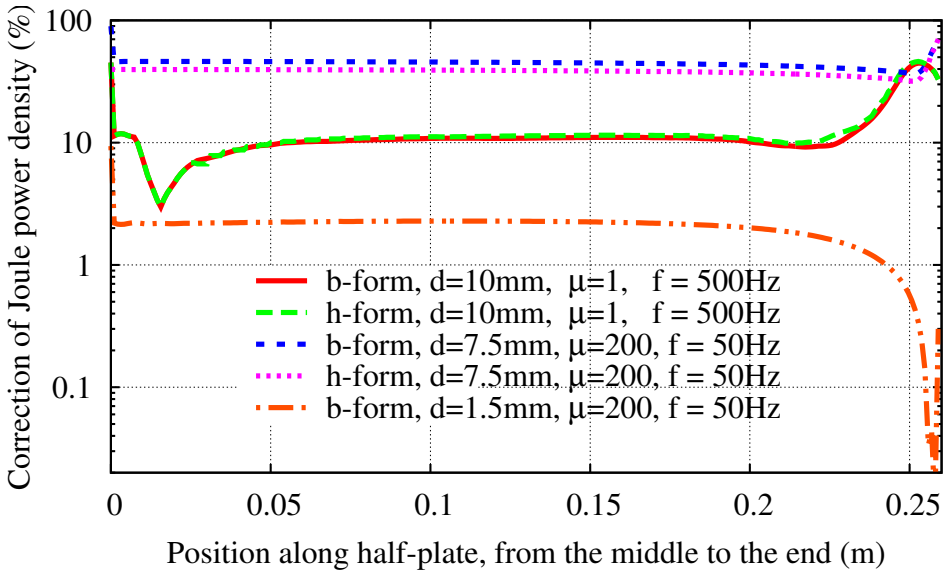

Figure 5.24: Relative correction of the Joule power density along the plate, with effects of d, μ and f for 2-D model ($\sigma = 6.484\,\mathrm{MS/m}$).

magnetic flux and the power loss density along the plate are shown in Figs. 5.23 and 5.24, respectively, which are then perfectly corrected by the correction SP k. The corrections on the magnetic flux and the Joule power loss density depend on several parameters. They can reach several tens of percents in the TS, such as

75% (Fig. 5.23) and 70% (Fig. 5.24) near the plate ends, with $\delta = 1.977\,\text{mm}$, $d = 7.5\,\text{mm}$, $f = 50\,\text{Hz}$, $\mu_r = 200$ and $\sigma = 6.484\,\text{MS/m}$ in both cases. For the smaller thicknesses, the errors are lower than 30% ($d = 3\,\text{mm}$) (Fig. 5.23) and 10% ($d = 1.5\,\text{mm}$) (Figs. 5.23 and 5.24). For the case of non-magnetic material, the inaccuracy on TS SP p is also up to 50% (Fig. 5.24), with $\delta = 8.84\,\text{mm}$, $d = 10\,\text{mm}$, $f = 500\,\text{Hz}$, $\mu = 1$ and $\sigma = 6.484\,\text{MS/m}$, and reduced to be lower 5%, with $\delta > d$ (no effect at all).

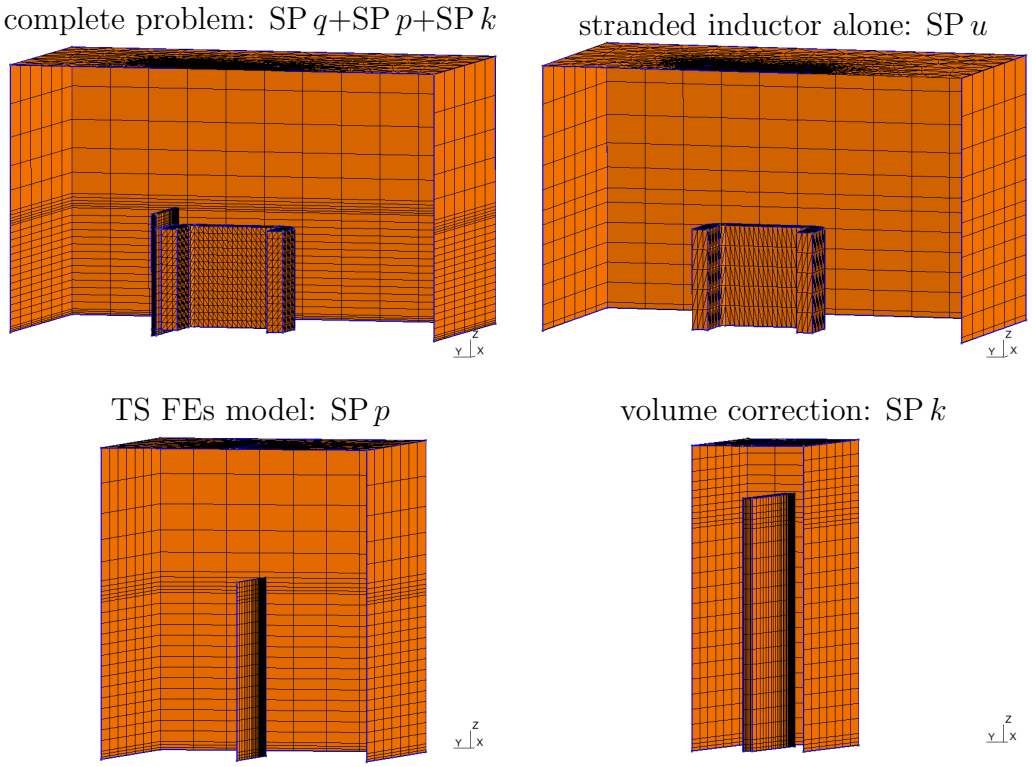

Figure 5.25: Mesh of the SPs in the SPM: mesh of complete problem (*top left)*, of inductor alone (*top right)*, of TS model (*bottom left)* and of volume correction (*bottom right)*.

Finally, a 3-D model also considers three SPs u, p and k (from Fig. 5.25 to Fig. 5.33). The details of the different meshes of each SP are decribed in Fig. 5.25. The mesh of SP k locally focuses on the plate and its neighborhood. Distributions of eddy current densities on the TS SP p generated by the stranded inductor SP u (Fig. 5.26, *top*) are shown (Fig. 5.26, *bottom left*). Then volume FEs (SP k) replace the TS FEs (SP p) with volume FEs covering the actual plate and its neighborhood with an adequate refined mesh (Fig. 5.26, *bottom right*). The error reaches 77.3% with ($d = 10\,\text{mm}$, $f = 50\,\text{Hz}$, $\mu_r = 100$, $\sigma = 6.484\,\text{MS/m}$). Significant errors on the power loss density are also depicted by SP k checked to be close to the reference or complete volume FE solution (Figs. 5.27 and 5.28). It reaches 85% (at the middle of plate) along the y-direction (Fig. 5.27), or being 68% along the z-direction (Fig. 5.28) ($\delta = 2.1\,\text{mm}$ and $d = 7.5\,\text{mm}$, $f = 50\,\text{Hz}$, $\mu = 200$, $\sigma = 6.484\,\text{MS/m}$) as well. For the case of $d = 10\,\text{mm}$, $\mu = 100$, and keeping the same f and σ, the errors also reach

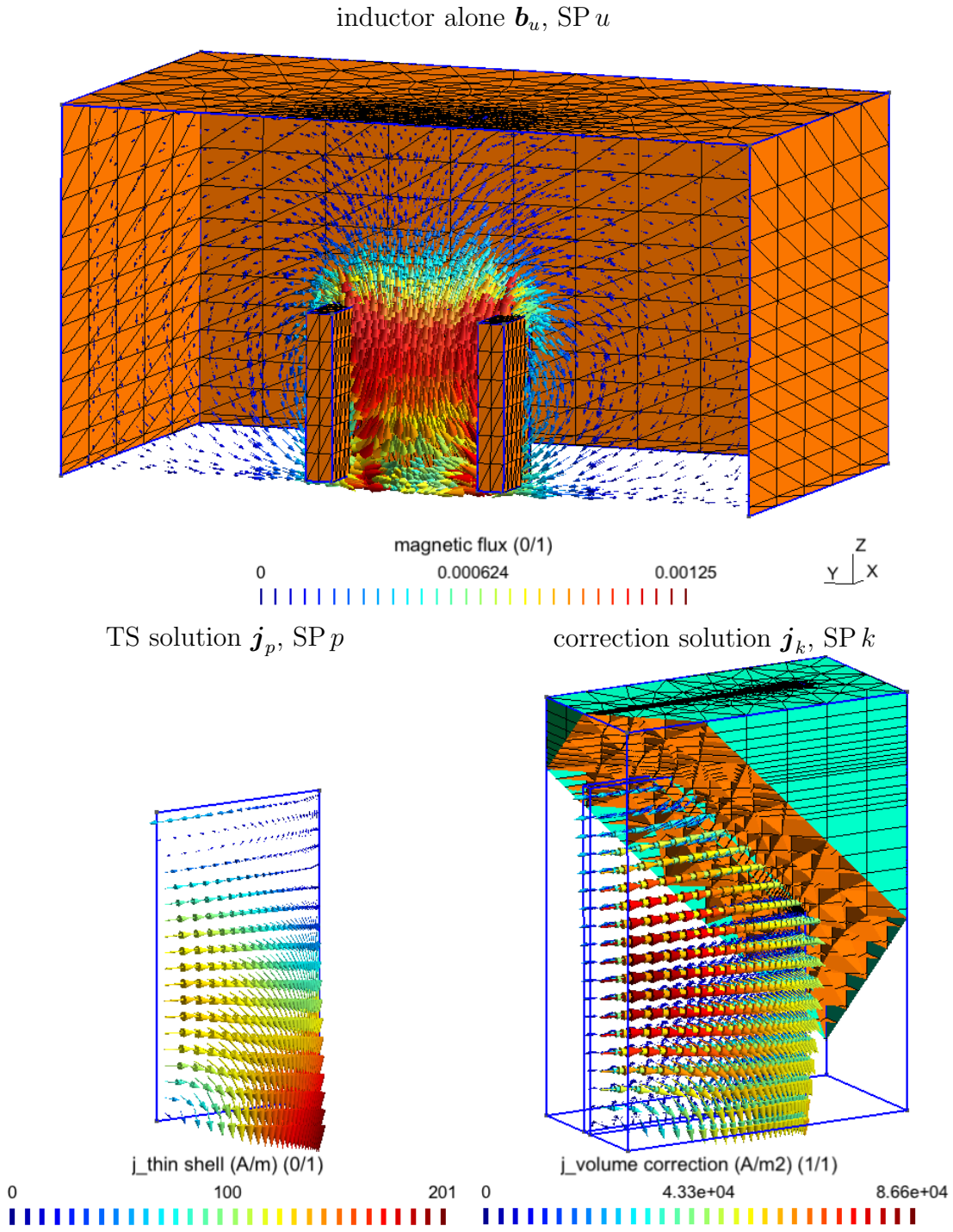

Figure 5.26: TEAM problem 21: magnetic flux density $\boldsymbol{b}_u$ (in a cut plane) generated by a stranded inductor (*top*), TS eddy current density $\boldsymbol{j}_p$ on TS model (*bottom left*) and its volume correction $\boldsymbol{j}_k$ (allowing to focus on the mesh of the plate and its neighborhood) (*bottom right*) ($d = 10\,\text{mm}$, $f = 50\,\text{Hz}$).

80% along the horizontal half inner width (y-direction) (Fig. 5.29), or 75% along the z-direction (Fig. 5.30), with $\delta = 2.975\,\text{mm}$ in both cases. The errors particularly

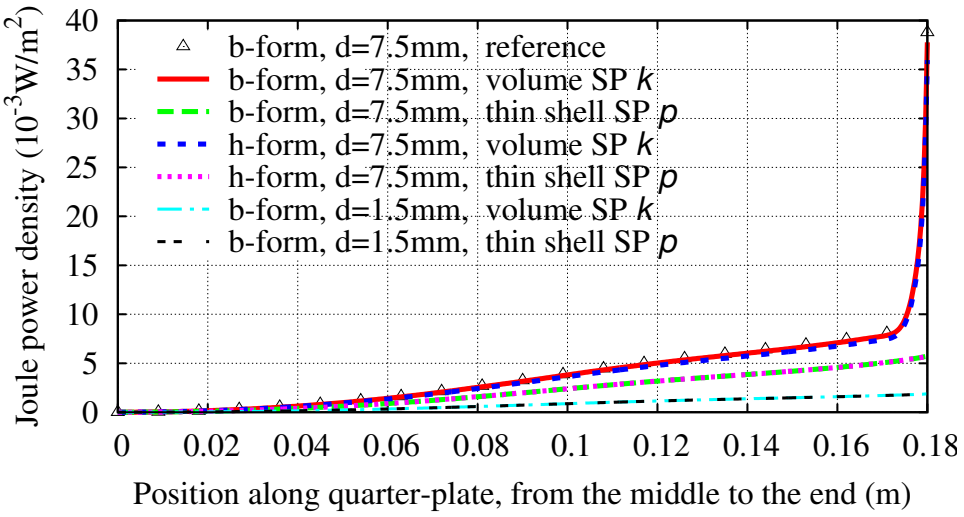

Figure 5.27: Power loss density with TS and VS solutions along horizontal half inner width (y-direction), with effects of different thicknesses d, for 3-D model ($f = 50\,\text{Hz}$, $\mu = 200$, $\sigma = 6.484\,\text{MS/m}$).

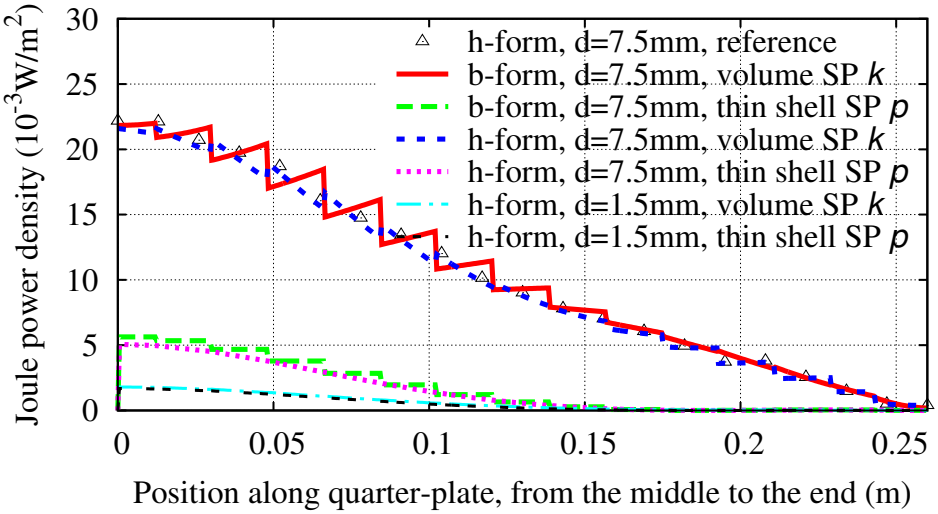

Figure 5.28: Power loss density with TS and VS solutions along vertical half edge (z-direction), with effects of different thicknesses d, for 3-D model ($f = 50\,\text{Hz}$, $\mu = 200$, $\sigma = 6.484\,\text{MS/m}$).

decrease with a smaller thickness ($d = 1.5\,\text{mm}$ and $d = 2\,\text{mm}$), being lower than 20% from Fig. 5.27 to Fig. 5.30.

For the non-magnetic material, the error on TS SP p is 37.5% ($\delta = 4.1\,\text{mm}$), or lower than 5% ($\delta = 9.2\,\text{mm}$), with $d = 10\,\text{mm}$ in both cases (Fig. 5.31). The relative error on the power loss density is also diminished with SP k for several parameters (Fig. 5.32), up to 70% ($\delta = 4.1\,\text{mm}$, $d = 10\,\text{mm}$), or 85% ($\delta = 3.5\,\text{mm}$, $d = 7.5\,\text{mm}$), and lower than 5%, with $\delta = 3.5\,\text{mm}$ and $d = 1.5\,\text{mm}$ in the end regions of the plate. Some TS inaccuracies are illustrated in Figure 5.33, showing local errors near the plate ends, that increase with the plate thickness.

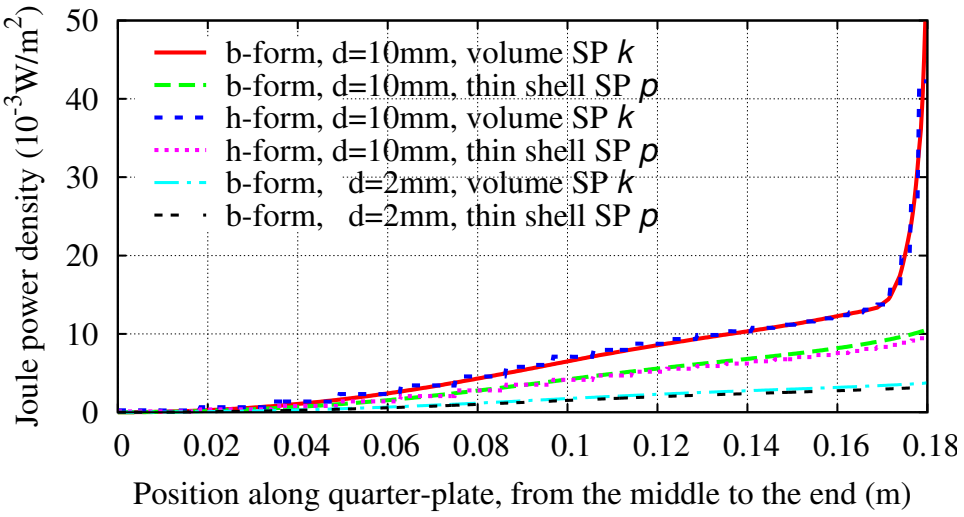

Figure 5.29: Power loss density with TS and VS solutions along horizontal half inner width (x-direction), with effects of different thicknesses d, for 3-D model ($f = 50\,\text{Hz}$, $\mu = 100$, $\sigma = 6.484\,\text{MS/m}$).

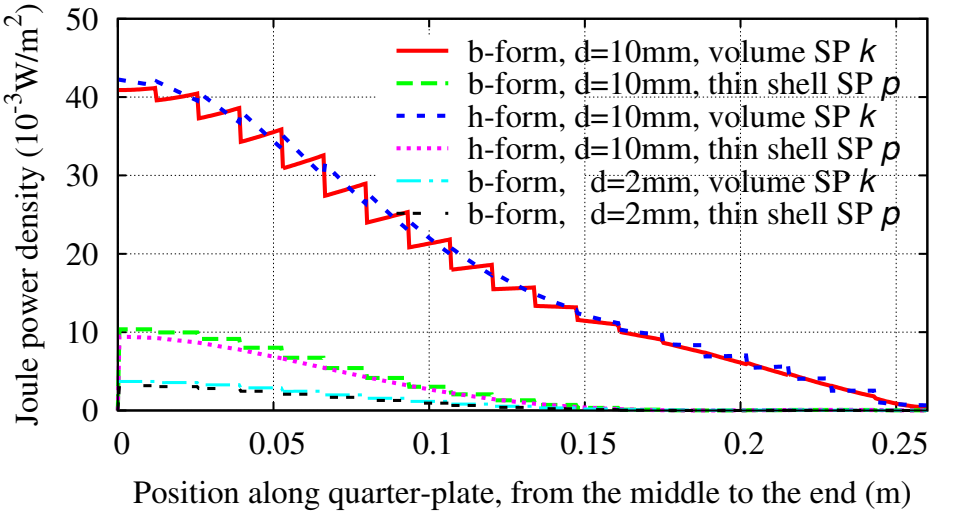

Figure 5.30: Power loss density with TS and VS solutions along vertical half edge (z-direction), with effects of different thicknesses d, for 3-D model ($f = 50\,\text{Hz}$, $\mu = 100$, $\sigma = 6.484\,\text{MS/m}$).

In particular, values of the Joule losses in the plate with an approximate BC for volume correction SP k are shown in Tables 5.3, 5.4 and 5.5. The exterior boundary (i.e. D_{bound}) of SP k is first chosen at a distance $D_{bound} = 200d$ from the thin region, with thickness of the plate $d = 10\,\text{mm}$. The inaccuracies on Joule losses for TS SP p reach 58.9%, or 1.2% for accurate volume SP k, with $f = 50\,\text{Hz}$, $\mu = 100$ and $\sigma = 6.484\,\text{MS/m}$ in both cases (Table 5.3). The proposed SP strategy allows to use an adequate mesh of the volume plate and its neighborhood in SP k. It is shown that even if D_{bound} is reduced to $2d$ (Fig. 5.25, *bottom left*), the error on SP k is 1.53%, which is still very accurate (Table 5.3). For the non-magnetic material,

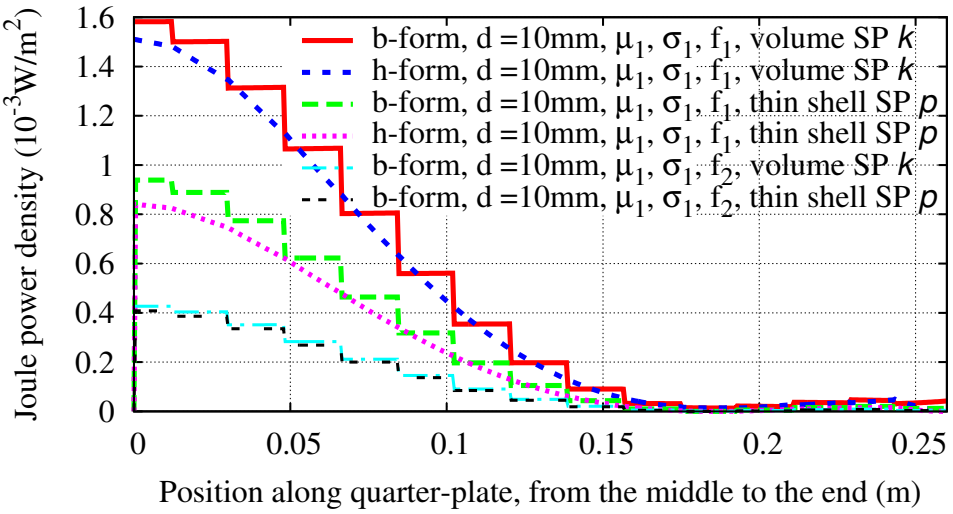

Figure 5.31: Power loss density with TS and VS solutions along vertical half edge (z-direction), with effects of different thicknesses d, for 3-D model ($f_1 = 250\,\text{Hz}$, $f_2 = 50\,\text{Hz}$, $\mu_1 = 1$, $\mu_2 = 200$, $\sigma_1 = 59\,\text{MS/m}$, $\sigma_2 = 6.484\,\text{MS/m}$).

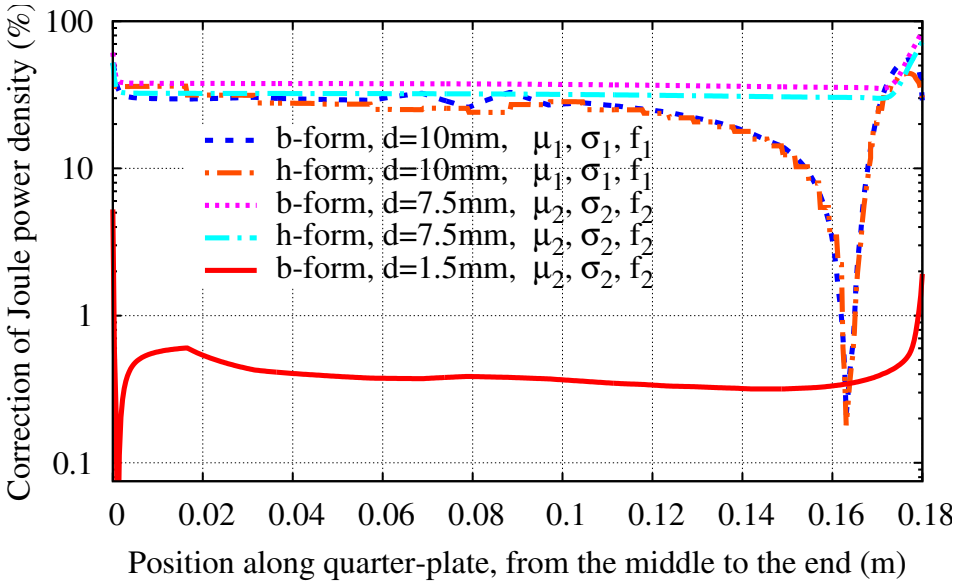

Figure 5.32: Relative correction of the power loss density along the plate (y-direction), with effects of different thicknesses d, for 3-D model ($f_1 = 250\,\text{Hz}$, $f_2 = 50\,\text{Hz}$, $\mu_1 = 1$, $\mu_2 = 200$, $\sigma_1 = 59\,\text{MS/m}$, $\sigma_2 = 6.484\,\text{MS/m}$).

the inaccuracies on SP p and accuracies on SP k are also pointed out in Table 5.4. Significant errors on Joule losses for SP p are reduced to 1.77%, or 0.05% for SP k, with $d = 1\,\text{mm}$, $f = 50\,\text{Hz}$, $\mu = 100$ and $\sigma = 6.484\,\text{MS/m}$ in both cases (Table 5.5).

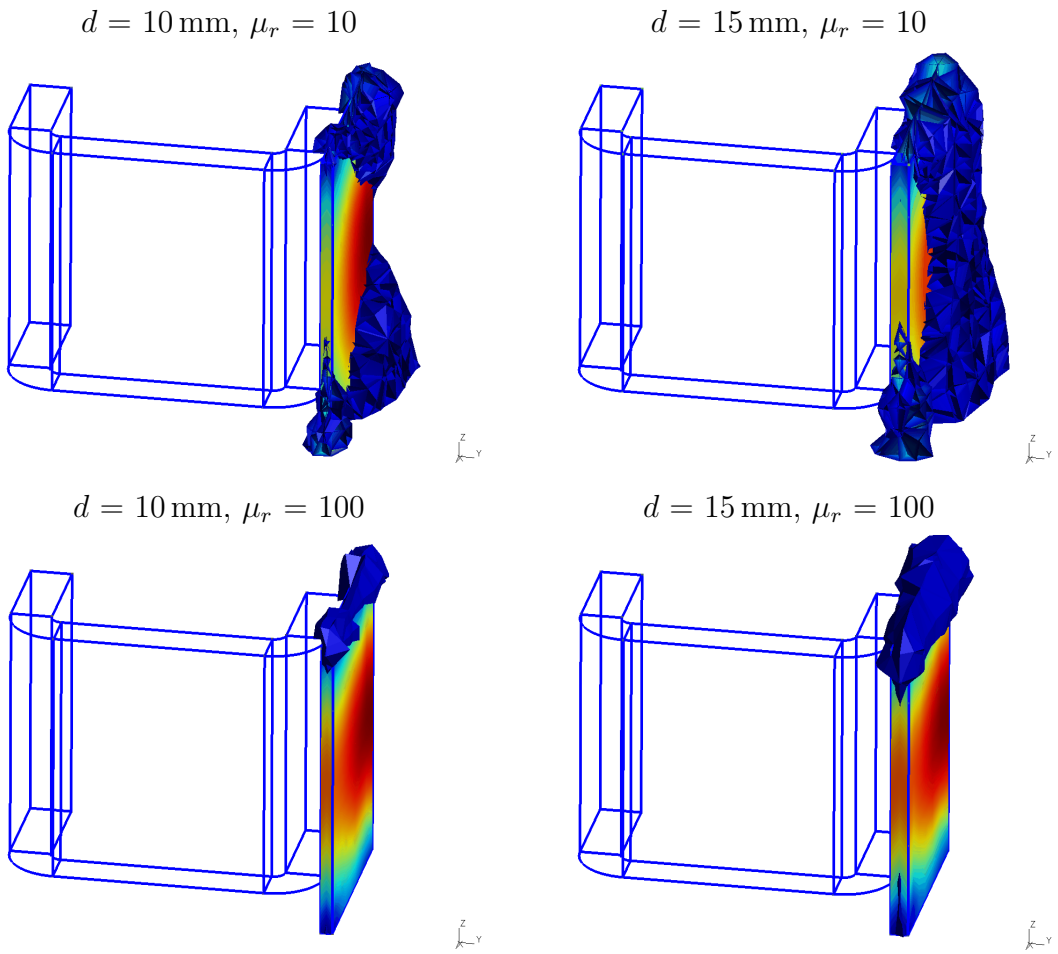

Figure 5.33: Highlighted regions (1/4th of the geometry, magnetostatics) with a relative correction higher than 1% (in the plate and their neighboring).

Table 5.3: Joule losses in the plate with approximate BCs (thickness of the plate $d = 10\,\text{mm}$, $f = 50\,\text{Hz}$, $\mu = 100$, $\sigma = 6.484\,\text{MS/m}$, skindepth $\delta = 2.975\,\text{mm}$).

Boundary of volume SP k (D_{bound})	Joule losses			Errors %	
	Thin shell P_{thin} (W)	Volume P_{vol} (W)	Reference P_{ref} (W)	Between P_{thin} and P_{ref}	Between P_{vol} and P_{ref}
$200d$	0.0196	0.0477	0.0483	58.9	1.2
$100d$	0.0196	0.0476	0.0483	58.8	1.35
...	...	...	...	...	...
$20d$	0.0196	0.0476	0.0483	58.8	1.35
...	...	...	...	...	...
$10d$	0.0196	0.0476	0.0483	58.8	1.35
reduce to $2d$	0.0196	0.0475	0.0483	58.7	1.53

Table 5.4: Joule losses in the plate with approximate BCs (thickness of the plate $d = 10\,\text{mm}$, $f = 500\,\text{Hz}$, $\mu = 1$, $\sigma = 6.484\,\text{MS/m}$, skindepth $\delta = 8.8\,\text{mm}$).

Boundary of volume SP k (D_{bound})	Joule losses			Errors %	
	Thin shell P_{thin} (W)	Volume P_{vol} (W)	Reference P_{ref} (W)	Between P_{thin} and P_{ref}	Between P_{vol} and P_{ref}
$200d$	0.168	0.226	0.224	25.7	0.58
$100d$	0.168	0.226	0.224	25.7	0.58
...	...	...	...	...	...
$20d$	0.168	0.226	0.224	27.7	0.58
...	...	...	...	...	...
$10d$	0.168	0.227	0.224	26.0	1.20
reduce to $2d$	0.168	0.228	0.224	26.3	1.65

Table 5.5: Joule losses in the plate with approximate BCs (thickness of the plate $d = 1\,\text{mm}$, $f = 50\,\text{Hz}$, $\mu = 100$, $\sigma = 6.484\,\text{MS/m}$, skindepth $\delta = 2.975\,\text{mm}$).

Boundary of volume SP k (D_{bound})	Joule losses			Errors %	
	Thin shell P_{thin} (W)	Volume P_{vol} (W)	Reference P_{ref} (W)	Between P_{thin} and P_{ref}	Between P_{vol} and P_{ref}
$200d$	0.0113	0.0115	0.0115	1.74	0.00
$100d$	0.0113	0.0115	0.0115	1.74	0.00
...	...	...	...	...	...
$20d$	0.0113	0.0115	0.0115	1.74	0.00
...	...	...	...	...	...
$10d$	0.0113	0.011504	0.0115	1.77	0.03
reduce to $2d$	0.0113	0.011506	0.0115	1.77	0.05

5.5 Bushing mounting plate

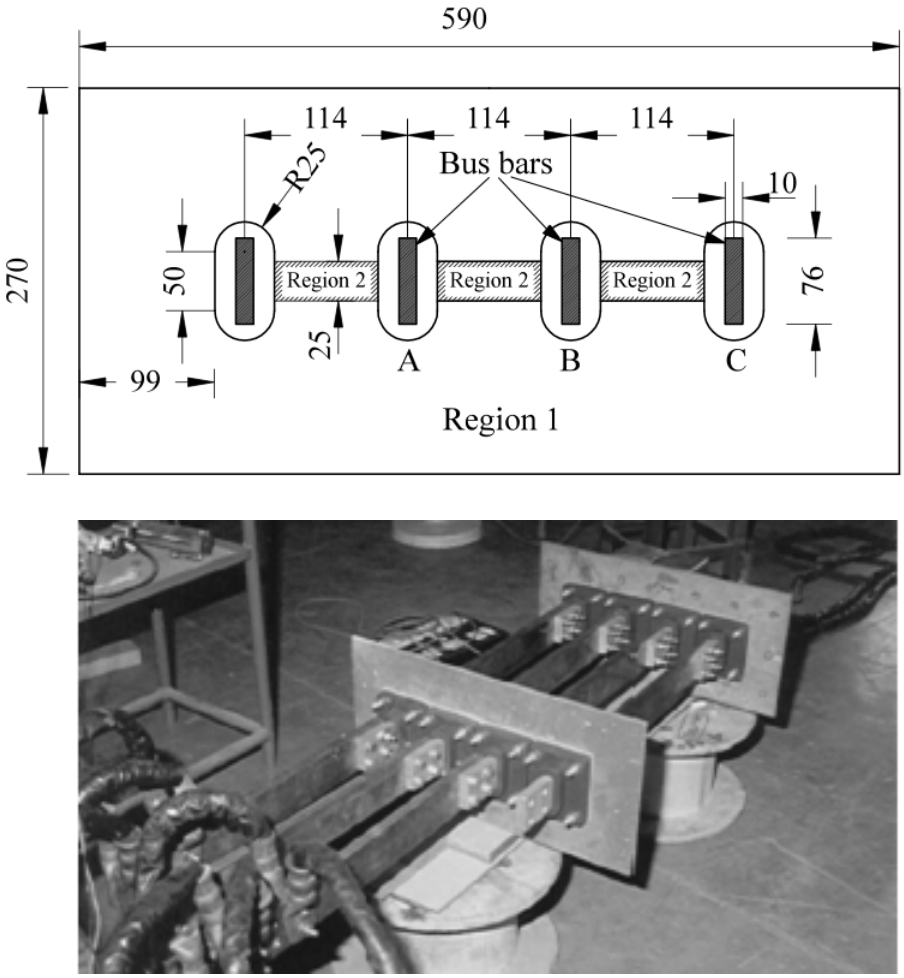

Figure 5.34: The geometrical details of the bushing mounting plate (*top*) and the experimental set-up (*bottom*) (all dimensions are in mm).

The following test problem is a bushing mounting plate problem of a transformer with ratings from 500 kVA upto 2 MVA. The geometrical details of the bushing mounting plate are shown in Fig. 5.34 (*top*) and the experimental set-up proposed by the authors in [90] is depicted in Fig. 5.34 (*bottom*). The three bus bars carry adjustable balanced three-phase currents up to $I_a = I_{max}\ \sin(\omega t{+}0)$, $I_b = I_{max}\ \sin(\omega t{-}2\pi/3)$ and $I_c = I_{max}\ \sin(\omega t{+}2\pi/3)$. The distance between phases is 114 mm and the plate dimensions are 270x590x6 mm (Fig. 5.34, *top*). The bushing mounting plate is made of two different regions and properties (magnetic and non-magnetic). The conductivities for the regions 1 and 2 are taken as $\sigma_1 = 4.07$ MS/m and $\sigma_2 = 1.15$ MS/m respectively and the relative permeabilities for the regions 1 and 2 are taken as $\mu_{r,1} = 300$ and $\mu_{r,2} = 1$, respectively.

The three-dimensional mesh of the bushing mounting plate is described in Fig. 5.35, with line terminations of the three phases. The non-magnetic material inserted in region 2 (25 mm wide) can also be clearly seen in both Figs. 5.34

and 5.35. As the previous tests, an SP scheme also considers the three SPs. The first test is discussed with the same properties or materials ($\sigma_1 = \sigma_2 = 4.07\,\mathrm{MS/m}$, $\mu_1 = \mu_2 = 300$). Field $\boldsymbol{b}$ calculated in a simplified mesh in SP u (with the bus bars considered as stranded inductors) is shown in Fig. 5.36 (*top*). A TS FE SP p (showing the distribution of eddy current density $\boldsymbol{j}_p$ on the surface) is then added (Fig. 5.36, *middle*). Next, a SP k replaces the TS FEs with volume FEs covering the actual mounting plate and its neighborhood with an adequate refined mesh (Fig. 5.36, *bottom*). By integrating the value of $\boldsymbol{j}_k$ (Fig. 5.36, *bottom*) along the thickness of the mounting plate and comparing the result to the TS solution $\boldsymbol{j}_p$, it is obtained. Thus, the TS error on $\boldsymbol{j}_p$ can locally reach 47% (Fig. 5.36, *middle*) ($d = 6\,\mathrm{mm}$, $f = 50\,\mathrm{Hz}$, $\delta = 2\,\mathrm{mm}$). Significant errors on the Joule power loss density of TS SP p along the mounting plate border and through the plate hole are indicated by the usefulness of the correction SP k (Figs. 5.37, 5.38 and 5.39). It can reach 33%, with $d = 6\,\mathrm{mm}$, $f = 50\,\mathrm{Hz}$ and $\delta = 2\,\mathrm{mm}$, with two different materials (Figs. 5.38 and 5.39). Accurate local corrections on the total Joule losses with volume correction SP k are verified to be very close to the reference or complete volme FE solution for both cases (i.e. massive and stranded inductors) (Tables 5.6 and 5.7).

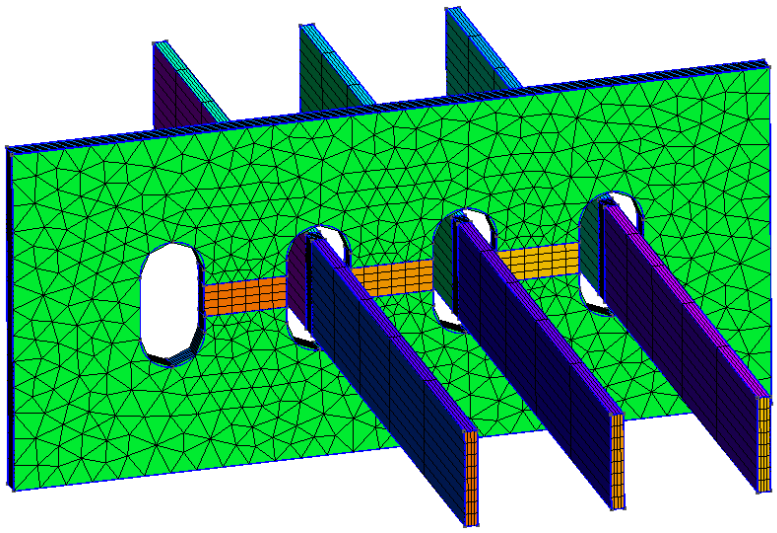

Figure 5.35: The 3-D mesh model of the brushing mounting plate.

Table 5.6: Stranded inductors. Joule losses in the bushing mounting plate using the same materials. ($\sigma_1 = \sigma_2 = 4.07\,\mathrm{MS/m}$, $\mu_1 = \mu_2 = 300$).

Current I (kA)	Frequency f (Hz)	Stranded inductors		
		Thin shell P_{thin} (W)	Volume correction P_{vol} (W)	Reference P_{ref} (W)
2000	50	471	518.3	523.2
2250	50	598.1	655.9	662.4
2500	50	737.2	809.1	817.8
2800	50	927	1015.1	1026.3

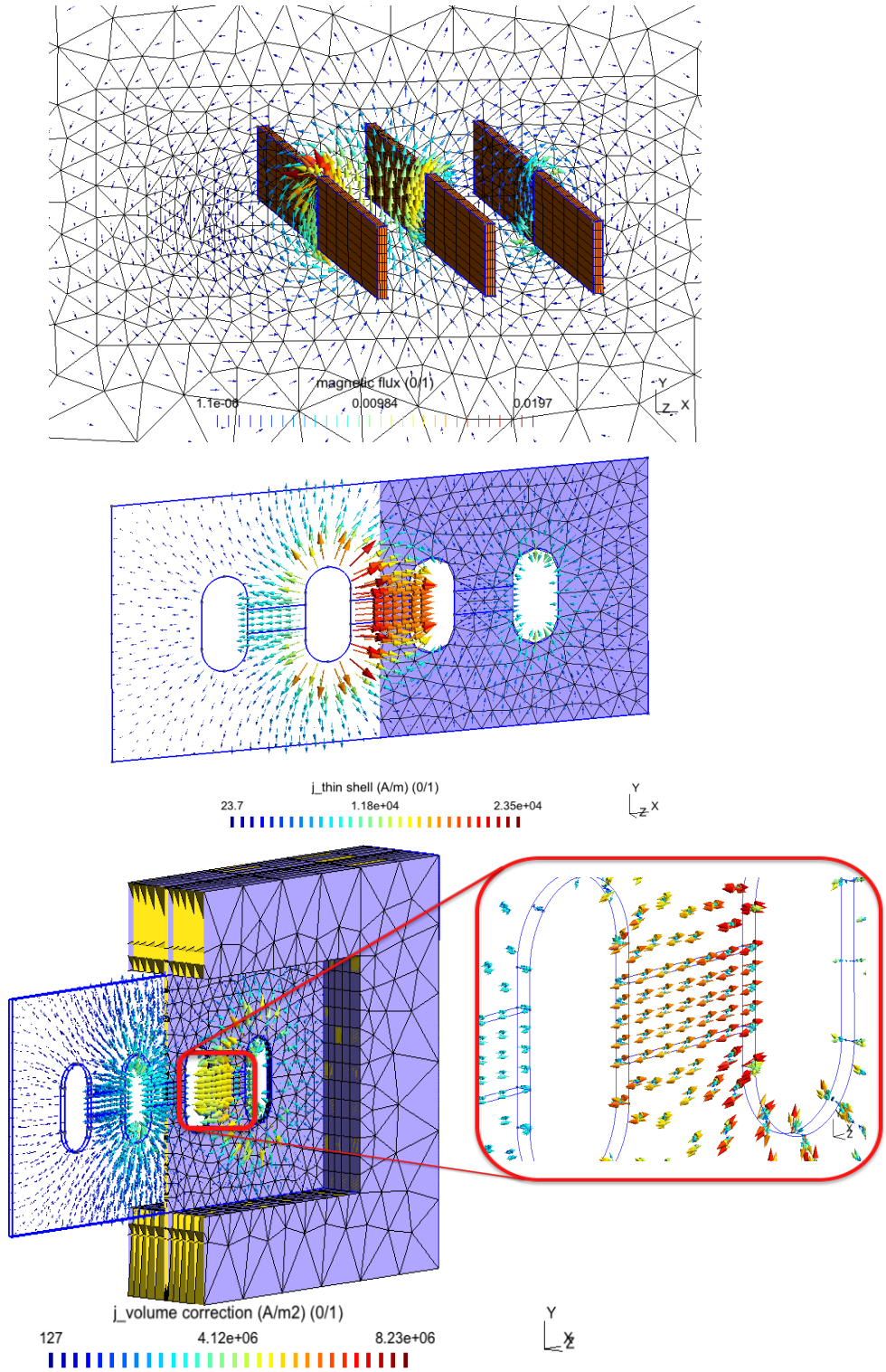

Figure 5.36: Magnetic flux density $\boldsymbol{b}_u$ (in a cut plane) generated by massive inductors (*top*), TS eddy current density $\boldsymbol{j}_p$ (*middle*) and its volume correction $\boldsymbol{j}_k$ (*bottom*) (thickness $d = 6\,\mathrm{mm}$, frequency $f = 50\,\mathrm{Hz}$).

Table 5.7: Massive inductors. Total Joule losses in the bushing mounting plate using the same materials ($\sigma_1 = \sigma_2 = 4.07\,\mathrm{MS/m}$, $\mu_1 = \mu_2 = 300$).

Current I (kA)	Frequency f (Hz)	Massive inductors			
		Thin shell P_{thin} (W)	Volume P_{vol} (W)	Reference P_{ref}	Bus bars P_{bars} (W)
2000	50	472	518.5	523.3	250
2250	50	598.4	656.2	662.4	317
2500	50	738.2	809.4	817.6	390
2800	50	926.2	1015.3	1025.5	491

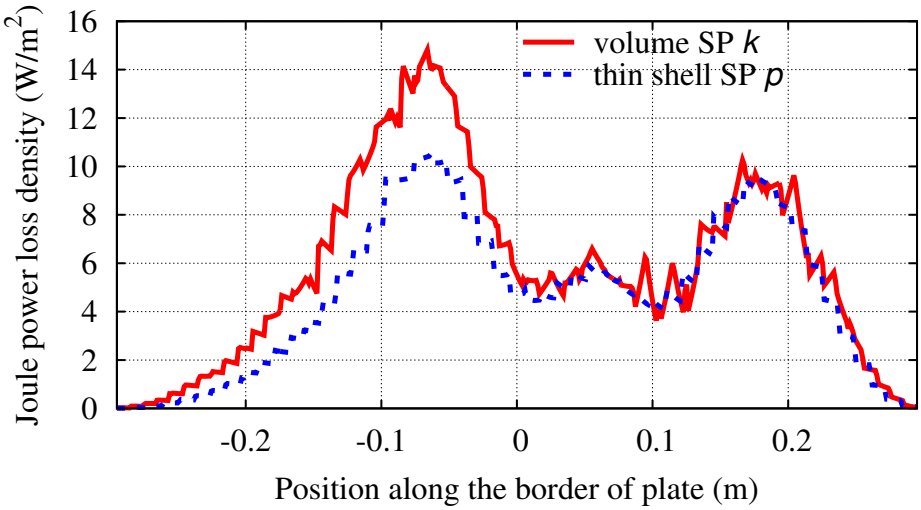

Figure 5.37: Joule power loss density for TS and VS solution along the plate border, with the same materials ($I = 2$ kA, $f = 50\,\mathrm{Hz}$).

Table 5.8: Comparison of the computed and measured Joule losses [90] in the bushing mounting plate using two different materials ($\sigma_1 = 4.07\,\mathrm{MS/m}$, $\sigma_2 = 1.15\,\mathrm{MS/m}$, $\mu_1 = 300$, $\mu_2 = 1$).

Current I (kA)	Frequency f (Hz)	Massive inductors		Stranded inductors		Measured values (W)
		Thin shell P_{thin} (W)	Volume P_{vol} (W)	Thin shell P_{thin} (W)	Volume P_{vol}(W)	
2000	50	51.8	62.58	51.1	62.55	65
2250	50	64.8	78.9	64.7	78.5	74
2500	50	80.8	97.5	80.5	97.3	95
2800	50	100.5	122.7	100.3	122.5	119
2000	250	84	292	84	292	

The second test is considered with the different properties or materials in two regions (i.e. regions 1 and 2) ($\sigma_1 = 4.07\,\mathrm{MS/m}$, $\sigma_2 = 1.15\,\mathrm{MS/m}$, $\mu_1 = 300$, $\mu_2 = 1$). The inaccuracy on TS SP p solution through the mounting plate hole (Fig. 5.38), and along the mounting plate border and near the plate ends (Fig. 5.39) can reach 37.5% and 50%, respectively ($d = 6\,\mathrm{mm}$, $f = 50\,\mathrm{Hz}$, $\delta = 2\,\mathrm{mm}$). The Joule losses calculated

for the mounting plate (with non-magnetic (region 2) inserted) by the SPM and the experimental method (proposed by authors in [90]), are given in Table 5.8. It can be shown that there is a very good agreement between the two computation methods. Complete solutions have been also validated.

This test problem has helped to standardise the type and material of the bushing mounting plate for various current ratings in tranformers rated between 500 kVA upto 2 MVA.

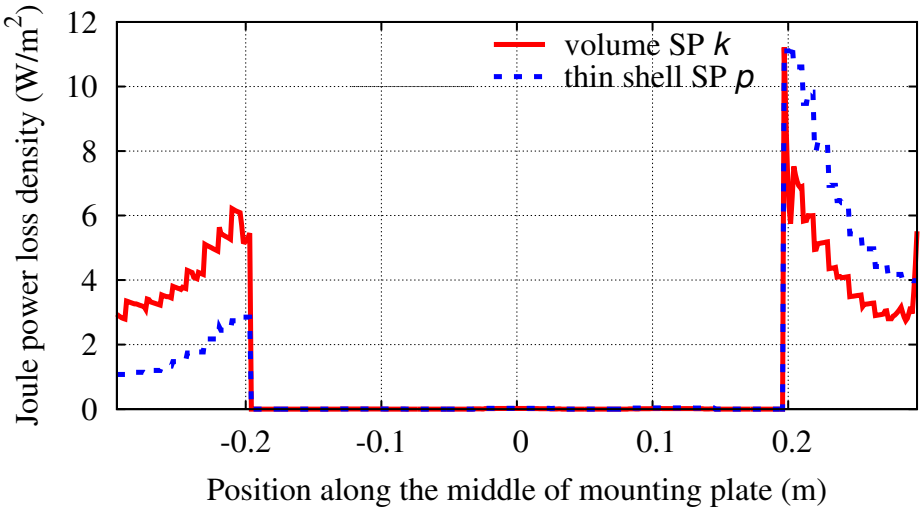

Figure 5.38: Joule power loss density for the TS and VS solution through the plate hole using two different materials (I_{max} = 2 kA, d = 6 mm, f = 50 Hz, σ_1 = 4.07 MS/m, σ_2 = 1.15 MS/m, μ_1 = 300, μ_2 =1).

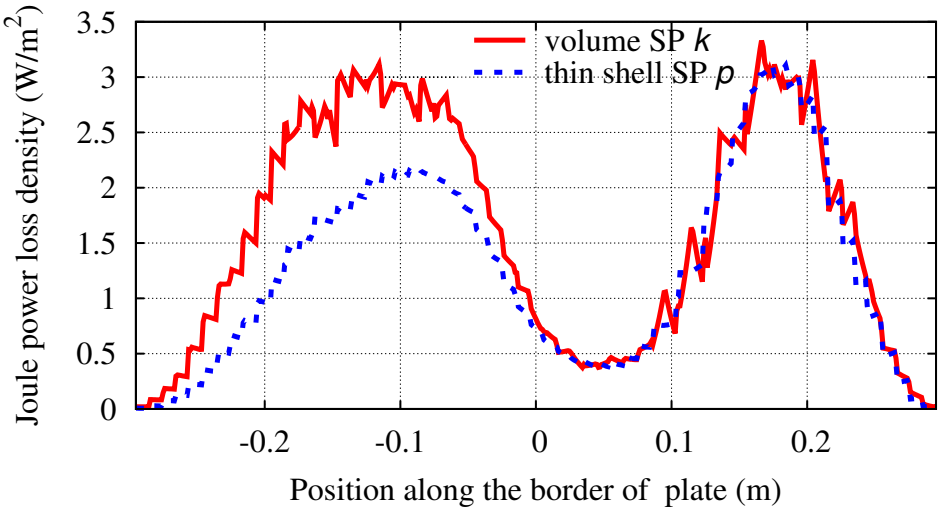

Figure 5.39: Joule power loss density for the TS and VS solution along the plate border using two different materials (I_{max} = 2 kA, d = 6 mm, f = 50 Hz, σ_1 = 4.07 MS/m, σ_2 = 1.15 MS/m, μ_1 = 300, μ_2 =1).

5.6 TEAM workshop problem 7

Another 3-D test is based on the international TEAM problem 7: a stranded inductor placed above a thin plate with a hole ($\mu_{r,plate} = 1$, $\sigma_{plate} = 35.26\,\mathrm{MS/m}$) (Fig. 5.40).

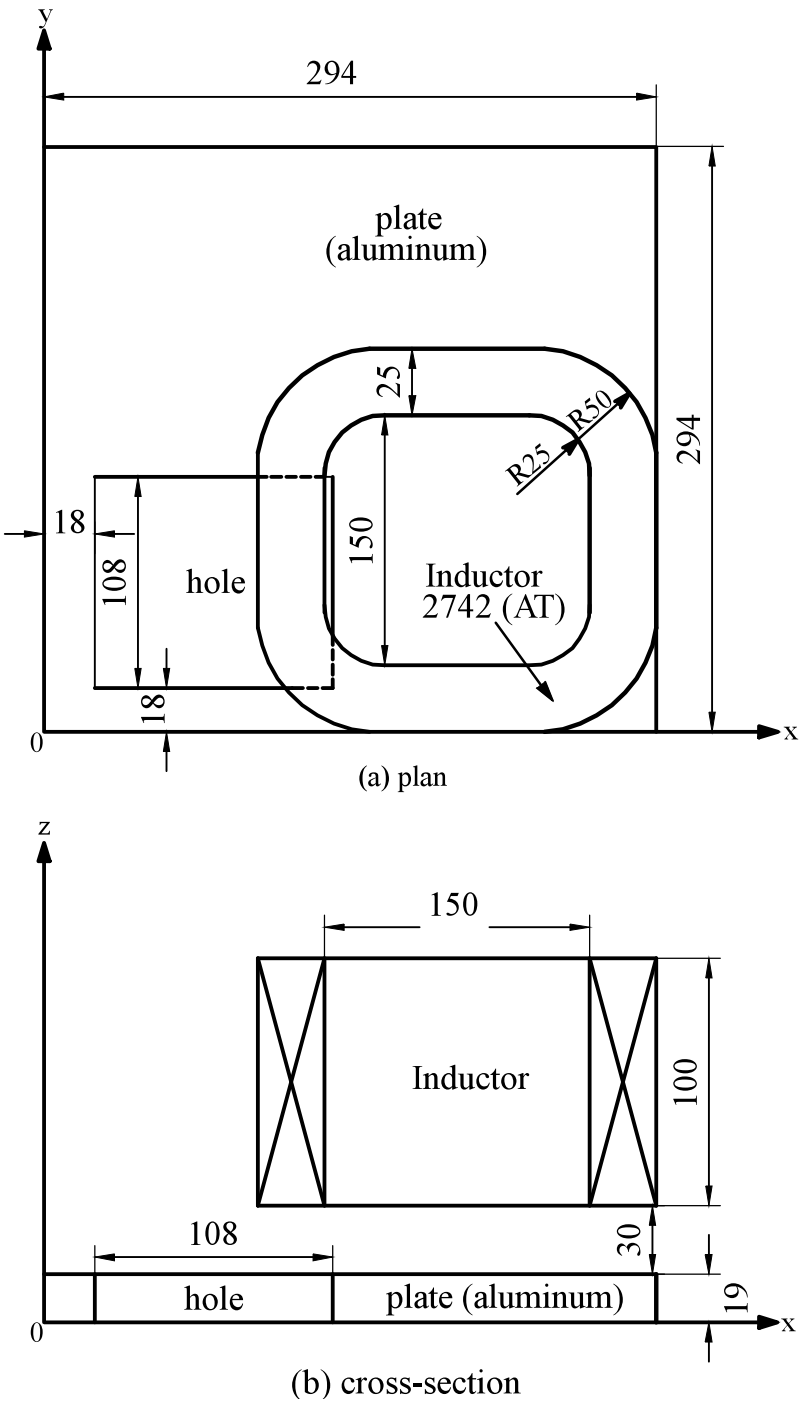

Figure 5.40: Geometry of TEAM problem 7 model: stranded inductor and conducting plate with hole inductor. All dimensions are in mm.

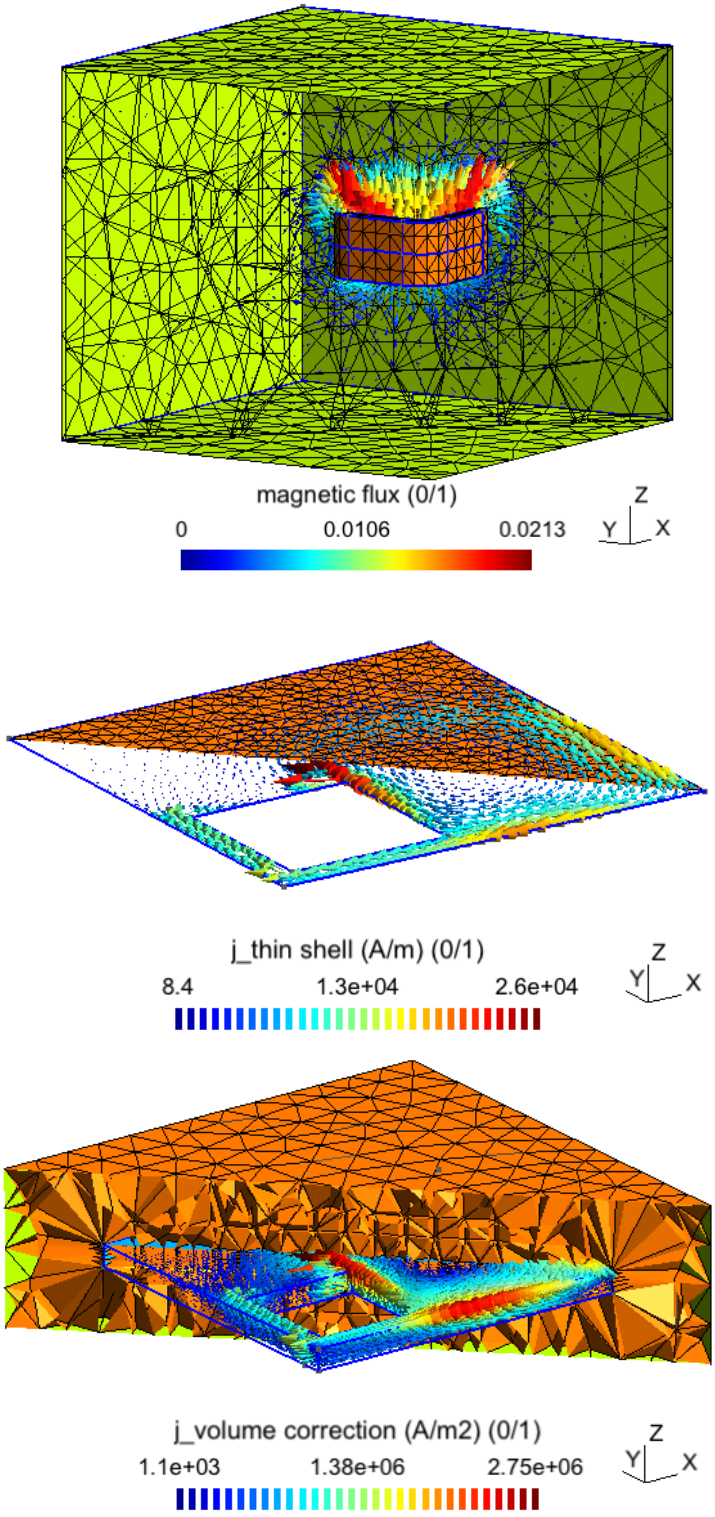

Figure 5.41: TEAM problem 7: magnetic flux density $\boldsymbol{b}_u$ (in a cut plane) generated by a stranded inductor (*top*), TS eddy current density $\boldsymbol{j}_p$ (*middle*) and its volume correction $\boldsymbol{j}_k$ (*bottom*) ($d = 19\,\text{mm}$, $f = 200\,\text{Hz}$).

The excitation current flowing in the inductor is 2472 Ampere-Turns at frequencies 50 Hz and 200 Hz. This test is done with the $\boldsymbol{h}$-formulation. A magnetodynamic SP scheme considering three SPs is proposed. A first FE SP u with the stranded inductor alone is solved on a simplified mesh (Fig. 5.41, *top*). Then a SP u is solved with the added thin region via a TS FE model (Fig. 5.41, *middle*). At last, a SP k replaces the TS FEs with volume FEs covering the actual plate and its neighborhood with an adequate refined mesh (Fig. 5.41, *bottom*). The TS error on $\boldsymbol{j}_p$ locally reaches 50% (Fig. 5.41, *middle*), with plate thickness $d = 19\,\text{mm}$ and frequency $f = 200\,\text{Hz}$ (skin depth $\delta = 6\,\text{mm}$). The inaccuracy on the Joule power loss densities of TS SP p is pointed out by the importance of the correction SP k (Figs. 5.42 and 5.43). It reaches several tens of percents along the plate borders and near the plate ends for some critical parameters: e.g., 28% (Fig. 5.42, *top*) and 32% (Fig. 5.43, *top*), with $f = 50\,\text{Hz}$ and $\delta = 11.98\,\text{mm}$ in both cases, or 53% (Fig. 5.42, *bottom*) and 61% (Fig. 5.43, *bottom*), with $f = 200\,\text{Hz}$ and $\delta = 6\,\text{mm}$ in both cases. The errors particularly decrease with a smaller thickness ($d = 2\,\text{mm}$), being lower than 15% (Fig. 5.44), with $f = 200\,\text{Hz}$ and $\delta = 6\,\text{mm}$.

Significant errors on the Joule losses and the global currents flowing around the hole for TS SP p are shown in Tables 5.9 and 5.10. For $d = 19\,\text{mm}$ and $f = 200\,\text{Hz}$, the TS error is 14% for the global current and 41.51% for the Joule loss (reduced to 26.18% for $f = 50\,\text{Hz}$). For $d = 2\,\text{mm}$ and $f = 200\,\text{Hz}$, it is respectively reduced to 1.1% and 6.44% (4.36% for $f = 50\,\text{Hz}$). Accurate local corrections with SP k are also checked to be close to the reference or complete FE solution (Tables 5.9 and 5.10).

Table 5.9: Joule losses in the plate

Thickness d (mm)	Frequency f (Hz)	Thin shell P_{thin} (W)	Volume P_{vol} (W)	Reference P_{ref} (W)	Errors (%) Between P_{thin} and P_{vol}
2	50	14.45	13.82	13.96	4.36
19	50	5.86	7.95	8.05	26.18
2	200	50.44	47.33	47.89	6.44
19	200	8.88	15.19	15.35	41.51

Table 5.10: Global currents flowing around the plate hole

Thickness d (mm)	Frequency f (Hz)	Thin shell I_{thin} (A)	Volume I_{vol} (A)	Reference I_{ref} (A)	Errors (%) Between I_{thin} and I_{vol}
2	50	94,5	93.5	93.3	1.1
19	50	173.3	199.8	201.9	13.2
2	200	190.4	186.5	187.8	1.8
19	200	179.3	206.3	208.2	14

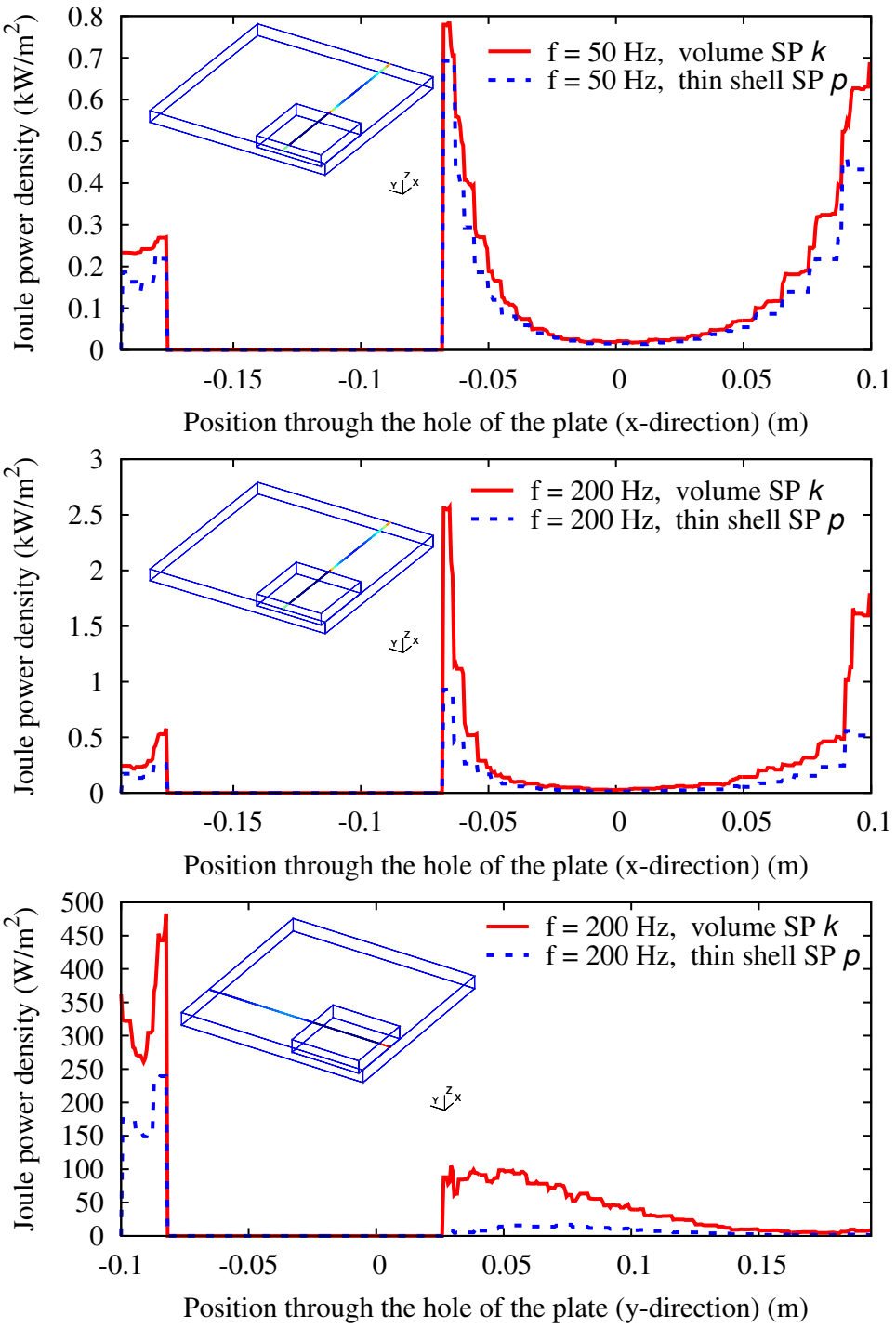

Figure 5.42: Joule power loss density with TS and VS solution through the hole in x-direction (*top and middle*) and y-direction (*bottom*) (along the line drawn in plate geometry), with affects of f ($d = 19\,\mathrm{mm}$).

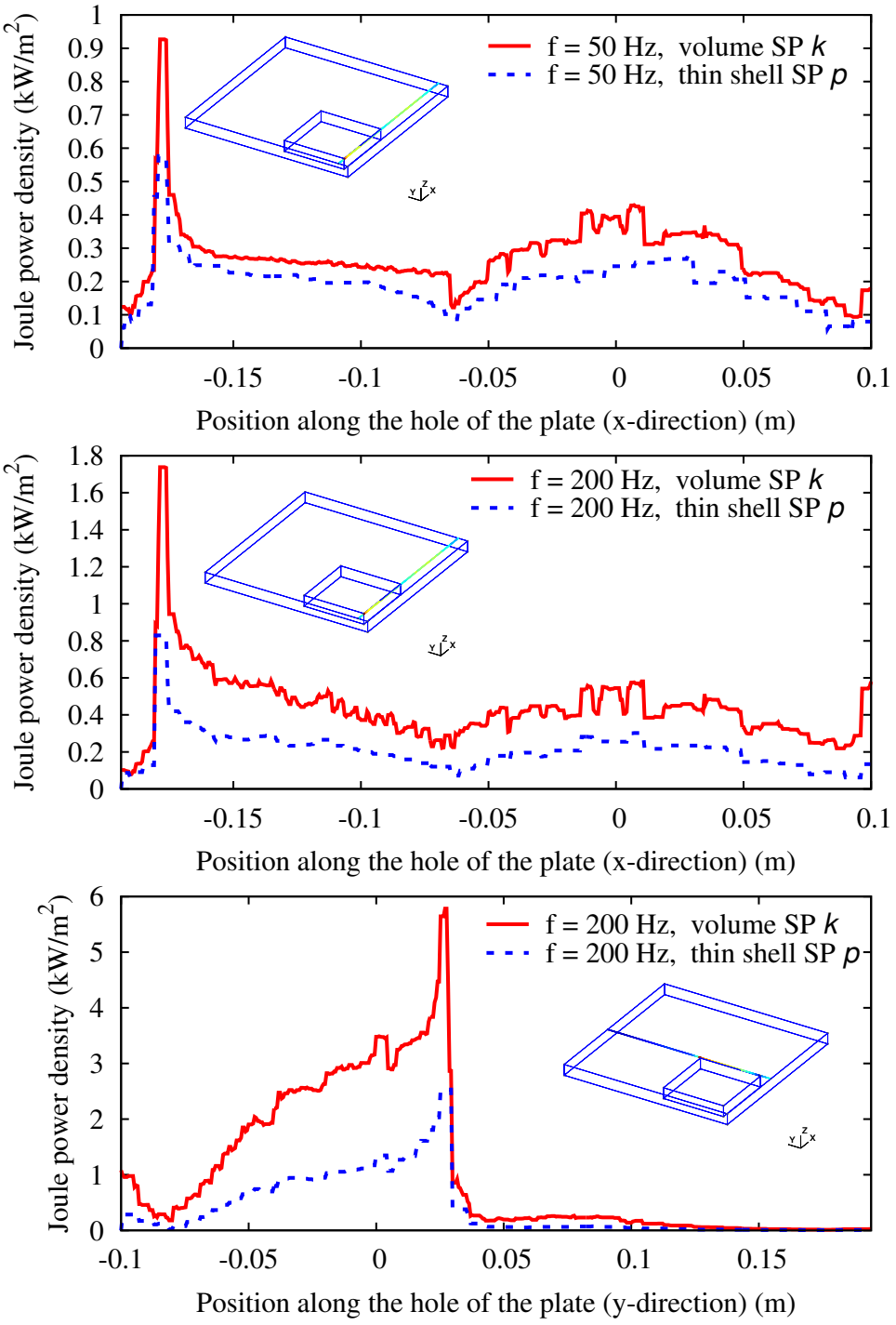

Figure 5.43: Joule power loss density with TS and VS solution along the hole and plate border in x-direction (*top and middle*) and y-direction (*bottom*) (along the line drawn in plate geometry), with affects of f ($d = 19\,\mathrm{mm}$).

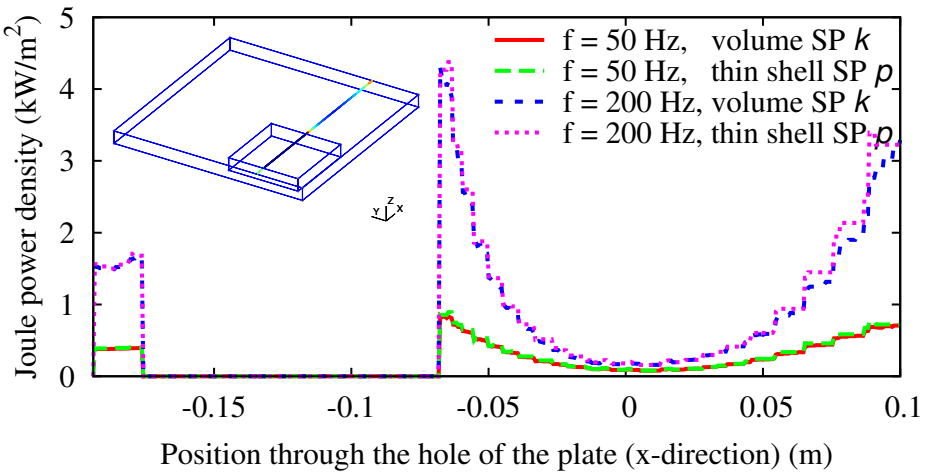

Figure 5.44: Joule power loss density with TS and VS solution through the hole in x-direction (along the line drawn in plate geometry), with affects of f ($d = 2\,\mathrm{mm}$).

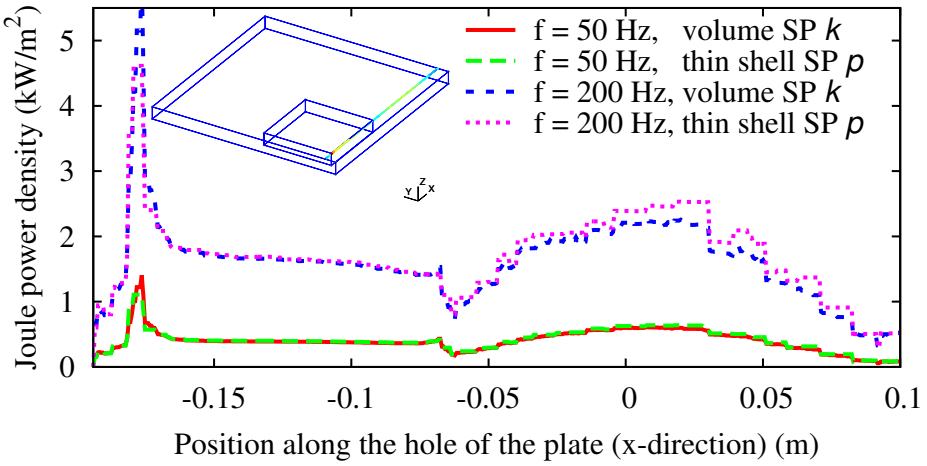

Figure 5.45: Joule power loss density with TS and VS solution and along the hole and plate border in x-direction (along the line drawn in plate geometry), with affects of f ($d = 2\,\mathrm{mm}$).

5.7 Thin region between conducting and nonconducting regions

Some test problems consider a thin region located between conducting regions (CRs) and between conducting and nonconducting regions (NCRs), with $f = 50\,\text{Hz}$, $\mu_{r,i}$ and σ_i for each region i (Fig. 5.46).

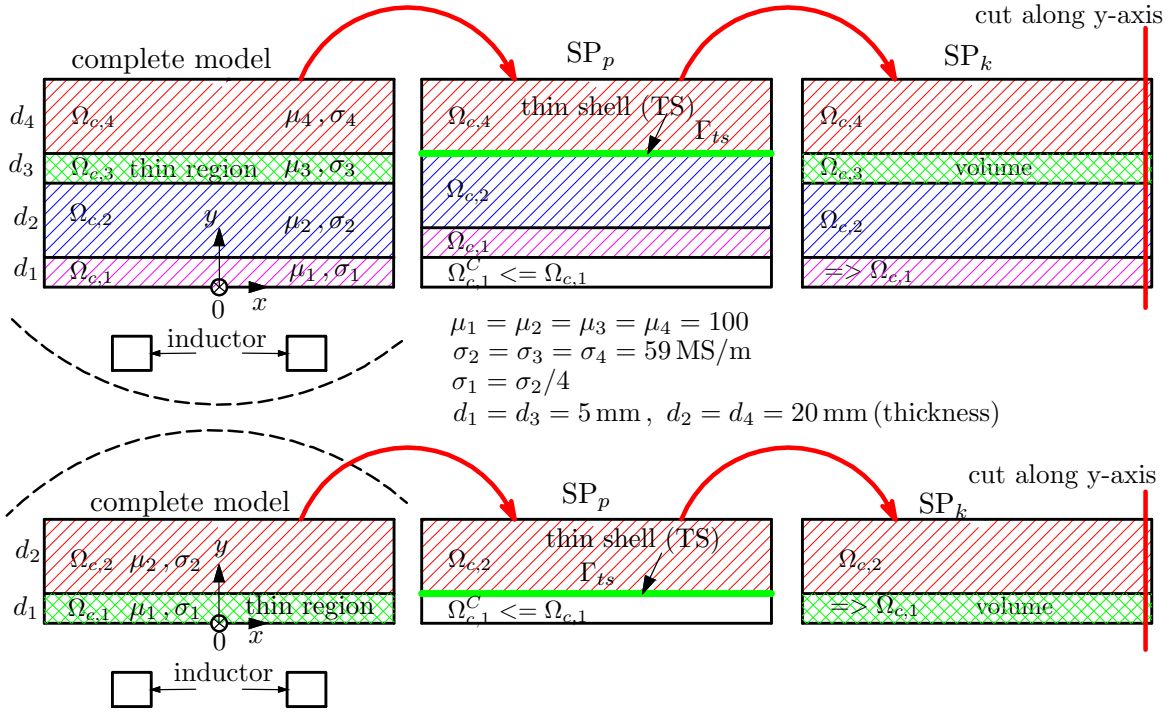

Figure 5.46: Geometry of SPs with a thin region located between conducting and nonconducting regions: complete problem, TS SP p, and volume correction SP k.

A thin region located between CRs (Fig. 5.46, *top*), it is first considered with the ***h***-formulation via an SP u with the inductor alone (Fig. 5.47, ϕ_u, *top left*), followed by the addition of a TS model SP p (Fig. 5.47, ϕ_p, *top right*); the discontinuity $\Delta\phi_p$ is defined to zero on both sides of the TS. An SP k eventually corrects the TS model (Fig. 5.47, ϕ_k, *bottom right*). The complete solution is indicated as well (Fig. 5.47, $\phi_u + \phi_p + \phi_k$, *bottom left*).

For $d_3 = 5\,\text{mm}$ (thickness of the thin region), the inaccuracy on the eddy current density of TS SP p along y-axis is shown via the importance of the volume correction SP k (Fig. 5.48). This is presented via a superposition of the SP solutions (i.e. TS + volume) is checked to be closed to the complete solution. The results are also illustrated and validated with ***b***-formulation (Fig. 5.49). Significant errors on the eddy current density decrease with a smaller thickness, e.g. $d_3 = 2\,\text{mm}$.

For a thin region located between CR and NCR (Fig. 5.46, *bottom*), the error on the eddy current density of TS SP p is also pointed out via SP k (Fig. 5.50).

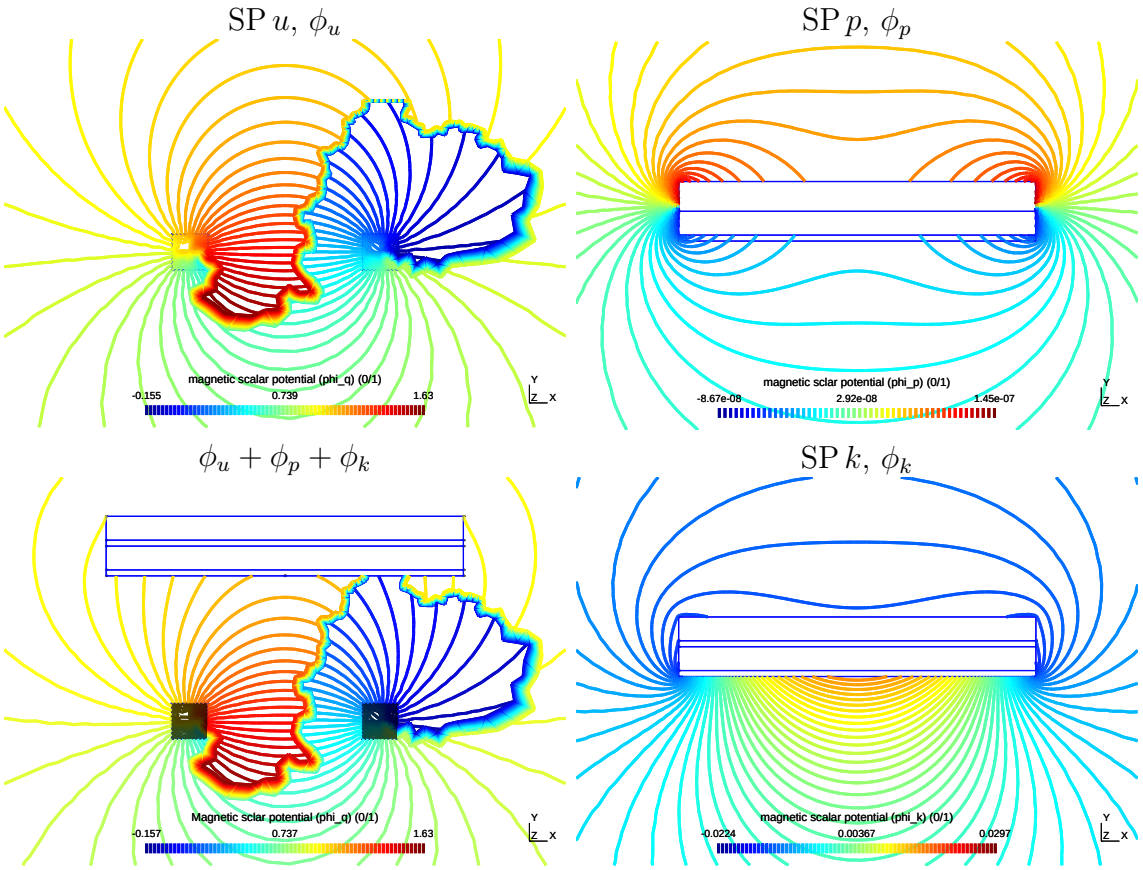

Figure 5.47: Distribution of magnetic scalar potential for SP u (ϕ_u), SP p added (ϕ_p), SP k solution (ϕ_k) and total solution ($\phi_u + \phi_p + \phi_k$) (***h***-formulation)

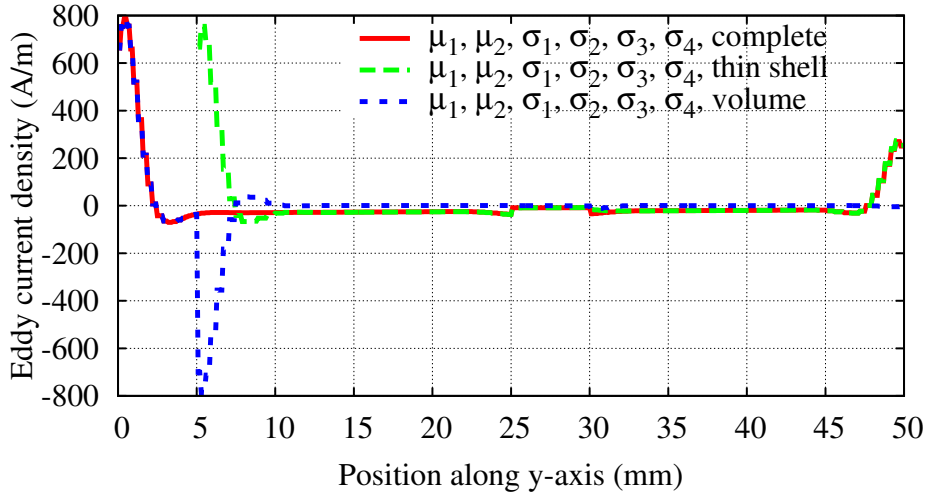

Figure 5.48: Eddy current density for the complete problem, TS SP p and volume correction SP k along y-axis (along the line drawn in the geometry), for a thin region located between CRs (***h***-formulation), with affects of μ_1, μ_2, σ_1, σ_2, σ_3 and σ_4 (given in Fig. 5.46).

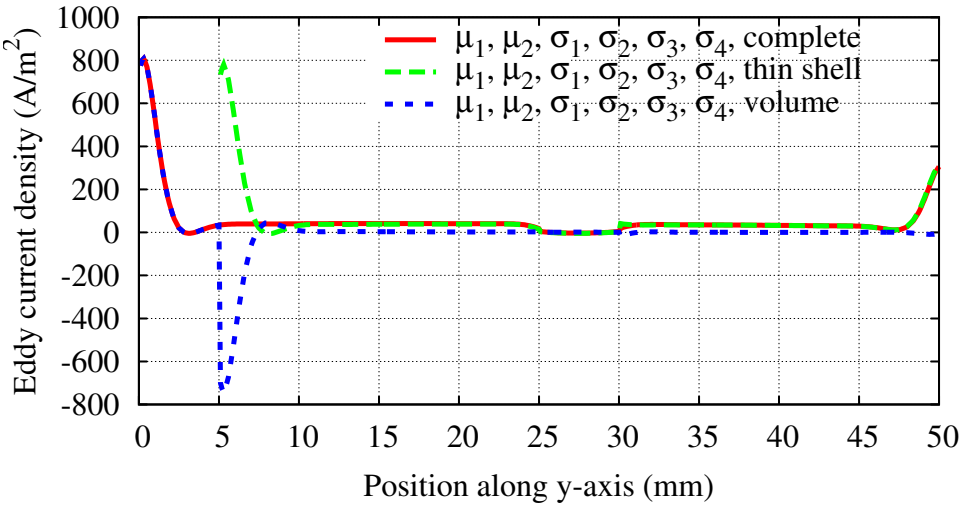

Figure 5.49: Eddy current density for the complete problem, TS SP p and volume correction SP k along y-axis, for a thin region located between CRs (***b***-formulation), with affects of μ_1, μ_2, σ_1, σ_2, σ_3 and σ_4 (given in Fig. 5.46).

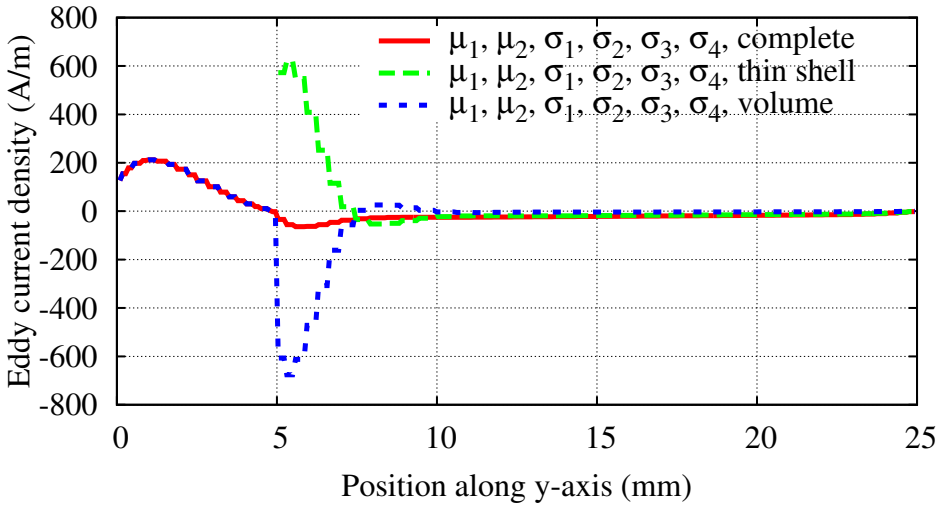

Figure 5.50: Eddy current density for the complete problem, TS SP p and volume correction SP k along y-axis (along the line drawn in the geometry), for a thin region located between CR and NCR (***h***-formulation), with affects of μ_1, μ_2, σ_1, σ_2, σ_3 and σ_4 (given in Fig. 5.46).

A superposition of the SP solutions is then checked to be closed to the complete solution.

Conclusions

The thin shell (TS) model and its local volumetric correction have been successfully developed in the frame of the subproblem method (SPM) with the $\boldsymbol{b}$- and $\boldsymbol{h}$-formulations. The main achievements of this thesis are summarized hereafter, as well as conclusions that can be pointed out from the numerical tests and some important future prospects. For a summary of the original contributions of the thesis (with the list of associated publications), please refer to the introduction, page 5.

The SPM has been developed for accurately correcting the inaccuracies on the local quantities inherent to the TS finite elements (FEs) models, for both simply connected and multiply connected TS regions. The method has been proposed for coupling SPs via one-way and two-way coupling. In addition, it has also been applied to thin regions located between conducting and non-conducting regions. The main points of the proposed method can be summarized as follows:

- The SPM allows to split a complete problem into a series of SPs that define a sequence of changes: a general SP scheme with massive or stranded inductor alone; addition of TS regions (one or more); volume correction of TS regions (in reduced domains).
- An adapted mesh can be used for each SP: each SP is independently solved on its own separate domain and adapted mesh, which facilitates meshing and potentially increases the computational efficiency, in particular for parameterized, optimization and sensitivity analyses.
- The SPM permits to reuse previous solutions for new problems (variation of geometrical and physical data) instead of solving a new complete problem for each new set of parameters.
- The step by step nature of the technique can lead to a better understanding of some physical behaviors (changing physical data and adding regions) and of model errors (correction of simplified models).
- The local volumetric TS correction can be seen as a particular step of the SPM developed in Chapters 2, 3, 4, to improve the accuracy of standard TS models near geometric discontinuities like corners and edges.

All the steps of the method have been illustrated and validated via practical tests with the $\boldsymbol{b}$- and $\boldsymbol{h}$-formulations. In particular, it has been successfully ap-

plied to international test problems (TEAM workshop problems 21 and 7). All the developments have been carried out in the frequency domain.

Future work

Many interesting prospects are in progress for defining additional types of SPs. Several suggestions for future research are given below:

- The correction of inaccuracies of the TS FE models via the SPM could be extended to the case of multi layers-TS with different properties (see e.g. [50, 119, 124, 139]).
- The correction of inaccuracies of the TS regions via the SPM could be performed in the time domain (see e.g. [53, 118, 119]). The extension to nonlinear cases could also be considered.
- On the two-way coupling, the iteration could be accelerated (to reduce the number of iterations), e.g. by extrapolation or by using Krylov subspace techniques [15, 59, 63, 129].

Appendix A

Mathematical framework

A.1 Function spaces

Scalar and vector fields are defined at any point $\boldsymbol{x} = (x, y, z) \in \mathbb{E}^3$ and at any time instant $t \in \mathbb{R}$. To be simple, the space-time dependence of the fields will be generally omitted: the scalar field $f(\boldsymbol{x}, t) = f(x, y, z, t)$ and the vector field $\boldsymbol{f}(\boldsymbol{x}, t) = \boldsymbol{f}(x, y, z, t)$ will thus be often simply denoted by f and $\boldsymbol{f}$. In Cartesian coordinates, the vector field $\boldsymbol{f}$ is denoted by $\boldsymbol{f} = (f_x, f_y, f_z)^T$ where f_x, f_y and f_z represent, respectively, its three components. The studied domain is an open set Ω of $\mathbb{E}^3$, of which the boundary is a closed surface Γ of exterior unit normal $\boldsymbol{n}$.

A.1.1 Square integrable field spaces

The spaces $L^2(\Omega)$ and $\boldsymbol{L}^2(\Omega)$ of square integrable scalar and vector fields on Ω, respectively, are defined by [54, 130]

$$L^2(\Omega) = \Big\{ u : \int_\Omega u^2(\boldsymbol{x})\, d\boldsymbol{x} < \infty \Big\}, \tag{A.1}$$

$$\boldsymbol{L}^2(\Omega) = \Big\{ \boldsymbol{u} : \int_\Omega \|\boldsymbol{u}(\boldsymbol{x})\|^2\, d\boldsymbol{x} < \infty \Big\}, \tag{A.2}$$

where $\boldsymbol{x}$ is a point of space, $d\boldsymbol{x}$ a volume element and $\|\boldsymbol{u}(\boldsymbol{x})\|$ represents the Euclidean norm of $\boldsymbol{u}(\boldsymbol{x})$. The scalar products of two elements $u, v \in L^2(\Omega)$ and $\boldsymbol{u}, \boldsymbol{v} \in \boldsymbol{L}^2(\Omega)$ are defined by

$$(u, v)_\Omega = \int_\Omega u(\boldsymbol{x})\, v(\boldsymbol{x})\, d\boldsymbol{x} \quad \text{and} \quad (\boldsymbol{u}, \boldsymbol{v})_\Omega = \int_\Omega \boldsymbol{u}(\boldsymbol{x}) \cdot \boldsymbol{v}(\boldsymbol{x})\, d\boldsymbol{x}. \tag{A.3}$$

The norms of $u \in L^2(\Omega)$ and $\boldsymbol{u} \in \boldsymbol{L}^2(\Omega)$ are defined by

$$\|u\|_{L^2(\Omega)} = (u, u)_\Omega^{1/2} = \Big[\int_\Omega u^2(\boldsymbol{x})\, d\boldsymbol{x} \Big]^{1/2}, \tag{A.4}$$

$$\|\boldsymbol{u}\|_{\boldsymbol{L}^2(\Omega)} = (\boldsymbol{u}, \boldsymbol{u})_\Omega^{1/2} = \Big[\int_\Omega \|\boldsymbol{u}(\boldsymbol{x})\|^2\, d\boldsymbol{x} \Big]^{1/2}. \tag{A.5}$$

If a space is normed, the distance between two elements $u, v \in L^2(\Omega)$ and $\boldsymbol{u}, \boldsymbol{v} \in \boldsymbol{L}^2(\Omega)$ is the norm of their difference, respectively, $d(u,v) = \|u - v\|$ and $d(\boldsymbol{u}, \boldsymbol{v}) = \|\boldsymbol{u} - \boldsymbol{v}\|$.

Two elements $u, v \in L^2(\Omega)$ and $\boldsymbol{u}, \boldsymbol{v} \in \boldsymbol{L}^2(\Omega)$ are said to be orthogonal if their scalar product is $(u,v)_\Omega = 0$ and $(\boldsymbol{u}, \boldsymbol{v})_\Omega = 0$. Two functional spaces are said to be orthogonal if all their elements are orthogonal.

The following notation is also adopted for integrals over a surface Γ of the scalar product of two functions:

$$\langle u, v \rangle_\Gamma = \int_\Gamma u(\boldsymbol{x})\, v(\boldsymbol{x})\, d\boldsymbol{x} \quad \text{and} \quad \langle \boldsymbol{u}, \boldsymbol{v} \rangle_\Gamma = \int_\Gamma \boldsymbol{u}(\boldsymbol{x}) \cdot \boldsymbol{v}(\boldsymbol{x})\, d\boldsymbol{x}. \tag{A.6}$$

A.1.2 Hilbert spaces

Let E be a vectorial space equipped with a norm. A sequence $\{x_n\}$ is called a Cauchy sequence if

$$\forall \epsilon > 0,\ \exists N(\epsilon) :\ n, m > N(\epsilon) \Rightarrow d(x_m, x_n) < \epsilon. \tag{A.7}$$

E is complete if every Cauchy sequence converges toward an element of E. A vector space that is normed and complete is called a Banach space.

If E is a vector space equipped with a scalar product and if E is complete for the norm derived from this scalar product, then E is a Hilbert space.

A.1.3 Sobolev spaces

The subspaces of $L^2(\Omega)$ and $\boldsymbol{L}^2(\Omega)$ for which all first order partial derivatives are also square integrable are known as the Sobolev spaces of the scalar fields $H^1(\Omega)$ and vector fields $\boldsymbol{H}^1(\Omega)$. They are defined by

$$H^1(\Omega) = \Big\{ u \in L^2(\Omega) : \partial_x u, \partial_y u, \partial_z u \in L^2(\Omega) \Big\}, \tag{A.8}$$

$$\boldsymbol{H}^1(\Omega) = \Big\{ \boldsymbol{u} \in \boldsymbol{L}^2(\Omega) : \partial_x \boldsymbol{u}, \partial_y \boldsymbol{u}, \partial_z \boldsymbol{u} \in \boldsymbol{L}^2(\Omega) \Big\}. \tag{A.9}$$

In the same way, the Sobolev spaces $H^p(\Omega)$ and $\boldsymbol{H}^p(\Omega)$, $\forall p > 1$ are defined by:

$$H^p(\Omega) = \Big\{ u \in H^{p-1}(\Omega) : \partial_x u, \partial_y u, \partial_z u \in H^{p-1}(\Omega) \Big\}, \tag{A.10}$$

$$\boldsymbol{H}^p(\Omega) = \Big\{ \boldsymbol{u} \in \boldsymbol{H}^{p-1}(\Omega) : \partial_x \boldsymbol{u}, \partial_y \boldsymbol{u}, \partial_z \boldsymbol{u} \in \boldsymbol{H}^{p-1}(\Omega) \Big\}. \tag{A.11}$$

The Sobolev spaces are well adapted to variational problems.

A.1.4 Differential operators

Normally, we have to solve, in a domain Ω, differential equations utilizing differential operators: the gradient, the rotational and the divergence. Such equations

describe the space distribution of vector fields and scalar fields. The **grad** operator in Cartesian coordinates for scalar fields f is classically defined as

$$\mathbf{grad}\, f = (\partial_x f, \partial_y f, \partial_z f)^T. \tag{A.12}$$

The Sobolev space for the **grad** is thus

$$H^1(\Omega) = H(\mathbf{grad}; \Omega) = \left\{u \in L^2(\Omega) : \mathbf{grad}\, u \in \boldsymbol{L}^2(\Omega)\right\}. \tag{A.13}$$

The classical definition of the **curl** and div operators for a vector field $\boldsymbol{f} = (f_x, f_y, f_z)^T$ are:

$$\mathbf{curl}\, \boldsymbol{f} = (\partial_y f_z - \partial_z f_y, \partial_z f_x - \partial_x f_z, \partial_x f_y - \partial_y f_x)^T, \tag{A.14}$$

$$\mathrm{div}\, \boldsymbol{f} = \partial_x f_x + \partial_y f_y + \partial_z f_z. \tag{A.15}$$

The associated Hilbert spaces are:

$$\boldsymbol{H}(\mathbf{curl}; \Omega) = \left\{\boldsymbol{u} \in \boldsymbol{L}^2(\Omega) : \mathbf{curl}\, \boldsymbol{u} \in \boldsymbol{L}^2(\Omega)\right\}, \tag{A.16}$$

$$\boldsymbol{H}(\mathrm{div}; \Omega) = \left\{\boldsymbol{u} \in \boldsymbol{L}^2(\Omega) : \mathrm{div}\, \boldsymbol{u} \in L^2(\Omega)\right\}. \tag{A.17}$$

A.1.5 de Rham complexes

The domains of the differential operators are built to satisfy $\mathbf{grad}\, H^1(\Omega) \subset \boldsymbol{H}(\mathbf{curl}; \Omega)$, $\mathbf{curl}\, \boldsymbol{H}(\mathbf{curl}; \Omega) \subset \boldsymbol{H}(\mathrm{div}; \Omega)$ and $\mathrm{div}\, \boldsymbol{H}(\mathrm{div}; \Omega) \subset L^2(\Omega)$, or, equivalently, $\mathcal{R}(\mathbf{grad}) \subset \mathcal{D}(\mathbf{curl})$, $\mathcal{R}(\mathbf{curl}) \subset \mathcal{D}(\mathrm{div})$, and $\mathcal{R}(\mathrm{div}) \subset L^2(\Omega)$. This property is represented by a sequence called de Rham complexes:

$$H^1(\Omega) \xrightarrow{\mathbf{grad}} \boldsymbol{H}(\mathbf{curl}; \Omega) \xrightarrow{\mathbf{curl}} \boldsymbol{H}(\mathrm{div}; \Omega) \xrightarrow{\mathrm{div}} L^2(\Omega) \tag{A.18}$$

If $\Omega = \mathbb{E}^3$, the sequence (A.18) is said to be exact if there exists $\mathcal{R}(\mathbf{grad}) = \mathcal{K}(\mathbf{curl})$ and $\mathcal{R}(\mathbf{curl}) = \mathcal{K}(\mathrm{div})$. In this case, the image of $H^1(\mathbb{E}^3)$ in $\boldsymbol{H}(\mathbf{curl}; \mathbb{E}^3)$ by the **grad** operator is exactly the kernel of the **curl** operator, which means that all curl-free fields are gradients. In the same way, the image of $\boldsymbol{H}(\mathbf{curl}; \mathbb{E}^3)$ in $\boldsymbol{H}(\mathrm{div}; \mathbb{E}^3)$ by the **curl** operator is exactly the kernel of the div operator, which means that all divergence-free fields can be expressed as the **curl** of some other field.

If Ω is a bounded set of $\mathbb{E}^3$, the sequence is not exact anymore, except for trivial topologies (for example if Ω is simply connected) [85, 95].

A.1.6 Helmholtz decomposition

The solutions of Maxwell's equations (1.1)–(1.4) are defined via four function spaces and three differential operators.

The four spaces are two copies of square integrable scalar fields $L^2(\Omega)$ and two copies of square integrable vector fields $\boldsymbol{L}^2(\Omega)$ [7, 10, 58, 81, 106, 117]. The three operators are the gradient (**grad**), the **curl** and the divergence (div). They are

linear and unbounded differential operators. The four spaces corresponding to four levels (0, 1, 2 and 3 for $L^2(\Omega)$, $\boldsymbol{L}^2(\Omega)$, $\boldsymbol{L}^2(\Omega)$ and $L^2(\Omega)$, respectively) are represented via horizontal axes (Fig. A.1) [10, 108]. Subdivisions of these axes represent their subspaces. Note that the axis at level 2 is exactly the inverted axis at level 1 (i.e. levels 1 and 2 correspond to the same $\boldsymbol{L}^2(\Omega)$). The arrows correspond to the application of the operators **grad**, **curl** and div, depending on the level (i.e. the distance between two arrows allowing to determine a subspace and its image).

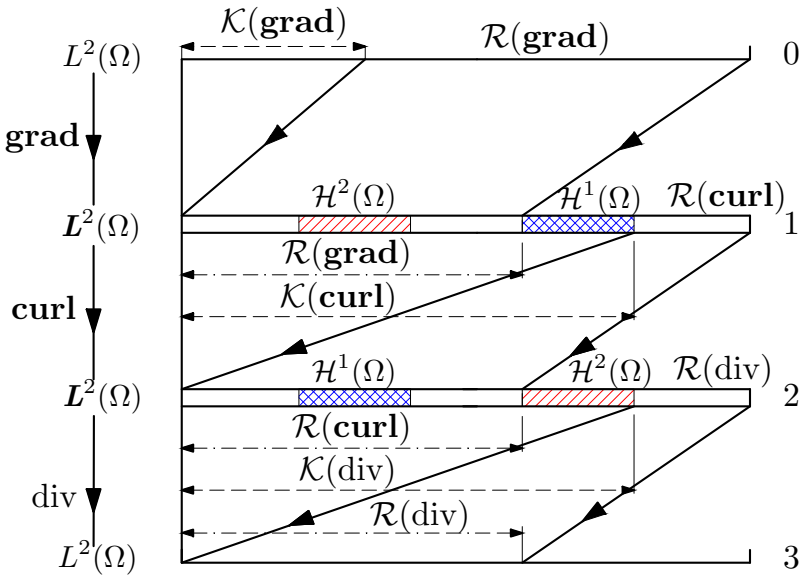

Figure A.1: Kernels and ranges of operators **grad**, **curl** and div in Ω.

We now consider the relation of two subspaces $\mathcal{H}^1(\Omega)$ and $\mathcal{H}^2(\Omega)$ appearing in Figure A.1. $\mathcal{H}^1(\Omega)$ and $\mathcal{H}^2(\Omega)$ are related to the loops and cavities in the domain Ω. They have the following properties [9, 10, 14, 28, 58]:

$$\mathcal{H}^1(\Omega) = \left\{\boldsymbol{u} \in \boldsymbol{L}^2(\Omega) : \mathbf{curl}\,\boldsymbol{u} = 0, \mathrm{div}\,\boldsymbol{u} = 0, \boldsymbol{n} \cdot \boldsymbol{u}\big|_\Gamma = 0\right\}, \tag{A.19}$$

$$\mathcal{H}^2(\Omega) = \left\{\boldsymbol{u} \in \boldsymbol{L}^2(\Omega) : \mathbf{curl}\,\boldsymbol{u} = 0, \mathrm{div}\,\boldsymbol{u} = 0, \boldsymbol{n} \times \boldsymbol{u}\big|_\Gamma = 0\right\}, \tag{A.20}$$

where Γ is the boundary of Ω. The dimension of $\mathcal{H}^1(\Omega)$ is finite and equal to the number of loops in Ω if there exist cutting surfaces in Ω (the determination of this subspace is presented in Section A.1.7). The dimension of $\mathcal{H}^2(\Omega)$ is also finite and equal to the number of cavities in Ω [9, 10, 14, 28, 58]. Note that $\mathcal{H}^1(\Omega)$ belongs to Null-space (kernel) $\mathcal{K}(\mathbf{curl})$ but not in range (co-domain) $\mathcal{R}(\mathbf{grad})$ and $\mathcal{H}^2(\Omega)$ belongs to $\mathcal{K}(\mathrm{div})$ but not in $\mathcal{R}(\mathbf{curl})$ (Fig. A.1).

A.1.7 Determination of subspace $\mathcal{H}^1(\Omega)$

From the developments in Section A.1.6, we briefly recall the following classical results characterizing $\mathcal{H}^1(\Omega)$ [26]. Since $\mathrm{div}\,\boldsymbol{u}_i = 0$ in Ω_i, $\boldsymbol{u}_i$ is locally the gradient of a harmonic function q_i. If l cutting surfaces Σ_i are defined, we have by analytic

prolongation $\boldsymbol{u}_i = \mathbf{grad}\, q_i$ in Ω_i, and thus [9, 28, 38, 58, 128]

$$\operatorname{div} \mathbf{grad}\, q_i = 0 \quad \text{in } \Omega_i. \tag{A.21}$$

The condition $\boldsymbol{n} \cdot \boldsymbol{u}_i\big|_{\Gamma_i} = 0$ becomes

$$\boldsymbol{n} \cdot \boldsymbol{u}_i\big|_{\Gamma_i} = \frac{\partial q}{\partial \boldsymbol{n}}\Big|_{\Gamma_i} = 0. \tag{A.22}$$

Let us now find the conditions on q imposed on the cut Σ_i of Ω_i. Two sides of the cut Σ_i are expressed via Σ_i^+ and Σ_i^-, and $\boldsymbol{n}$ is a normal vector of Σ_i (Fig. A.2). The discontinuity of the field ϕ_i across the cuts defined on Ω_i are

$$\big[\phi_i\big]_{\Sigma_i} = \phi_i\big|_{\Sigma_i^+} - \phi_i\big|_{\Sigma_i^-} = 0. \tag{A.23}$$

In particular, we get $\big[\boldsymbol{u}_i\big]_{\Sigma_i} = \boldsymbol{u}_i\big|_{\Sigma_i^+} - \boldsymbol{u}_i\big|_{\Sigma_i^-} = 0$, $i = 1, \ldots, l$, and since $\boldsymbol{u}$ defined in Ω_i, one has

$$\big[q_i\big]_{\Sigma_i} = q_i\big|_{\Sigma_i^+} - q_i\big|_{\Sigma_i^-} = c_i\,, \quad i = 1, \ldots, l, \tag{A.24}$$

where c_i is a constant associated with the cut Σ_i. Using Green's formula (A.37), applied to the field $\boldsymbol{u}_i$ and to any function $\phi_i \in \mathcal{H}^1(\Omega_i)$, one has

$$(\boldsymbol{u}_i, \mathbf{grad}\, \phi_i)_{\Omega_i} + (\operatorname{div} \boldsymbol{u}_i, \phi_i)_{\Omega_i} = \langle \boldsymbol{n} \cdot \boldsymbol{u}_i, \phi_i \rangle_{\Gamma_i}, \quad \forall \phi_i \in \mathcal{H}^1(\Omega_i), \tag{A.25}$$

The last term of (A.25) is equal to zero if boundary condition is taken into account.

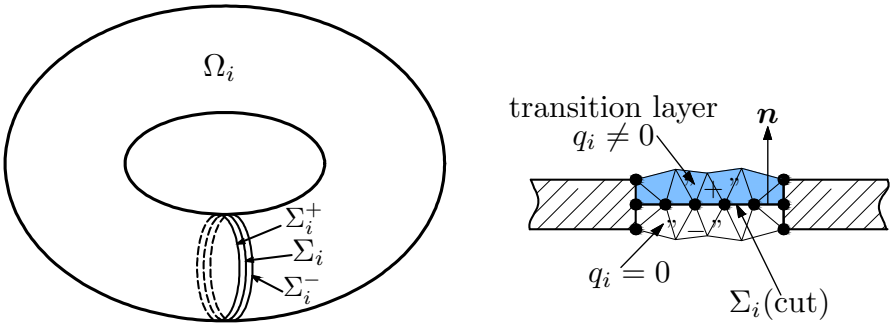

Figure A.2: Both sides of a cut Σ_i and the associated normal.

The second term of (A.25) is equal to zero following to conservative law. (A.25) can then be reduced to

$$(\boldsymbol{u}_i, \mathbf{grad}\, \phi_i)_{\Omega} = 0, \quad \forall \phi_i \in \mathcal{H}^1(\Omega_i), \tag{A.26}$$

with $\boldsymbol{u}_i = \mathbf{grad}\, q_i$, it get

$$(\mathbf{grad}\, q_i, \mathbf{grad}\, \phi_i)_{\Omega_i} = 0, \quad \forall \phi_i \in \mathcal{H}^1(\Omega_i). \tag{A.27}$$

For a new application of Green's formula, the last form becomes

$$\int_{\partial\Omega_i} \frac{\partial q_i}{\partial \boldsymbol{n}} \phi_i \, ds = 0, \quad \forall \phi \in \mathcal{H}^1(\Omega_i), \tag{A.28}$$

and finally one has

$$\sum_{i=1}^{N_i} \int_{\Sigma_i} \left[\frac{\partial q_i}{\partial \boldsymbol{n}}\right]_{\Sigma_i} \phi \, ds = 0, \quad \forall \phi_i \in \mathcal{H}^1(\Omega_i). \tag{A.29}$$

One can then show that

$$\left[\frac{\partial q_i}{\partial \boldsymbol{n}}\right]_{\Sigma_i} = \frac{\partial q_i}{\partial \boldsymbol{n}}\Big|_{\Sigma_i^+} - \frac{\partial q_i}{\partial \boldsymbol{n}}\Big|_{\Sigma_i^-} = 0, \quad i = 1, \ldots, l. \tag{A.30}$$

The function $q_i \in \mathcal{H}^1(\Omega_i)$ defined by (A.21), (A.22), (A.24) and (A.30), linearly depends on the l constant jumps $c_i = \left[q_i\right]_{\Sigma_i}$ of the function q_i across the cuts Σ_i. A basis of the space $\mathcal{H}^1(\Omega_i)$ can therefore be defined by the l functions q_j, solutions of (A.21), (A.22), (A.24) and (A.30) and

$$\left[q_{ij}\right]_{\Sigma_i} = q_{ij}\Big|_{\Sigma_i^+} - q_{ij}\Big|_{\Sigma_i^-} = \delta_{ij}, \quad i = 1, \ldots, l, \tag{A.31}$$

for $j = 1, \ldots, l$ (δ_{ij} denotes the Kronecker symbol). The basis function q_{ij} of $\mathcal{H}^1(\Omega_i)$ is thus a function defined in Ω_i which expresses a unit discontinuity across the cut Σ_j. One should note that the field q_{ij} only depends on the topology of Ω_i: the way q_{ij} varies does not matter. In order to simplify further developments, we will always assume that the field q_j varies from 1 on one side of the cut (Σ_j^+) to 0 on the other side (Σ_j^-) (Fig. A.2).

A.2 Strong and weak formulations

The generalized Green relation is defined by

$$(Lu, v)_\Omega - (u, L^* v)_\Omega = \int_\Gamma Q(u, v) ds, \quad \forall u \in \mathcal{D}(L) \quad \text{and} \quad \forall v \in \mathcal{D}(L^*) \tag{A.32}$$

where L is a differential operator of order n defined on Ω, the operator L^* (of order n) is the adjoint of L, and Q is a bi-linear function of u and v and in their derivatives up to the order $n-1$.

Let us now consider the partial derivative problem

$$Lu = f \text{ in } \Omega \tag{A.33}$$

$$Bu = g \text{ in } \Gamma \tag{A.34}$$

where B is an operator which defines a BC, the two functions f and g are defined on Ω and Γ respectively. The problem (A.33 - A.34) is called a strong formulation. A function u that verifies this problem is called a strong solution. A weak formulation of problem (A.33-A.34) is given by

$$(u, L^* v)_\Omega - (f, v)_\Omega + \int_\Gamma Q_g(v) \, ds = 0, \quad \forall v \in V(\Omega), \tag{A.35}$$

where L^* is the dual operator of L, defined by the generalized Green formula (A.32), Q_g is a linear form in v which depends on g, and the space $V(\Omega)$ is a space of test functions which has to be defined according to the operator L^* and particularly according to the BC (A.34). A function u that satisfies (A.35) for all test functions $v \in V(\Omega)$ is called a weak solution. The generalized Green formula (A.32) can be applied to (A.35) in order to get L instead of L^*, which is in general consists of performing an integration by parts. It is then possible to find again, thanks to a judicious choice of test functions, the equations and relations of the classical formulation of the problem, i.e. equation (A.33) and BC (A.34).

The extensively used **grad**-div and **curl-curl** Green formulas are two particular cases of the generalized Green relation (A.32). Let u be a function of $\Omega \mapsto \mathbb{R}$ and $\boldsymbol{v}$ a function of $\Omega \mapsto \mathbb{E}^3$. A first relation of vectorial analysis

$$\boldsymbol{v} \cdot \mathbf{grad}\, u + u \operatorname{div} \boldsymbol{v} = \operatorname{div}(u\boldsymbol{v}), \tag{A.36}$$

integrated in the domain Ω, after applying the divergence theorem, gives the Green formula of type **grad**-div in Ω, i.e.

$$(\boldsymbol{v}, \mathbf{grad}\, u)_\Omega + (\operatorname{div} \boldsymbol{v}, u)_\Omega = \langle u, \boldsymbol{n} \cdot \boldsymbol{v} \rangle_\Gamma, \quad \forall \boldsymbol{v} \in \boldsymbol{H}^1(\Omega), \quad \forall u \in H^1(\Omega), \tag{A.37}$$

where $\boldsymbol{H}^1(\Omega)$ and $H^1(\Omega)$ are function spaces built for scalar and vector fields, respectively.

Let $\boldsymbol{w}$ be a function of $\Omega \mapsto \mathbb{E}^3$. Another relation of vectorial analysis

$$\boldsymbol{v} \cdot \mathbf{curl}\, \boldsymbol{w} - \boldsymbol{w} \cdot \mathbf{curl}\, \boldsymbol{v} = \operatorname{div}(\boldsymbol{w} \times \boldsymbol{v}), \tag{A.38}$$

integrated in the domain Ω, after applying the divergence theorem, gives the Green formula of type **curl-curl** in Ω, i.e.

$$(\boldsymbol{v}, \mathbf{curl}\, \boldsymbol{w})_\Omega - (\mathbf{curl}\, \boldsymbol{v}, \boldsymbol{w})_\Omega = \langle \boldsymbol{v} \times \boldsymbol{n}, \boldsymbol{w} \rangle_\Gamma, \quad \forall \boldsymbol{v}, \quad \boldsymbol{w} \in \boldsymbol{H}^1(\Omega). \tag{A.39}$$

Appendix B

Discretization of problems

B.1 Finite element (K, S_K, Σ)

This section is extracted from the development by P. Dular [28,31]. Its purpose is to define a discrete structure similar to the continuous one. The discretization process consists in defining what are called finite elements (FEs). A FE is defined by the triplet (K, S_K, Σ), where [28,35,58,78,104]:

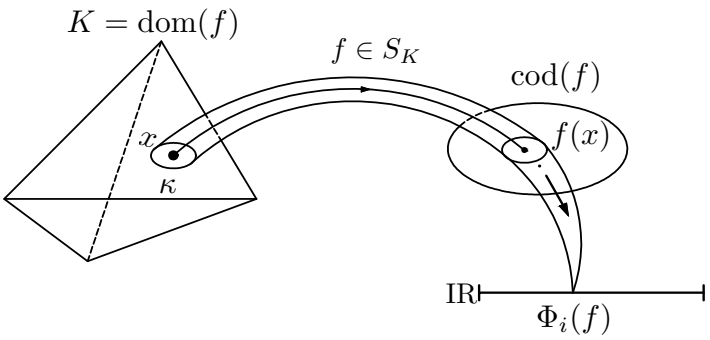

Figure B.1: Spaces associated with a finite element (K, S_K, Σ)

- ✓ K is a domain of space called a geometrical element of $\mathbb{E}^3$ (usually of simple shape, e.g. a tetrahedron, a hexahedron or a prism);
- ✓ S_K is a function space of finite dimension N_K, of the space of scalar or vector valued functions, defined in K with basis functions;
- ✓ Σ is a set of N_K degrees of freedom (or connectors) represented by N_K linear functionals Φ_i, $1 \leq \mathrm{i} \leq N_K$, on the space of scalar or vector-valued functions, defined in space P_K and with values in IR.

Furthermore, any function $u \in P_K$ must be uniquely defined by the degrees of freedom of Σ, which defines the unisolvance of the FE (K, S_K, Σ).

The role of a FE is to interpolate a field in a function space of finite dimension, and this, locally, and generally in a space of simple topology, called a geometric

element. Several FEs can be defined on the same geometric element and then, under certain conditions, can form mixed FEs. Fig. B.1 shows the various spaces which appear in the definition of a FE; the definition of the subspace of points $\kappa \subset K$ is actually associated with the definition of the functionals.

For the most commonly used FEs, the degrees of freedom are associated with nodes of K and the functionals Φ_i are reduced to functions of the coordinates in K; these elements are called nodal FEs. However, the above definition is more general thanks to the freedom let in the choice of the functionals. It will be shown that these can be, in addition to nodal values, integrals along segments, on surfaces or in volumes; the subspace of points $\kappa \subset K$ (Fig. B.1) is then respectively a point, a segment, a surface or a volume.

The FE (K, S_K, Σ) is unisolvant if

$$\forall p \in S_K, \quad \Phi_i(p) = 0; \quad \forall \Phi_i \in \Sigma_K \quad \Rightarrow p \equiv 0. \tag{B.1}$$

In this case, for any function u regular enough, one can define a unique interpolation u_K, called S_K-interplant, such as

$$\Phi_i(u - u_K) = 0; \quad \forall \Phi_i \in \Sigma_K; \quad u_k \in S_K. \tag{B.2}$$

The set Σ_K is said S_K-unisolvant.

Each function $p \in S_K$ can be written as linear combination of functions of a base of S_K, denoted $\{p_i, 1 \leq i \leq n_k\}$, i.e.

$$p = \sum_{i=1}^{n_K} a_i p_i, \quad p \in S_K, \tag{B.3}$$

where a_i and p_i are coefficients and basis functions respectively. As the functionals Φ_j, $1 \leq j \leq n_K$, are linear, we have

$$\Phi_j(p) = \sum_{i=1}^{n_K} a_i \Phi_j(p_i), \quad 1 \leq j \leq n_K. \tag{B.4}$$

And, as $\Phi_j(p) = 0$, $1 \leq j \leq n_k$, leads to $p \equiv 0$, the determinant of the matrix Φ $(\Phi_{ji} = \Phi_j(p_i))$, $1 \leq i, j \leq n_k$, is not equal to zero; indeed the solution of the corresponding system must be identically equal to zero (i.e. $a_i = 0$, $1 \leq i \leq n_k$). Consequently, the system

$$\Phi_j(u) = \Phi_j(u_K) \Leftrightarrow \Phi_j(u) = \sum_{i=1}^{n_K} a_i \Phi_j(p_i), \quad 1 \leq j \leq n_k, \tag{B.5}$$

has a unique solution.

B.2 Sequence of discrete spaces

B.2.1 Basis functions

A mesh of a domain is considered as built with a collection of geometric elements which can be tetrahedra (4 nodes), hexahedra (8 nodes) and prisms (6 nodes)

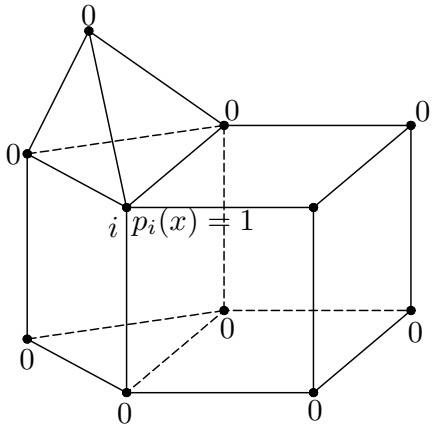

Figure B.2: Collection of different geometric elements.

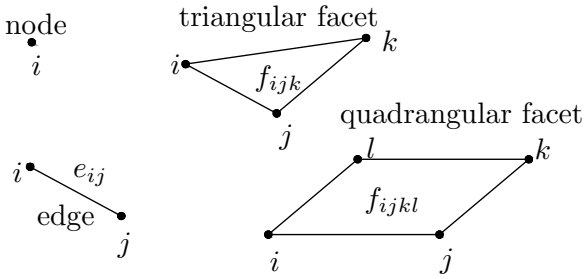

Figure B.3: Geometric entities: node, edge and facets (i,j,k,$l \in N$).

(Fig. B.2) [28, 35]. [28, 35, 58]. The elements are called volumes and their vertices represent nodes. The sets of nodes, edges, facets and volumes of this mesh are denoted by N, E, F and V, respectively. Their sizes are $\#N$, $\#E$, $\#F$ and $\#V$. The *i-th* node of the mesh is denoted by n_i or i. The edges and facets can be defined with ordered sets of nodes. An edge is denoted by e_{ij} or i, j, a triangular facet by f_{ijk} or i, j, k, and a quadrangular facet by f_{ijkl} or i, j, k, l (Fig. B.3).

B.2.2 The nodal functions

For each node $i \in N$, we have the function $p_i(x)$ of coordinates of point x and relative to node n_i, which is equal to 1 at this node, continuously varies in the geometric elements having this node in common, and becomes equal to 0 in other nodes without discontinuity. These functions define the function space of nodal FEs built on the considered geometric elements. The function subspaces associated with each of the finite elements get respective dimensions 4, 8 or 6, for tetrahedra, hexahedra and prisms (Fig. B.2) [28, 35]. For each node $n_i = \{i\}$, is associated the function

$$s_{n_i}(x) = p_i(x). \tag{B.6}$$

The set of functions s_n, $\forall n \in N$, generates the space denoted by S^0.

B.2.3 The edge functions

For each edge $e_{ij} = \{i, j\}$, is associated the vector field [28, 35]

$$\boldsymbol{s}_{e_{ij}} = p_j \, \mathbf{grad}(\sum_{r \in N_{F,j,\bar{i}}} p_r) - p_i \, \mathbf{grad}(\sum_{r \in N_{F,i,\bar{j}}} p_r). \tag{B.7}$$

In this expression, $N_{F,m,\overline{n}}$ is the set of nodes belonging to the face F of the geometrical element including evaluation elements with point x, and including node m but not node n (such a face is uniquely defined for elements with three edges per node) (Fig. B.4) The vector field is zero in all the element non-adjacent to edge e_{ij}. The vector field space generated by $\boldsymbol{s}_{e_{ij}}$, $\forall e \in E$, is denoted by S^1.

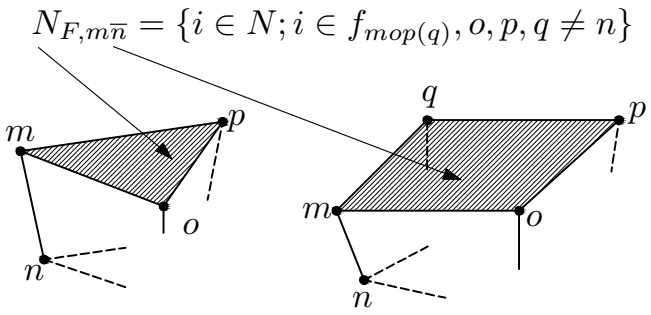

Figure B.4: Definition of the facet associated with notation $N_{F,j,\bar{i}}$.

B.2.4 The facet functions

For a triangular facet $f = f_{ijk} = \{i, j, k\} = \{q_1, q_2, q_3\}$ or a quadrangular facet $f = f_{ijkl} = \{i, j, k, l\} = \{q_1, q_2, q_3, q_4\}$, is associated the vector field [28, 35]

$$\boldsymbol{s}_f = a_f \sum_{c=1}^{N_f} p_{q_c} \, \mathbf{grad}(\sum_{r \in N_{F,q_c,\overline{q}_{c+1}}} p_r) \times \mathbf{grad}(\sum_{r \in N_{F,q_c,\overline{q}_{c-1}}} p_r), \tag{B.8}$$

where N_f is the number of nodes of facet f, $a_f = 2$ if $N_f = 3$ and $a_f = 1$ if $N_f = 4$; with $q_{N_f} = q_0$ and $q_{N_f+1} = q_1$ will be considered. This vector field is zero for all the elements non adjacent to facet f. The vector field space generated by $\boldsymbol{s}_{f_{ijk(l)}}$, $\forall f \in F$, is denoted by S^2.

B.2.5 The volume functions

With a geometric element of the mesh, is associated the scalar function s_v considered as

$$s_v = \frac{1}{\mathrm{vol}(v)} \tag{B.9}$$

This function is equal to zero in all the elements other than element v. The vector field space generated by s_v, $\forall v \in V$, is denoted by S^3.

B.2.6 Properties of basis functions

The developed basis functions give the following results: s_{n_i} is equal to 1 at node n_i, and to 0 at other nodes; the circulation of $\boldsymbol{s}_{e_{ij}}$ is equal to 1 along edge e_{ij}, and to 0 along other edges; the flux of $\boldsymbol{s}_{f_{ijk(l)}}$ is equal to 1 across facet $f_{ijk(l)}$, and to 0 across other facets; and the volume integration of s_v is equal to 1 over volume, and to 0 over other volumes; i.e.

$$s_i(\boldsymbol{x}_j) = \delta_{ij}, \forall i, j \in N \tag{B.10}$$

$$\oint_j \boldsymbol{s_i} \cdot d\boldsymbol{l} = \delta_{ij}, \forall i, j \in E \tag{B.11}$$

$$\int_j \boldsymbol{s_i} \cdot \boldsymbol{n} ds = \delta_{ij}, \forall i, j \in F \tag{B.12}$$

$$\int_j s_i dv = \delta_{ij}, \forall i, j \in V, \tag{B.13}$$

where $\delta_{i,j} = 1$ if $i = j$ and $\delta_{i,j} = 0$ if $i \neq j$.

These properties show up various kinds of functionals and involve that functions s_n, $\boldsymbol{s}_s$ $\boldsymbol{s}_f$, s_v from bases for the spaces they generate. They are then called nodal, edge, facet and volume base functions. The associated FEs are called nodal, edge, facet and volume FEs.

A geometric interpretation of edge and facet functions may be helpful to verify some of their properties. The vector field

$$\mathbf{grad}\, P_{F,m,\overline{n}} = \mathbf{grad}(\sum_{r \in N_{F,m,\overline{n}}} p_r), \tag{B.14}$$

involved in both expressions (B.7) and (B.8), should be analyzed at first. The continuous scalar field,

$$P_{F,m,\overline{n}} = \sum_{r \in N_{F,m,\overline{n}}} p_r, \tag{B.15}$$

gets the characteristic of being equal to 1 at every point on the facet associated with $N_{F,m,\overline{n}}$. This is a property of the nodal functions. Therefore, vector field (B.14) is orthogonal to this facet at every point (see Fig. B.5). The vector field which is the product of p_m and (B.14),

$$p_m\, \mathbf{grad}(\sum_{r \in N_{F,m,\overline{n}}} p_r), \tag{B.16}$$

is consider now. The function p_m is equal to zero on all the edges of the geometric element including point x, except those which are incident to node m. Thus, the circulation of (B.16) is equal to zero along all the edges except $e_{\{m,n\}}$. The field (B.16) is either simply equal to zero on them, or orthogonal to them (Fig. B.5). The combination of two fields in (B.16) with the edges $\{j, i\}$ and $\{i, j\}$ in (B.7) leads

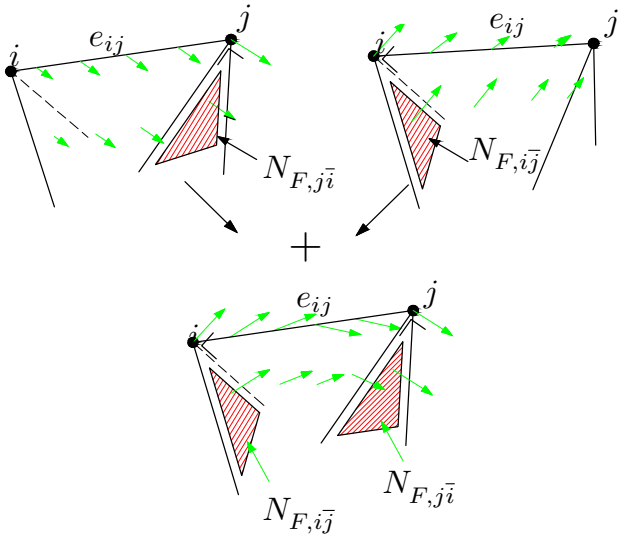

Figure B.5: Geometric interpretation of the edge function s_e.

to a vector field which has the same properties as in (B.16) (Fig. B.5), and has consequently the announced properties of $s_{e_{i,j}}$. The vector field

$$p_{q_c}\,\mathbf{grad}(P_{F,q_c,\bar{q}_{c+1}}) \times \mathbf{grad}(P_{F,q_c,\bar{q}_{c-1}}), \tag{B.17}$$

which occurs in expression (B.8) of $\boldsymbol{s}_f$, is considered now. Both gradients in (B.17)

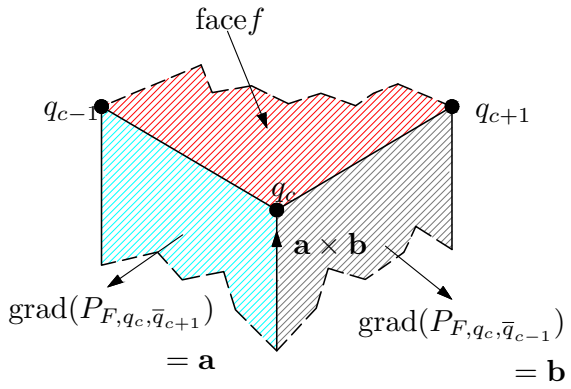

Figure B.6: Vector field $\boldsymbol{a} \times \boldsymbol{b}$ involved in $\boldsymbol{s}_f$.

are shown in Fig B.6. Each one is orthogonal to its associated facet and, thus, their cross product (i.e. $\boldsymbol{a} \times \boldsymbol{b}$ in Fig. B.6) is parallel to both these facets. The flux of this cross product, and in consequence the one of (B.17), is then equal to zero across these facets. The term p_{q_c} in (B.17) enables the flux of (B.17) to be equal to zero across all other facets except facet f. The summation in (B.8) keeps the same property. The flux of $\boldsymbol{s}_f$ across facet f is then the only one to differ from zero (Fig. B.7).

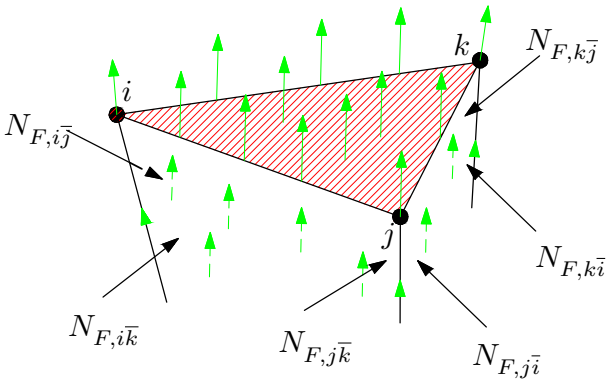

Figure B.7: Geometric interpretation of the facet function s_f.

B.3 Degrees of freedom

The expression of a field in the base of a space S^i $-S^0$ or S^3 for a scalar field, S^1 or S^2 for a vector field $-$gives scalar coefficients, called degrees of freedom. Fields $\phi_i \in S^0$, $\boldsymbol{h} \in S^1$, $\boldsymbol{j} \in S^2$, $\rho \in S^3$ can be respectively expressed as:

$$\phi = \sum_{n \in N} \phi_n s_n, \quad \phi \in S^0, \quad \phi_n = \phi(\boldsymbol{x_n}), \quad n \in N, \tag{B.18}$$

$$\boldsymbol{h} = \sum_{e \in E} h_e \boldsymbol{s}_e, \quad h_e \in S^1, \quad h_e = \int_e \boldsymbol{h} \cdot d\boldsymbol{l}, \quad e \in E, \tag{B.19}$$

$$\boldsymbol{j} = \sum_{f \in F} j_f \boldsymbol{s}_f, \quad j \in S^2, \quad j_f = \int_f \boldsymbol{j} \cdot \boldsymbol{n} ds, \quad f \in F, \tag{B.20}$$

$$\sigma = \sum_{v \in V} \sigma_v s_v, \quad \sigma \in S^3, \quad \sigma_v = \int_v \sigma_i dv, \quad v \in V. \tag{B.21}$$

The degrees of freedom ϕ_n, h_e, j_f and ρ_v are thus, respectively, values at nodes, circulations along edges, fluxes across facets or volume integrals, of the associated fields. This is a consequence of the base functions. The associated linear functionals, as mentioned in the definition of FEs, are thus respectively point-wise evaluations, line, surface and volume integrals.

B.4 Reference elements

We define here the reference elements which are associated with the considered geometric elements, i.e. tetrahedra, hexahedra and prisms. Nodal, edge, facet and volume FEs are defined in these geometric elements.

B.4.1 Reference tetrahedron

The reference tetrahedron T is an element with 4 nodes, 6 edges, 4 facets and 1 volume (Fig. B.8). For $\{i \in N\}$ and $p_i(u, v, w) = s_i(u, v, w)$, the basis functions p_i

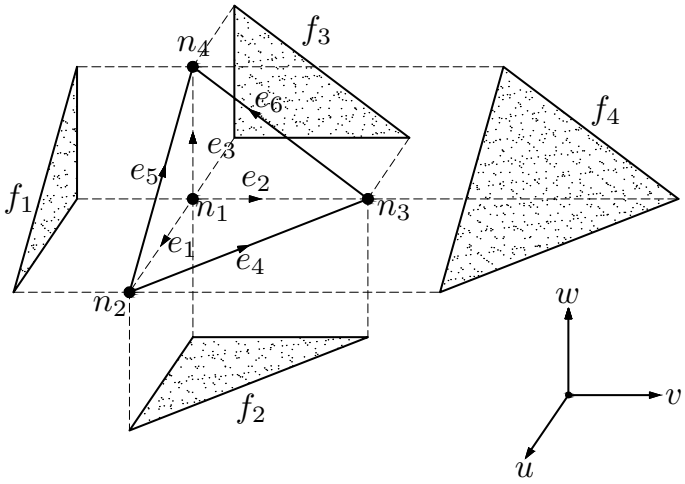

Figure B.8: Reference tetrahedron T.

are [28, 35]:

$$p_1 = 1 - u - v - w, \qquad p_2 = u, \qquad p_3 = v, \qquad p_4 = w. \tag{B.22}$$

B.4.2 Reference hexahedron

The reference hexahedron H is an element with 8 nodes, 12 edges, 6 facets and 1 volume (Fig. B.9). The basis functions p_i are [28, 35]:

$$\begin{aligned}
p_1 &= 1/8\,(1-u)(1-v)(1-w), & p_2 &= 1/8\,(1+u)(1-v)(1-w),\\
p_3 &= 1/8\,(1+u)(1+v)(1-w), & p_4 &= 1/8\,(1-u)(1+v)(1-w),\\
p_5 &= 1/8\,(1-u)(1-v)(1+w), & p_6 &= 1/8\,(1+u)(1-v)(1+w),\\
p_7 &= 1/8\,(1+u)(1+v)(1+w), & p_8 &= 1/8\,(1-u)(1+v)(1+w).
\end{aligned} \tag{B.23}$$

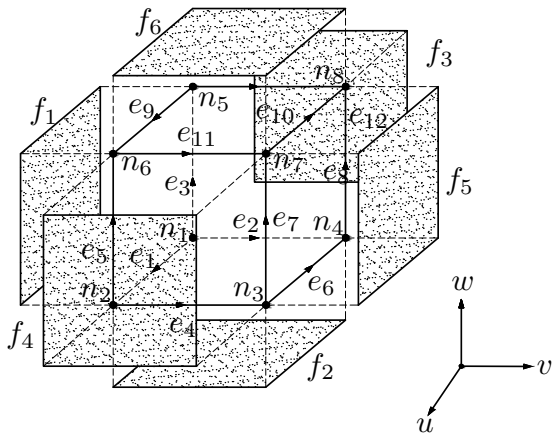

Figure B.9: Reference hexahedron H.

B.4.3 Reference prism

The reference prism P is an element with 6 nodes, 9 edges, 5 facets and 1 volume (Fig. B.10). The basis functions p_i are [28, 35]:

$$\begin{aligned} p_1 &= 1/2\,(1-u-v)(1-w), & p_2 &= 1/2\,u\,(1-w), \\ p_3 &= 1/2\,v\,(1-w), & p_4 &= 1/2\,(1-u-v)(1+w), \\ p_5 &= 1/2\,u\,(1+w), & p_6 &= 1/2\,v\,(1+w). \end{aligned} \tag{B.24}$$

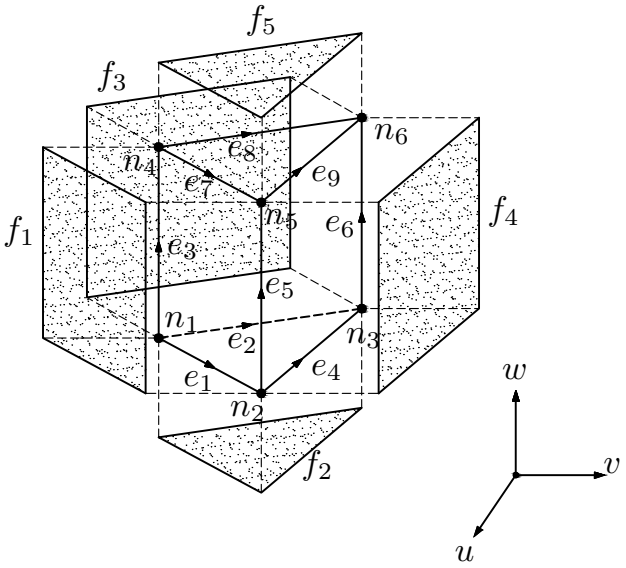

Figure B.10: Reference prism P.

Appendix C

Analytic solutions

The purpose of this part is to find a relation linking the traces $\boldsymbol{n} \times \boldsymbol{h}$ and $\boldsymbol{n} \times \boldsymbol{e}$ of the magnetic and electric fields on both sides of thin regions written in (1.56) and (1.57). Maxwell's equations (1.32) and (1.33) can be rewritten, in harmonic regime, as

$$\mathbf{curl}\,\mathbf{curl}\,\boldsymbol{h} = -\jmath\omega\sigma\mu\,\boldsymbol{h} \quad \text{and} \quad \mathbf{curl}\,\mathbf{curl}\,\boldsymbol{e} = -\jmath\omega\sigma\mu\,\boldsymbol{e}. \tag{C.1a,b}$$

Let us consider an infinitely wide structure Ω_t illustrated in Fig. C.1. The equation involving the magnetic field is written in Cartesian coordinates. Due to the sym-

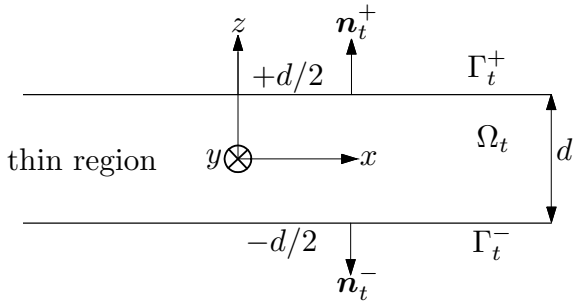

Figure C.1: Infinitely wide region Ω_t of finite thickness d

metry of the problem, all derivatives with respect to x and y vanish, as well as the z-component of the field. Equation (C.1 a) thus simply leads to two one-dimensional equations [58, 60, 61, 92], i.e.

$$\frac{\partial^2 h_x}{\partial z^2} = \jmath\omega\sigma\mu\,h_x \quad \text{and} \quad \frac{\partial^2 h_y}{\partial z^2} = \jmath\omega\sigma\mu\,h_y. \tag{C.2a,b}$$

Posing $\theta^2 = \jmath\omega\sigma\mu$, (C.2 a) becomes

$$\frac{\partial^2 h_x}{\partial z^2} = \theta^2 h_x, \quad \text{with} \quad \theta = \frac{1+i}{\delta} \quad \text{and} \quad \delta = \sqrt{\frac{2}{\omega\sigma\mu}}. \tag{C.3}$$

Equation (C.3) has solutions of the forms

$$h_x(z) = K_1 \exp^{-\theta z} + K_2 \exp^{\theta z}, \tag{C.4}$$

where the two constants K_1 and K_2 are determined thanks to the BCs [58], i.e. $h_x(d/2) = h_x^+$ and $h_x(-d/2) = h_x^-$. After some elementary transformations, (C.4) becomes

$$h_x(z) = \frac{1}{\sinh(\theta d)}\Big[h_x^- \sinh\big(\theta(d/2 - z)\big) + h_x^+ \sinh\big(\theta(d/2 + z)\big)\Big]. \tag{C.5}$$

Let us now consider the actual case of a finite width thin shell Ω_t (Fig. C.2), which is assumed sufficiently thin and flat. The magnetic field has no component along the thickness of the shell, and the other components fulfill relations similar to (C.5). If we denote the tangential component $\boldsymbol{n}\times(\boldsymbol{f}\times\boldsymbol{n})$ of a field $\boldsymbol{f}$ on a surface of normal $\boldsymbol{n}$ by $\boldsymbol{f}_t$, we can define a local coordinate system (v, w, t) whose t-coordinate is chosen in the same direction as the tangential component $\boldsymbol{f}_t$, and whose w-component is directed along the thickness of the shell (Fig. C.2). The expression of the magnetic

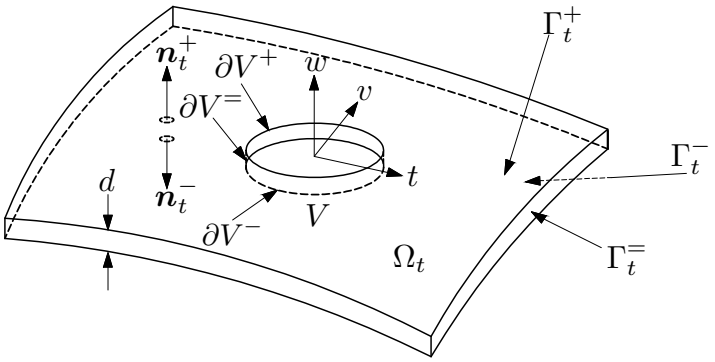

Figure C.2: Thin shell Ω_t

field can be written inside the shell as

$$\boldsymbol{h}_t(w) = \frac{1}{\sinh(\theta d)}\Big[\boldsymbol{h}_t\big|_{\Gamma_t^-} \sinh\big(\theta(d/2 - w)\big) + \boldsymbol{h}_t\big|_{\Gamma_t^+} \sinh\big(\theta(d/2 + w)\big)\Big], \tag{C.6}$$

where $\boldsymbol{h}_t^-$, $\boldsymbol{h}_t^+$ are the tangential magnetic field on both sides of Ω_t. To get a relation linking the traces $\boldsymbol{n}\times\boldsymbol{h}$ and $\boldsymbol{n}\times\boldsymbol{e}$ of the magnetic and electric fields on positive side γ_t^+ and negative side γ_t^- of Ω_t, we consider a magnetic field $\boldsymbol{h}$ whose only non-zero component is directed along t. Integrating (1.32) over the elementary volume V of boundary $\partial V = \partial V^+ \cup \partial V^- \cup \partial V^=$ (Fig. C.2), we get, assuming that the area of ∂V^+ and ∂V^- is equal to a:

$$\int_V \mathbf{curl}\,\boldsymbol{h}\, dV = \int_V \boldsymbol{j}\, dV = \sigma a \int_{-d/2}^{d/2} \boldsymbol{e}_t(w)\, dw = \sigma a \frac{1}{\theta}\tanh\big(\frac{\theta d}{2}\big)(\boldsymbol{e}_t\big|_{\Gamma_t^-} + \boldsymbol{e}_t\big|_{\Gamma_t^+}). \tag{C.7}$$

Since $\int_V \mathbf{curl}\,\boldsymbol{h} = \int_{\partial V^+} \boldsymbol{n}_t^+ \times \boldsymbol{h} + \int_{\partial V^-} \boldsymbol{n}_t^- \times \boldsymbol{h}$, we thus locally have

$$\boldsymbol{n}_t^+ \times \boldsymbol{h}\big|_{\Gamma_t^+} + \boldsymbol{n}_t^- \times \boldsymbol{h}\big|_{\Gamma_t^-} = \sigma \frac{1}{\theta}\tanh\big(\frac{\theta d}{2}\big)(\boldsymbol{e}_t\big|_{\Gamma_t^-} + \boldsymbol{e}_t\big|_{\Gamma_t^+}). \tag{C.8}$$

Analogously, considering an electric field $\boldsymbol{e}$ whose only non-zero component is directed along t and integrating (1.33) over the elementary volume V, we get

$$\boldsymbol{n}_t^+ \times \boldsymbol{e}\big|_{\Gamma_t^+} + \boldsymbol{n}_t^- \times \boldsymbol{e}\big|_{\Gamma_t^-} = -j\omega\mu\frac{1}{\theta}\tanh\big(\frac{\theta d}{2}\big)(\boldsymbol{h}_t\big|_{\Gamma_t^-} + \boldsymbol{h}_t\big|_{\Gamma_t^+}). \tag{C.9}$$

The normals for the thin shell Ω_t are defined $\boldsymbol{n}_t = \boldsymbol{n}_t^+ = -\boldsymbol{n}_t^-$ and we can impose

$$\beta = \frac{1}{\theta}\tanh\big(\frac{\theta d}{2}\big). \tag{C.10}$$

Relations (C.8) and (C.9) are finally written as

$$\boldsymbol{n}_t \times \boldsymbol{h}\,\big|_{\Gamma_t^+} - \boldsymbol{n}_t \times \boldsymbol{h}\,\big|_{\Gamma_t^-} = \sigma\beta\,(\boldsymbol{e}_t\big|_{\Gamma_t^+} + \boldsymbol{e}_t\big|_{\Gamma_t^-}), \tag{C.11}$$

$$\boldsymbol{n}_t \times \boldsymbol{e}\,\big|_{\Gamma_t^+} - \boldsymbol{n}_t \times \boldsymbol{e}\,\big|_{\Gamma_t^-} = -\partial_t\big[\mu\beta\,(\boldsymbol{h}_t\big|_{\Gamma_t^+} + \boldsymbol{h}_t\big|_{\Gamma_t^-})\big]. \tag{C.12}$$

Relations (C.11) and (C.12) relate the magnetic field and the electric field on both sides of Ω_t. They are often called the impedance boundary conditions (IBCs) for the thin shell Ω_t [5,74,97]. Note that if θd is small enough, (C.10) approaches to $\beta \approx d/2$, and the magnetic and electric fields vary linearly along the shell thickness.

Bibliography

[1] F. Alauzet and M. Mehrenberger, *P^1-conservative solution interpolation on unstructured triangular meshes*, International Journal of Numerical Modelling **84** (2010), no. 13, 1552–1588.

[2] R. Albanese and G. Rubinacci, *Magnetostatic field computations in terms of two-component vector potentials*, International Journal for Numerical Methods in Engineering **29** (1990), 515–532.

[3] P. Alotto, F. Freschi, and M. Repetto, *Multiphysics problems via the cell method: The role of tonti diagrams*, IEEE Transactions on Magnetics **46** (2010), no. 8, 2959–2962.

[4] C. A. Balanis, *Advanced engineering electromagnetics*, John Wiley & Sons, 1988.

[5] O. Biró, I. Bárdi, K. Preis, W. Renhart, and K. R. Richter, *A finite element formulation for eddy current carrying ferromagnetic thin sheets*, IEEE Transactions on Magnetics **33** (1997), no. 2, 1173–1178.

[6] O. Biró and K. Preis, *On the use of the magnetic vector potential in the finite element analysis of three-dimensional eddy currents*, IEEE Transactions on Magnetics **25** (1989), no. 4, 3145–3159.

[7] M. J. Bluck and S. P. Walker, *High-order discrete helmholtz decompositions for the electric field integral equation*, IEEE Transactions on Antennas and Propagation **55** (2007), no. 5, 1338–1347.

[8] A. Bossavit, *Two dual formulations of the 3D eddy currents problem*, in Proc. COMPEL **4** (1984), 103–116.

[9] ———, *Magnetostatic problems in multiply connected regions: some properties of the curl operator*, IEE Proceedings **135, Pt. A** (1988), no. 3, 179–187.

[10] ———, *Whitney forms: a class of finite elements for three-dimensional computations in electromagnetism*, IEE Proceedings **135, Pt. A** (1988), no. 8, 493–499.

[11] ———, *Un nouveau point de vue sur les éléments mixtes*, Bulletin de la Société de Mathématiques Appliquées et Industrielles **20** (1989), 23–35.

[12] ———, *Computational electromagnetism. Variational formulations, edge elements, complementarity*, Academic Press, 1998.

[13] ———, *A rationale for "edge-elements" in 3-D fields computations*, IEEE Transactions on Magnetics **24** (1998), no. 1, 74–79.

[14] A. Bossavit, A. Vourdas, and K. J. Binns, *Correspondence on "magnetostatics with scalar potentials in multiply connected regions"*, IEE Proceedings **136, Pt. A** (1989), no. 5, 260–261.

[15] Y. Boubendir, X. Antoine, and C. Geuzaine, *A quasi-optimal non-overlapping domain decomposition algorithm for the helmholtz equation*, Journal of Computational Physics **231** (2012), no. 2, 262–280.

[16] M. Boutaayamou, R. V. Sabariego, and P. Dular, *An iterative finite element perturbation method for computing electrostatic field distortions*, IEEE Transactions on Magnetics **44** (2008), no. 6, 746–749.

[17] X. Brunotte and G. Meunier, *Line element for efficient computation of the magnetic field created by thin iron plates*, IEEE Transactions on Magnetics **26** (1990), no. 5, 2196–2198.

[18] ———, *Line element for efficient computation of the magnetic field created by thin iron plates*, IEEE Transactions on Magnetics **26** (1990), no. 5, 2196–2198.

[19] J. L. Coulomb, P. Dular, F. Pirou, Z. Ren, F. Bouiliault, B. Bendelier, F. R. Damidau, A. K. Lebouc, G. Meunier, F. Ossart, C. Geurin, Y. Lefevre, P. Lombard, Y. L. Floch, V. Leconte, J. Lobry, E. Nens, C. Broche, M. Felitachi, J. Foulargar, G. Reyne, F. Flunian, and P. Masse, *Finite element method for electromagnetic modeling*, John Wiley & Sons, 2002.

[20] Vuong Q. Dang, P. Dular, R. V. Sabariego, M. V. Ferreira da Luz, P. Kuo-Peng, L. Krahenbuhl, and C. Geuzaine, *Subproblem method with dual finite element formulations for accurate thin shell models*, Proceedings of the XV International Symposium on Electromagnetic Field in Mechatronics, Electrical Engineering (Madeira, Portugal), September 2011.

[21] Vuong Q. Dang, P. Dular, R. V. Sabariego, L. Krähenbühl, and C. Geuzaine, *Accurate $\boldsymbol{h}$-conform finite element of multiply connected thin regions via subproblem method*, Proceedings of 5th Biennial IEEE Conference on the Electromagnetic Field Computation (Oita, Japan), November 2012.

[22] ———, *Subproblem approach for thin shell dual finite element formulations*, IEEE Transactions on Magnetics **48** (2012), no. 2, 407–410.

[23] ———, *Dual formulations for accurate thin shell models in a finite element subproblem method*, Proceedings of 19th Biennial IEEE Conference on the Computation of Electromagnetic Fields (Budapest, Hungary), July 2013.

[24] ———, *Subproblem approach for modeling multiply connected thin regions with an* $\boldsymbol{h}$*-conformal magnetodynamic finite element formulation*, European Physical Journal Applied Physics, accepted for publication, 2013.

[25] ———, *Subproblem* $\boldsymbol{h}$*-conform formulation for accurate thin shell models between conducting and nonconducting regions*, Proceedings of 9th International Symposium on Electric and Magnetic Fields (Bruges, Belgium), April 2013.

[26] R. Dautray and J.-L. Lions, *Analyse mathématique et calcul numérique*, vol. 5, Spectres des Opérateurs, Masson, 1988.

[27] D. M. Drury, *The unification of the lorentz and coulomb gauges of electromagnetic theory*, IEEE Transactions on Magnetics **19** (2000), no. 1, 69–72.

[28] P. Dular, *Modélisation du champ magnétique et des courants induits dans des systèmes tridimensionnels non linéaires*, Ph.D. thesis 152, University of Liège, Belgium, Faculty of Applied Sciences, November 1994.

[29] ———, *The benefits of nodal and edge elements coupling for discretizing global constraints in dual magnetodynamic formulations*, Journal of Computational and Applied Mathematics **168** (2004), 165–178.

[30] P. Dular, Vuong Q. Dang, R.V. Sabariego, L. Krähenbühl, and C. Geuzaine, *Correction of thin shell finite element magnetic models via a subproblem method*, IEEE Transactions on Magnetics **47** (2011), no. 5, 1158–1161.

[31] P. Dular, A. Genon, J.-Y.Hody, W. Legros, J. Mauhin, and A. Nicolet, *Coupling between edge finite elements, nodal finite elements and boundary elements for the calculation of 3-D of eddy currents*, IEEE Transactions on Magnetics **29** (1993), no. 2, 1470–1473.

[32] P. Dular, C. Geuzaine, and W. Legros, *A natural method for coupling magnetodynamic* $\boldsymbol{h}$*-formulations and circuit equations*, IEEE Transactions on Magnetics **35** (1999), no. 3, 1626–1629.

[33] P. Dular, F. Henrotte, and W. Legros, *A general and natural method to define circuit relations associated with magnetic vector potential formulations*, IEEE Transactions on Magnetics **35** (1999), no. 3, 1630–1633.

[34] P. Dular, F. Henrotte, F. Robert, A. Genon, and W. Legros, *A generalized source magnetic field calculation method for inductors of any shape*, IEEE Transactions on Magnetics **33** (1997), no. 2, 1398–1401.

[35] P. Dular, J.-Y. Hody, A. Nicolet, A. Genon, and W. Legros, *Mixed finite elements associated with a collection of tetrahedra, hexahedra and prisms*, IEEE Transactions on Magnetics **30** (1994), no. 5, 2980–2983.

[36] P. Dular and P. Kuo-Peng, *Dual finite element formulation for the three-dimensional modeling of both inductive and capacitive effects in massive inductors*, IEEE Transactions on Magnetics **42** (2006), no. 4, 743–746.

[37] P. Dular, P. Kuo-Peng, C. Geuzaine, N. Sadowski, and J. P. A. Bastos, *Dual magnetodynamic formulations and their source fields associated with massive and stranded inductors*, IEEE Transactions on Magnetics **36** (2000), no. 4, 1293–1299.

[38] P. Dular, P. Kuo-Peng, and W. Legros, *Une méthode efficace et robuste de discrétisation temporelle pour le couplage éléments finis – équations de circuit*, Proceedings of NUMELEC'2000, 3ème Conférence Européenne sur les Méthodes Numériques en Électromagnétisme (Poitiers, France), March 2000, pp. 92–93.

[39] P. Dular, W. Legros, and A. Nicolet, *Coupling of local and global quantities in various finite element formulations and its application to electrostatics, magnetostatics, and magnetodynamics*, IEEE Transactions on Magnetics **34** (1998), no. 5, 3078–3081.

[40] P. Dular, A. Nicolet, A. Genon, and W. Legros, *A discrete sequence associated with mixed finite elements and its gauge condition for vector potentials*, IEEE Transactions on Magnetics **31** (1995), no. 3, 1356–1359.

[41] P. Dular and R. V. Sabariego, *A perturbation finite element method for modeling moving conductive and magnetic regions without remeshing*, in Proc. COMPEL **26** (2007), no. 3, 700–711.

[42] ———, *A perturbation method for computing field distorions due to conductive regions with $\boldsymbol{h}$-conform magnetodynamic finite element formulations*, IEEE Transactions on Magnetics **43** (2007), no. 4, 1293–1296.

[43] P. Dular, R. V. Sabariego, M. V. Ferreira da Luz, P. Kuo-Peng, and L. Krahenbuhl, *Perturbation finite-element method for magnetic circuits*, IET Sci., Meas. Technol **2** (2008), no. 6, 440–446.

[44] ———, *Magnetic model refinement via a perturbation finite element method-from 1-D to 3-D*, in Proc. COMPEL (2009), 974–988.

[45] ———, *Perturbation finite element method for magnetic model refinement of air gaps and leakage fluxes*, IEEE Transactions on Magnetics **45** (2009), no. 3, 1400–1403.

[46] P. Dular, R. V. Sabariego, C. Geuzaine, M. V. Ferreira da Luz, P. Kuo-Peng, and L. Krahenbuhl, *Finite element magnetic models via a coupling of subproblems of lower dimensions*, IEEE Transactions on Magnetics **46** (2010), no. 8, 2827–2830.

[47] P. Dular, R. V. Sabariego, J.Gyselinck, and L. Krähenbühl, *Subdomain finite element method for efficiently considering strong skin and proximity effects*, in Proc. COMPEL (2007), 974–985.

[48] P. Dular, N. Sadowski, and J. P. A. Bastos, *Dual complete procedures to take stranded inductors into account in magnetic vector potential formulations*, IEEE Transactions on Magnetics **36** (2000), no. 4, 1600–1605.

[49] C. R. I. Emson and J. Simkin, *An optimal method for 3-D eddy currents*, IEEE Transactions on Magnetics **19** (1983), no. 6, 2450–2452.

[50] G. Eriksson, *Efficient 3d simulation of thin conducting layers of arbitrary thickness*, IEEE Transactions on Electromagnetic Compatibility (2007), 1–6.

[51] Z. Badics et al, *An effective 3D finite element scheme for computing electromagnetic field distorsions due to defects in eddy-current nondestructive evaluation*, IEEE Transactions on Magnetics **33** (1997), no. 2, 1012–1020.

[52] P.E. Farrell and J. R. Maddison, *Conservative interpolation between volume meshes by local galerkin projection*, Computer Methods in Applied Mechanics and Engineering **200** (2011), no. 1-4, 89 – 100.

[53] M. Feliziani and F. Maradei, *Edge element analysis of complex configurations in presence of shields*, IEEE Transactions on Magnetics **33** (1997), no. 2, 1548–1551.

[54] A. C. Fowler, *Mathematical models in the applied sciences*, Cambridge University Press, 1997.

[55] F. Gardiol, *Traité d'électricité*, Électromagnétisme Vol. III, Éditions Georgi, 1979.

[56] C. Garing, *Milieux magnétiques*, Ellipses, 1995.

[57] *GetDP, a general environment for the treatment of discrete problems*, 1997–2012, http://www.geuz.org/getdp/.

[58] C. Geuzaine, *High order hybrid finite element schemes for Maxwell's equations taking thin structures and global quantities into account*, Ph.D. thesis, University of Liège, Belgium, Faculty of Applied Sciences, December 2001.

[59] C. Geuzaine, O. Bruno, and F. Reitich, *On the $\mathcal{O}(1)$ solution of multiple-scattering problems*, IEEE Transactions on Magnetics **41** (2005), no. 5, 1488–1491.

[60] C. Geuzaine, P. Dular, and W. Legros, *Dual formulations for the modeling of thin conducting magnetic shells*, COMPEL **18** (1999), no. 3, 385–397.

[61] C. Geuzaine, P. Dular, B. Meys, and W. Legros, *Dual formulations for the modeling of thin electromagnetic shells using edge elements*, IEEE Transactions on Magnetics **36** (2000), no. 4, 799–803.

[62] C. Geuzaine, B. Meys, P. Dular, F. Henrotte, and W. Legros, *A galerkin projection method for mixed finite elements*, IEEE Transactions on Magnetics **35** (1999), no. 3, 1438–1441.

[63] C. Geuzaine, A. Vion, R. Gaignaire, P. Dular, and R. V. Sabariego, *An amplitude finite element formulation for multiple-scattering by a collection of convex obstacles*, IEEE Transactions on Magnetics **46** (2010), no. 8, 2963–2966.

[64] C. Golovanov, Y. Maréchal, and G. Meunier, *3D edge element based formulation coupled to electric circuits*, IEEE Transactions on Magnetics **34** (1998), no. 5, 3162–3165.

[65] C. Guérin and G. Meunier, *3-D magnetic scalar potential finite element formulation for conducting shells coupled with an external circuit*, IEEE Transactions on Magnetics **48** (2012), no. 2, 323–326.

[66] C. Guérin, G. Tanneau, G. Meunier, X. Brunotte, X. Albertini, and B. J, *Three dimensional magnetostatic finite elements for gaps and iron shell using magnetic scalar potentials*, IEEE Transactions on Magnetics **30** (1994), no. 5, 2885–2888.

[67] J. Gyselinck, P. Dular, C. Geuzaine, and W. Legros, *Harmonic balance finite element modelling of electromagnetic devices: a novel approach*, IEEE Transactions on Magnetics **38** (2002), no. 2, 521–524.

[68] M. Hafner, F. Henrotte, M. H. Gracia, and K. Hameyer, *An energy-based harmonic constitutive law for magnetic cores with hysteresis*, IEEE Transactions on Magnetics **44** (2008), no. 6, 922–925.

[69] R. F. Harrington, *Time-harmonic electromagnetic fields*, McGraw-Hill, 1961.

[70] H. Hedia, *Modélisation non linéaire des effets thermiques dans les systèmes magnétodynamiques*, Ph.D. thesis 176, University of Liège, Belgium, Faculty of Applied Sciences, February 1997.

[71] F. Henrotte, *Modélisation des efforts électromagnétiques et de leurs effets dans des structures quelconques*, Ph.D. thesis 201, University of Liège, Belgium, Faculty of Applied Sciences, February 2000.

[72] C. Herault, *Boundary and interface conditions meshless methods for EM field analysis*, IEEE Transactions on Magnetics **35** (1999), no. 3, 1450–1453.

[73] C. L. Holloway, *Impedance-type boundary conditions for a periodic interface between a dielectric and a highly conducting medium*, IEEE Transactions on Antennas and Propagation **48** (2000), no. 10, 1660–1672.

[74] H. Igarashi, A. Kost, and T. Honma, *A three dimensional analysis of magnetic fields around a thin magnetic conductive layer using vector potential*, IEEE Transactions on Magnetics **34** (1998), no. 5, 2539–2542.

[75] J. D. Jackson, *Classical electrodynamics*, third ed., John Wiley & Sons, 1998.

[76] D. Jiles, *Magnetism and magnetic materials*, Chapman and Hall, 1991.

[77] J. Jin, *The finite element method in electromagnetics*, John Wiley & Sons, 2002.

[78] C. Johnson, *Numerical solution of partial differential equations by the finite element method*, Cambridge University Press, 1987.

[79] A. Kameari, *Calculation of transient 3D eddy current using edge-elements*, IEEE Transactions on Magnetics **26** (1990), no. 2, 466–469.

[80] Y. Kanai, T. Abe, M. Sengoku, T. Iijima, M. Iizuka, and K. Mukasa, *New formulation of finite-element method with gauge condition for three-dimensional magnetic field analysis*, IEEE Transactions on Magnetics **24** (1988), no. 6, 3123–3125.

[81] L. Kettunen, K. Forsman, and A. Bossavit, *Discrete spaces for div and curl-free fields*, IEEE Transactions on Magnetics **34** (1998), no. 5, 2551–2554.

[82] ———, *Gauging in Whitney spaces*, IEEE Transactions on Magnetics **35** (1999), no. 3, 1466–1469.

[83] A. G. Kladas and J. A. Tegopoulos, *A new scalar potential formulation for 3-D magnetostatics necessitating no source field calculation*, IEEE Transactions on Magnetics **28** (1992), no. 2, 1103–1106.

[84] S. Koruglu, R. Sergeant, R. V. Sabariego, Q. V. Dang, and M. De Wulf, *Influence of contact resistance on shielding efficiency of shielding gutters for high-voltage cables*, IET Electric Power Application **5** (2011), no. 9, 715–720.

[85] P. R. Kotiuga, *Hodge decomposition and computational electromagnetics*, Ph.D. thesis, Mc Gill University, Montreal, 1984.

[86] ———, *On making cuts for magnetic scalar potentials in multiply connected regions*, Journal of Applied Physics **63** (1987), no. 8, 3916–3918.

[87] ———, *An algorithm to make cuts for magnetic scalar potentials in tetrahedral meshes based on the finite element method*, IEEE Transactions on Magnetics **25** (1989), no. 5, 4129–4131.

[88] ———, *Magnetostatics with scalar potentials in multiply connected regions*, IEE Proceedings **137, Pt. A** (1990), no. 4, 231–232.

[89] L. Krähenbühl and D. Muller, *Thin layers in electrical engineering. Example of shell models in analyzing eddy-currents by boundary and finite element methods*, IEEE Transactions on Magnetics **29** (1993), no. 2, 1450–1455.

[90] S. V. Kulkarni, J. C. Olivares, R. Escarela-Perez, V. K. Lakhiani, and J. Turowski, *Evaluation of eddy currents losses in the cover plates of distribution transformers*, IET Sci., Meas. Technol **151** (2004), no. 5, 313–318.

[91] G. Lacroux, *Les aimants permanents*, Lavoisier, 1989.

[92] T. Le-Duc, C. Guérin, O. Chadebec, and J.-M. Guichon, *A new integral formulation for eddy current computation in thin conductive shells*, IEEE Transactions on Magnetics **48** (2012), no. 2, 427–430.

[93] P. J. Leonard and D. Rodger, *Voltage forced coils for 3D finite element method electromagnetic model*, IEEE Transactions on Magnetics **24** (1988), no. 5, 2579–2581.

[94] P. Lombard and G. Meunier, *A general purpose method for electric and magnetic combined problems for 2D, axisymmetric and transient problems*, IEEE Transactions on Magnetics **29** (1993), no. 2, 1737–1740.

[95] W. S. Massey, *Homology and cohomology theory*, Marcel Dekker, 1978.

[96] Matthew and N. O. Sadiku, *Numerical techniques in electromagnetics*, CRC Press, 1992.

[97] I. D. Mayergoyz and G. Bedrosian, *On calculation of 3-D eddy currents in conducting and magnetic shells*, IEEE Transactions on Magnetics **31** (1995), no. 3, 1319–1324.

[98] G. Meunier, H. T. Luong, and Y. Maréchal, *Computation of coupled problem of 3D eddy current and electric circuit using t_0-t-ϕ formulation*, IEEE Transactions on Magnetics **34** (1998), no. 5, 3074–3077.

[99] B. Meys, *Modélisation des champs électromagnétiques aux hyperfréquences par la méthode des éléments finis. Application aux problème du chauffage diélectrique*, Ph.D. thesis, University of Liège, Belgium, Faculty of Applied Sciences, December 1999.

[100] B. Meys, C. Geuzaine, F. Henrotte, P. Dular, and W. Legros, *Dual harmonic and time approaches for the design of microwave device*, IEEE Transactions on Magnetics **35** (1999), no. 3, 1829–1832.

[101] T. Morisue, *A comparison of the coulomb gauge and lorentz gauge magnetic vector potential formulations for 3d eddy current calculations*, IEEE Transactions on Magnetics **19** (1993), no. 2, 1372–1375.

[102] T. Nakata, N. Takahashi, K. Fujiwara, and Y. Okada, *Improvements of the T-Ω method for 3-D eddy current analysis*, IEEE Transactions on Magnetics **24** (1988), no. 1, 94–97.

[103] M. H. Nayfeh and M. K. Brussel, *Electricity and magnetism*, John Wiley & Sons, 1985.

[104] J.-C. Nédélec, *A new family of mixed finite elements in R^3*, Numerische Mathematik **50** (1986), 57–81.

[105] S. Niikura and A. Kameari, *Analysis for coupled problems between eddy currents and dynamic deflections of a thin shell structure*, IEEE Transactions on Magnetics **30** (1994), no. 5, 3284–3287.

[106] O.Biro, K. Preis, and W. Renhart, *Finite element analysis of 3D multiply connected eddy current problems*, IEEE Transactions on Magnetics **25** (1989), no. 5, 4009–4011.

[107] T. Ohnishi and N. Takahashi, *Effective optimal design of 3-d magnetic device having complicated coil using edge element and biot-savart method*, IEEE Transactions on Magnetics **38** (2002), no. 2, 1021–1024.

[108] F. Olyslager, *Field decomposition and factorization of the helmholtz determinant operator for bi-anisotropic media*, IEEE Transactions on Antennas and Propagation **49** (2001), no. 4, 660–665.

[109] T. Onuki, S. Wakao, and T. Yamamura, *Physical meaning of gauge conditions in eddy current analysis*, IEEE Transactions on Magnetics **29** (1993), no. 6, 2452–2454.

[110] G. Parent, P. Dular, J.-P. Ducreux, and F. Piriou, *Using a galerkin projection method for coupled problems*, IEEE Transactions on Magnetics **44** (2008), no. 6, 830–833.

[111] G. Parent, P. Dular, F. Piriou, and A. Abakar, *Accurate projection method of source quantities in coupled finite-element problems*, IEEE Transactions on Magnetics **45** (2009), no. 3, 1132–1135.

[112] K. Preis, I. Bárdi, O. Biró, C. Magele, G. Vrisk, and K. R. Richter, *Different finite element formulations of 3D magnetostatic fields*, IEEE Transactions on Magnetics **28** (1992), no. 2, 1056–1059.

[113] S. Ramo, J. R. Whinnery, and T. Van Duzer, *Fields and waves in communication electronics*, John Wiley & Sons, 1984.

[114] F. Rapetti, F. Bouillault, L. Santandrea, A. Buffa, Y. Maday, and A. Razek, *Calculation of eddy currents with edge elements on matching grids in moving structures*, IEEE Transactions on Magnetics **36** (2000), no. 4, 1351–1355.

[115] D. Q. Ren, T. Park, B. Mirican, S. McFee, and D. Giannacopoulos, *A methodology for performance modeling and simulation validation of parallel 3-d finite element mesh refinement with tetrahedra*, IEEE Transactions on Magnetics **44** (2008), no. 6, 1406–1409.

[116] Z. Ren, *Influence of the R.H.S. on the convergence behaviour of the curl-curl equation*, IEEE Transactions on Magnetics **32** (1996), no. 3, 655–658.

[117] R. V. Sabariego, *The fast multipole method for electromagnetic field computation in numerical and physical hybrid systems*, Ph.D. thesis, University of Liège, Belgium, Faculty of Applied Sciences, December 2004.

[118] R. V. Sabariego, C. Geuzaine, P. Dular, and J. Gyselinck, *Nonlinear time-domain finite element modeling of thin electromagnetic shells*, IEEE Transactions on Magnetics **45** (2009), no. 3, 976–979.

[119] M. S. Sarto, *A new model for the FDTD analysis of the shielding performances of thin composite structures*, IEEE Transactions on Electromagnetic Compatibility **41** (1999), no. 4, 298–306.

[120] S. A. Schelkunoff and H. T. Friis, *Antennas theory and practice*, John Wiley & Sons, 1952.

[121] I. Sebatyen, S. Gyimothy, J. Pavo, and O. Biro, *Calculation of losses in laminated ferromagnetic materials*, IEEE Transactions on Magnetics **40** (2004), no. 2, 924–927.

[122] T. B. A. Senior, *Impedance boundary conditions for imperfectly conducting surface*, IET Sci., Meas. Technol **8** (1960), 418–436.

[123] J. A. Stratton, *Electromagnetic theory*, McGraw-Hill, 1941.

[124] P. Thomas and Y. Le Menach, *A three-dimensional electromagnetic shell finite element for coupled vector-scalar potential formulations*, IEEE Transactions on Magnetics **48** (2012), no. 2, 823–826.

[125] E. Tonti, *On the geometrical structure of electromagnetism*, Gravitation, Electromagnetism and Geometrical Structures (Pitagora, Bologna, Italy) (G. Ferrarese, ed.), 1996, pp. 281–308.

[126] H. Tsuboi, *Transient eddy current analysis of pulsed eddy current testing by finite element method*, IEEE Transactions on Magnetics **40** (2004), no. 2, 1330–1333.

[127] H. Tsuboi, T. Asahara, F. Kobayashi, and T. Misaki, *Eddy current analysis on thin conducting plate by an integral equation method using edge elements*, IEEE Transactions on Magnetics **33** (1997), no. 2, 1346–1349.

[128] P. A. Tuan, O. Chadebec, P. Labie, Y. L. Floch, and G. Meunier, *Automatic cuts for magnetic scalar potential formulations*, IEEE Transactions on Magnetics **41** (2005), no. 5, 1668–1671.

[129] A. Vion, R. V. Sabariego, and C. Geuzaine, *A model reduction algorithm for solving multiple-scattering problems using iterative methods*, IEEE Transactions on Magnetics **47** (2011), no. 5, 1470–1473.

[130] R. Wait and A. R. Mitchell, *Finite element analysis and applications*, John Wiley & Sons, 1985.

[131] H. Wallén, I.V. Lindell, and A. Sihvola, *Mixed-impedance boundary conditions*, IEEE Transactions on Magnetics **59** (2010), no. 5, 1580–1586.

[132] B-Z. Wang, *A domain decomposition finite-difference method utilizing characteristic basis functions for solving electrostatic problems*, IEEE Transactions on Electromagnetic Compatibility **50** (2008), no. 4, 946–952.

[133] J. P. Webb and B. Forghani, *A single scalar potential method for 3D magnetostatics using edge elements*, IEEE Transactions on Magnetics **25** (1989), no. 5, 4126–4128.

[134] T. Weiland, *Time domain electromagnetic field computation with finite difference methods*, International Journal of Numerical Modelling **9** (1996), 295–319.

[135] R. M. Wojciechowski, A. Demenko, and J. K. Sykulski, *Comparative analysis of a-v and A-T-T0 calculations of induced currents in multiply connected regions*, IET Sci., Meas. Technol **6** (2012), no. 5, 312–318.

[136] H. T. Yu, *A finite element method for computing 3D eddy current problems*, IEEE Transactions on Magnetics **32** (1996), no. 5, 4320–4322.

[137] Z. Zhang, Z. Yun, and M.F. Iskander, *3D tetrahedron ray tracing algorithm*, IEEE Transactions on Magnetics **4** (2001), no. 4, 730–733.

[138] D. Zheng and K. R. Davey, *A boundary element formulation for thin shell problems*, IEEE Transactions on Magnetics **32** (1996), no. 3, 675–677.

[139] M. Zucca, G. Lorusso, F. Fiorillo, P. E. Roccato, and M. Annibale, *Highly efficient shielding of high-voltage underground power lines by pure iron screens*, Journal of Magnetism and Magnetic Materials **320** (2008), 1065–1069.

Contents

List of Figures

List of Tables

Version history

April 20, 2013 : original revision

Generated on July 14, 2013